

# University of Southampton Research Repository

Copyright © and Moral Rights for this thesis and, where applicable, any accompanying data are retained by the author and/or other copyright owners. A copy can be downloaded for personal non-commercial research or study, without prior permission or charge. This thesis and the accompanying data cannot be reproduced or quoted extensively from without first obtaining permission in writing from the copyright holder/s. The content of the thesis and accompanying research data (where applicable) must not be changed in any way or sold commercially in any format or medium without the formal permission of the copyright holder/s.

When referring to this thesis and any accompanying data, full bibliographic details must be given, e.g.

Thesis: Author (Year of Submission) "Full thesis title", University of Southampton, name of the University Faculty or School or Department, PhD Thesis, pagination.

Data: Author (Year) Title. URI [dataset]

# **University of Southampton**

FACULTY OF ENGINEERING AND PHYSICAL SCIENCES

Engineering Materials, Mechanical Engineering

# Mechanistic evaluation of fatigue mitigation approaches to extend the fatigue lifetime of low-pressure steam turbine blades

DOI: 10.5258/SOTON/T0078

by

Ara Masis Khodavirdi

ORCID ID: 0009-0008-8717-0673

THESIS FOR THE DEGREE OF DOCTOR OF PHILOSOPHY

April 2025

# University of Southampton

#### **Abstract**

#### FACULTY OF ENGINEERING AND PHYSICAL SCIENCES

**Engineering Sciences Unit** 

Thesis for the degree of Doctor of Philosophy

# Mechanistic evaluation of fatigue mitigation approaches to extend the fatigue lifetime of low-pressure steam turbine blades

By

Ara Masis Khodavirdi

The increasing use of renewable energy sources requires the energy output demand from fossil-fuel fired power plants to become increasingly sporadic. Thus, the Steam Turbines (ST) used in fossil fuel power plants are now subjected to a higher frequency of start-stop cycles and the use of ageing plant needs to be safely extended for the remaining proposed lifetime. ST blades are typically manufactured using martensitic stainless steel (MSS) due to the corrosion resistant properties and high achievable strength and fatigue resistance. This increase of loading frequency leads to premature end of predicted life compared to the original design, leading to more frequent maintenance cycles and potentially sooner than expected blade replacements. Also, due to an earlier than predicted decommissioning of power plants, the blades are too costly to replace hence an enhanced maintenance schedule was considered. The proposed maintenance process consists in grinding out of any observed fatigue short cracks in the fir tree notch root and shot peening. The process was evaluated by previous studies as potentially effective in increasing fatigue lifetimes in some MSS alloys, FV566 and FV448 namely. The focus of the current study is to evaluate the blade-to-blade variability effects of another MSS, FV520B, on shot-peening and its effects on a lifing model proposed to reduce the conservatism of fatigue lifetime prediction of ST blades. The current study focuses on FV520B, a stainless-steel alloy with a precipitation hardened martensitic microstructure. The delivered material was from exservice blades, hence an initial analysis to verify the provided material matched expected FV520B features was conducted. Chemical and microstructural analysis confirmed the material to be FV520B. Mechanical and hardness testing was performed to analyse potential variability between blades. Results from microstructural and mechanical testing showed FV520B having scatter in fine microstructural features, mainly lath size, which correlated to hardness variations explaining scatter observed in both hardness and mechanical properties.

Fatigue testing was performed to study the effect of the variation in properties and microstructural features on baseline fatigue properties and to compare FV520B with prior literature. Results showed consistency in stage II fatigue growth rates between FV520B samples from different blades, as well as consistency with FV566 performance. The threshold values from different blade of FV520B were found to be different and dependent on fine microstructural features like lath size. Crack tip opening displacement results indicated some effects from yield stress variation on fatigue crack opening effects near

threshold but in stage II the consistency between samples remained. Fracture surface observations between tested samples indicated a higher dependency of crack growth on laths at near threshold  $\Delta K$  levels. The crack was observed to grow more tortuously at  $\Delta K_{th}$  levels progressively transitioning to smoother more transgranular growth as  $\Delta K$  increased, the phenomena was observed consistently between blades.

Short crack testing was performed on FV520B U-notched samples in 3-point bend under load control with two different surface conditions, polished and shot peened. The peening process was consistent with prior research on similar martensitic alloys from turbine blades. The residual compressive stresses after peening on FV520B were found to be consistent with the peening of FV566, indicating the peening process is equally effective on different blade alloys. Short fatigue crack growth testing was carried out at different strain ranges to evaluate the beneficial effects of peening, compared to polished unpeened samples, in terms of lifetimes and crack growth rates. Shot peening was found to increase fatigue lifetime in FV520B even at quite high local strain levels in a notch root under bending. Results also suggest FV520B was able to retain residual compressive stresses and have increased lifetimes at higher strain ranges when compared to FV566. Crack growth rate analysis in terms of  $\Delta K$  showed strain range to have little effect on crack growth rate in polished samples, with growth rates being comparable to rates derived from long crack testing when characterised in terms of  $\Delta K$ . The crack growth rate in peened samples showed a reduced growth rate at relatively low  $\Delta K$  levels with some increase for higher  $\Delta K$ compared to the unpeened case. Indicating residual compressive stresses retarded crack growth in the near-surface residual stress layer but had a decreased effect as they grow further into the depth. Paris law constants were also extrapolated from short crack tests and long crack tests.

A mechanistic based lifetime prediction model originally proposed by Cunningham was applied with some modifications to FV520B. The model accounted for different phases of fatigue lifetimes, initiation, short crack growth and long crack growth. The number of cycles in each phase was either extrapolated from empirical data or iteratively calculated based on crack growth rate information gathered experimentally. The model was found to be conservative in lifetime prediction of fatigue in polished samples, but significantly overestimated lifetime for peened conditions. The conservative prediction for polished samples were attributed to the unaccounted-for arrested cracks and the assumptions on growth rate homogeneity. The overestimations in peened cases were likely due to the equally spaced initiation site assumption which strongly affects the expected coalescence phase, and given the greater number of initiation sites in the shot peened case this is likely to overestimate the onset of coalescence. Another factor to consider was the expected variations in crack growth rate through the residual compressive stress layer were not taken into account.

Further data collection and analysis will be necessary to improve the model as well as highlighting the need to account for the spacing of initiation sites and the onset of coalescence as well as the varying crack growth rates in peened samples.

# Table of contents

AbstractTable of contents	
List of figures	
Research Thesis: Declaration of Authorship	17
Acknowledgement	
Chapter 1 Introduction	
1.1 Background	
1.2 Research question	22
1.3 Aims and objectives	22
Chapter 2 Literature review	23
2.1 Introduction to steam turbine operation and related issues	23
2.2 Low pressure steam turbine blades materials	23
2.3 9-12 Cr precipitation hardened stainless steels	24
2.4 Fatigue in metals	26
2.4.1 Fatigue life evolution	27
2.4.2 Crack initiation behaviour	28
2.4.3 Fatigue crack propagation of long and short cracks	29
2.4.4 Crack coalescence behaviour	34
2.4.5 Fatigue life approaches	37
2.4.6 Total life approaches	37
2.4.7 Damage tolerance approach	38
2.4.8 Effects of austenite volume fraction in fatigue crack initiation and propagation	39
2.4.9 Notch effects on fatigue	40
2.5 Shot peening effect on fatigue	41
2.5.1 Effects of residual compressive stresses in fatigue lifetime models	43
2.6 Summary	44
2.6.1 Material characterisation	44
2.6.2 Fatigue Summary	44
2.6.3 Shot peening and the effects on fatigue	44
Chapter 3 Materials Characterisation	45
3.1 Introduction	45
3.2 Methodology	46
3.2.1 Sample extraction and references to blade geometry	46
3.2.2 Sample preparation for metallography	16

	3.2.3 Microstructural characterisation	47
	3.2.4 Chemical analysis	47
	3.2.5 Electron backscatter diffraction analysis	48
	3.2.6 Hardness testing	48
	3.2.7 Monotonic tensile testing	49
3.3	3 Results	49
	3.3.1 Microstructural characterisation	49
	3.3.2 Material composition	53
	3.3.3 Compositional and microstructural comparison of blade steel alloys.	54
	3.3.4 Hardness results	56
	3.3.5 Microstructural feature size analysis	57
	3.3.6 XRD crystallographic analysis	59
	3.3.7 Monotonic tensile testing	59
3.4	4 Discussion	60
3.	5 Conclusions	64
Cha	pter 4 Baseline fatigue properties related to microstructure variations	65
4.	1 Introduction	65
4.2	2 Methods	65
,	4.2.1 Long crack testing	65
	4.2.2 Fractography	67
4.3	3 Results	67
,	4.3.1 Baseline Paris law behaviour and crack tip opening displacement	
	behaviour	
ı	4.3.2 Fatigue threshold relation to microstructural and mechanical properti 72	es
,	4.3.3 Effect of $\Delta K$ and microstructure on crack path behaviour	73
4.4	4 Discussion	79
4.	5 Summary and conclusions	80
	4.5.1 Summary	80
	4.5.2 Conclusions	80
Cha	pter 5 Mitigation strategy effectiveness from shot peening	82
5.	1 Introduction	82
5.2	2 Methods	83
	5.2.1 Shot peening residual stress measurement via XRD	83
	5.2.2 Shot peening	84

5.2.3 Rougnness testing	85
5.2.4 Short crack fatigue testing	85
5.2.5 Depth to length ratio measurement	87
5.3 Results	88
5.3.1 Fatigue lifetime of blade steels	88
5.3.2 Residual stress profile from shot peening	89
5.3.3 Comparison of measured roughness after peening	92
5.3.4 Fatigue lifetime comparison between peened and un-peened sample 92	S
5.3.5 Fracture surface analysis of polished and peened steel	94
5.3.6 Crack initiation and coalescence analysis in relation to strain range a shot peening	
5.3.7 Crack aspect ratio	98
5.3.8 Crack growth behaviour	99
5.3.9 Lifetime predictions	102
5.4 Discussion	104
5.4.1 Fatigue lifetimes	104
5.4.2 Peening effects in residual compressive stresses and surface roughness	105
5.4.3 Peening effects on fatigue lifetimes	105
5.4.4 Fracture surface, crack initiation and coalescence behaviour of peen and polished steels	
5.4.5 Crack aspect ratio comparison between peened and polished steels	106
5.4.6 Crack growth rate comparison of peened and polished steels	107
5.4.7 Mechanistic based fatigue lifetime prediction model	107
5.5 Summary and conclusions	109
Chapter 6 Summary and Conclusions	111
6.1 Summary	111
6.2 Materials characterisation	111
6.3 Baseline fatigue properties	112
6.4 Short crack fatigue behaviour in U-notches with residual compressive stresses	113
6.5 Mechanistic based fatigue lifetime prediction model	113
6.6 Conclusions	114
Chapter 7 Future work	116
Chapter 8 Appendix A: Long crack testing procedure	118

8.1 Appendix A: SEN bend test setup		
8.1.1 Calculation of load range for target ΔK value	119	
8.1.2 Calculating adjusted $\Delta K$ value during post-test analysis	120	
8.1.3 Noise reduction	121	
Chapter 9 Appendix B: Crack growth rate calculations	122	
Chapter 10 Appendix C: Determination of short crack ΔKsurface	125	
Chapter 11 Appendix D: Summary of tested samples	128	
Chapter 12 References	129	

# List of figures

Figure 2-1Firtree connection (in yellow square) of low pressure stage turbine (Type LD66) blade [2]
Figure 2-2 microstructure of FV520B changes depending on final stage heat treatment temperature
and holding time [7] the three microstructures differ in the amount of austenite25
Figure 2-3 schaeffler diagram representing the Nickel and Chromium equivalents from the alloying
elements, this suggests the microstructural phases present in the steel [15]26
Figure 2-4 Illustration of the occurrence of persistent slip marling or persistent slip bands. (a), (b)
represent small surface defects in single and polycrystalline materials and (c) larger defects in single
crystal materials [36]
Figure 2-5. Atomic force microscopy observation of early stage crack initiation within a grain of 316L
stainless steel scanned from a plastic surface replica (showing the inverse of the sample surface) [37]29
Figure 2-6. Visual representation of the three fundamental loading modes a) Mode I is tensile
opening, b) Mode II is in-plane sliding and c) Mode III is anti-plane shear [33]
Figure 2-7 Schematic of the definition of crack tip opening displacement from [33]
Figure 2-8. Log $\Delta K$ versus crack growth rate representing the three regimes of typical long crack
propagation from [33]
Figure 2-9. Effects of crack opening and closing in stage II crack growth resulting in striation
creations[46]32
Figure 2-10 Schematic representing the semi-elliptical crack aspect ratio of short cracks in bending
under uniform applied tension[52]33
Figure 2-11 The illustration of two semi-elliptical cracks coalescing, causing the a/c ratio to be
temporarily much lower as the surface length doubles[35]
Figure 2-12. (A) Half crack length c (a in figure) versus number of cycles during crack coalescence
(solid line) and without coalescence (dashed line) from [56]. (B) Evolution of crack coalescence of
two in plane short cracks in stages (I) initial growth, (II) meeting, (III) coalescence, (IV) single short
crack growth and (V) evolution in long crack growth[57].
Figure 2-13 (A) representation of out-of-plane cracks developing at different $\Delta X$ and $\Delta Y$ crack tip
distances, typical of short crack behaviour[56]. (B) Out-of-plane crack growing example in U-
notched FV448 stainless steel[9]
Figure 2-14 Distribution of tensile stresses around the crack tip of (a) a single crack and (b) two
overlapping cracks[58]
Figure 2-15 Short crack growth evolution in pure copper, showing different stages of crack initiation
and coalescence. By 94% of lifetime all cracks were observed to be coalesced. The cracks
represented are only those contributing to the main crack, other cracks were not presented[56]36
Figure 2-16 summary from Nakagawa of changes in mechanical properties with varying retained
austenite [12]39
Figure 2-17 Fatigue life time relation to the percentage of austenite volume fraction from Yokoi [21]
39
Figure 2-18 visualisation of the effect of a peen impact on the surface of the material, where R is
the diameter of the peen, Z the indentation depth and hp the plastic zone depth [29]41
Figure 2-19 visualisation of surface roughness depending on varying parameters (a) is un-peened
ground surface, (b) T1, (c) T0, (d) T2, (e)T3 [32]42
Figure 2-20 comparison of shot peening residual stress in relation to depth, between flat and u-
notched samples [31]43
Figure 2-21 Comparison of notched samples (4.5 x 1.25 mm) with varying shot peening processes
[31]43
, = = ,

Figure 3-1 Sample extraction from turbine blade schematic, (a) representative turbine blade
geometry (add axes) (b) blade root cut out (add triangle), (c) geometric equivalent of extraction site
from blade root, (di-ii) original extracted blank and resulting bend from extraction site, (ei-ii) final
sample geometries in the form of U-notched fatigue samples and cuboids for microscopy46
Figure 3-2 Sample mounted in conductive bakelite, polished and etched using Villella's reagent47
Figure 3-3 Vickers indenter geometry, d1 and d2 being the diagonals of the indentation, h the
indentation depth, W the working depth48
Figure 3-4 Reduced dimensions of non-standard dog bone samples for tensile testing, dimension
ratios follow BS EN ISO 6892-1:2016 standards49
Figure 3-5 3D visualisation of the microstructure of FV520B etched samples at a 200x magnification
under optical microscope. Arrow indicates apparent directionality in ZX plane50
Figure 3-6 optical microscopy 3D image of FV520B microstructure at 1000x magnification51
Figure 3-7 SEI imaging of FV520B microstructure at 500x magnification, showing (A) alumina
inclusions, (B) martensite laths, and (C) reverted austenite pockets at grain boundaries51
Figure 3-8 martensite laths and reverted austenite pockets (A) with barely visible precipitates(B)52
Figure 3-9 alumina inclusion (indicated by arrow) in in the FV520B martensite laths53
Figure 3-10 The microstructure of FV566 in three planes. Optical microscope image of FV566 etched
with Vilella's reagent showing a stringer. FEG SEM (SEI mode) image showing the microstructure of
FV566 etched with Vilella's reagent [6]
Figure 3-11 FV448 microstructure representation in 3 dimension (L) longitudinal/rolling direction,
(T) transverse and (s) short transverse. FV448 presents with a typical martensitic structure
composed of visible prior austenite grain boundaries and martensite lath packs, aluminium oxide
stringers are also found. The alloy has been found to be stronger in the rolling direction[35]56
Figure 3-12 comparison of measured hardness in different FV520B flat erosion plates from different
blades (labelled as BX75, BX2 etc), these include possible scatter due to microstructural features like
reverted austenite, and compared to other blade alloys from literature (FV448,FV566) [18], [109]57
Figure 3-13 FV520B blade to blade variation in martensitic lath size distribution in relation to
hardness. The measurement was taken from a grain boundary angle graph via line intercept58
Figure 3-14 Visualisation of prior austenite grains superimposed to martensitic lath microstructure.
BX75 was likely subjected to strain induced grain boundary refinement which skewed parent grain
analysis results. in order from softer to hardest AX73,BZ71,BW1, with BW1 having a relatively
smaller prior austenite grain size
Figure 3-15 XRD pattern of 4 FV520B blades, 71, 73, 75 and 1. The peaks represent the points at
which X-rays diffract from the crystal lattice planes of the analysed material. The 4 patterns match
and indicate peaks only typical of martensitic structure for FV520B, with no peaks suggesting
austenite content
Figure 3-16 Comparison between FV520B blade mechanical properties and estimated UTS via 3xHV.
Each blade was tested twice, the datapoints were plotted as the average value of the two tests60
Figure 3-17. FV520B micrograph in peak hardened condition from Clark[98] (A) and FV520B peak
hardened condition micrograph taken from ex-service blades61
Figure 3-18 XRD pattern of FV520B ex-service blades (above) measured in the current study. Peak
hardened FV520B XRD pattern from literature[98] (below), the two pattern present the same Bragg
angle but different peak intensities63
Figure 4-1 FV520B sample dimensions for SENB3 testing [115], detail shows depth of the notch, the
width is equivalent to the EDM wire diameter (0.33mm) used to cut the notch. Where L=55 mm,
Span = 40 mm, a = 1.6 mm, W = 6.8 mm and B = 7.5 mm66
Figure 4-2 Typical DCPD set up for long crack testing, this includes current wires at the ends of the
sample, the reference PD wires approximately 10mm apart to read the uninterrupted voltage
sample, the reference is wines approximately follow apart to read the diffillentapted voltage

through the material and crack growth PD wires to read the voltage increase as the crack grows. Typically, the set up includes a thermocouple for testing at high temperatures but was not used...66 Figure 4-3 comparison of measured hardness in different FV520B flat erosion plates from different blades (labelled as BX75, BX2 etc), these include possible scatter due to microstructural features like reverted austenite, and compared to other blade alloys from literature (FV448,FV566) [18], [109]68 Figure 4-4 Sample extraction from turbine blade schematic, (a) representative turbine blade geometry (b) blade root cut out, (c) geometric equivalent of extraction site from blade root with 1,2,3 corresponding to A,B,C in the sample ID first letter, (di-ii) original extracted blank and resulting bendbars from extraction site with u, um Im I corresponding respectively to W, X, Y and Z in the ID Figure 4-5 Long crack test data comparison between different blade samples. Test consisted in an initial load shedding test to identify the threshold load range and subsequent constant load test. The Paris law regime is consistent between blades, while threshold behaviour varies between samples. ......69 Figure 4-6 Paris law behaviour plot comparing FV520B and FV566. The two martensitic stainless steels used in LP steam turbine blades present very similar crack growth rate behaviours in Paris law Figure 4-7 Prediction of number of cycles to failure with increasing ΔK of FV520B and FV566 using Paris law material constants and assuming LEFM. ......71 Figure 4-8 Crack tip opening displacement comparison between samples of different FV520B blades. Blades differ in yield strength and UTS as well as HV with blade 75 being the softest and 1 being the hardest. The crack tip opening displacement accounts for differences in strengths, Paris law regime behaviour is relatively unaffected while crack growth near threshold is more affected. 72 Figure 4-9 Comparison of strength and ΔKth with hardness for FV448, FV520B and FV566 ......73 Figure 4-10 Long crack test fracture surface (a-i,d-i,c-i) and cross-section imaging (a-ii, d-ii, c-ii) at  $\Delta K_{th}$ ,  $\Delta K = 10$  MPaVm,  $\Delta K = 22$  MPaVm. (a-i-ii) At  $\Delta K_{th}$  fracture surface suggests grain morphology, mainly the martensite laths, influence crack growth. This is also observed in the cross section of the fracture surface. (b-i-ii) As ΔK increases and load remains constant (Paris law regime) the lath microstructure has less of an effect. The crack propagates more trans-granularly. Visible alumina inclusions show no effect on crack path. (d-i-ii) At high ΔK the fine microstructure (laths) has a Figure 4-11 Long crack test fracture surface (a-i,d-i,c-i) and cross-section imaging (a-ii, d-ii-iii, c-ii) at  $\Delta K_{th}$ ,  $\Delta K = 10$  MPaVm,  $\Delta K = 22$  MPaVm. (a-i-ii) At  $\Delta K_{th}$  fracture surface suggests grain morphology, mainly the martensite laths, influence crack growth. This is also observed in the cross section of the fracture surface. (b-i-ii) As ΔK increases and load remains constant (Paris law regime) the lath microstructure has less of an effect. The crack propagates more trans-granularly. Visible alumina inclusions show no effect in crack path. (d-i-ii) At high ΔK the fine microstructure (laths) has a lesser effect on the crack growth rate. (d-iii) Secondary cracks are also observed to be halted by alumina inclusion in their path.......75 Figure 4-12 Long crack test fracture surface (a-i, d-i, c-i) and cross-section imaging (a-ii, dii, c-ii) at  $\Delta K_{th}$ ,  $\Delta K = 10$  MPa $\sqrt{m}$ ,  $\Delta K = 19$  MPa $\sqrt{m}$ . (a-i-ii) At  $\Delta K_{th}$  fracture surface suggests grain morphology, mainly the martensite laths, influence crack growth. This is also observed in the cross section of the fracture surface. (b-i-ii) As ΔK increases and load remains constant (Paris law regime) the lath microstructure has less of an effect. The crack propagates more trans-granularly. Visible alumina inclusions show no effect in crack path. (d-i-ii) At high  $\Delta K$  the fine microstructure (laths) has a lesser effect on the crack growth rate. Secondary cracks are also observed.......76 Figure 4-13 Long crack test fracture surface (a-i, d-i, c-i) and cross-section imaging (a-ii, dii, c-ii) at  $\Delta Kth$ ,  $\Delta K = 10 \text{ MPa} \sqrt{m}$ ,  $\Delta K = 20 \text{ MPa} \sqrt{m}$ . (a-i-ii) At  $\Delta K_{th}$  fracture surface suggests grain morphology, mainly the martensite laths, influence crack growth. This is also

observed in the cross section of the fracture surface. (b-i-ii) As ΔK increases and load
remains constant (Paris law regime) the lath microstructure has less of an effect. The crack
propagates more trans-granularly. Visible alumina inclusions show no effect in crack path.
(d-i-ii) At high $\Delta K$ the fine microstructure (laths) has a lesser effect on the crack growth rate.
Secondary cracks are also observed77
Figure 5-1 Schematic of XRD [108] set up for residual compressive stress analysis.(A) The stresses
were measured in the longitudinal direction using radial x-rays and the transverse stresses using
axial x-rays. The top grey area was peened,(B) measurements were taken both in the U-notch and
on the peened flat surface83
Figure 5-2 schematic representing the shot peening process effects when a shot hits the
surface of the material treated [90]84
Figure 5-3 characteristic U-notch geometry with k=1.685
Figure 5-4 surface replication method workflow based on predicted fatigue lifetime of samples86
Figure 5-5 Projected length of crack in u-notched samples[35]86
Figure 5-6 visual representation of the depth to length ratio of the measured cracks and of method
used to determine the a/c ratio of cracks after heat tinting. The real fatigue crack region observed
on a fracture surface is measured and then interpreted as a semi-ellipse with given length c,
allowing to extrapolate a. [35]
Figure 5-7 replica analysis example where the final fracture crack is measured in the last replica and
the constituent cracks are then measured (and designated) in reverse chronological order87
Figure 5-8 Representation of the process of coalescence between multiple crack in a short
fatigue crack growth scenario. In (I) we observe two cracks initiating then growing in a
semi-elliptical fashion (II) until fully coalesced (III) to then grow until the crack is extended
through the width (IV) and (V)[35]
Figure 5-9 Fatigue lifetime comparison of 3 alloys (FV448, FV566 and FV520B) in the as received and
polished surface conditions (All Un-peened) (with FV520B being only in the polished condition) of
U-notched bend samples89
Figure 5-10 Compressive residual stress profile in the longitudinal and transverse direction
measured via XRD of FV520B(a) and FV566 (b). The measurements were performed in the as-
peened condition in the root of a U-notch bend sample and the flat region of the sample for
comparison90
Figure 5-11 Compressive residual stress profile in the transverse direction measured via XRD of
FV448. The measurements were performed in the as-peened, 50% fatigue lifetime and after 1
fatigue cycle in the root of a U-notch bend sample[8]91
Figure 5-12 Compressive residual stress profile in the longitudinal direction measured via XRD of
FV448. The measurements were performed in the as-peened, 50% fatigue lifetime and after 1
fatigue cycle in the root of a U-notch bend sample[8]91
Figure 5-13 Roughness measurement comparison of peened samples between FV520B and FV448.
Showing higher roughness levels in FV448 as it's the softest of the two alloys. FV520B samples show
a consistent surface roughness condition
Figure 5-14 Lifetime comparison of FV520B U-notched polished (un-peened) and Peened
samples at different strain ranges. The peened samples show an increase in lifetime in
most cases at different strain ranges93
Figure 5-15 Lifetime in the polished (un-peened) and peened conditions of FV566 and FV520B, for
equivalent strain ranges FV520B shows longer lifetime. At high strain ranges FV520B in its peened
condition shows higher lifetimes compared to FV566, which indicated a higher retention of residual compressive stresses
·
Figure 5-16 SEM fractography of FV520B fatigue crack initiation site in polished (a) and peened (b)
samples. Polished sample crack initiation was observed to be microstructural dependent, while shot

peened samples cracks were prevalently observed to originate by defects caused by the peening
process
Figure 5-17 fracture surface of polished (a) and peened (b) FV520B samples tested at 1.2% $\Delta\epsilon$ and
scanned using a focus-variation microscope. The fracture surfaces were not observed to have
significant changes in number of crack initiations and crack growth behaviour after initiation95
Figure 5-18 number of crack initiation events versus strain range applied to the U-notch for the
peened and polished surface condition96
Figure 5-19 Short fatigue crack initiation and coalescence events of FV520B polished U-notched
samples at a strain range of $1.2\%\Delta\epsilon$ where it was observed at the end of lifetime an increase of
coalescence events and no initiations in the end 10% of lifetime97
Figure 5-20 Short fatigue crack initiation and coalescence events of FV520B polished U-notched
samples at a strain range of 0.95%Δε where it was observed a minor presence of initiations at the
end stages of lifetime and lower number of coalescence events as opposed to higher strain range
tests
Figure 5-21 Short fatigue crack initiation and coalescence events of FV520B peened U-notched
samples at a strain range of 0.95%Δε where it was observed a minimal number of main crack
contributor crack initiation for the majority of the lifetime except for in the last 5%98
Figure 5-22 Comparison of peened and polished surface crack half-length to crack depth ratio a/c vs
surface half length c. The crack depth was measured by using the semi-ellipse fit method. The
resultant trend shows how cracks in peened samples are shallower for increasing surface crack
length99
Figure 5-23 FV520B crack growth rate vs ΔK of u-notched polished samples tested at two different
strain ranges. The crack growth behaviour was observed to be consistent for the given surface
condition regardless of strain range100
Figure 5-24 FV520B crack growth rate vs ΔK of u-notched polished and peened samples tested at
two different strain ranges. The crack growth behaviour was observed to have a lower growth rate
in the peened condition for the same strain range, the lower growth rate was linked to residual
stresses in the peened samples100
Figure 5-25 FV520B crack growth rate vs $\Delta K$ of u-notched polished and peened samples tested at
two different strain ranges compared to long crack testing of FV520B at constant load. The crack
growth behaviour of long crack tests was observed to be consistent with short crack growth rate
behaviour in the polished case. The Shot peened condition was observed to have an overall lower
growth rate compared to long crack results101
Figure 5-26 Comparison between long crack test results and shot peened U-notched crack growth
rates in FV520B. The crack growth rate of peened samples were found to be lower than long crack
results
Figure 5-27 workflow to calculate the number of cycles for a short crack to reach a critical length in
the multiphase predictive model[6]102
Figure 5-28 Crack initiation sites versus strain range comparison for FV520B U-notched samples in
polished and peened conditions determined via fracture surface observations103
Figure 5-29 Comparison of predicted and real fatigue lifetimes of FV520B (Alloy A). Predicted
lifetime for peened samples showed an overestimation of the lifetime by 3 times. Polished surface
condition lifetime predictions underestimated the lifetime104
Figure 8-1 Schematic model of the SEN bend sample showing the configuration of the wires spot
welded to the sample and the roller locations for 3-point bending118
Figure 8-2 SENB3 sample drawing showing the dimensions of a (crack length), $\it W$ (sample width) and
B sample breadth118
Figure 9-1 Smoothed DCPD data output for a SEN fatigue test. Where the variable voltage output is
plotted against time122

Figure 9-2 Calibrated crack length (a) plotted against number of cycles	.123
Figure 9-3 Secant method to determine the gradient of a vs N to determine da/dN	.124
Figure 9-4 Crack growth rate plotted against calibrated crack length for a SEN fatigue test using	
DCPD crack monitoring	.124
Figure 10-1 Drawing of U-notch sample with dimensions labelled. Cross section of U-notched	
sample through notch centre containing semi-elliptical crack with dimensions labelled	.125

Research Thesis: Declaration of Authorship

Print name: Ara Masis Khodavirdi

Title of thesis: MECHANISTIC EVALUATION OF FATIGUE MITIGATION APPROACHES TO EXTEND THE FATIGUE LIFETIME OF LOW-PRESSURE STEAM TURBINE BLADES

I declare that this thesis and the work presented in it are my own and has been generated by me as the result of my own original research. I confirm that:

- This work was done wholly or mainly while in candidature for a research degree at this University;
- Where any part of this thesis has previously been submitted for a degree or any other qualification at this University or any other institution, this has been clearly stated;
- Where I have consulted the published work of others, this is always clearly attributed;
- Where I have quoted from the work of others, the source is always given. With the exception of such quotations, this thesis is entirely my own work;
- I have acknowledged all main sources of help;
- Where the thesis is based on work done by myself jointly with others, I
  have made clear exactly what was done by others and what I have
  contributed myself;
- Parts of this work have been published as:

Signature: Date: 11/07/2024

# Acknowledgement

First and foremost, I would like to thank my supervisors Philippa (Prof Philippa Reed) and Andy (Dr Andrew Hamilton), whose unwavering support, guidance, and patience have been invaluable throughout the course of the last five years and I'm very grateful for it. The journey of my PhD was a long one, a "bit" longer than I had originally planned. But as an experimentalist will tell you, nothing ever goes to plan, it's the nature of experimental work. I was warned about how lonely a PhD can be, I'll admit it definitely can feel that way, but I was lucky, looking back, as I was never alone trough it. I want to take this chance to be grateful, for all the good that I've received throughout this journey. There is a very long list of people that I need to thank for being there and helping me get here, I'll do my best to include as many as I can.

A heartfelt thank you to my parents. To my Mum, who from day one, far before the PhD, believed in me, supported me with infinite love and patience. I am not sure I would have even come anywhere near where I am without you. If there is anyone to dedicate this work to, that's you mum. To my Dad, who did his best to love and support me, a thank you.

A very special thank you to my uncle Saro and aunt Siran, who supported and helped me in my journey from day 1, I wouldn't be here without your support, I always have you both in my thoughts.

To all my family, around the world, no matter how far, thank you for always being proud of me and making me grateful for being part of this big, wonderful family.

My colleagues and friends from 3021. Ben Cunningham, who taught me everything in my early days, whose friendship and mentorship will always be invaluable. Dieguito, thank you for all the laughs and kicks in the behind that helped me get though it, you were a rock to lean on for the past five years. Yuanguo, for all the good laughs and late evenings in the office together. Joe, our fun times, in the office, pub and conferences will never be forgotten. Luke, thank you for the XRD scans and for allowing me to give back to the "3021 universe" a little of the good I had received. Maruti, somehow the universe got us both to Southampton and I'm grateful it did. Anthony Tony, thank you for the walks, the gym , the friendship.

To Yousef, Rosie, Rob E, Aga, Jay, Mostafa, Andy R, Rob Hamil, Terry, Alvaro, Kim, Mike, Sebastian, Corentin, Anqi, Anto, Charlie BT, Zef, Cesar, Maria, Ahmed, Deepak, Efi, Danae, Talha from the office and beyond, thank you all.

A big thank you to my friend Charlie and his partner Oana who was there from the early days of the journey, who was infinitely patient and supportive through the thick and thin of it all. Lokesh and Caolin, thank you for the years of friendship, the advice and adventures together.

A very special thank you to my cherished friend and housemate Vanessa, for being there and going above and beyond through the best and the worst of this journey. I wouldn't have made it through if it wasn't for your support. I wish the universe will be always as kind as you.

To my brothers from Itsoc, Sade and Giacomo, it is difficult to put in words how invaluable our times together were, so I'll just say thank you and wish for much more to come.

Jerry and Ludo, you two have been like a shining star in dark times, good friends and brothers, thank you.

The following people I need to thank in the my native languages, Armenian and Italian. I will start with Italian.

Caro Luca, grazie per essere stato un mentore, un amico e un coach fantastico. Hai creduto in me e mi hai insegnato come tenere duro quando ne avevo il piu' bisogno. Mi hai trasmesso molto piu' di quanto qualche parola possa descrivere. Ma una cosa la posso dire, senza cio che mi hai insegnato e tutto il tuo sostegno, non ce l'avrei mai fatta. A te e Silvia, un abbraccio caloroso.

Oshin, sei stato e sempre sarai mio fratello, potrei scrivere piu' di qualche libro su di noi, ma mi limito, per ora, a darti un abbraccio dal profondo del mio cuore.

Giorgio, ti diro' questo, a scrivere il tuo nome ho sorriso e mi sono commossso allo stesso tempo, anche tu, fratello o come preferiamo noi "Akhper", grazie di tutto. Dalle giornate passate a Milano 3, le chimate infinite per studiare ognuno nel proprio angolo di mondo, e per l'infinita fede l'uno nell'altro.

Bav, Fede, mi hai visto evolvere attraverso molte fasi di vita, e mi hai sempre incoraggiato a spingere oltre, grazie, per tutto il tuo supporto.

Grande Ale, sono felice di aver trovato un amico e fratello come te, grazie per avermi fatto ridere quando piu mi serviva.

Nico, le serate, le risate, la fratellanza, l'amicizia, sempre li nonostante tutto, grazie mille fratello.

Filo, Ema JC, Dalpa, Vale, Ale Binaz e tutti gli altri che sono stati li in questi anni, grazie.

Gaia, cara amica, grazie per esserci stata in questo viaggio, le parole non sono sufficienti a descrivere la mia gratitudine, un abbraccio.

Rebecca, grazie per il supporto che mi hai dato in questi anni. Sei stata una cara amica dal principio, sono felice di aver condiviso momenti belli della vita con te, amica mia, un abbraccio.

Un grazie a tutti I miei Prof delle superiori per avermi trasmesso le loro passioni nelle materie che mi insegnarono, e per il sostegno nel mio percorso nel Regno Unito.

Infine un grazie ai miei Fratelli e Sorelle, Scout e Guide AGESCI, per l'impatto positive che avete avuto nella mia strada.

And finally, a few words in Armenian, the language of my forefathers, my native land, Armenia.

եւ վերջապես, մի քանի բառ Հայերենով՝ իմ նախնիկների լեզուն, հայրենիքս Հայաստան։

Նրանք որ վերևից են նայում, կը ցանկանայի որ այստեղ լինեին որ մասնակցէին այս ռոպեները ինձ հետ։ Փափագում եմ որ նրանք այստեղ լինեին որ իրենց գրկեի և շնորհակալութիւն հայտնեի նրանց անձամբ, բայց վստահ եմ որ նրանք ինձանով հպարտ են նույնիսկ հեռվից։

Իմ սիրելի մեծպապներս և մեծմամերս՝ Լևոն, Ջարիկ, Արմենակ և Սոնիկ, շնորհակալ եմ ձեզնից, դուք էք իսկ պատճառը որ այսօր ես այստեղ եմ, Վերջին հատվածը նվիրում եմ ձեզ , ձեր ջանքերին, ձեր զոհաբերություններին, որոնք ոչ թէ միայն ապահովել են ձեր զավակներն և թոռնիկներն ունենան լավ կյանք, նաև մեր ազգը և մեր հոգին կարողանա ապրի, դիմանա և ծաղկի, չնայած պայքարներին։ Վերջում, ցանկանում եմ շնորհակալություն հայտնել Աստծուն ՝ միշտ զգացել եմ քո օգնությունը, դու միշտ լսել ես իմ աղոթքը, և ես դրանից միշտ երախտապարտ եմ։

#### Արա Մասիս Խոդավիրդի

Finally, I would like to thank God, far too often I felt your helping, you have always listened to my prayers, and for that I am grateful.

# **Chapter 1 Introduction**

#### 1.1 Background

The increasing use of renewable energy sources is morphing the landscape of energy production and its related issues[1]. The transition between "old" generation power plants, such as coal and gas plants, to the "new" renewable power generation units (e.g. photovoltaic panels and wind turbines) are the source of fatigue related problems in the "old" plants. The lack of constant and controllable output from renewable sources requires the old generation plants to compensate by varying their output at a higher frequency[2]. Turbines in old plants are designed to withstand a predetermined number of cycles, which includes a safety margin to avoid premature failures. They are typically made of martensitic stainless steel (MSS) and were commissioned 30-50 years ago[3]. The higher frequency of start-stop cycles results in the total lifetime cycles of the turbine being reached sooner than anticipated[4]. This increased frequency of cycling has been reported as exacerbating fatigue cracks in the root region of blades within the low-pressure stage of turbines. Given the pending decommissioning of many power plants in the medium term, the cost of replacing large portions of the turbines to overcome the issue of premature failure is not viable[3]. Hence solutions which extend the lifetime of the blade's maintenance are now required. The proposed maintenance process for turbines consists in grinding out of fatigue cracks in stress concentration features such as fir tree roots and shot peening of the ground surface. The changes in geometry and residual stress field from the maintenance process requires an effective method to predict fatigue lifetime post treatment[5]. The effects of geometric change after crack grind out has been previously studied and was not further investigated in this work [6], [7]. The effects of shot peening on the stress in the notch and its effects on fatigue crack behavior has been investigated in previous literature for a few MSS ex-service blades. Previous studies included the effects of overloads and effects of surface roughness on the fatigue behavior of peened notches[5], [8], [9], [10], [11], [12], [13], [14], [15], [16]. Furthermore, lifetime prediction models were proposed that accounted for crack growth in residual stress fields of notches and the resulting complex fatigue short crack behavior[6]. The effects of blade-to-blade material variability on the response to shot peening, subsequent fatigue crack growth and hence fatigue life predictions were the main focus of this work. The project studies the influencing factors in blade durability for commonly used stainless steel turbine materials in legacy power plants, FV520B and FV566. A mechanistically informed lifing model was previously developed by Cunningham [6] to improve the prediction of fatigue life of the low pressure steam turbine material (FV566) after maintenance, we evaluate the method and its applicability to FV520B and how this interacts with the potential effects of blade-to-blade variability.

#### 1.2 Research question

The need to assess maintenance processes for steam turbine blades in the energy sector to reduce costs, is becoming increasingly essential. The gradual phasing out of fossil fuel plants makes the refurbishment of turbine blades, where possible, more favourable than scrapping old blades. Research is being conducted to extend the fatigue life of low-pressure steam turbines at the fir tree root. The proposed method is to grind out cracks and shot peen the surface. Studies have been conducted on the effectiveness of the method with results suggesting an increase in lifetime. Nonetheless, further research is necessary to verify the effectiveness of the process with different steel alloys, on which the method may have a different quantifiable impact.

The research question of this PhD is: "What is the impact of the microstructure and mechanical property blade-to-blade variability on the fatigue behaviour after shot peening of a steam turbine blade and how does this affect the use of a mechanistic based lifing model to predict its fatigue life?"

#### 1.3 Aims and objectives

The aim of the project then was to evaluate blade-to-blade microstructure and mechanical property variability effects on fatigue behaviour of ex-service stainless steel steam turbine blades after shot peening and assess a mechanistic based fatigue lifing model to reduce unnecessary conservatism of fatigue lifetime predictions.

A set of objectives were set to achieve the aim of the project:

- Characterise the microstructure and mechanical properties of FV520B to evaluate the blade-to-blade variability of ex-service blade material.
- Study the effects of blade-to-blade variability on baseline fatigue properties and crack growth behaviour.
- Study the effects of shot peening on fatigue lifetime for FV520B compared to other blade steel alloys.
- Evaluate a mechanistic based fatigue lifing model to confidently reduce the conservatism of turbine blade fatigue life after shot peening.

# **Chapter 2 Literature review**

#### 2.1 Introduction to steam turbine operation and related issues

Fossil fuel power generation plants commonly operate by using heat to generate high pressure steam, which is then channeled through turbines to generate power. The turbines are subdivided in stages, high pressure (HP) intermediate pressure (IP) and low pressure (LP) stage, each composed of several blades mounted on a rotor disk. The LP stage, which is the focus of the current study, operates at lower pressures and temperatures (250°C). compared to the other stages. The operation of the turbines consists in varying the speed of the turbine stages to match a desired output. The output demand of the power plants has been varying due to an increase in renewable energies usage[17]. The increase in output demand requires a higher frequency of speed-up/speed-down of the steam turbines. The turbine fatigue life is measured in cycles, each one consisting of the acceleration and deceleration of the turbine. The consequence is the number of cycles allowed for the lifetime of the blades is being rapidly depleted. Low pressure turbines are subject to fatigue crack initiations at multiple locations of the blade, including leading edge and at the fir tree root of the blade seen in Figure 2-1 [18]. The original maintenance timelines have been changed to allow for more frequent shutdowns. The increasing shutdowns for maintenance have driven up the cost of maintenance due to the more frequent need to change the blades that have reached end of life. Hence maintenance processes are being evaluated to increase, where possible, the fatigue life of the blades. The study will focus on the fatigue performance of the fir tree root of LP stage of the turbines.

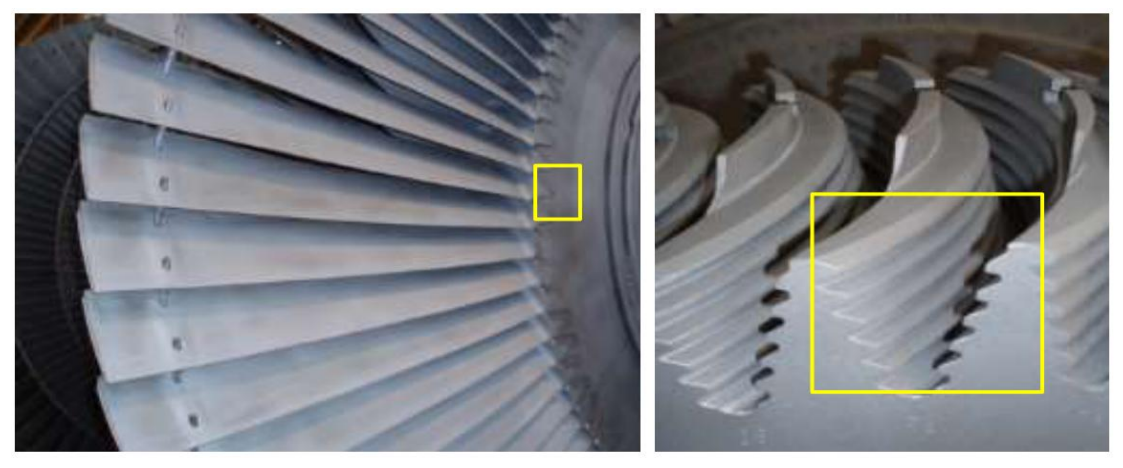


Figure 2-1Firtree connection (in yellow square) of low pressure stage turbine (Type LD66) blade [2]

The blades presenting cracks need to be extracted, evaluated and when possible maintained to continue service. The goal of current maintenance procedures in evaluation is to increase life of the blades from a fatigue perspective. The currently evaluated method of maintenance involves the grinding out of crack initiation sites at the notch and shot peening. The grind out of the crack removes the microcracks, while shot peening adds a residual compressive stress layer at the surface, which retards the formation of new cracks.

#### 2.2 Low pressure steam turbine blades materials

Low pressure steam turbines are required to have high tensile strength, corrosion resistance and good fatigue resistance. Stainless steels have been widely used as a steam turbine component material as it fulfills the necessary requirements both from a mechanical and corrosion aspect. Blades are subjected to stress fluctuations in various locations which are fatigue crack initiation sites. Fatigue failures in the blades occur 40% of the time on the aero foil, 26% on the shroud, 20% on the lacing hole and 14% on the blade attachment to the rotor

disk [19], [20]. The stress ranges at the different locations vary hence the material has to perform well both in Low cycle fatigue (LCF) and High cycle fatigue (HCF) regimes. In particular, blades are designed to last 40-50 years or a set number of start-up shut-down cycles. These cycles are equivalent to the designed LCF life of the blade. The number of starts per year have been increasing due to the irregular power demand from power stations with the increasing use of renewable energy systems. This has led to the expected fatigue life of the blades to be reached early compared to the original design. The blade material selected for this purpose is martensitic stainless-steel (MSS). Martensite is the result of a diffusionless transformation of austenite in a non-equilibrium single-phase structure, hence does not appear in the Fe-C phase diagram [21]. Further classification of MSS used for turbine blade are the precipitation hardened stainless steels (PHSS) which can be alloyed, and heat treated to achieve high strength levels mixed with good corrosion resistant properties. The current project focuses on the fatigue performance of FV520B PHSS.

#### 2.3 9-12 Cr precipitation hardened stainless steels

Precipitation hardened stainless steel (PHSS) are a class of stainless steels characterised by the precipitation strengthening mechanism employed to achieve high strength. The treatment involves the creation of precipitates at the grain boundaries, these are commonly nucleated by copper and chromium additions. The temperature and holding times of the treatments are what determines the final mechanical properties of the steel [22]. FV520B as a PHSS which is characterised by having chromium, nickel, and copper as its main alloying elements. Additional alloying elements are present, such as Ti, Mo, Mn that allow the precipitation of carbides during heat treatment and control the microstructure formation and provide high strength levels in the PHSS. The precipitates in FV520B are thought to be copper based [23] or preferentially Ni<sub>3</sub>Mo and Fe<sub>2</sub>Mo [24], [25]. From a corrosion standpoint Cr and Ni (and Cu where present) contribute to the enhanced corrosion resistance characteristics. Corrosion properties will not be discussed in this study, but it should be noted that it is a widely studied characteristic of PHSS in general and of FV520B [26], [27]. PHSS can be subdivided in martensitic (M), austenitic (y) or as a M+ y dual-phase fraction. FV520B falls in the last group with an M+ y microstructure, which is composed mainly from martensitic laths and contains a low percentage of austenite as seen in Figure 2-2.

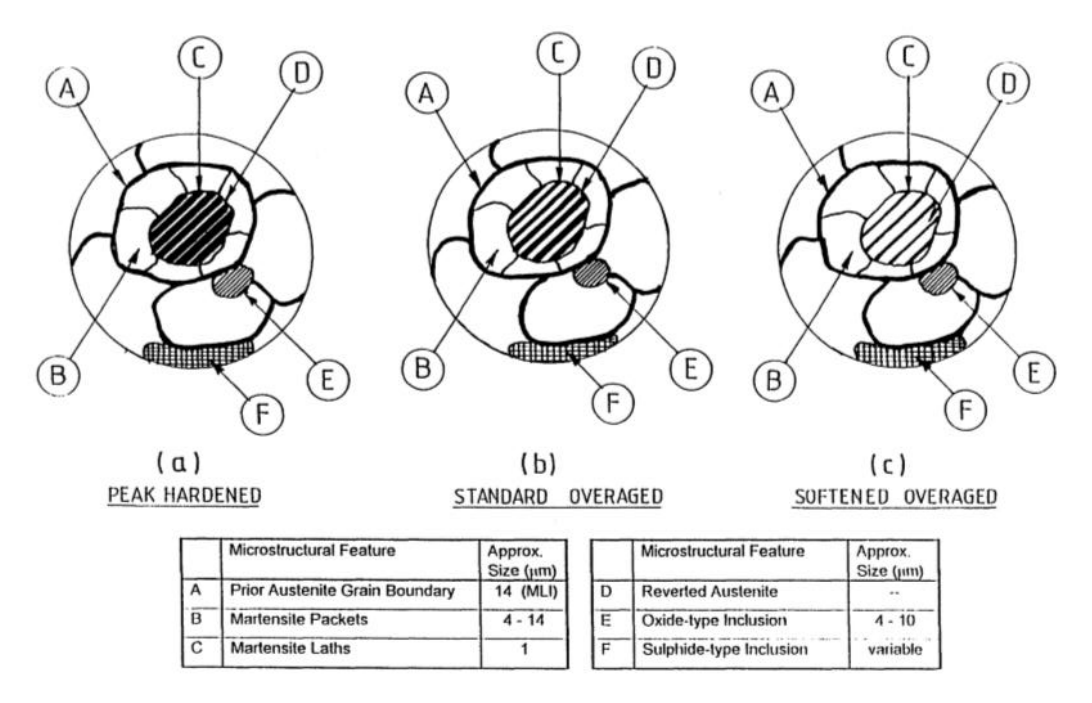


Figure 2-2 microstructure of FV520B changes depending on final stage heat treatment temperature and holding time [7] the three microstructures differ in the amount of austenite.

The percentage of  $\gamma$  is determined by the alloying elements and heat treatment process steps. The retained austenite in PHSS affects the fatigue performance[28], a characteristic which will be further explored in the present study. Precipitation of carbides occurs preferentially at the prior austenitic grain boundaries as well as in the retained or reverted austenite pockets. PHSS are generally classified by the percentage of Cr and Ni present, in the case of FV520B this is 13-5 PH (where PH stands for precipitation hardened). The percentage of Cr and Ni may vary within the class of PHSS depending on the specific alloy, Table 2-1 summarises the compositional range of FV520B from the Firth Vickers data handbook [29].

Table 2-1Compositional standard of FV520B from the Firth Vickers data book [29]

С	Si	Mn	Cr	Ni	Мо	Cu	Nb
0.07	0.7 Max	1.0 Max	13.2/14.7	5.0/6.0	1.2/2.0	1.2/2.0	0.2/0.7
Max							

The additional elements such as Ti, V, Co and W are not specified in the standards but are present in the alloy and contribute as carbide formers and stabilisers [22], [30], these are also indicators for the type of phases to expect in the microstructure. The Schaeffler diagram Figure 2-3 is a tool used to make such determination. The Schaeffler diagram is used to determine the microstructure of highly alloyed steels in terms of their Nickel and Chromium equivalents[31]. The Chromium equivalence is calculated by adding the weight percentages

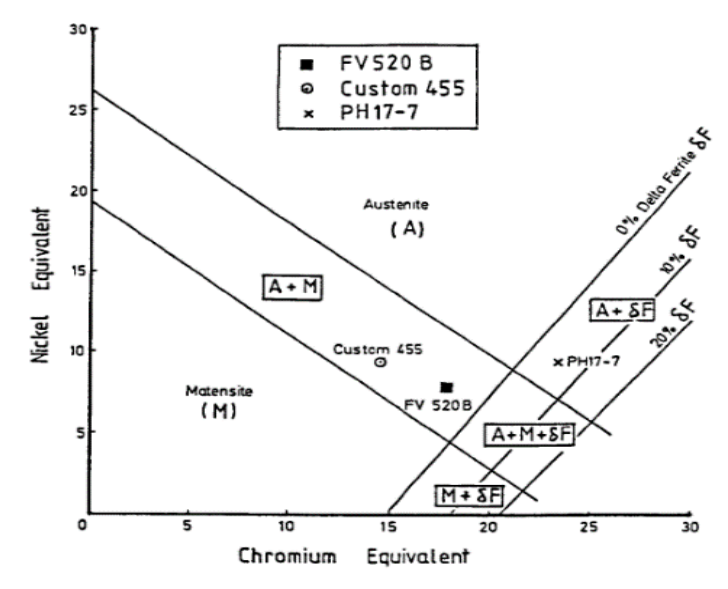


Figure 2-3 schaeffler diagram representing the Nickel and Chromium equivalents from the alloying elements, this suggests the microstructural phases present in the steel [15]

of ferrite forming elements and similarly the Nickel equivalent for the austenite forming elements[31].

The heat treatment (HT) of PHSS, and specifically FV520B, is what determines the ultimate microstructure and mechanical properties of the material. The HT of FV520B also varies fatigue performance [30] and ultimate mechanical properties. By observing the microstructure, it is possible to infer the heat treatment applied to the alloy. In Figure 2-2 the microstructure depending on heat treatment is illustrated, this allows comparison of the microstructure of the available material with a template which illustrates the expected microstructure dependent on the HT process used. The graph therefor allows the observed microstructure from metallography to be compared to an existing template.

In Figure 2-2 the reverted austenite (D) is austenite formed during the final aging process where the temperature is close to that where martensite reverts to austenite [23]. Oxide (E) and sulphite (F) type inclusions differ in composition and effect on the properties of the steel. Sulphite inclusions influence pit formation by being soluble in corrosive environments while oxide based inclusions tend to act as stress concentrators, influencing fatigue[23]. The differences between the three microstructures are mostly in terms of reverted austenite content (D) which is dependent on the amount of ageing[23].

#### 2.4 Fatigue in metals

Fatigue is the mechanism by which a component develops cracks as it is loaded cyclically, the cracks grow as the number of cycles increases until eventually the crack propagates rapidly, and the component fails. The three stages of fatigue crack growth are commonly defined as Stage I, crack initiation, Stage II, crack propagation, Stage III, final failure stage. The process may start from an undamaged part or propagate from existing defects/features. Persistent slip bands (PSBs) are a common initiation mechanism in undamaged smooth

components, where no surface defects or stress concentration features are present. Subsurface inclusions or microstructural features (E.g. a softer austenitic phase in a martensitic matrix) can also be the source. In practical engineering applications the possible causes for fatigue crack formations are not individual. A steam turbine blade, for example, may present stress concentration features in the form of notches as well as corrosion pits. But fatigue can be summarised in 5 main steps as described by Suresh (1998) [32].

- 1. Changes in the microstructure or substructure causing the nucleation of permanent damage,
- 2. Microscopic cracks are formed at the location of the permanent damage,
- 3. The growth and coalescence of the microcracks into dominant cracks, this part of the fatigue mechanism is usually referred to in engineering as the transition point between the initiation and propagation of fatigue cracks,
- 4. The stable growth/propagation of the dominant crack which will eventually lead to catastrophic failure or irreversible damage,
- 5. The final failure stage, which in engineering applications is usually seen as an acceleration of crack growth leading to a final fracture in the component.

The development of fatigue cracks can occur both at relatively low and high stresses compared to the monotonic mechanical properties (e.g. yield strength) of the material or component. Also, the number of cycles necessary for a component to fail can change drastically depending on the dominance of applied stress or strain. The distinction between the two cases is classified as Low cycle fatigue (LCF) for strain dominated loading and High cycle fatigue (HCL) for stress dominated loading[32]. The former is a strain dominated mechanism occurring at high stresses where plastic deformation occurs in each cycle, the latter is stress dominated and occurs at low stress levels and with predominantly elastic deformations occurring. Commonly the distinction is made between LCF and HCF in terms of cycles to failure separating the two at 10<sup>5</sup> cycles. In either case, fatigue crack formation is initiated at local stress concentration features such as surface roughness, voids or inclusions and is dominated by the irreversible movement of slip bands along shear planes which can occur even in the absence of other microstructural defects or local stress concentrations. The persistent slip bands (PSBs) initiating fatigue roughen even a planar surface of the material, hence creating a stress concentration point which causes a crack to initiate if one is not already present [32].

#### 2.4.1 Fatigue life evolution

The typical fatigue life stages in a simple tensile loading condition of a finite width and depth component, such as a bend bar or uniaxially loaded component, can be subdivided and characterised in 4 main phases[33]:

- 1. Crack initiation:
  - a. Microstructural and/or sub-structural changes occur in the material which cause permanent damage.
  - b. Progression of irreversible damage to the surface of the material causes the creation of microscopic cracks observable via microscopic equipment.
- 2. Short crack propagation:
  - a. The microscopic crack or flaws increase in size and transition to short cracks.
  - b. Stable propagation of macro-cracks.
- Crack coalescence:
  - a. The growth of two or more macro-cracks towards each other and join.

- b. One or more dominant cracks of different sizes grow and coalesce to eventually form a crack of length equal to the width of the component, which is defined as primary or main crack.
- 4. Crack propagation of the main crack:
  - a. The main crack grows in depth through the component (we define this as long crack growth) until complete fracture or structural instability is reached.

The stages described above will be further discussed in the following chapters in relation to the effects of cyclic loading and microstructural influence.

#### 2.4.2 Crack initiation behaviour

Fatigue crack initiation often occurs when surface defects, such as machining marks or scratches, act as stress concentration features causing crack nucleation. This is particularly true for components in industry. Other features may also cause crack initiation, that are derived by microstructural defects such as inclusions or voids, similarly environmentally derived factors such as corrosion pits can cause initiation. In some cases, cracks can occur sub-surface due to defects, this can occur in FV520B when inclusions cause sub-surface initiation in high cycle fatigue conditions[34]. And can occur in low cycle fatigue conditions due to sub-surface defects caused by surface treatments such as shot peening[35]. Regardless of loading conditions, defects deriving from surface treatments are likely to cause initiation of fatigue cracks and facilitate growth in fewer cycles compared to relatively "defect less" surfaces.

The formation of microscopic flaws can occur due to cyclic loading on defect free surfaces with no stress concentration features. Irreversible dislocation movement and shear displacement occurs due to repeated cyclic straining along preferentially oriented planes, these are referred to as persistent slip bands (PSBs). PSBs present as protrusions formed by intrusion and extrusion of material along slip bands, which increase surface roughness and where intrusions act as "micro-notches" acting as stress concentration features[36], these are illustrated in Figure 2-4.

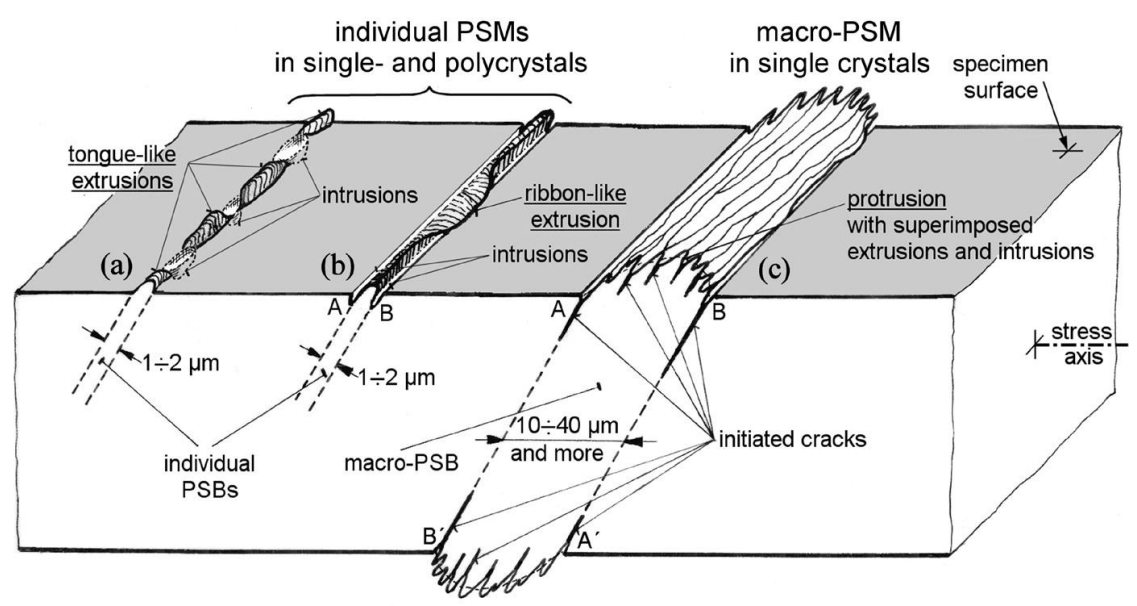


Figure 2-4 Illustration of the occurrence of persistent slip marling or persistent slip bands. (a), (b) represent small surface defects in single and polycrystalline materials and (c) larger defects in single crystal materials [36].

Slip bands in austenitic 316L stainless steels was observed using atomic force microscopy (AFM) and scanning electron microscopy[36], [37], [38], [39], [40]. Slip bands were observed as presenting ribbon like features similar to Figure 2-5. From a material science prospective, the crack initiation occurs at the microstructural level from the described protrusions. These features are challenging to observe using non-destructive techniques (NDT) which can typically be used to identify cracks of 0.5-1 mm in length. The methods used in the current project and in similar research can successfully identify cracks of 20  $\mu$ m in size[8].

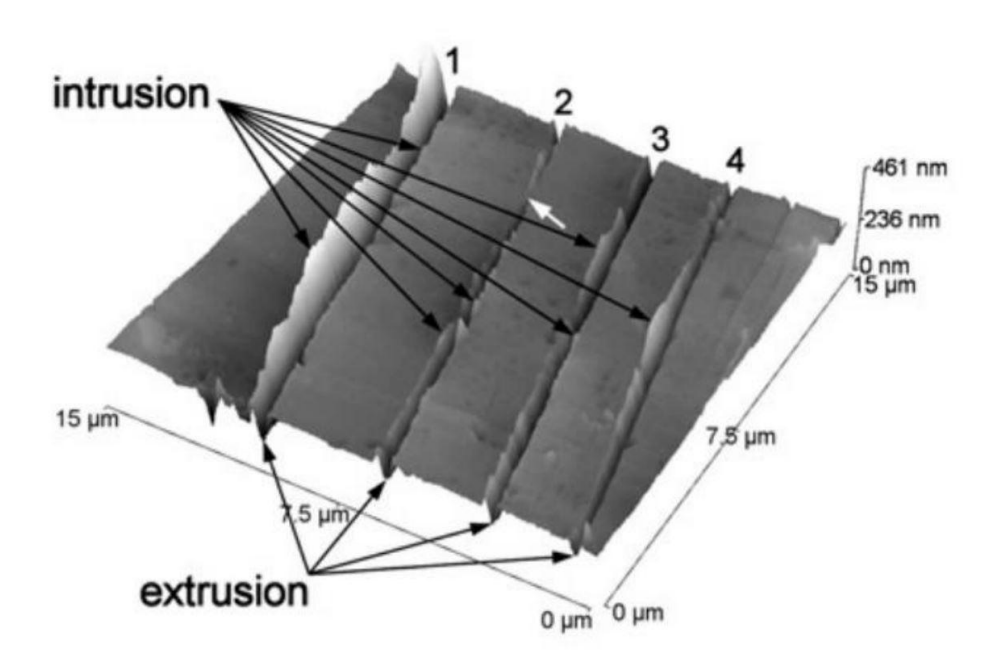


Figure 2-5. Atomic force microscopy observation of early stage crack initiation within a grain of 316L stainless steel scanned from a plastic surface replica (showing the inverse of the sample surface) [37].

#### 2.4.3 Fatigue crack propagation of long and short cracks

The cyclic loading that induces fatigue crack propagation can be defined in three modes, which are also applicable to monotonic loading. Tensile opening which is referred to as Mode I, as seen in Figure 2-6 (a) is the most common loading that causes fatigue and is the best analogue of the turbine blade service loading scenario that will be used in this thesis for the majority of testing. Mode II and Mode III are shearing modes Figure 2-6 (b),(c).

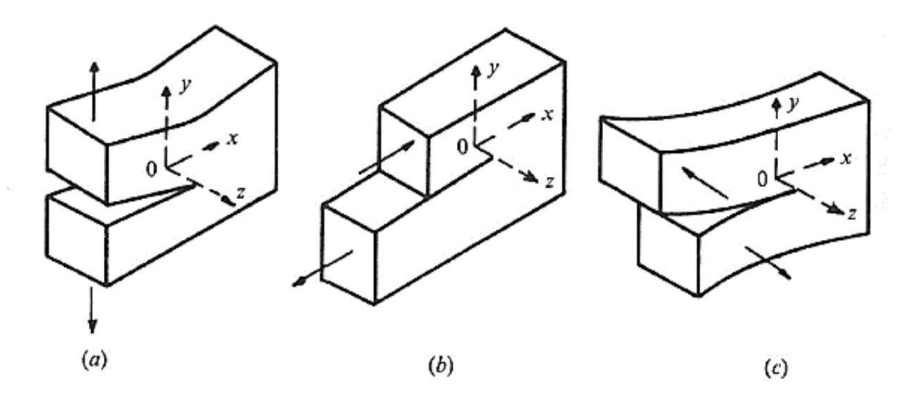


Figure 2-6. Visual representation of the three fundamental loading modes a) Mode I is tensile opening, b) Mode II is in-plane sliding and c) Mode III is anti-plane shear [33].

The magnitude of the fatigue crack driving force is commonly known as the stress intensity factor range ( $\Delta K$ ) and it has been found to control the rate of crack propagation and so is often used to describe crack growth behaviour. The original equation defining K was described by Griffith [41] and Westergaard (1939) as cited in [33] and is commonly used in linear elastic fracture mechanics (LEFM) to calculate the stress intensity factor range for mode I opening (Equation 2-1) taken from BS ISO 12108:2012.

$$\Delta K_I = f\left(\frac{a}{W}\right) \Delta \sigma \sqrt{\pi a}$$
 Equation 2 – 1

Where  $\Delta K_I = K_{Imax} - K_{Imin}$ ,  $f(\frac{a}{W})$  is the geometry correction factor as a function of crack length a and the sample depth W, and  $\Delta \sigma$  is the cyclic stress range. The equation can be used to describe the local crack tip stress state in components of varying geometry, with varying crack sizes and under different applied stresses, where crack growth is described consistently by  $\Delta K$ , i.e. similitude holds for varying cracks and applied stresses. The assumption used in the analysis is that of linear elasticity, with an asymptote in the elastic stresses approaching a theoretically atomically sharp crack tip, in reality the crack tip stresses will cause crack tip plasticity, creating a finite crack tip radius and a re-distribution of the expected elastic stress field around the crack tip. It is possible to calculate the radius of the plastic zone size around the crack tip under plane strain using Irwin's approach in Equation 2-2:

$$r_p = \frac{1}{3\pi} \left(\frac{K_I}{\sigma_v}\right)^2$$
 Equation 2-2

Where  $r_p$  is the radius of the plastic zone and  $\sigma_y$  is the yield strength of the material. As long as the crack tip plastic zone is small, and the crack and uncracked ligament are relatively large, K still defines the overall crack tip stress state reasonably well (small scale yielding). In cases of large scale yielding, such as may occur in short crack growth, where the crack is small with respect to the crack tip plastic zone, LEFM is no longer adequate in describing the crack stress or strain state and no longer describes crack growth behaviour (similitude breaks down). The use of elastic plastic fracture mechanics (EPFM) methods can then be used to account for the non-linear behaviour of the material (e.g.  $\Delta J$ ).

The quantification of the amount of plastic deformation that has occurred at the crack tip can also be done via the calculation of the crack tip opening displacement (CTOD) [42] where the distance between the two crack faces ( $\delta_t$ ) as seen in Figure 2-7.

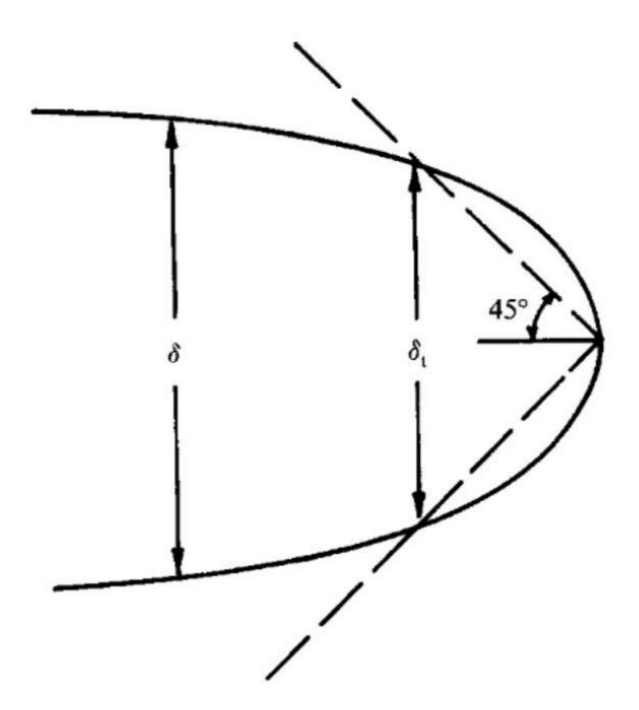


Figure 2-7 Schematic of the definition of crack tip opening displacement from [33]

Where the crack-tip yielding is sufficiently limited (small scale yielding), the stress intensity factor provides a reliable representation of the overall crack tip stress. The stress intensity factor can be related to the crack tip opening displacement via Equation 2-3.

$$\delta_t = \frac{{\kappa_I}^2}{{\sigma_{\nu}}E}$$
 Equation 2-3

Where  $K_I$  is the stress intensity factor in mode I loading,  $\sigma_y$  is the yield strength of the material and E is the young's modulus.

Long crack growth behaviour is typically used when referring to data obtained by testing a sample with an existing through-thickness crack and crack growth rate is presented as a function of  $\Delta K$ . Long crack growth rate and stress intensity factor range ( $\Delta K$ ) can be divided in three regimes of crack propagation as shown in Figure 2-8.

Stage I crack growth or Regime A in Figure 2-6 occurs in near threshold  $\Delta K_{th}$  and low  $\Delta K$  where the plastic zone in the crack tip wake is smaller than the grain size of the material. Crack growth in stage I and near to  $\Delta K_{th}$  are highly dependent on local microstructure both in long and short crack behaviour[43], [44]. In long crack testing the threshold value is usually obtained by load shedding techniques, where loads are reduced until the crack slows to under 10E-8 mm/cycle growth or fully arrests. In a short crack growth scenario, the low  $\Delta K$  values which normally result in slow growth rates in long crack testing may result in significantly higher crack growth rates, this is due to the limitations of the LEFM assumptions made for short crack  $\Delta K$  calculations as well as the reduced effect or lack of crack closure[33].

Stage II crack growth rate or regime B in Figure 2-8 occurs at typically higher  $\Delta K$  levels and is less dependent on the local microstructure of the material. The crack in stage II has typically grown through multiple grains and grows perpendicular to the direction of longitudinal tensile stress. The crack path is also typically less tortuous than stage I growth. The stage II growth rate relationship with  $\Delta K$  follows a power law relationship and can be modelled with the Paris-law fit[45]. We define the power law fit as Equation 2-4, where da/dN is the crack growth rate, C and m are empirically derived constants. The cyclic

loading effect on crack tip opening and closing in Stage II can cause striations and crack blunting effects[46] as illustrated in Figure 2-9.

$$\frac{da}{dN} = C(\Delta K)^m$$
 Equation 2-4

Stage III or regime C in Figure 2-8, the crack growth rate is exacerbated by monotonic bursts of plastic failure at ever increasing  $\Delta K$  levels, where a mixture of trans- and intergranular crack growth occurs.

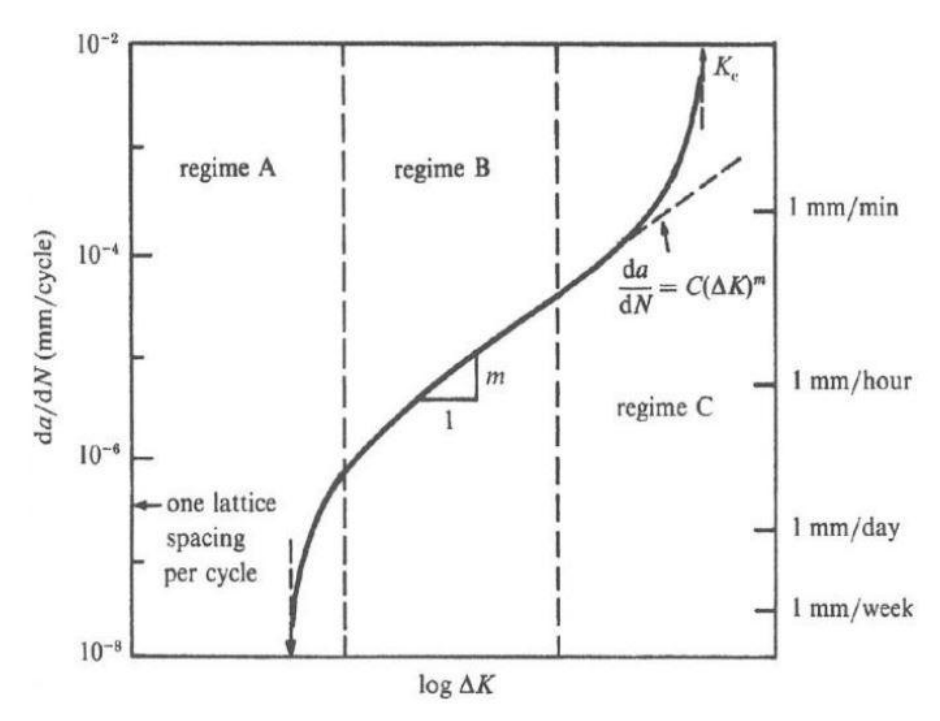


Figure 2-8. Log  $\Delta K$  versus crack growth rate representing the three regimes of typical long crack propagation from [33]

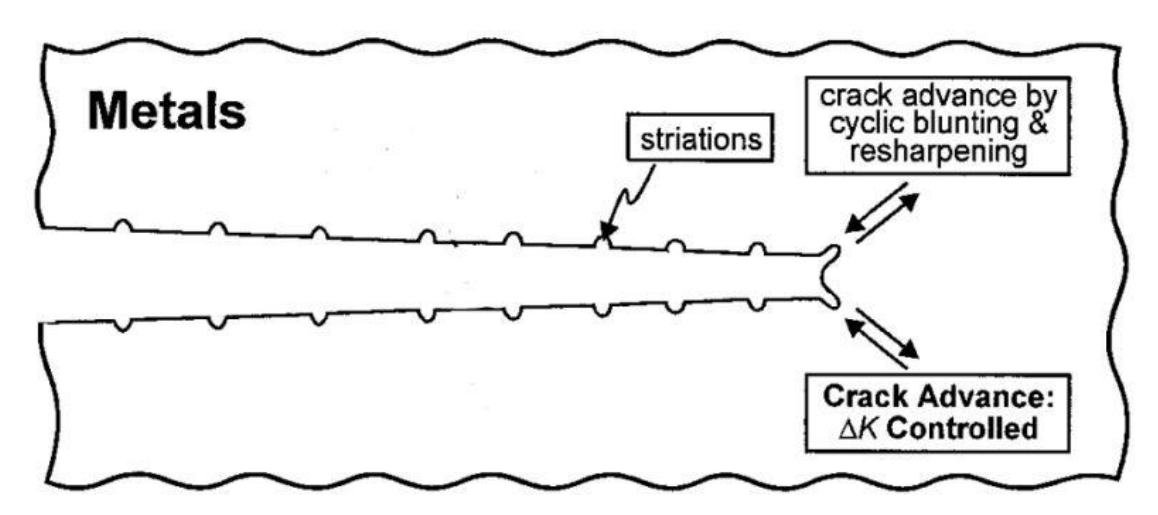


Figure 2-9. Effects of crack opening and closing in stage II crack growth resulting in striation creations[46].

In short crack growth scenarios, after crack initiation, the cracks may grow along the top surface and in-depth direction, which results in a semi-elliptical crack shape. Short cracks can be categorised in four types[33], dependent on crack length, microstructural feature size and ambient condition:

- Microstructurally small cracks: where the crack after initiation is smaller than the grain size of the material. The growth of these cracks is highly affected by the microstructural features surrounding it, such as inclusions, precipitates and grain boundaries, all of which can retard or arrest the crack[47]. These cracks typically grow transgranularly along slip bands.
- 2. Mechanically short cracks: these cracks have a surface length comparable to the near tip plastic zone size. These are typically larger than microstructurally small cracks and are less influenced by the microstructure. Both mechanically and microstructurally small cracks grow at a relatively higher rate for a given ΔK compared to long cracks, when assuming LEFM. This discrepancy is know as the short crack problem in literature [48], [49].
- 3. Physically short cracks: Generally of length smaller than 1 mm and with little dependence on plastic zone size, which is smaller than the crack length in this type of cracks. For physically short cracks the crack path is less tortuous and the crack growth behaviour is quite well described using LEFM. These cracks may exhibit less crack closure compared to longer cracks due to them often having no significant crack wake.
- 4. Chemically short cracks: the variability of environmental factors in harsh environments causes unpredictable crack growth behaviour, these cases will not be investigated in the thesis as they are not relevant to the service condition being investigated.

The crack shape factor in short cracks is defined as the ratio of the half surface crack (c) and crack depth (a), the ratio of which is interpreted as a semi-elliptical shape with length to depth ratio of a/c as illustrated in Figure 2-10. In specimens subjected to tension the a/c ratio is expected to be 1. In bending, such as the testing in the current thesis, the a/c ratio is expected to be lower than 1, this is due to the decreasing stress range gradient as the crack grows towards the neutral axis. The a/c ratios measured for other martensitic stainless steel blade materials, FV448 resulted in a range of a/c ratios of 0.9 to 1.2 which is higher than the expected 0.8 for a three-point bend loading condition[50]. The a/c ratio of FV566 another similar alloy was consistent with the expected 0.8 ratio. The increased ratios may be caused in FV448 from inclusions that exacerbate the crack growth[6], [35], [51].

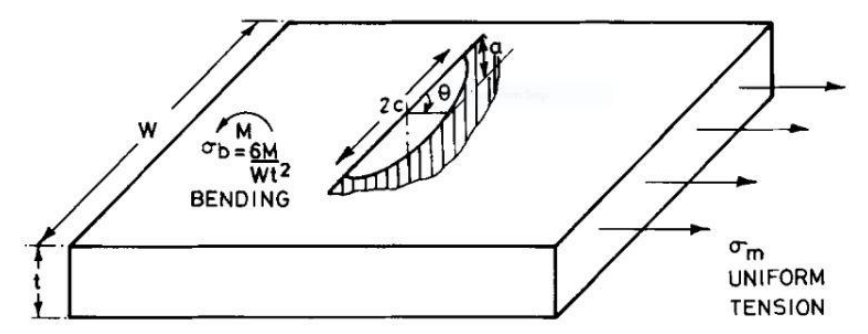


Figure 2-10 Schematic representing the semi-elliptical crack aspect ratio of short cracks in bending under uniform applied tension[52].

The stress intensity factor  $\Delta K$  for short cracks in a finite plate under bending was found to be related to its surface length from Holdbrook and Dover[53] and Scott and Thorpe [52]. The calculation of  $\Delta K_{Surface}$  is affected by a/c ratio, hence in case of coalescence of cracks, similarly to Figure 2-11, the calculation of  $\Delta K_{Surface}$  would be inaccurate as the crack would theoretically have a much lower a/c ratio.

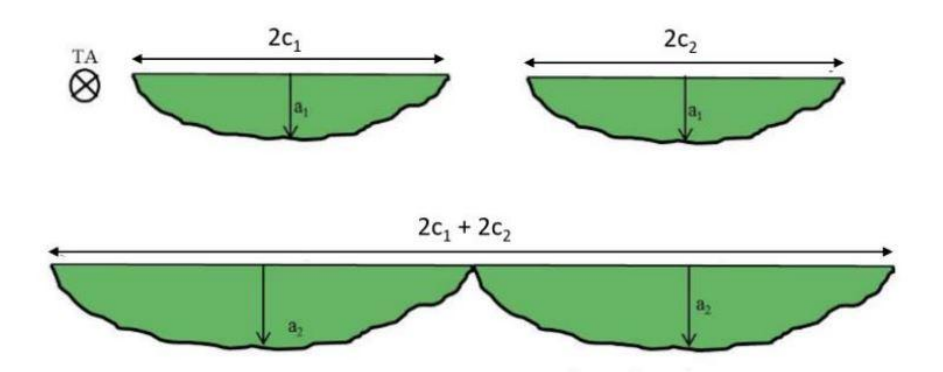


Figure 2-11 The illustration of two semi-elliptical cracks coalescing, causing the a/c ratio to be temporarily much lower as the surface length doubles[35].

#### 2.4.4 Crack coalescence behaviour

Crack coalescence can be interpreted, in its simplest form, as two in-plane cracks growing towards each other and joining to from one larger crack. The coalescence of short cracks will affect the growth rate of the two, or more, cracks as represented in Figure 2-12 (A). The half crack length after coalescence is increased significantly from  $a_1$  to  $a_2$  in Figure 2-12 (A) between cycles  $N_b$  and  $N_c$ , equivalent to stages I and II of Figure 2-12 (B) to then a fully coalesced crack in stage III of the same figure. During the coalescence process, the crack growth rate initially increases due to the higher localised stress at the crack tips. After coalescence at  $N_c$  the crack, although longer, temporarily has an abnormally low a/c ratio which causes the driving force to be biased in the depth direction, retarding the crack temporarily. Investigations on the  $\Delta K$  values during the coalescence process was investigated by Kamaya [54] and Tan and Chen [55]. They found that as the crack depth of the coalesced crack increases to an equilibrium of a/c, the crack growth rate of the crack approaches that of a single crack of the new length  $a_2$ .

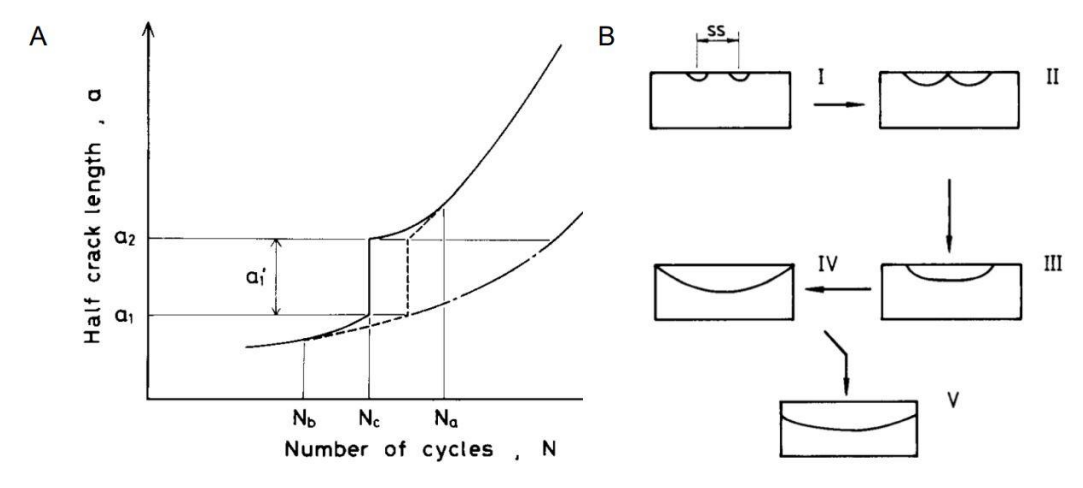


Figure 2-12. (A) Half crack length c (a in figure) versus number of cycles during crack coalescence (solid line) and without coalescence (dashed line) from [56]. (B) Evolution of crack coalescence of two in plane short cracks in stages (I) initial growth, (II) meeting, (III) coalescence, (IV) single short crack growth and (V) evolution in long crack growth [57].

The above scenario assumes in-plane crack coalescence, which is unlikely in most scenarios. The most likely growth pattern in flat surfaces or notches with large radiuses is out-of-plane growth as shown in Figure 2-13 (A,B).

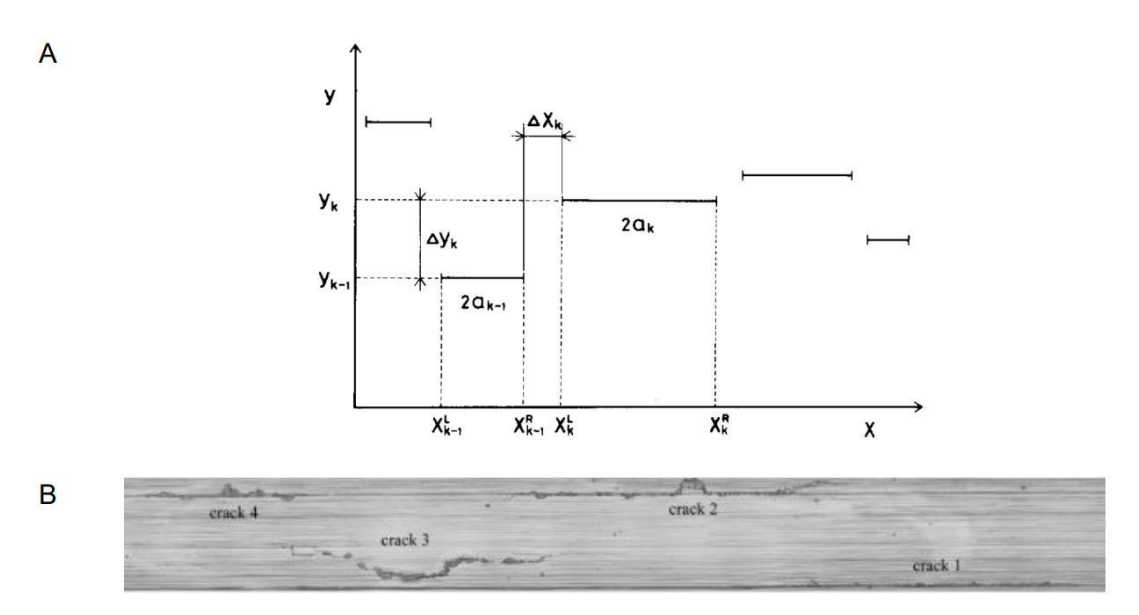


Figure 2-13 (A) representation of out-of-plane cracks developing at different  $\Delta X$  and  $\Delta Y$  crack tip distances, typical of short crack behaviour[56]. (B) Out-of-plane crack growing example in U-notched FV448 stainless steel[9].

The interaction of crack growth rates and related stress states has been investigated by several authors. When a single crack grows, the stresses on and below the crack redistributes causing a stress concentration at the crack tip and a region of reduced stress or shielded zone around the main length of the crack Figure 2-14 (a). Two cracks growing towards each other, Figure 2-14 (b), will overlap in the crack shielded zone causing the stress range at the intercepting crack tips to reduce, but the opposing crack tips will have increased stress range [58].

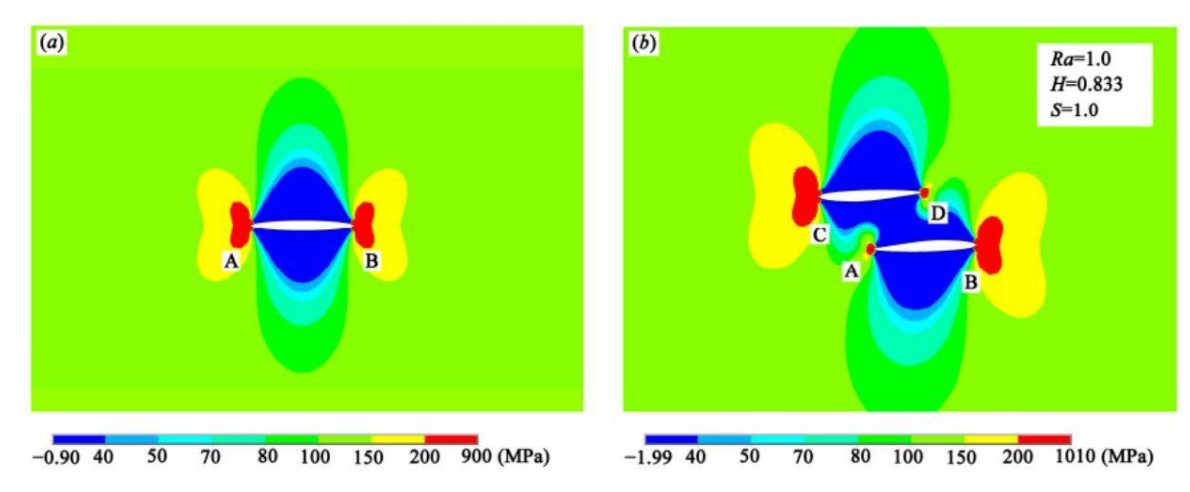


Figure 2-14 Distribution of tensile stresses around the crack tip of (a) a single crack and (b) two overlapping cracks[58].

The phenomena was observed in 2024-T351 aluminium alloy by Lefebvre and Sinclair [59]. Two cracks growing out-of-plane from each other were seen crossing into the crack shielded region, retarding the crack growth at the overlapping crack. The opposing crack tips were observed to accelerate significantly. The described shielding effect in coalescing cracks is typical in polycrystalline materials[60].

Hoshide [56] constructed an idealised schematic of short crack evolution to observe the interaction of multiple crack interactions. A pure copper flat plate of 5 x 1 mm was cyclically loaded with a strain range of 0.42% in the low cycle regime. The surface was replicated 20 times during the lifetime using acetyl cellulose. At crack initiation or 0% crack propagation lifetime, multiple short cracks were observed Figure 2-15. The initial high number of cracks indicates that multiple cracks initiated between two replication steps. At 36% of lifetime cracks started coalescing, reaching full coalescence at 94% of crack propagation life. The resultant crack progression visual indicates a very complex crack evolution process with likely very complex stress state interactions between cracks.

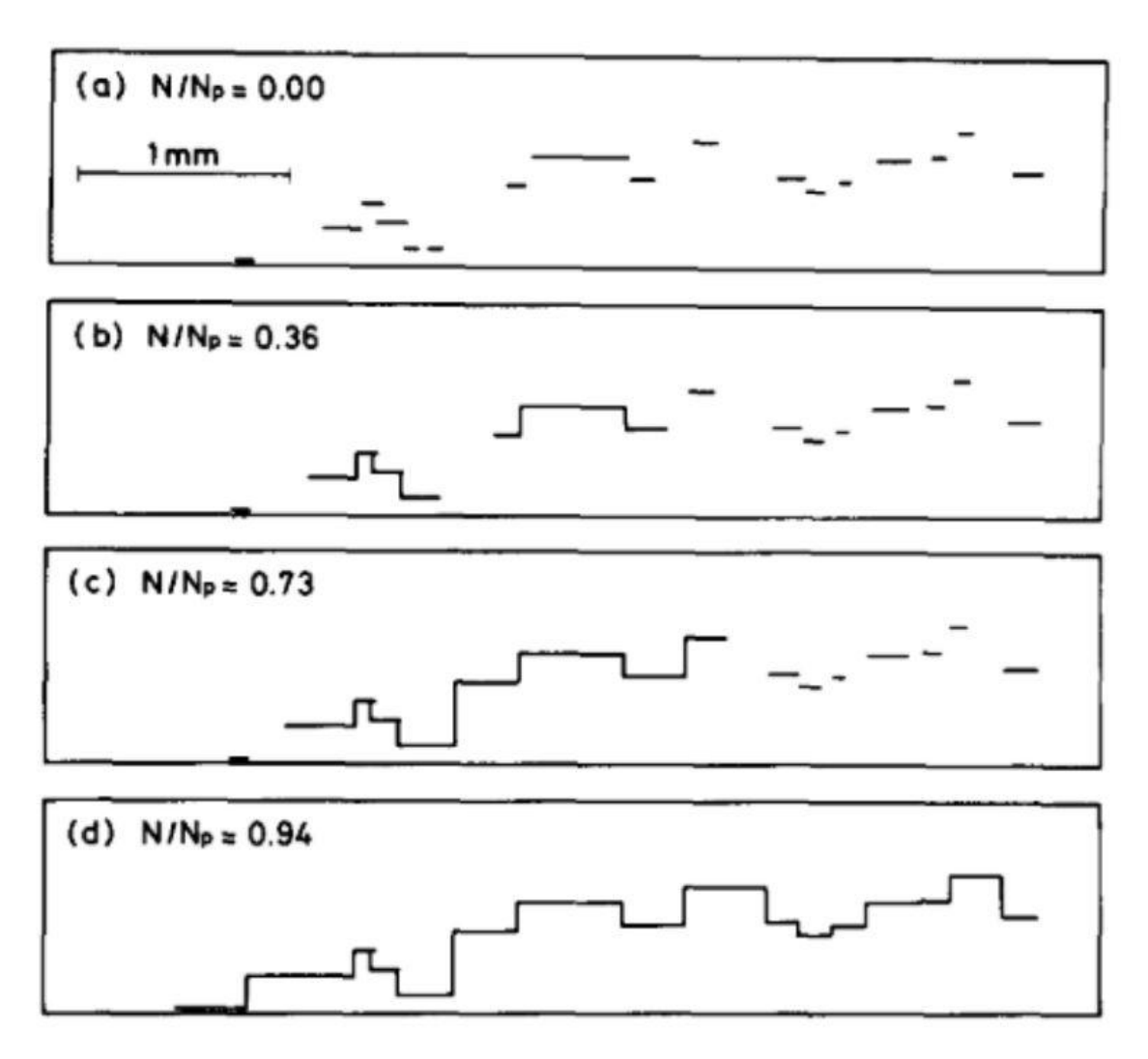


Figure 2-15 Short crack growth evolution in pure copper, showing different stages of crack initiation and coalescence. By 94% of lifetime all cracks were observed to be coalesced. The cracks represented are only those contributing to the main crack, other cracks were not presented[56].

The effects of out-of-plane distances between cracks and the effect on coalescence was investigated for a flat surface [9], [56], [57], [58], [59], [60]. When the distance of out-of-plane cracks is large, the sum of two coalesced cracks length is also large. The a/c ratio of the coalescing cracks did not seem to affect the behaviour. The short crack coalescence behaviour is consistent across a variety of materials, including steels and across different loading conditions [54], [60], [61], [62], [63], [64].

#### 2.4.5 Fatigue life approaches

An important aspect of component design and fatigue study is the distinction between fatigue life approaches used. The two main approaches are the *total-life approach* and the *damage-tolerant approach*. The former is typically used in fatigue design accounting the life from initial loading to final failure. The latter is what is most commonly used in industrial applications and assumes components to already have a pre-existing crack and has been discussed in section 2.4.6 where crack growth rate data is known[32].

#### 2.4.6 Total life approaches

The relationship between fatigue life and applied stress or strain can be expressed as a plot of cyclic stress (S) in relation to the number of cycles (N) to failure. The resulting S-N curve is used to illustrate fatigue life in materials and components. Stress range is used in High cycle fatigue (HCF) conditions where a lifetime of more than 10<sup>5</sup> is experienced, in this case the component is subjected to elastic stresses. In the case of Low cycle fatigue (LCF) the S-N curve is constructed using strain range, the cycles to failure are lower than 10<sup>5</sup> and components are subjected to elastic-plastic loading conditions.

The relationship used in HCF conditions where stress ranges are considered can be approximated by the Basquin relationship.

$$\frac{\Delta \sigma}{2} = \sigma_a = \sigma'_f (2N_f)^b$$
 Equation 2 – 5

Where  $\sigma'_f$  is the fatigue strength coefficient adjusted to account for necking,  $\Delta \sigma$  is the stress range applied, b is the fatigue strength exponent and N<sub>f</sub> is the number of cycles to failure.

When considering fatigue life in relation to strain range the Coffin Manson relationship is used as in equation:

$$\frac{\Delta \varepsilon_p}{2} = \varepsilon_f' (2N_f)^c \qquad Equation 2 - 6$$

Where  $\Delta \varepsilon_p$  is the plastic strain amplitude,  $\varepsilon'_f$  is the fatigue ductility coefficient and c is the fatigue ductility exponent. By using Hook's law to express the Basquin relation in terms of strain a relationship combining the two equations, Equation 2-5 and 2-6, can be obtained for the total strain amplitude as:

$$\frac{\Delta \varepsilon}{2} = \frac{\sigma'_f - \sigma_m}{E} \left( 2N_f \right)^b + \varepsilon'_f \left( 2N_f \right)^c$$
 Equation 2 – 7

Where  $\Delta\epsilon$  is the total strain amplitude and  $\sigma_m$  is the mean stress. The equation considers the effect of mean stress on the fatigue life. Which signifies a reduction in fatigue life as the mean stress increases. The approaches on calculating the reduction of fatigue life as a

function of stress can be obtained from Soderberg[65] equation 2-8, a modified Goodman[66] equation 2-9 and Gerber[67] equation 2-10 respectively:

$$\sigma_{a} = \sigma_{m=0} \left( 1 - \frac{\sigma_{m}}{\sigma_{y}} \right)$$

$$Equation 2 - 8$$

$$\sigma_{a} = \sigma_{m=0} \left( 1 - \frac{\sigma_{m}}{\sigma_{TS}} \right)$$

$$Equation 2 - 9$$

$$\sigma_{a} = \sigma_{m=0} \left[ 1 - \left( \frac{\sigma_{m}}{\sigma_{TS}} \right)^{2} \right]$$

$$Equation 2 - 10$$

Where  $\sigma_a$  is the non-zero mean stress amplitude,  $\sigma_{m=0}$  is the zero mean stress amplitude,  $\sigma_y$  is the yield stress and  $\sigma_{TS}$  is the ultimate tensile strength. The Soderberg is a conservative estimate of the mean stress effect which doesn't fit with experimental results, the Goodman model can be used for brittle metals which is validated experimentally. The Gerber model is suitable for ductile materials[32].

Furthermore, a linear damage accumulation rule, developed by Miner[68], is commonly used as a life prediction model.

$$\sum_{i=1}^{n} \frac{1}{N_f} = 1$$
 Equation 2 – 11

Which assumes a component has a given fatigue life which reduces after every cycle.

#### 2.4.7 Damage tolerance approach

Fatigue lifetime approaches for industrial applications are often modelled assuming already existing defects in a component. The existing defect is modelled as a crack of initial length a, and the final possible crack length before failure is estimated using LEFM.

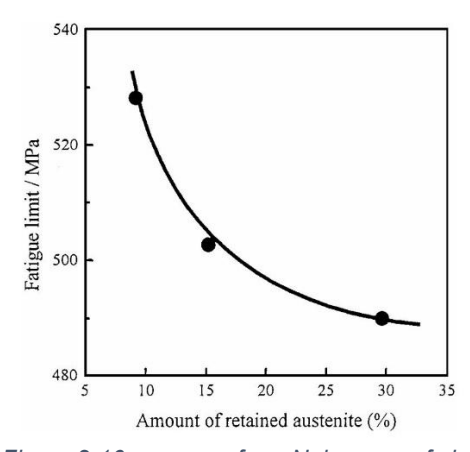
The crack growth of the defect under cyclic loading is modelled using the Paris Law equation mentioned in section 2.4.3 as Equation 2-4[45] . Where the  $\Delta K$  is the stress intensity factor and the constants C and m are empirically determined. The Paris law equation is used to describe Stage II crack growth rate. Stage I and Stage III can be modelled but are typically not used in industrial applications[12]. We can estimate the total number of cycles a crack will grow from an initial length  $a_i$  to a final length  $a_f$  by rearranging the Paris law equation and integrating from initial crack to final crack length Equation 2-12.

$$N = \frac{1}{C} \int_{a_f}^{a_i} \frac{1}{\Delta k(a)^m} da$$
 Equation 2 – 12

Where K(a) is the stress intensity factor described as a function of crack length a.  $\Delta K$  is typically a function of the geometry factor which accounts for crack length. For cases where the geometry is complex the approach in Equation 2-12 should be calculated iteratively.

# 2.4.8 Effects of austenite volume fraction in fatigue crack initiation and propagation

When studying a multi-phase steel, as in the present study, it is necessary to assess the influence of the secondary phases in the fatigue mechanism. Retained or reverted austenite (RA), depending on the applied HT process, content in steels can influence the overall mechanical properties and the fatigue life of the material. Nakagawa et all (1999)[28] showed the changes of mechanical properties as the RA percentage was altered in a Martensitic Austenitic stainless steel Figure 2-16.



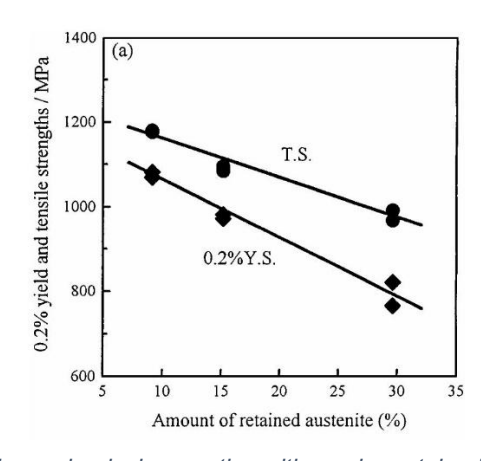


Figure 2-16 summary from Nakagawa of changes in mechanical properties with varying retained austenite [12]

It was also noted that an increase of RA does not constitute a benefit for mechanical properties in itself but allows to tailor the properties where needed. A relationship between RA and mechanical properties, where tensile and yield strength increase, was found by Nakagawa but can only be applied to the specific alloy. Nakagawa also concludes that a high percentage of RA is not beneficial to fatigue of the material as increasing RA% corresponds to a lower fatigue limit. The findings are consistent with studies in other steels from Yokoi et all (1996) [69] where an increase in RA reduced the overall fatigue life Figure 2-17.

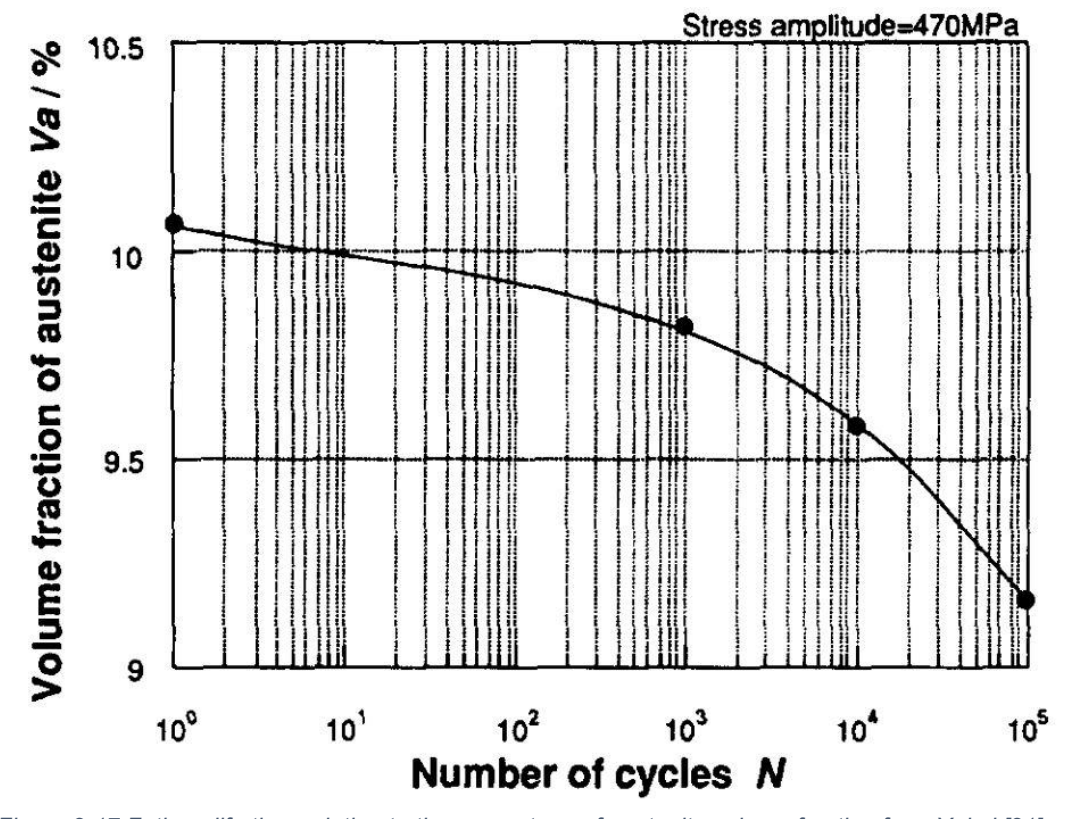


Figure 2-17 Fatigue life time relation to the percentage of austenite volume fraction from Yokoi [21]

This is in contrast with the findings of Da Silva et all (1999) [70] which suggests how higher RA levels present higher fatigue life. Nakagawa also highlights the effect of strain induced martensitic transformation in the steel which is hypothesised to benefit the mechanical properties overall. Martensitic transformation involves a volumetric change induced by strain or strain where face cantered cubic (FCC) austenite transforms to body cantered tetragonal (BCT), the crystal structure of martensite, causing compressive stresses in the material due to the volumetric change between FCC to BCT. Additionally, Yokoi observe how near surface RA retards the micro-crack propagation as it is transformed to martensite due to high local strains benefitting fatigue, when RA% is not at an excessive levels. The RA% most beneficial for the fatigue performance of a steel is not universal and often dependent on the microstructure and RA morphology. Gao et all (2020) [71] observe how RA morphologies influence the fatigue mechanism in bainitic steels. They observe how a film intergranular RA retards and arrests the crack development when strain induced martensitic transformation occurs. On the other hand, granular RA at the prior austenite boundaries promotes crack formation due to the easier slip band activation in the RA. Hilditch et all (2011) [72] compare the effect of RA in different multi-phase steels and further validates the influence on microstructure and RA% on the benefits of fatigue life. It was also noted how depending on strain range levels RA% can be of detriment or benefit in different class steels. Hu et all (1997) [73] report two scenarios depending on the strain level applied to the RA. For low strain fatigue the RA has been observed to reduce notch sensitivity as it absorbs strain energy at the crack tip as RA transform to martensite, this increases the cycles to crack initiation and crack propagation rate. When a high strain loading occurs, the martensitic transformation occurs early in the fatigue life, this promotes crack initiation and growth. Hu highlights how in high strain ranges a high RA% will significantly reduce fatigue life. Chai (2006) [74] reports how in two-phase steels, Martensitic austenitic in particular, the crack initiation occurs at the softer austenitic phase where cyclic plastic deformation causes intrusion/extrusion or dislocation pile-up at the grain boundaries. The process is in contrast with a typical inclusion caused crack initiation as explained by Chai. It should be noted that Chai does not report strain induced martensitic transformation.

#### 2.4.9 Notch effects on fatigue

Notches are a common feature in engineering components. These constitute a meso or macroscopic stress concentration feature, although they are often introduced with a geometry designed to mitigate fatigue crack initiation. The introduction of a notch on a macroscopic level creates a region of maximum stress per applied load in the component. When assessing fatigue lifting models the effect of the notch on the fatigue sensitivity must be taken into account. In general terms the stress concentration factor of a notch can be formulated as the ratio between the endurance limit of an unnotched bar and a notched bar of the same material as in equation:

$$k_f = \frac{unnotched\ bar\ endurance\ limit}{notched\ bar\ endurance\ limit}$$
 Equation 2 – 13

Where  $k_f$  is the fatigue notch factor. The equation is used to calculate the fatigue notch factor, but can be used only in reversed torsional cyclic testing and typically  $k_f > k_t$ . When analysing fatigue in terms of Strain range a similar factor to the stress concentration factor is used. In this case the strain concentration factor is maximum strain over nominal strain. Neuber [75] conjoins the total stress and strain concentration factor by the geometrical mean of the two.

$$k_t = k_f = \sqrt{k_\sigma k_\epsilon} = \frac{\sqrt{\Delta \sigma \Delta \epsilon E}}{\Delta \sigma^\infty}$$
 Equation 2 – 14

Where  $K_{\sigma}$  is the stress concentration factor and  $K_{\epsilon}$  is the strain concentration factor and  $\Delta\sigma^{\infty}$  is the nominal stress amplitude. Topper et all [76] found that the stress concentration factor  $K_{t}$  can be substituted by  $K_{f}$  to define the fatigue notch factor equation 9. Neubers rule applied to notches is material dependent but can be combined in the Ramberg Osgood relation to form the following equation 2-13.

$$\frac{(\Delta\sigma)^2}{2E} + \Delta\sigma \left(\frac{\Delta\sigma}{2K'}\right)^{\frac{1}{n_f}} = \frac{\left(k_f \Delta\sigma^{\infty}\right)^2}{2E}$$
 Equation 2 – 15

The derived equation 10 can be used to predict the fatigue life of notched samples.

## 2.5 Shot peening effect on fatigue

Shot peening is a surface treatment process which creates residual compressive stresses at the surface of a component. The process consists in shooting small spheres at the desired

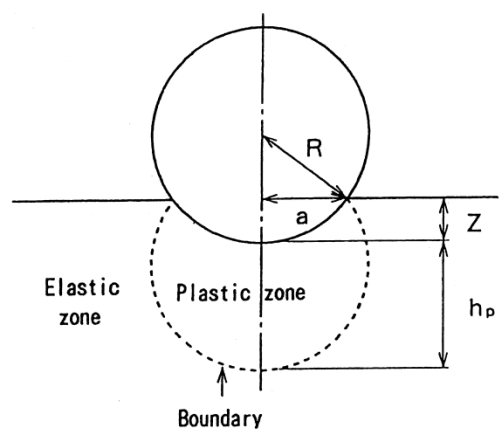


Figure 2-18 visualisation of the effect of a peen impact on the surface of the material, where R is the diameter of the peen, Z the indentation depth and hp the plastic zone depth [29]

location of the component to induce plastic induced residual stresses as described by Kobayashi et all (1997) [77] and visualised in Figure 2-18. The final effect can be regulated by changing the size of the pellets and the speed at which they hit the surface. The compressive residual stresses have been observed to increase fatigue life in metallic components from Dalaei et al (2010) [78] and Soady et al (2011) [79]. Soady et al[79], [80] performed tests on FV448 a blade material classified as 12% Cr steel (similar class to FV520B). Shot peening also causes strain hardening on the surface of components which also contributes to fatigue life extension and was found to be influenced by mechanical and microstructural properties[10],

[15], [81], [82], [83].

A notable side effect of shot peening is the increase in surface roughness due to the dimples created from the peens as shown in Figure 2-19.

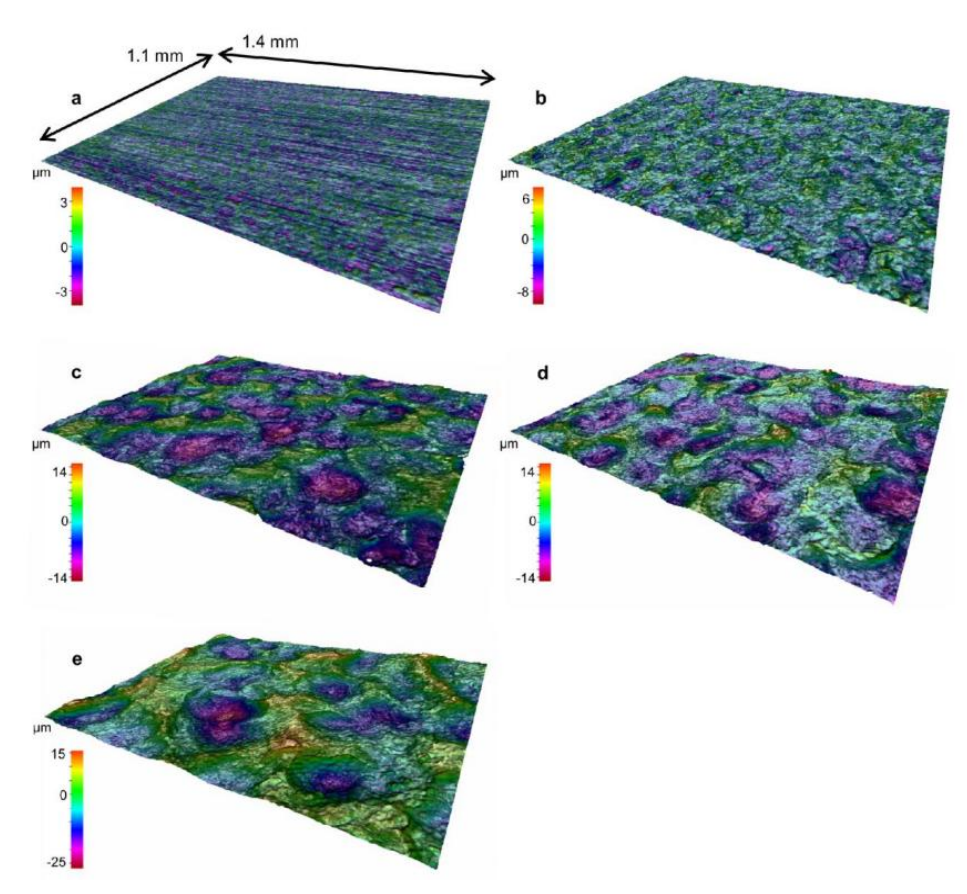


Figure 2-19 visualisation of surface roughness depending on varying parameters (a) is un-peened ground surface, (b) T1, (c) T0, (d) T2, (e) T3 [32]

The benefit from residual compressive stresses outweighs the roughening of the surface as found by Soady et al[79] and other authors [16], [82], [84]. Soady et all[79], [85] also highlight how the effects are beneficial in bend regardless of geometry, a comparison of shot peen residual stress between a notched and un-notched sample shown a consistent level of residual stress as seen in Figure 2-20 the findings were overall found to be in agreement with other authors [5], [11], [12], [13], [14], [86].

The effect of shot peening on the bending fatigue life has been verified by Soady et al (2011)[79] by comparing U-notched samples in the as ground state with 4 samples in which different shot peening settings were applied. In all cases the fatigue life showed an improvement per given strain range (calculated in the notch root) as seen in Figure 2-21 with the highest benefit being in the T0 setting which is commonly used in industry, while T1,T2,T3 are modifications of T0. The above mentioned peening processes are can be summarised in Table 2-2, where the intensity, coverage, shot diameter and shot velocity was varied.

Table 2-2 summary of settings for T0,T1,T2,T3 shot peening processes [80]

Process	Intensity	Coverage	Shot	Shot	Shot
		%	diameter	hardness	velocity
			[mm]	[HRC]	[m/s]
T1	4A	200	0.28	45-52	26
T0	13A	200	0.58	45-52	57
T2	13A	200	0.84	45-52	35
T3	18A	200	0.84	45-52	54

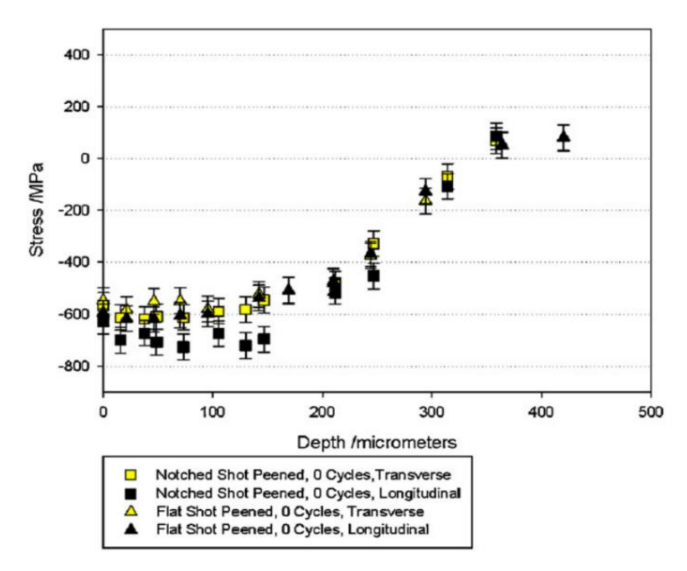


Figure 2-20 comparison of shot peening residual stress in relation to depth, between flat and u-notched samples [31]

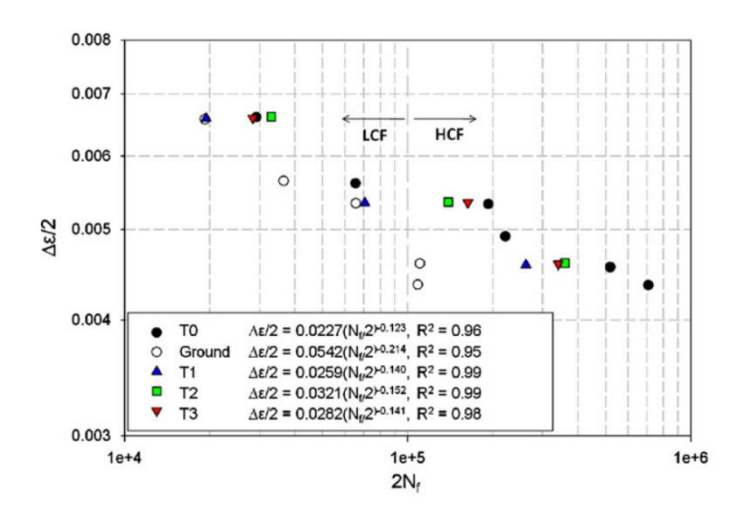


Figure 2-21 Comparison of notched samples (4.5 x 1.25 mm) with varying shot peening processes [31]

The effects of shot peening and variable notch geometries was further explored by Cunningham [6], [7], [51]. The findings from Cunningham confirm that residual compressive stresses in peened U-notch samples have a beneficial effect on the lifetime and crack growth retardation in bend testing. Cunningham also proposes a mechanistic based lifetime prediction model for U-notched peened steel alloys accounting for variable number of cycles in four stages of fatigue crack growth (initiation, short crack growth, coalescence, long crack growth)[6]. The model was applied to FV566 stainless steel, showing promising results, that require verification on other steel alloys with varying fatigue crack behaviour responses due to microstructure differences.

#### 2.5.1 Effects of residual compressive stresses in fatigue lifetime models

The shot peening process induces residual compressive stresses that in turn, especially in the LCF regime, generate crack closure and crack retardation[87]. There are challenges in modelling the lifetime prediction of shot peened components as it has been researched by many authors[12], [88], [89]. The issues stem from the difficulty in modifying the stress or strain field to determine the effective stress intensity factors during crack growth after peening[90]. One proposed method by Webster was to account for the changes in stress range and  $\Delta K$  by the principal of superimposition[91]. Although the approach is only

suitable for HCF applications. Xiang and Liu [92]proposed an alternative approach based on LEFM where the geometric factor of the component and the plastic deformation in the LCF regime to be accounted for but failed to account for initial stress relaxation.

Models have been proposed by authors to account for some of the issues encountered. De Los Rios *et al* (2000) [93] has accounted for closure stress at the crack, the material resistance to plastic deformation in the plastic zones and barrier strength at the grain boundary. Which allowed for a modified Paris law equation as the model for crack growth. Fathallah *et al* (2004)[94] have proposed a model to account for strain hardening models and surface damage. More recent models have been able to more consistently predict lifetimes and crack growth rates by accounting for defects, sample geometry and stress relaxation but the models were tailored to specific materials and conditions such as additively manufactured parts, where defects play a greater role in fatigue lifetime[95], [96].

#### 2.6 Summary

#### 2.6.1 Material characterisation

The properties of martensitic stainless steels and in particular FV520B was reviewed. Literature highlighted the dependence of FV520B and similar alloys on the heat treatment process applied, in particular the end stage HT. The variability of mechanical properties and fatigue properties is highly dependant on the control of HT. FV520B, being a legacy material, was found to have limited available literature in the conditions most likely to have been manufactured in the past.

#### 2.6.2 Fatigue Summary

The fundamentals of crack initiation, propagation and coalescence behaviour in long and short crack was described. The effect of notches in the stress field of the component was reviewed. Traditional lifetime approaches, total life and damage tolerant, were presented as the baseline for lifetime prediction modelling in fatigue.

#### 2.6.3 Shot peening and the effects on fatigue

The effects of shot peening on the topology and stress field of material was described. The shot peening process induces surface roughness and defects on the affected surface. These defects cause sub-surface crack initiation sites under cyclic loading. The residual stress field induced by the peening process was described to generally retard the crack initiation and slow the crack propagation where the cyclic loading was sufficiently low to avoid the dissipation of residual stresses. The beneficial residual compressive stresses obtained via the shot peening process have been investigated for polycrystalline materials. The extension of fatigue life after shot peening was explored showing beneficial effects in notches tested under bend in similar martensitic stainless steels. The effects of peening are overall shown to be beneficial for the likely service conditions, nonetheless a quantification of the benefit on the particular service material in the current study, FV520B, is unassessed. An analysis on the effects of peening process on legacy alloys still in service that may present variable mechanical properties due to variations in HT is needed. Short crack fatigue behaviour and lifetime modelling in polycrystalline materials has been analysed by many authors. The review highlighted how valid fatigue lifetime models have been proposed by prior authors but there is no consensus on a universally effective model, to consider the effects of residual stresses, defect populations and component geometries.

## **Chapter 3 Materials Characterisation**

#### 3.1 Introduction

The martensitic stainless steel FV520B used in the study has been provided by the project sponsor and extracted from ex-service low pressure (LP) turbine blade fir tree roots. The information provided with the material was limited, hence it required investigation to confirm it is FV520B and with regard to its microstructural, mechanical and fatigue properties. Characterisation of the material is necessary as fatigue crack initiation and growth is expected to be dependent on the microstructure and mechanical properties. In this chapter, a description of the characterisation methods used and an analysis to observe the blade-to-blade material variability is presented. The analysis consisted of metallography, elemental analysis, Electron backscatter diffraction (EBSD), Xray diffraction Spectroscopy (XRD) and tensile testing which analysed the microstructure of FV520B, the likely HT applied and the mechanical properties of the alloy. Chemical analysis was performed by an external testing laboratory using optical emission spectroscopy (OES), on 2 different turbine blades (numbered as 23 and 37) to confirm the composition matched that of the standard (Table 3-1) and the extraction of samples is described in section 3.2.1.

Table 3-1 Standard composition range of FV520B from the Firth-Vickers data book [97]

[%]	С	Si	Mn	Р	S	Cr	Ni	Мо	Nb	Ti	Со	Cu	V	W	Ν	Fe
	0.07	0.7	1.0	0.04	0.04											
Standard	max	max	max	max	max	13.2/14.7	5.0/6.0	1.2/2.0	0.2/0.7	N/A	N/A	1.2/2.0	N/A	N/A	N/A	Bal.

FV520B is a precipitation hardened martensitic stainless steel which was extracted from ex-service blades. The typical service heat treatment of FV520B for this type of service application is peak hardened, which typically involves a homogenisation at 1050 °C for 30 minutes with air cooling, solution treatment for 2 hours at 750/850 °C with air cooling, and artificial precipitation hardening for 4 hours at 450 °C with air cooling. This was the hypothesised HT used for the FV520B ex-service blades in this study, which was identified from subsequent characterisation as the peak hardened condition, and is summarised in Table 3-2 [98], [99]. The treatment starts with a homogenisation treatment to Austenitization the alloy, the second phase is a solution treatment where the Martensitization occurs, and the final phase is an artificial aging treatment where grain boundary precipitation is formed. Martensitization in the second step of the HT is indicated by the original produces to occur in air, which is likely possible by the content of martensitization elements such as Cr, Mo and Ni. The ex-service blades in this study were deployed in the 1980s in coal fired power plants, they were expected to operate for approximately 50 years at operating temperatures of 250°C, the service temperature was below that of HT that would affect this class of steels, hence testing performed at room temperature was expected to be representative of service temperature behaviour. . The microstructure of the material was analysed using standard metallographic methods. The cumulative heat treatment history experienced by the FV520B blades was also assessed by inspection using metallographic comparisons with literature reports.

Table 3-2 Heat treatment process applied to FV520B to achieve peak hardened condition [23], [100]

Temperature	Time + cooling medium
1050°C	30 minutes hold + cooled in air
750/850°C	2 hours hold + cooled in air
450°C	2 hours hold + cooled in air

### 3.2 Methodology

#### 3.2.1 Sample extraction and references to blade geometry

Samples were extracted from the firtree root of an LD66 model low pressure (LP) ex-service turbine blade. Within the fir tree root three extraction sites were identified (A, B, C) as shown in Figure 3-1, and plates were extracted using water jet cutting. The plates were machined flat and cut into four plain bend bars (PBBs) of 7.5 x 6.5 x 55 mm. The process also produced offcuts, some of which were salvaged for metallography. To identify the samples an ID was engraved that specified the location and depth of extraction in the blade root and is alphanumeric in the form of two letters and a number. The first letter (A,B,C) in the ID identifies the extraction site as either Site 1, 2, 3 in Figure 3-1 (c) and the second letter corresponds to one of the four depths in Figure 3-1 (d-ii) as W, X, Y or Z. The number following the letters represents the corresponding blade number. To describe the orientation of the samples during analysis a coordinate system was assigned to the samples with respect to the fir tree root extraction as seen in Figure 3-1.

The coordinate system is oriented with X as the direction of blade rotation, Y as the direction parallel with the axis of rotation and Z being the direction of the centripetal acceleration during operation.

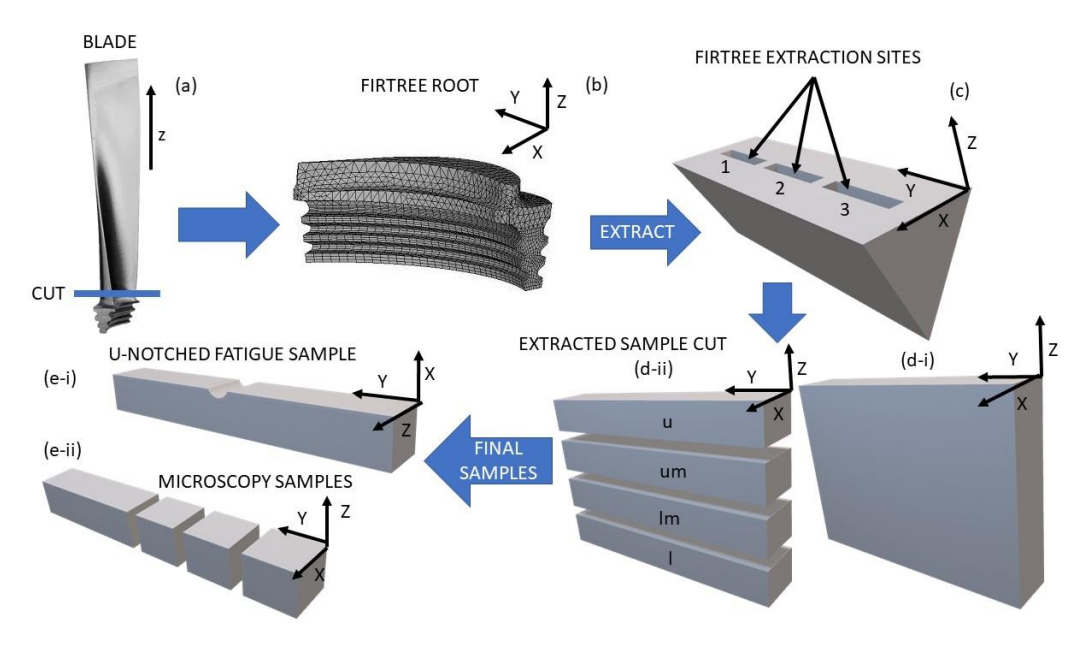


Figure 3-1 Sample extraction from turbine blade schematic, (a) representative turbine blade geometry (add axes) (b) blade root cut out (add triangle), (c) geometric equivalent of extraction site from blade root, (di-ii) original extracted blank and resulting bend from extraction site, (ei-ii) final sample geometries in the form of Unotched fatigue samples and cuboids for microscopy

#### 3.2.2 Sample preparation for metallography

FV520B samples were provided in the form of PBBs, erosion plates and offcuts. For metallography, samples were cut from PBBs or offcuts and mounted in electroconductive

Bakelite. Three cubes were cut from a PBB and mounted in Bakelite as shown in Figure 3-2, to observe the microstructure in XZ, XY and ZY directions (see coordinates in Figure 3-1), the orientation of interest referred to in the following sections is the ZY plane in reference to Figure 3-1, which is the plane normal to the notches in the blade. The mounted samples were then ground successively with 120 grit paper and increasingly finer paper until 4000 grit before polishing. Polishing was performed using 6 µm then 1 µm diamond suspension on a polishing cloth. Samples for hardness testing were not processed further.

#### 3.2.3 Microstructural characterisation

The mounted and polished FV520B samples were etched to reveal the microstructure for further observation. The etchant used was Villella's reagent (5 ml hydrochloric acid with 1 g picric acid in 100 ml ethanol), it was applied by submerging the sample surface in the etchant for 30-50 s and rinsing with methanol. Submersion time was dependent on the observed effect under an optical microscope, after the first 30 s the surface was observed and if needed 5-10 s intervals of immersions was applied. Observations of the microstructure were made using an Olympus BH2 optical microscope at magnifications from 50 to 1000 times. Further observations were performed using a JSM 7500F Field Emission Gun (FEG) Scanning Electron Microscope (SEM) with a working distance of ~10 mm and an accelerating voltage of 15 kV. Secondary electron imaging was used to observe the microstructural features of the samples and assess the presence of inclusions or secondary phases highlighted by the etching process. Electron diffraction spectroscopy (EDS) using Oxford Instruments Aztec software was performed to verify the chemical composition of possible inclusions.

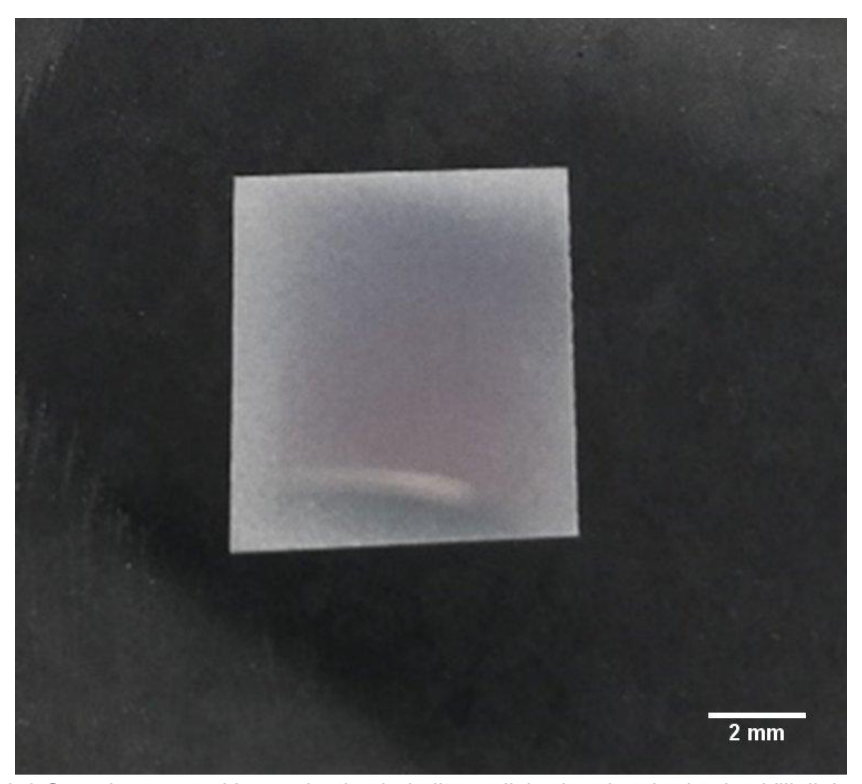


Figure 3-2 Sample mounted in conductive bakelite, polished and etched using Villella's reagent

#### 3.2.4 Chemical analysis

The chemical analysis presented in Table 3-3 was commissioned from SOUTHDOWN MATERIALS Ltd. The analysis was performed using OES. The method involves vaporising the material to be analysed using electric discharges and using optical detectors to identify

the elements. OES can identify most elements commonly found in metallic samples, with the exception of gaseous elements such as Hydrogen and oxygen. The chemical composition of two erosion plates from 2 different blades was analysed using OES.

#### 3.2.5 Electron backscatter diffraction analysis

Electron backscatter diffraction was performed on samples from four different FV520B blades, the samples were cut from PBBs into cuboids and mounted in Bakelite. The samples were oriented to scan in the orientation of interest. The samples were ground using 400 grit, 800 grit and 1200 grit paper, polished using 3 $\mu$ m and 1 $\mu$ m polishing suspensions and final polished using OPA (0.3  $\mu$ m) and OPUS (0.04  $\mu$ m) suspensions.

The EBSD detector used was Oxford Instruments® C-NANO mounted on a JEOL JSM-7200F Field Emission Scanning Electron Microscope, paired with Oxford Instruments Aztec software and MTEX open source code for data processing. The samples were scanned using an accelerating voltage of 20 keV, a nominal probe current of 12 nA and an objective lens aperture (ORL) of 2. The area scanned was 400 x 500 µm and the step size was 1 µm. The resulting EBSD data was initially processed in Aztec Crystal to generate inverse pole figure (IPF) maps which were used to measure martensitic lath thicknesses using the line intercept method. Further analysis was performed using MTEX open-source code implemented in MATLAB® to identify the parent grains in the microstructure by applying the Kurjumov-sachs orientation relationship. The resultant parent grain pattern was measured to compare size differences in prior austenite grain sizes in relation to resultant hardness.

#### 3.2.6 Hardness testing

Hardness testing was performed using a Future-Tech FM-300 with a load of 200 g and a hold time of 15 s. Hardness testing methods were used from previous literature and standards (BS EN ISO 6507-1:2008) to allow comparability between FV520B and other alloys[51], [101], [102]. A schematic of the Vickers indenter geometry is presented in Figure 3-3. The testing was performed on samples from different blades mounted in Bakelite and polished as described above in section 3.2.2. Micro hardness indentations were performed at a distance of 500  $\mu m$  apart, to avoid any plastic effects in the area surrounding each indentation, where the size of indentation was approximately 80  $\mu m$  diagonally. The indenter tip was diamond with a known Young's modulus and geometry and hardness was calculated from the measured dimensions of the indentation using equation 3-1 where 1.854 is the derived geometric constant of the indenter tip geometry and d1/d2 are the diagonals of the indentation [103].

$$HV = 1.854 \times \frac{Load}{\left[\frac{d1+d2}{2}\right]^2}$$
 (3.1)

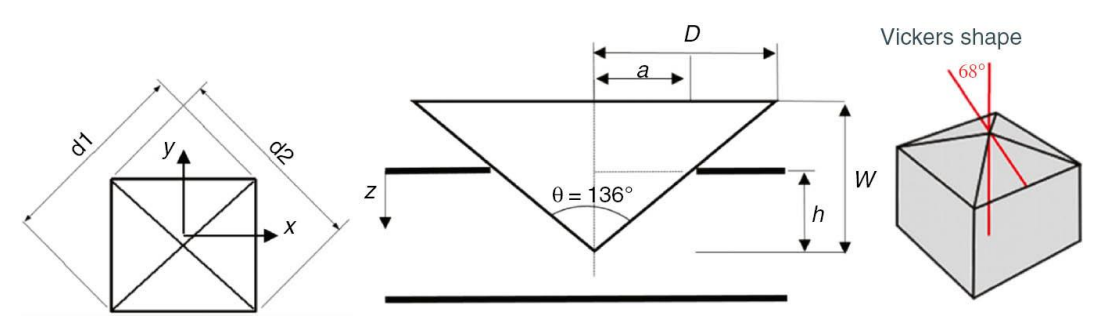


Figure 3-3 Vickers indenter geometry, d1 and d2 being the diagonals of the indentation, h the indentation depth, W the working depth.

#### 3.2.7 Monotonic tensile testing

Tensile testing was performed following standard BS EN ISO 6892-1:2016 and using a servo mechanical testing Instron 5569 machine. The strain was measured using dynamic extensometer Instron 8800ML2165 with a total strain range of 30% and a maximum travel distance of  $\pm$  5 mm and a gauge length of 12 mm. The samples were machined from PBBs of 55 x 7.5 x 6.8 mm in size. The limited material dimensions required smaller tensile dog bone specimen dimensions than specified as standard, but the recommended ratios for gauge length and width were maintained as shown in Figure 3-4.

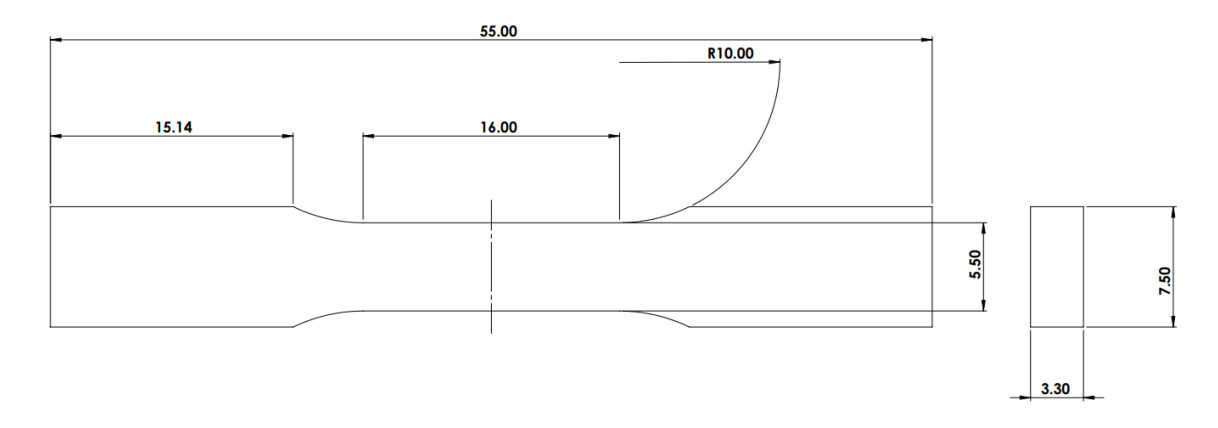
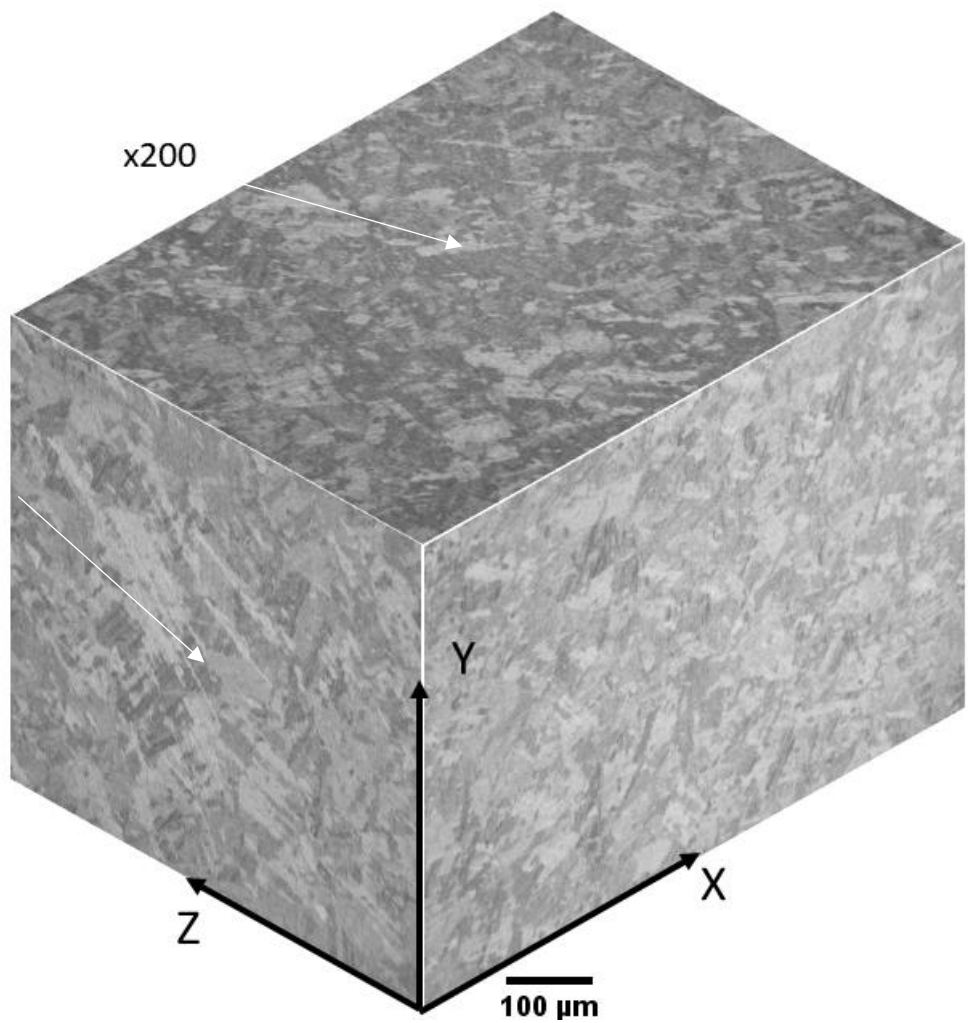


Figure 3-4 Reduced dimensions of non-standard dog bone samples for tensile testing, dimension ratios follow BS EN ISO 6892-1:2016 standards.

#### 3.3 Results

#### 3.3.1 Microstructural characterisation

The microstructure of FV520B was observed using samples from different blades. Optical microscopy was used to generate a 3D visualisation of the microstructure at different magnifications to qualitatively observe directionalities in the grain. As seen in in Figure 3-5, there was an apparent alignment on the ZX and YZ planes indicated by an arrow at 200x magnification. As the magnification increases the directionality in the planes is less apparent, as in Figure 3-6.



100 μm

Figure 3-5 3D visualisation of the microstructure of FV520B etched samples at a 200x magnification under optical microscope. Arrow indicates apparent directionality in ZX plane.

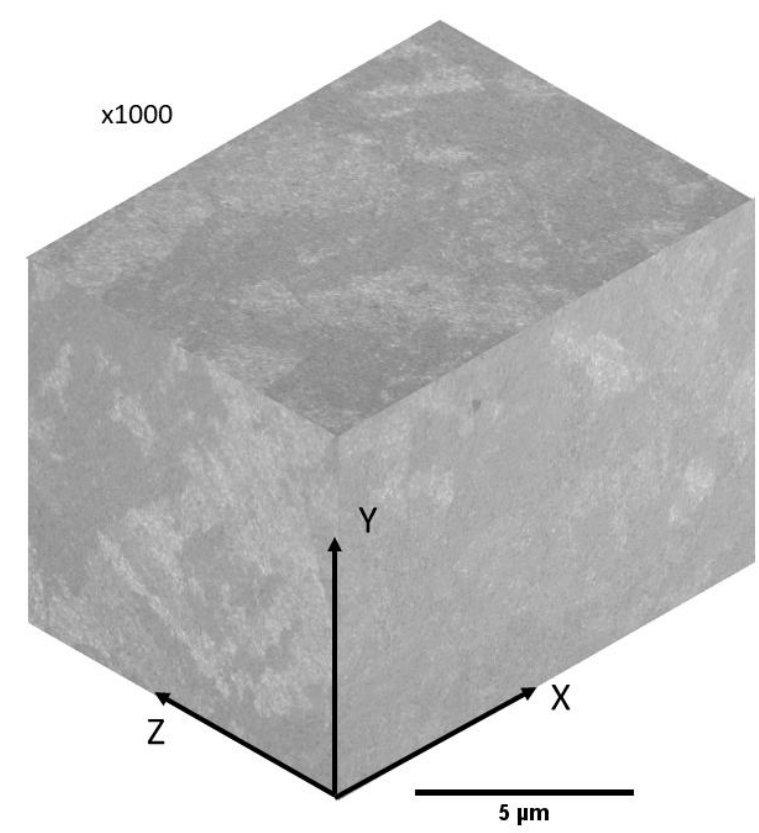


Figure 3-6 optical microscopy 3D image of FV520B microstructure at 1000x magnification

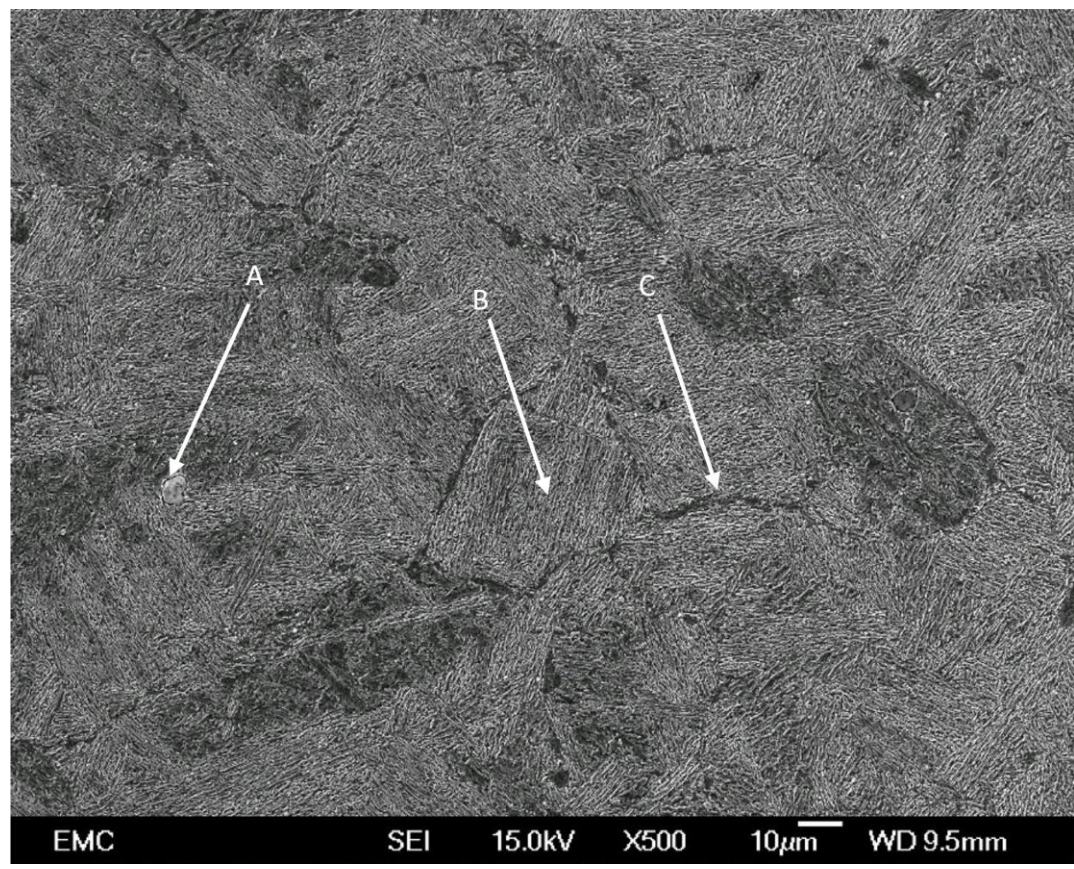


Figure 3-7 SEI imaging of FV520B microstructure at 500x magnification, showing (A) alumina inclusions, (B) martensite laths, and (C) reverted austenite pockets at grain boundaries.

Using SEM, the microstructure of blades 73, 75 and 1 were observed to include martensite laths, prior austenite grain boundaries and a secondary phase, hypothesised to be reverted austenite, at the grain boundaries Figure 3-7 which is seen occurring in literature during HT[98]. At magnifications higher than 3000x, as in Figure 3-8, precipitates can be observed in the reverted austenite phase, these are likely copper precipitates[98], but the composition was not investigated. These are submicron in size and were barely visible in SEM imaging, these are theorised to be copper and Mo based precipitates [98], [104], [105].

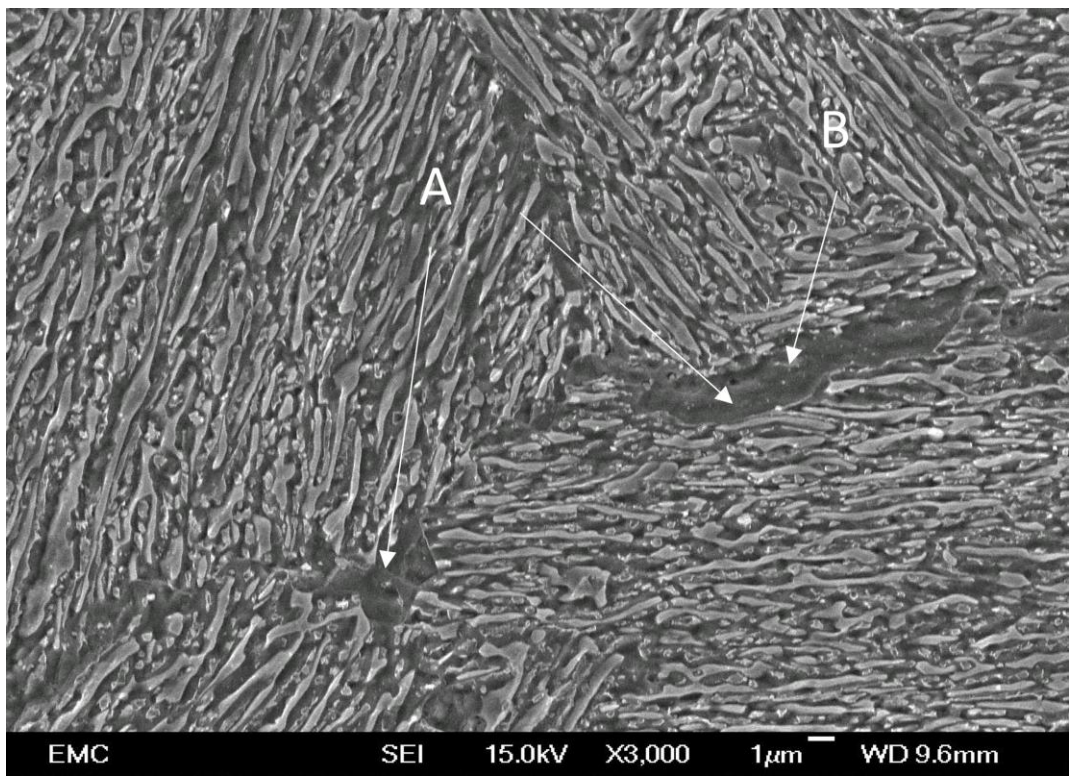


Figure 3-8 martensite laths and reverted austenite pockets (A) with barely visible precipitates(B).

Inclusions were identified, via the use of energy dispersive electron spectroscopy (EDX), in the microstructure as globular alumina inclusions as seen in Figure 3-7 and Figure 3-9, which are approximately  $\sim$ 6  $\mu$ m in diameter.

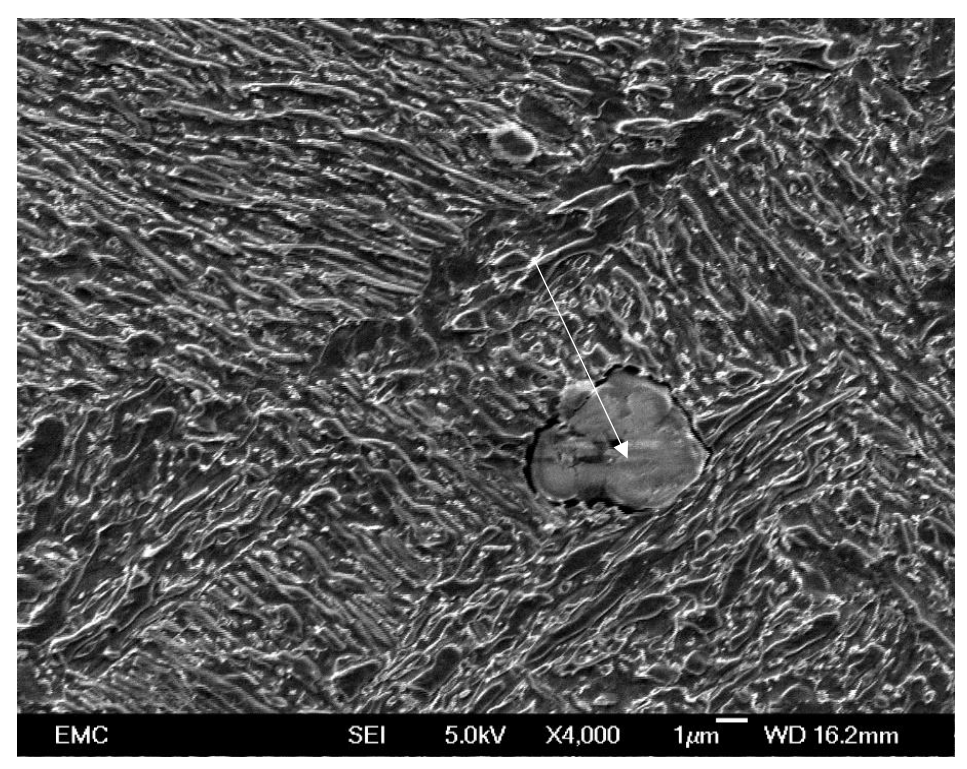


Figure 3-9 alumina inclusion (indicated by arrow) in in the FV520B martensite laths.

#### 3.3.2 Material composition

The chemical analysis performed gave results comparable to that of the available standards of the material. The standard was taken from the Firth Vickers handbook on FV520B, the original manufacturer of the alloy [29]. Additionally, any deviation between blades is low (maximum difference of 30% for Nickel, 10% or less for other elements). Although only two samples were tested, we assume that the blades compositions are within the materials standards for all blades. The main factor affecting FV520B is its heat treatment, where in the final stage (precipitation hardening phase), copper and molybdenum based precipitates occur, which influences the final mechanical properties of the alloy, hence any notable variations in mechanical properties may be partially influenced by the HT[105], [106], [107]. Additional elements were found in the analysis which were not in the standard, but no further investigation was carried out on the effects of the additional elements.

Table 3-3 comparison between FV520B standard chemical composition and two samples tested B23 and B37

FO/ 1	С	Si	Mn	D	S	Cr	Ni	Мо	Nb	Ti	Со	Cu	\/	W	Ν	Fe
[%]	J	Si	IVIII	Γ	3	CI	INI	IVIO	IND	11	CO	Cu	٧	۷V	IN	ге
Standard					0.04	40.0/44.7	E 0/0 0	4 0/0 0	0.0/0.7	<b>.</b> 1 / A		4 0/0 0	<b>.</b> 1 / A	<b>.</b> 1 / A	<b>.</b> 1 / A	Б.
[2]	max	max	max	max	max	13.2/14.7	5.0/6.0	1.2/2.0	0.2/0.7	N/A	N/A	1.2/2.0	N/A	N/A	N/A	Bal.
FV520B sample 1	0.03	0.28	0.43	0.01	0.002	13.48	5	1.53	0.24	0.015	0.09	1.47	0.022	0.05	0.06	Bal.
FV520B sample2	0.05	0.24	0.38	0.019	0.002	13.26	5.63	1.53	0.26	0.015	0.1	1.66	0.031	0.05	0.05	Bal.

#### 3.3.3 Compositional and microstructural comparison of blade steel alloys

Comparison between FV520B and materials of similar class analysed in previous studies (Table 3-4) shows an overall higher number of alloying elements in FV520B, a higher Chromium and Nickel content and the presence of Cu and Molybdenum as alloying elements[7], [98], [102], [107]. The higher Cr and Ni content contributes to increased corrosion resistance which is in line with the application of the alloy in a steam turbine. The molybdenum content improves pitting resistance. Additionally, Nickel acts as an austenite stabilizer during the normalisation phase of the heat treatment and slows martensite formation during quenching, which can promote the formation of a finer martensitic microstructure and is achieved by the retardation of carbon diffusion during quenching but reduces overall hardenability and martensite in large parts. Chromium, similar to Nickel, retards martensitic formation during quenching, but has the opposite effect on hardenability in that it promotes martensite formation by homogenising martensite formation through the thickness of the component. Copper promotes precipitation hardening at the grain boundaries which improves fatigue properties and tensile strength. Chromium contributes to carbide formation, and in conjunction with copper they contribute to the precipitation hardening phase of the HT of FV520B. In this precipitation hardening phase, fine copper based precipitates form preferentially at the grain boundaries. It should be noted that precipitation hardened steels, similar to maraging steels, can experience a reversion of lath microstructure into austenite during the precipitation hardening phase of the HT. The reversion mechanism is temperature and time dependent. At lower temperatures the time required is higher and vice versa. The austenisation temperature of the alloy also plays a role in the resultant volume fraction of austenite after precipitation hardening. In the case of FV520B some reverted austenite was detected during metallographic analysis, but EBSD and XRD phase identification has been inconclusive in detecting austenite in the examined samples. The percentage of reverted austenite may be too small or too scarcely distributed to be detected using these techniques.

Table 3-4. Compositional comparison of FV520B and similarly tempered martensitic stainless steels used in LP turbine blades from literature[6], [108]. Selected differences highlighted by different shading (orange).

Material	С	Si	Mn	P	S	Cr	Ni	Mo	Nb	Ti	Со	Cu	V	W	N	Fe
FV520B	0.04	0.26	0.41	0.01	0.00	13.37	5.32	1.53	0.25	0.02	0.10	1.57	0.03	0.05	0.06	Ba I
FV566	0.1	0.35	0.61	0.02	0.01	11	2.4	1.35	0.28	х	Х	Х	0.15	Х	х	Ba
	0.12							0.58			Х		0.31		Х	Ba I

The two alloys we compare with FV520B have typical martensitic microstructures, Figure 3-10 shows FV566 [6] which main difference with FV520B is the lack of reverted austenite packs and inclusions consisting in stringer alumina rather than globular alumina. Similarly, FV448 in Figure 3-11 has a noticeable rolling direction, as it was taken from rolled bars, and has stringer like inclusions [35].

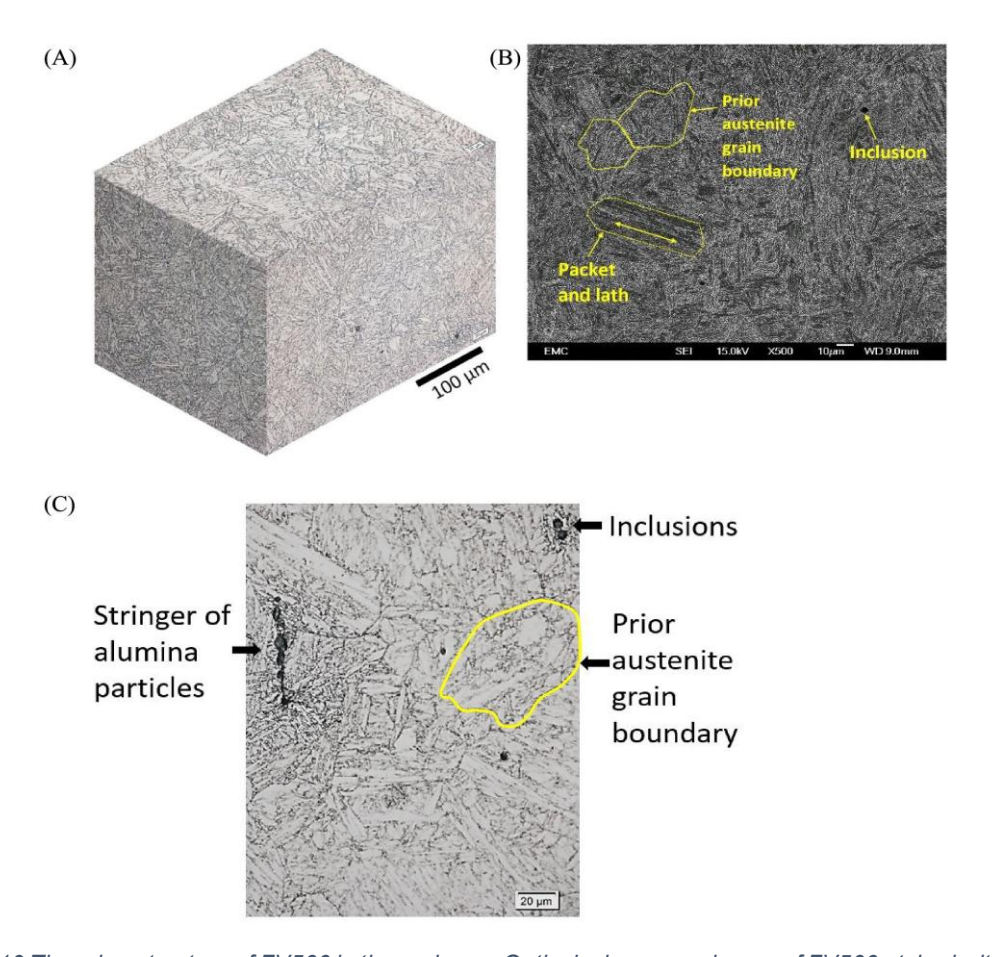


Figure 3-10 The microstructure of FV566 in three planes. Optical microscope image of FV566 etched with Vilella's reagent showing a stringer. FEG SEM (SEI mode) image showing the microstructure of FV566 etched with Vilella's reagent [6].

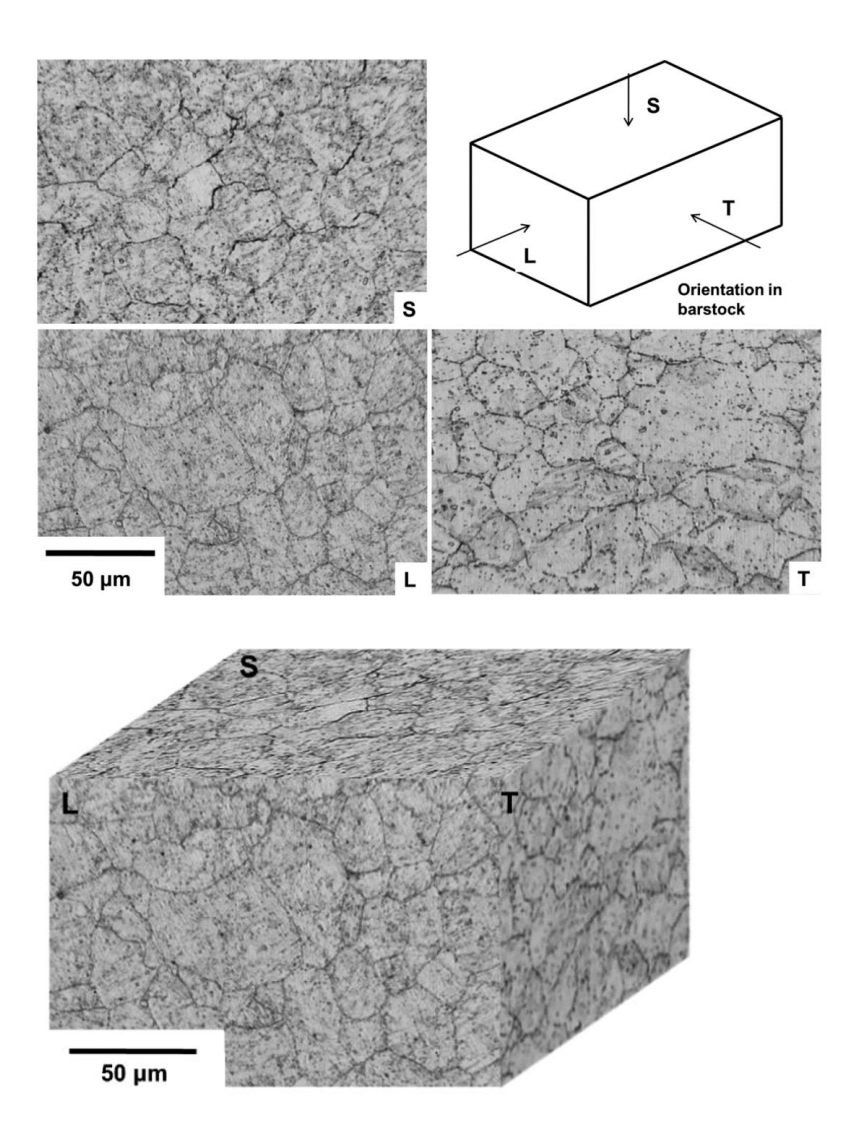


Figure 3-11 FV448 microstructure representation in 3 dimension (L) longitudinal/rolling direction, (T) transverse and (s) short transverse. FV448 presents with a typical martensitic structure composed of visible prior austenite grain boundaries and martensite lath packs, aluminium oxide stringers are also found. The alloy has been found to be stronger in the rolling direction[35].

#### 3.3.4 Hardness results

Hardness testing was performed on polished plates, in the YZ direction, which was the direction normal to the maximum bending stress in subsequent 3-point bend tests. 10 indentations per sample were performed and the values presented in a bar chart in Figure 3-12. The hardness in FV520B is highly dependent on the hold time and temperature of the last stage HT [98]. The figure reveals a variation from the HV standard for peak hardened FV520B of 420 HV, variation of up to 80 HV, taken from the Firth Vickers handbook [97] and a significant scatter of hardness values. Samples from five different blades presented values as low as 315 HV and high as 368, some of the scatter may be attributed to indents hitting large pockets of reverted austenite. Figure 3-12 also compares the measured values from FV520B to other martensitic stainless steels, FV448 and FV566, where FV448 is softer and FV566 harder than FV520B. FV520B is presented with a distribution of hardness within each individual specimen (labelled on the x axis) and between specimens from

different blades (the naming convention indicated different blades, for example BX1 and BY1 are both from blade 1).

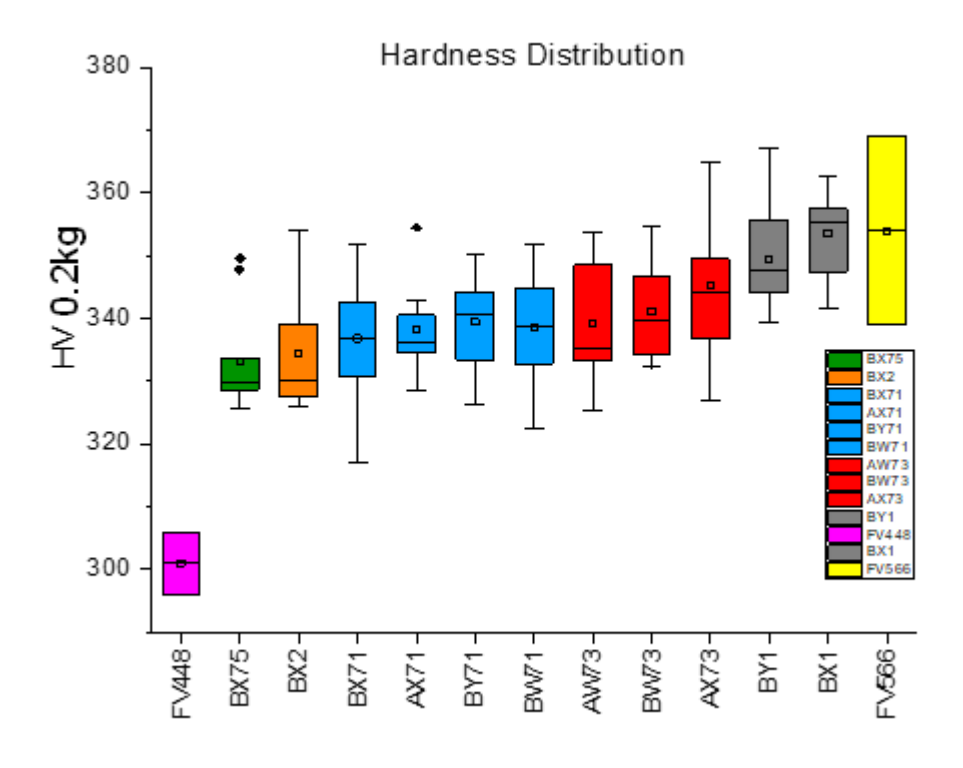


Figure 3-12 comparison of measured hardness in different FV520B flat erosion plates from different blades (labelled as BX75, BX2 etc), these include possible scatter due to microstructural features like reverted austenite, and compared to other blade alloys from literature (FV448,FV566) [18], [109]

#### 3.3.5 Microstructural feature size analysis

Measurements were taken of the martensitic lath sizes using the line intercept method. The distribution of the lath thickness was plotted against the measured hardness in Figure 3-13. The low angle grain boundary EBSD scans were taken to measure lath sizes via a line intercept method. Although more accurately measured using TEM, EBSD scans can show individual laths[110], [111]. As expected, a smaller average lath size correlates to a higher Hardness on average. Furthermore, a parent grain analysis was performed on the EBSD scans using the Kurdjumov-Sachs orientation relation. A qualitative observation of the parent grains shows a correlation to the lath thickness results, where larger parent grains produced thicker laths on average in Figure 3-14. The outlier in the analysis is blade 75, the resulting parent grain results show unlikely parent grain patterns. These samples had been previously tested in bend for fatigue testing and extracted from the spent sample, and so the analysis could have been influenced by plastic deformation of the material, although the sample was extracted from beyond the expected stress field region during testing. The analysis, as expected, shows a correlation between lath and grain size with hardness, which can can be utilised as an estimation tool for grain size and mechanical properties as will be observed in chapter 3.3.7.

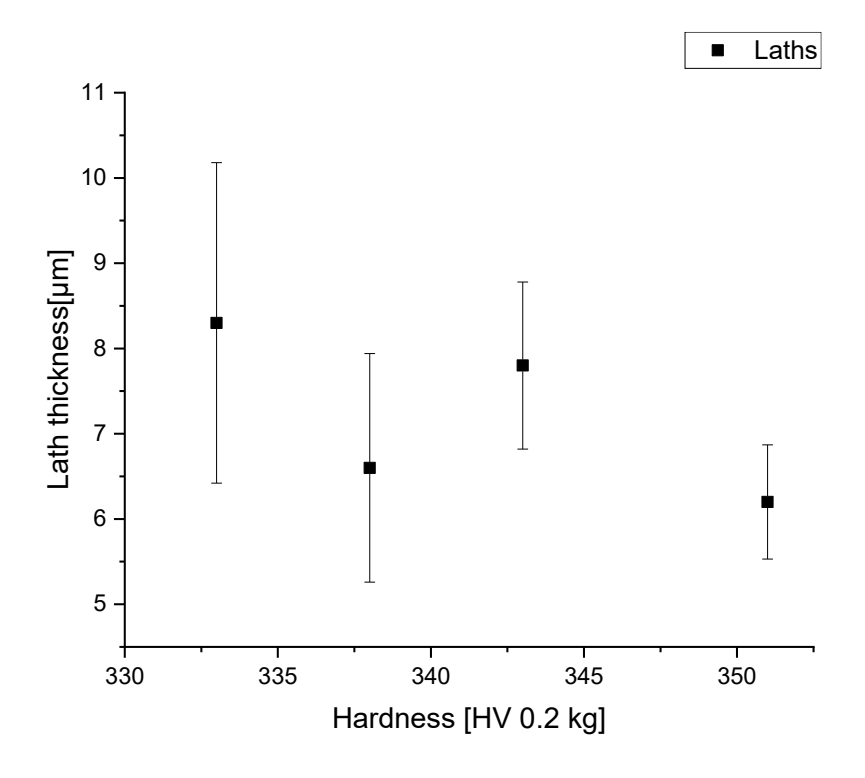


Figure 3-13 FV520B blade to blade variation in martensitic lath size distribution in relation to hardness. The measurement was taken from a grain boundary angle graph via line intercept.

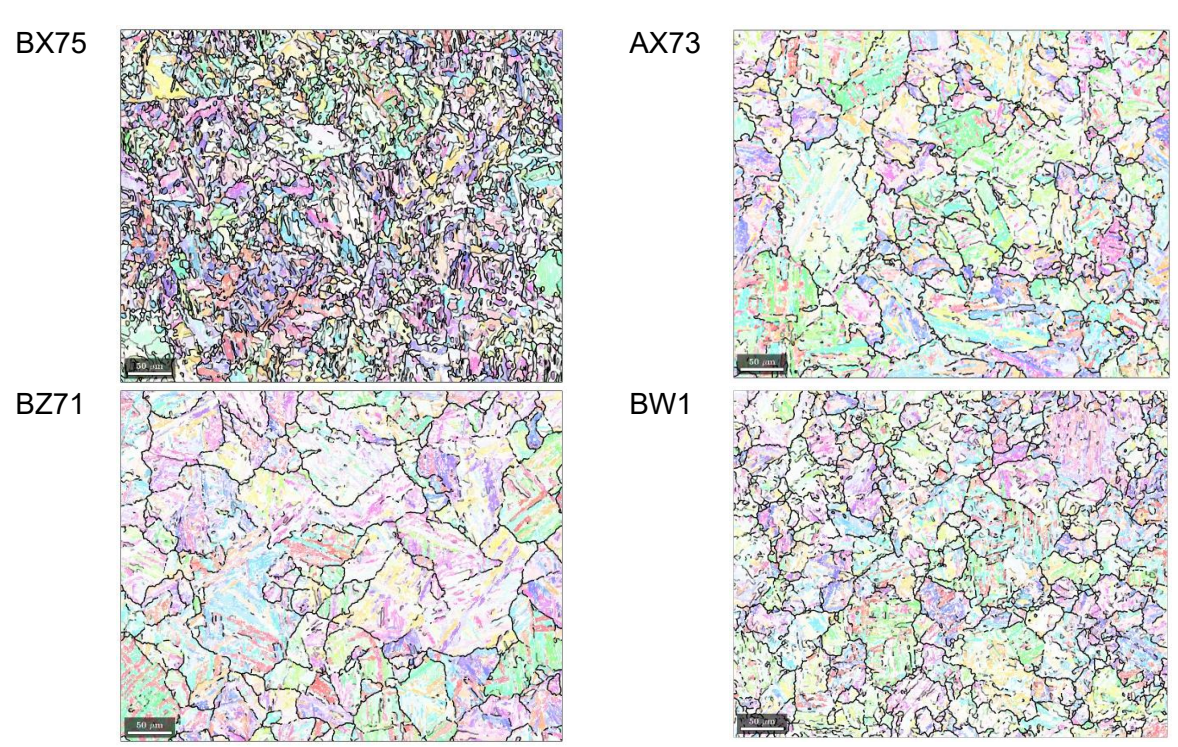


Figure 3-14 Visualisation of prior austenite grains superimposed to martensitic lath microstructure. BX75 was likely subjected to strain induced grain boundary refinement which skewed parent grain analysis results. in order from softer to hardest AX73,BZ71,BW1, with BW1 having a relatively smaller prior austenite grain size.

#### 3.3.6 XRD crystallographic analysis

Microstructural analysis using X-ray diffraction (XRD) on four blades (1, 71, 73, 75) resulted in peaks, Figure 3-15, in line with a martensitic structure when compared to literature results[106]. The analysis was performed originally to determine phase volume fraction of the martensitic matrix and the reverted austenite at the grain boundaries. The hypothesised HT should yield a relatively low volume fraction of austenite which, as mentioned previously, is dependent on the HT final stage temperature and hold time. The resulting XRD pattern showed no signs of typical austenite peaks, these were observed in Clark (1999) on FV520B with a variety of HT applied [106]. The presence of reverted austenite is dependent on the last stage temperature and hold time, which suggests the heat treatment performed on the FV520B was optimised to minimising reverted austenite. The XRD peaks contrast with the metallographic analysis using SEM which showed austenite pockets at prior austenite grain boundaries. The observed austenite from metallography may not be scarce, hence not being able to be detected by the XRD, which was performed on bend bars of the above-mentioned blades, with a machined surface condition. Due to the variation in hardness between blades and hardness being an indicator of HT outcome, we can hypothesise that there may have been variations in the final stages of the HT. These possible variations might have resulted in relatively low presence of austenite in XRD results.

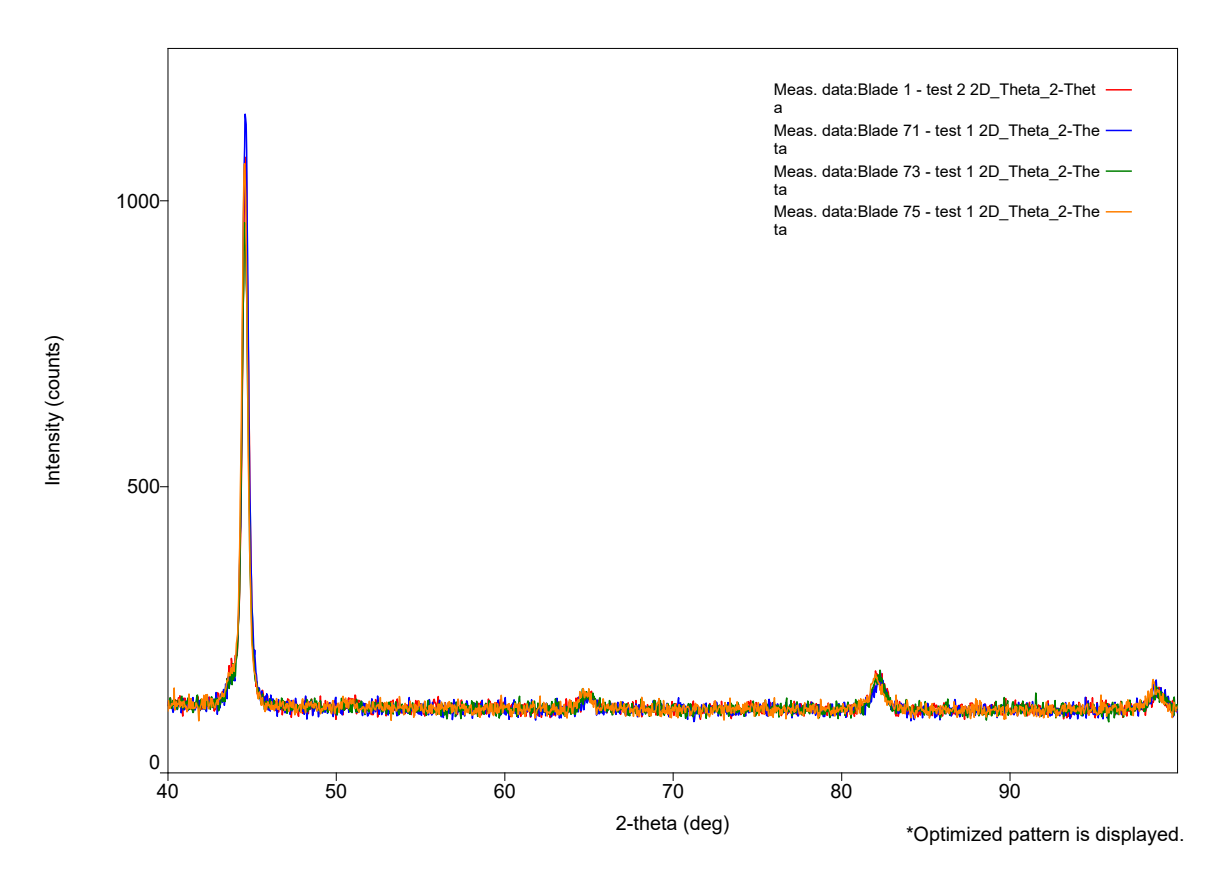


Figure 3-15 XRD pattern of 4 FV520B blades, 71, 73, 75 and 1. The peaks represent the points at which X-rays diffract from the crystal lattice planes of the analysed material. The 4 patterns match and indicate peaks only typical of martensitic structure for FV520B, with no peaks suggesting austenite content.

#### 3.3.7 Monotonic tensile testing

Monotonic tensile testing was carried out to measure and compare yeld and UTS between blades and other alloys Table 3-5. Tests were conducted on two samples per each blade, and the results in table are an average of two for each blade. The properties were

compared to 3 times the average hardness as a way to estimate UTS, which was observed to give a reasonable estimate for UTS in Figure 3-16. FV520B presented with a standard deviation of 30 MPa for the yield strength and a standard deviation of UTS of 25 MPa. FV448 has a lower overall yield than FV520B but comparable UTS indicating a higher strain hardening potential, while FV566 has lower yield and UTS overall indicating a lower strain hardening potential.

Table 3-5 Comparison between FB520B blades (75,71,73,1) and similar martensitic alloys (FV448, FV566)

	FV448	75	71	73	1	FV566
Yield						
[MPa]	813	980.5	965.5	992	1035.5	829
UTS						
[MPa]	1025	1038	1005.5	1027.5	1066	976
3 x HV	903	999	1014	1029	1053	1062

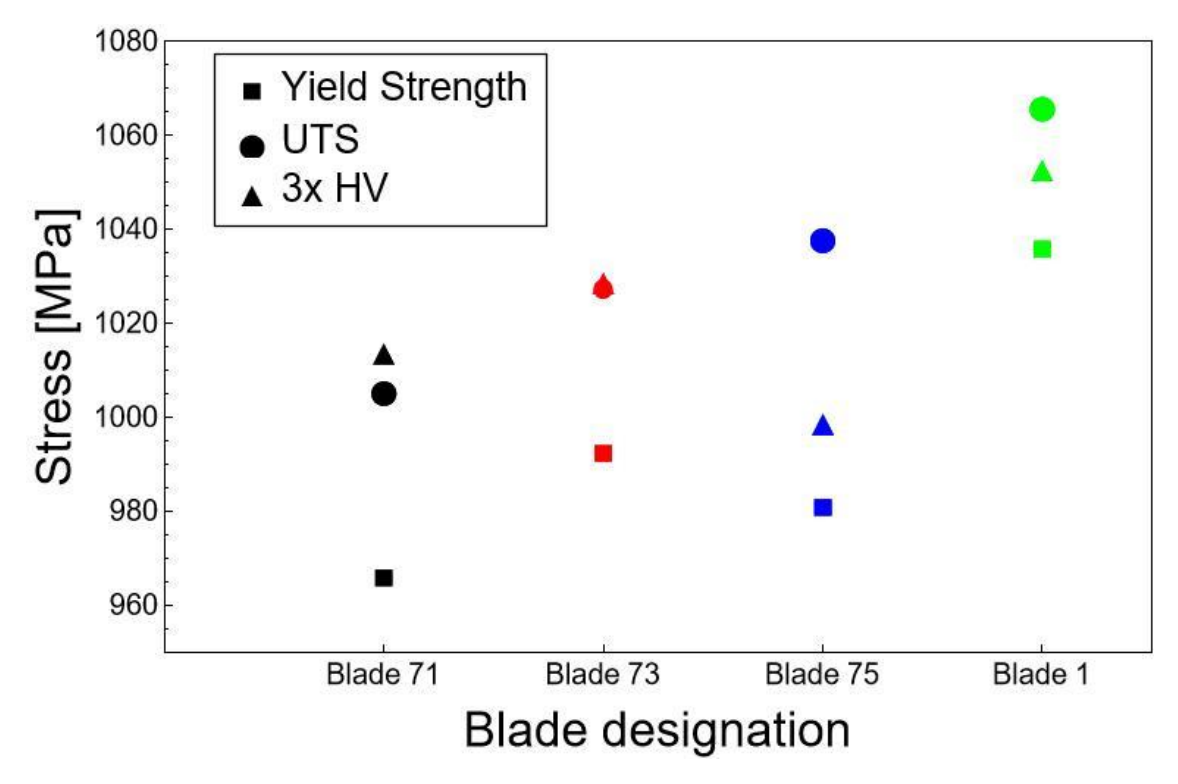


Figure 3-16 Comparison between FV520B blade mechanical properties and estimated UTS via 3xHV. Each blade was tested twice, the datapoints were plotted as the average value of the two tests.

#### 3.4 Discussion

The microstructural analysis has shown a similarity in martensite morphology with the peak hardened condition microstructure of FV520B observed in literature (Figure 3-17) [14][98]. The lath size obtained were higher than what found in literature, where individual laths were 1  $\mu$ m thick[98], while our measure size between 6-10  $\mu$ m. Furthermore, the average measured yield strength shows similarity with the peak hardened condition requirements from manufacturers datasheets which indicates an expected yield strength of 1050 MPa and slightly lower UTS expected between 1170-1310 MPa[97].

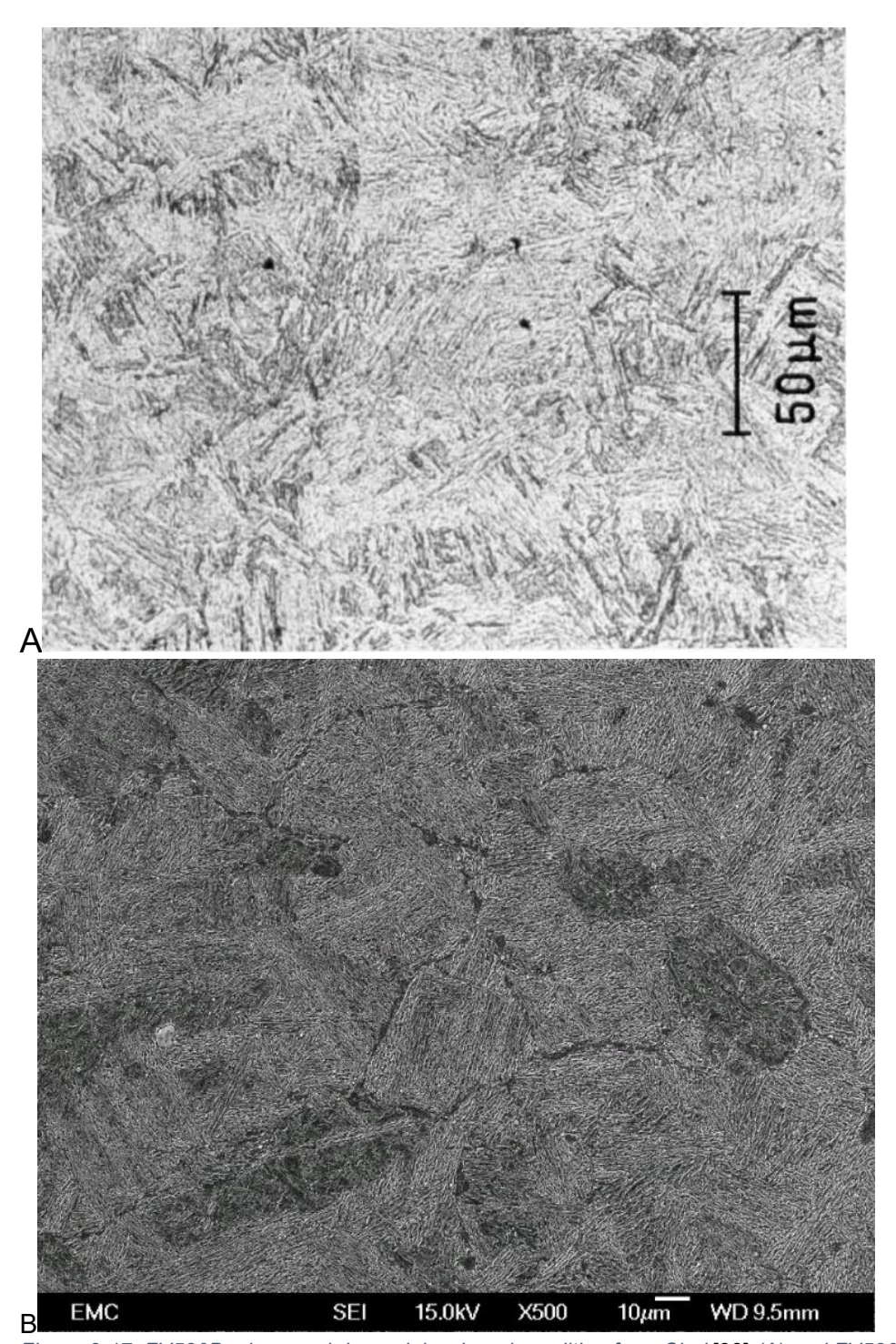
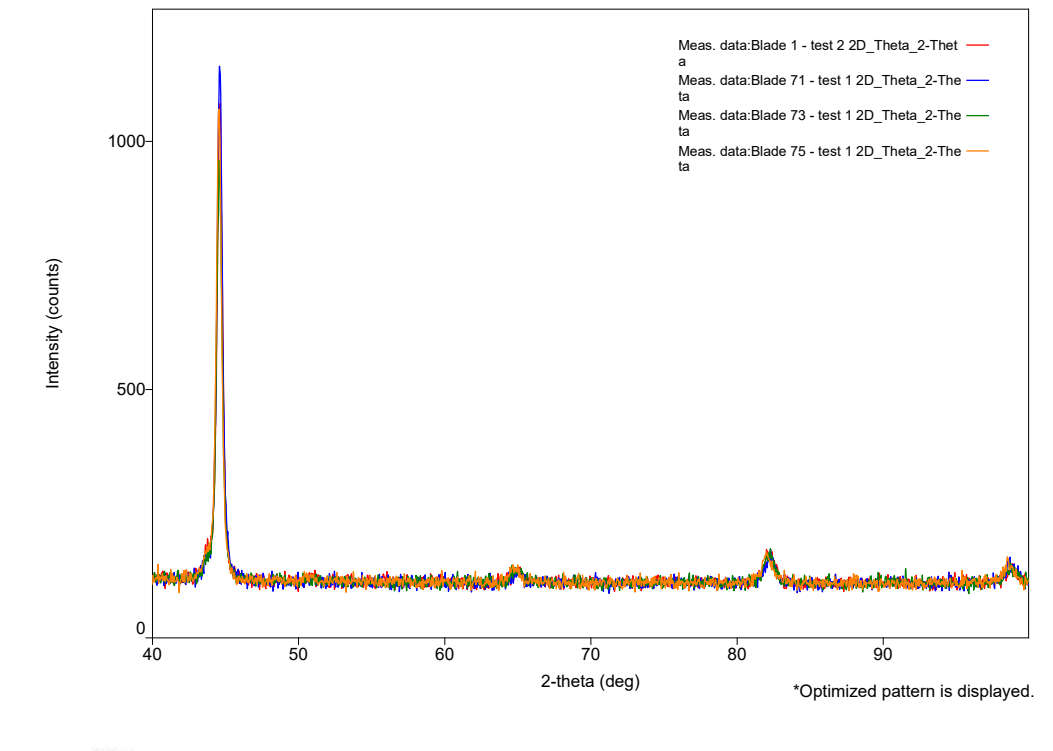


Figure 3-17. FV520B micrograph in peak hardened condition from Clark[98] (A) and FV520B peak hardened condition micrograph taken from ex-service blades.

The microstructural observations using SEM imaging shows a typical martensitic microstructure with prior austenite grain boundaries, martensitic packs and laths. Furthermore, reverted austenite pockets were observed at the prior austenite grain boundaries. FV520B is a precipitation hardened steel and presents fine precipitates at grain boundaries, these were not characterised due to time and equipment limitations, but are believed to be copper based precipitates as found commonly in this class of materials [6], [14]. Metallography qualitatively revealed a low presence of inclusions in the microstructure with globular alumina as the only confirmed inclusion found, the quantification of the inclusions was not carried out. The low population density of inclusions can be explained by a high manufacturing standard of the blades due to the critical application in turbomachinery. Reverted austenite was observed from metallography at the

prior austenite grain boundaries. The content of reverted austenite is influenced by the final stage of the heat treatments temperature and hold time. Typical temperature for aging to peak hardened condition is 450°C with a hold time of 4 hours. A higher temperature or hold time will result in higher reverted austenite content and can be an indicator of potential variations in the HT[98], [105], [112], [113]. The HT end stage induces the precipitation of copper based inclusions at the grain boundaries, is the main strengthening mechanism in the alloy. The elemental analysis results show values comparable to the standards of FV520B from the Firth-Vickers Databook, it is also similar to that of literature [6], [13], [14]. The analysis supports the hypothesis that the material is FV520B, and additional elements were detected not included in the standard. The additional detected elements and their effects were not further investigated. Given the consistency between the two samples tested from different blades it is expected that all blades will have comparable chemical composition to those tested.

The hardness test results showed a variation in the values between blades, as well as a lower average hardness, of ~80HV, from that expected in the peak hardened condition reported in literature. Hardness measurements were carried out in the plane of interest which is the plane where maximum stresses will occur during fatigue testing, but no additional investigation on hardness variations between planes was carried out. Literature suggests the presence of reverted austenite to be attributed to the variation of temperature and hold time in the final phase of HT as mentioned above. The end stage of HT also affects overall mechanical properties and hardness, with a drop in hardness if overaged [98], [105]. A possible explanation could be attributed to the last stage HT changes in the precipitation hardening process of FV520B. The XRD analysis to identify the phases present in FV520B matched the pattern found in literature for the peak hardened condition, although the peak angles were similar the intensities were different (Figure 3-18).



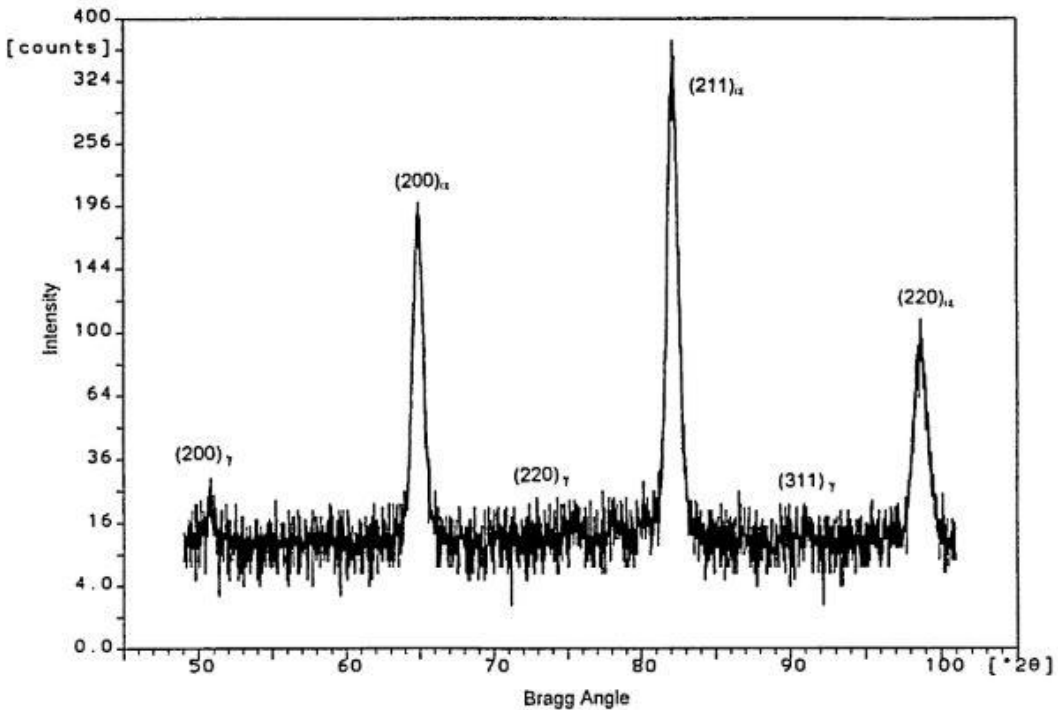


Figure 3-18 XRD pattern of FV520B ex-service blades (above) measured in the current study. Peak hardened FV520B XRD pattern from literature[98] (below), the two pattern present the same Bragg angle but different peak intensities.

Measurements of martensite lath sizes indicated a possible correlation between average lath size and hardness as would typically be expected form the Hall-Petch relationship[114] in Equation 3-2.

$$\sigma = \sigma_0 + Kd^{-1/2}$$
 Equation 3-2

Parent grain analysis on FV520B highlighted prior austenite grain sizes. Qualitative observation of the prior austenite grain sizes showed a possible correlation between relatively small prior austenite grain and smaller lath size and potentially higher hardness, but this requires additional investigation.

Monotonic tensile testing results were similar to the conditions of peak hardened FV520B with some variation. The standard deviation between the blades was found to be relatively low. Hardness was provided a reasonable estimate the UTS for FV520B by taking 3 times the average hardness of a blade.

#### 3.5 Conclusions

The results of this study confirmed that the ex-service material from LP turbine blades was FV520B, a precipitation hardened martensitic stainless steel. Samples of FV520B were tested for composition which matched the standard from the Firth-Vickers foundry datasheets as well as literature focused on FV520B in its varied heat treated conditions. Metallography indicated a typical martensitic structure, composed of laths arranged in packs and the presence of prior austenite grain boundaries. A small population of globular alumina inclusions was identified, which was not further investigated, it was only noted that it had a different geometry when compared to FV566 and FV448 which had stringer like alumina inclusions. Reverted austenite pockets were observed at the prior austenite grain boundary sites, the presence of which is influenced by the heat treatment. When compared to other blade steels of similar class, FV520B presented a wider variety of alloying elements and a higher chromium and nickel content, and cooper, the three of which contribute to enhanced corrosion resistance and overall mechanical properties. The hardness study on FV520B shows a variation of hardness between blades and within blades. Mechanical properties variation between blades is relatively low and UTS was observed to correlate with 3 times the hardness. Hardness measurements is hence a reasonable estimation method for tensile strengths for FV520B. EBSD scans and subsequent analysis showed a correlation between lath size and prior austenite grain boundary size and hardness. The lath and prior austenite size are dependent on the HT process applied to the alloy. Due to the lack of certain information on the applied HT we assumed peak hardened condition as its most likely outcome. The mechanical property and hardness results match those from literature for the above mentioned condition. This is further confirmed by XRD scans which showed a pattern matching that of a peak hardened FV520B as found in literature.

# Chapter 4 Baseline fatigue properties related to microstructure variations.

#### 4.1 Introduction

The material of the study, FV520B, was evaluated to measure baseline fatigue properties using long crack testing methods. Samples from different ex-service blades of FV520B were tested to compare the fatigue threshold and Paris law regime behaviour between samples. Material constants for FV520B were calculated and estimated fatigue life comparisons were made between these values and other similar alloys[51]. Fractography of the samples was done via Scanning electron microscopy to evaluate differences and/or similarities between fracture surfaces at different ΔK levels. Fracture surfaces were nickel plated, cut and etched to observe the crack propagation path through the microstructure. Fracture surface comparison showed little to no differences in crack path behaviour between different blades, the same was true when observing cross section view of the crack. The only feature of note was one blade with a relatively larger alumina inclusion population, where the alumina particles provided crack halting properties in secondary cracks at high ΔK levels. The fracture surface observations indicated a higher microstructural influence at lower ΔK on the crack path, where it follows the intergranular path of the martensitic laths. At higher ΔK the fine microstructure was observed to have a lesser effect, with the crack propagating in a transgranular way. Crack Tip Opening Displacement (CTOD) calculations were also made to compare crack growth behaviour between samples when accounting for mechanical property variations (e.g. yield strength variations). The ΔCTOD trends showed a minor effect in stage II crack growth behaviour but a relatively more significant influence at near threshold related to yield strength differences.

#### 4.2 Methods

#### 4.2.1 Long crack testing

Four plain bend bars were cut into single edge notch bend specimens to be tested under 3 point bend loading (SENB3) with the dimensions shown in Figure 4-1. These long crack testing samples were extracted from ex-service FV520B (blades 1, 71, 73, 75) and evaluated following standard BS EN ISO 12108:2002. One sample per each blade was tested, due to limited material availability. The surfaces of the SENB3 specimens were ground with 800 and 1200 grit paper, and further polished using 3µm and 1µm diamond suspension to allow crack propagation observations. The samples were cleaned in an ultrasonic bath immersed in acetone before testing. The sharp notch was scraped at the root using a razor blade to induce a uniform crack initiation during pre-cracking.

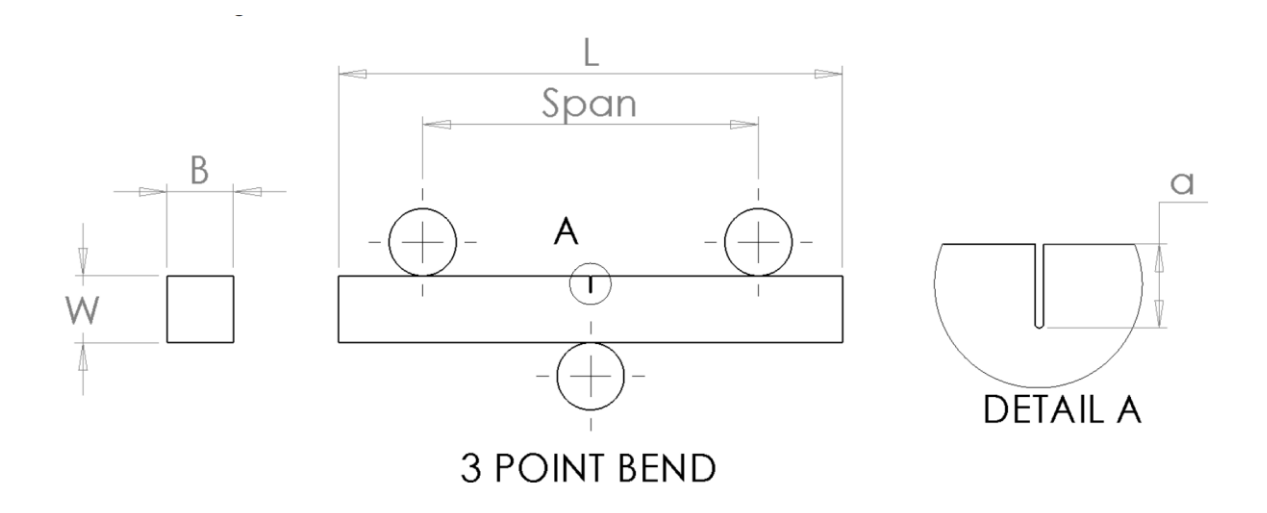


Figure 4-1 FV520B sample dimensions for SENB3 testing [115], detail shows depth of the notch, the width is equivalent to the EDM wire diameter (0.33mm) used to cut the notch. Where L=55 mm, Span = 40 mm, a = 1.6 mm, a = 1.6 mm, a = 1.6 mm, a = 1.6 mm and a = 1.5 mm.

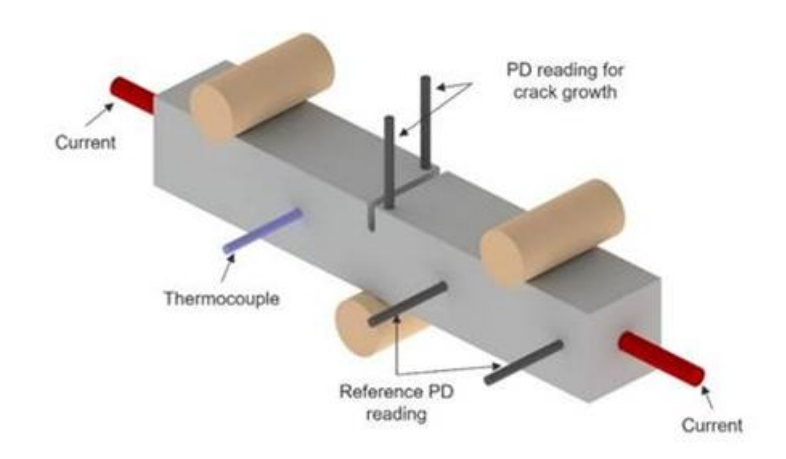


Figure 4-2 Typical DCPD set up for long crack testing, this includes current wires at the ends of the sample, the reference PD wires approximately 10mm apart to read the uninterrupted voltage through the material and crack growth PD wires to read the voltage increase as the crack grows. Typically, the set up includes a thermocouple for testing at high temperatures but was not used.

The samples were loaded in a 3-point bending rig, with top roller span of 40mm, mounted on an electrodynamic test machine Instron E10000. The test was performed at room temperature applying a sinusoidal waveform at 10Hz frequency and a R-ratio of 0.1. A Direct Current Potential Drop set up, Figure 4-2, was used to measure the crack growth during testing. The test was carried out in two phases. The first consisting of an initial precracking and load shedding, starting at a  $\Delta K = 15 \text{ MPa}\sqrt{m}$ , to ensure the crack grew through at least six monotonic plastic zone sizes (approximately 0.5 mm) using the Irwin approximation of plane strain[116] at each  $\Delta K$  level (equation 4-1)

$$r_p = 6 \times \frac{1}{3\pi} \left( \frac{\Delta K}{(1-R)\sigma_y} \right)^2$$
 Equation 4 – 1

where  $r_p$  is monotonic plastic zone size and  $\sigma_v$  is the yield strength.

After pre-cracking at a constant  $\Delta K$  = 15 MPa $\sqrt{m}$ , crack growth rates at decreasing  $\Delta K$  levels were established. At each constant  $\Delta K$  level the crack grew through six monotonic plastic zone sizes before the  $\Delta K$  was dropped by a 10% decrement and then grown

through another six monotonic plastic zone sizes at the new lower  $\Delta K$ . This allowed da/dN to be established over a constant  $\Delta K$  regime whilst allowing enough growth to escape the load history effects of the previous  $\Delta K$  level. This load shedding approach was carried out to reach the  $\Delta K_{th}$ . The second testing phase, to measure grow-out at constant load range, was carried out by applying a  $\Delta K=7$  MPa $\sqrt{m}$  and testing under constant load range and increasing  $\Delta K$  levels until final failure. This growth out test with constant load amplitude was performed to measure crack growth rate with corresponding  $\Delta K$  values to be compared with short crack testing (Chapter 5). The resulting da/dN vs  $\Delta K$  behaviour from this long crack testing was used to determine Paris-law constants using empirical fits to the data. The methods are explained in Appendix A for  $\Delta K$  calculation and Appendix B for crack growth calculations.

#### 4.2.2 Fractography

Fracture surface analysis on FV520B samples which underwent long crack testing was performed in two phases. Initially the fracture surfaces were observed using a macroscope to measure the effective crack length at threshold and before final fracture. The effective crack length was measured at 5 different locations on the fracture surface to average the length as the crack front is typically semi-elliptical and in some cases asymmetrical. The effective crack length was used to calibrate the P.D. predictions of crack length and thus to establish da/dN versus  $\Delta K$ , and also  $\Delta K$  levels as a function of crack length, a. This allowed identification of locations on the fracture surface with particular ΔK levels for fracture surface observation. The imaging of the fracture surface was performed using the SEM as described in Chapter 3, at 3 different ΔK levels, at threshold, at medium ΔK (~10 MPa $\sqrt{m}$ ) and at high  $\Delta K$  (~20 MPa $\sqrt{m}$ ). The samples were then nickel plated to protect the features on the fracture surface during handling and cutting. The samples were cut perpendicularly to the fracture surface to expose the cross section. Fracture surface cross sections were mounted in Bakelite and polished to 1µm diamond suspension. Vilella's reagent was used to etch the cross section to expose the microstructure. Etched cross section samples were observed via SEM at locations closely matching the observed locations on the fracture surface based on the known  $\Delta K$  vs a.

#### 4.3 Results

# 4.3.1 Baseline Paris law behaviour and crack tip opening displacement behaviour

The FV520B blades were tested to determine the hardness distribution of the tested samples, the distribution is shown in Figure 4-3. The hardness graph represents the blades in order of hardness from softest to hardest and is used as a reference for comparison between samples in this chapter. The sample extraction and resulting sample nomenclature was summarised in Figure 4-4. We observed in Chapter 3 the microstructural variations between blades and the relation to monotonic mechanical properties. The overall trend, in relation to hardness, was that a higher hardness represented a finer martensitic lath microstructure and an indicatively finer prior austenite grain boundary.

Long crack testing of FV520B revealed an overall homogeneous trend in stage II crack growth between samples regardless of relative blade hardness as observed in *Figure 4-5*. Threshold behaviour in da/dN vs  $\Delta$ K plots show relatively higher variations between blades, which will be further discussed in the below subsections.

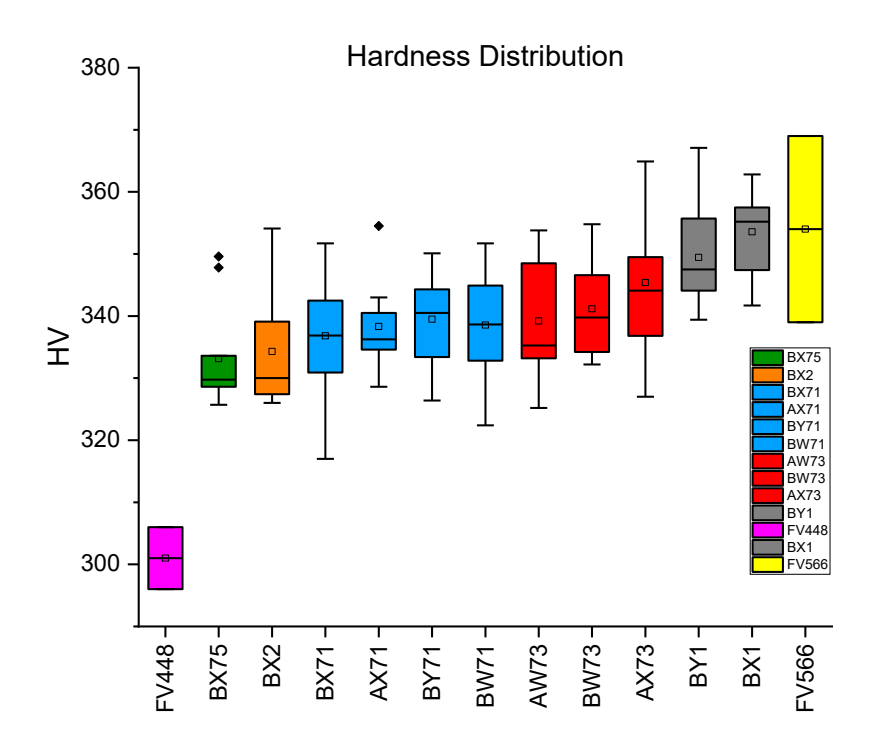


Figure 4-3 comparison of measured hardness in different FV520B flat erosion plates from different blades (labelled as BX75, BX2 etc), these include possible scatter due to microstructural features like reverted austenite, and compared to other blade alloys from literature (FV448,FV566) [18], [109]

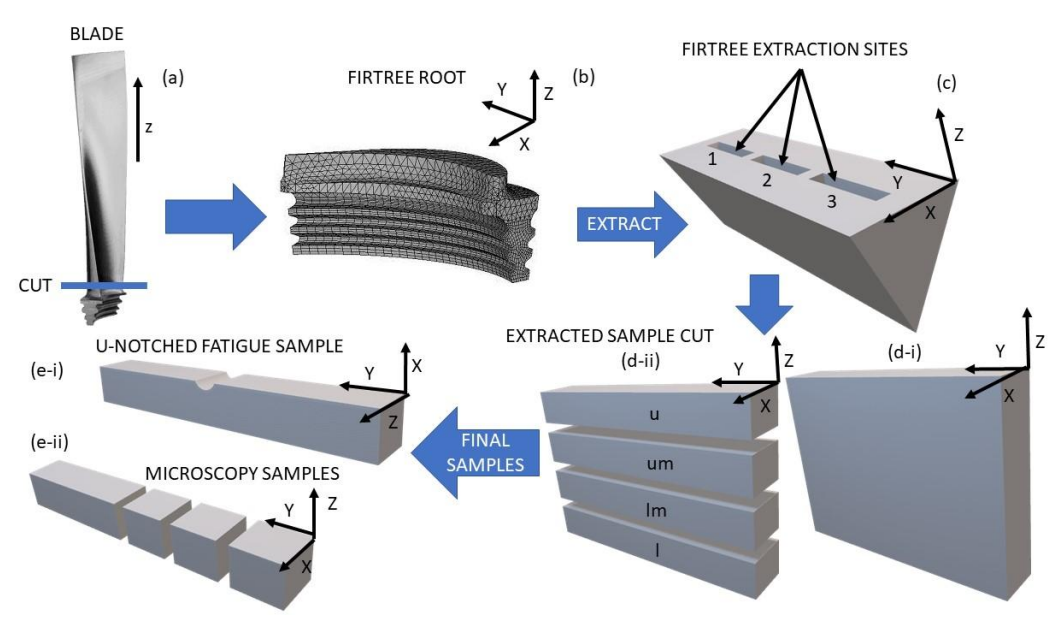


Figure 4-4 Sample extraction from turbine blade schematic, (a) representative turbine blade geometry (b) blade root cut out, (c) geometric equivalent of extraction site from blade root with 1,2,3 corresponding to A,B,C in the sample ID first letter, (di-ii) original extracted blank and resulting bendbars from extraction site with u, um Im I corresponding respectively to W, X, Y and Z in the ID number, (ei-ii) final sample geometries for fatigue samples and cuboids for microscopy

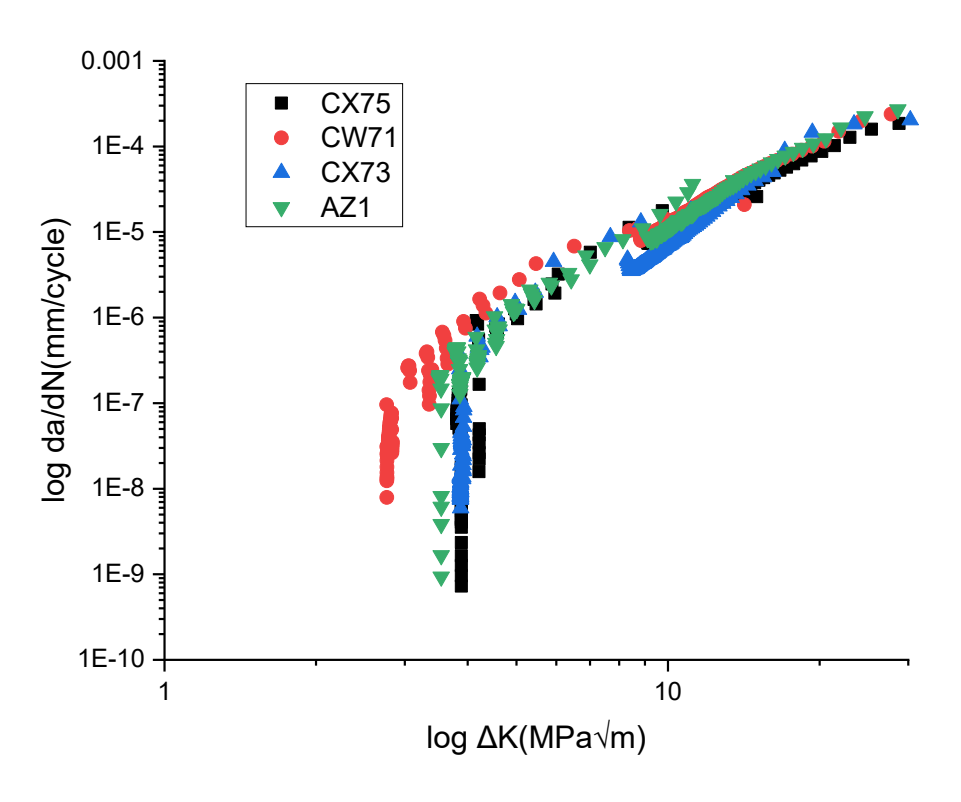


Figure 4-5 Long crack test data comparison between different blade samples. Test consisted in an initial load shedding test to identify the threshold load range and subsequent constant load test. The Paris law regime is consistent between blades, while threshold behaviour varies between samples.

The Paris law behaviour of FV520B was compared to FV566, a martensitic stainless steel used in similar applications[51]. The overall trend in stage II crack growth showed little variation between FV566 and FV520B in the Paris regime as shown in Figure 4-6. When comparing material constant variations between FV520B and FV566, in *Table 4-1*, the variations were relatively small, while the threshold  $\Delta K$  in FV566 is higher compared to FV520B, which is not consistent with literature where a harder steel with finer microstructure tends to present lower  $\Delta K_{th}$  [117]. The differences within FV520B were minor compared to the relatively higher difference between FV566 and FV520B.

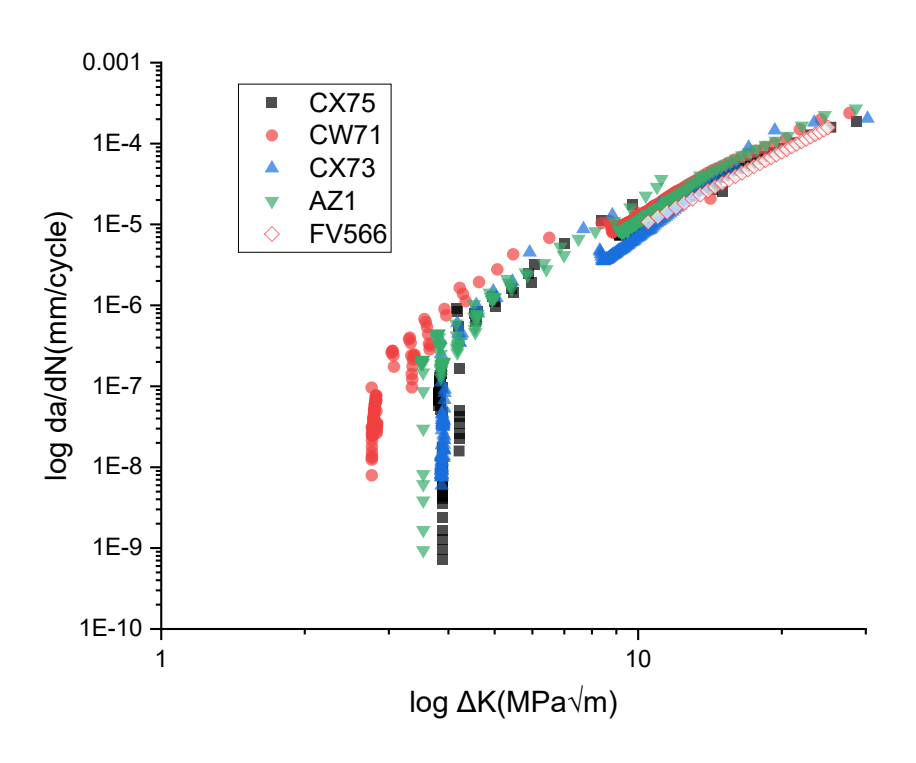


Figure 4-6 Paris law behaviour plot comparing FV520B and FV566. The two martensitic stainless steels used in LP steam turbine blades present very similar crack growth rate behaviours in Paris law regime and threshold regime.

Paris law constants for the different blades are shown in *Table 4-1* . For each blade the material constants were used, by integrating the Paris law equation to estimate the number of cycles to failure. The initial crack length for each case was set to  $20\mu m$  and the final crack length was estimated using  $K_{IC}$  estimated from the long crack fatigue test assuming a through thickness crack. The lifetime prediction was also calculated for FV566 to compare with FV520B in Figure 4-7. Fatigue lifetime estimations were calculated for varying  $\Delta\sigma$  levels. The resultant figure shows little difference in lifetimes at high  $\Delta\sigma$ . While at lower  $\Delta\sigma$  the lifetime spread increases, this is particularly noticeable between FV520B blade variants, while the FV566 lifetime tends to have a lower fatigue lifetime compared to FV520B with lower  $\Delta\sigma$  and a slightly higher fatigue lifetime compared to the FV520B lifetime variants at higher  $\Delta\sigma$ .

Table 4-1 Paris-law constants of FV520B and FV566 long crack tests carried out at constant amplitude and corresponding threshold values for the test carried out.

Material/sample name	Loading condition	С	m	$\Delta K_{th}$
FV520B/ CX75	CA	4.80E-12	3.3	3.8
FV520B/CW71	CA	2.60E-12	3.7	2.8
FV520B/CX73	CA	2.99E-13	4.4	3.9
FV520B/AZ1	CA	2.04E-12	3.7	3.54
FV566 [115]	CA	7.30E-12	3.1	4.3

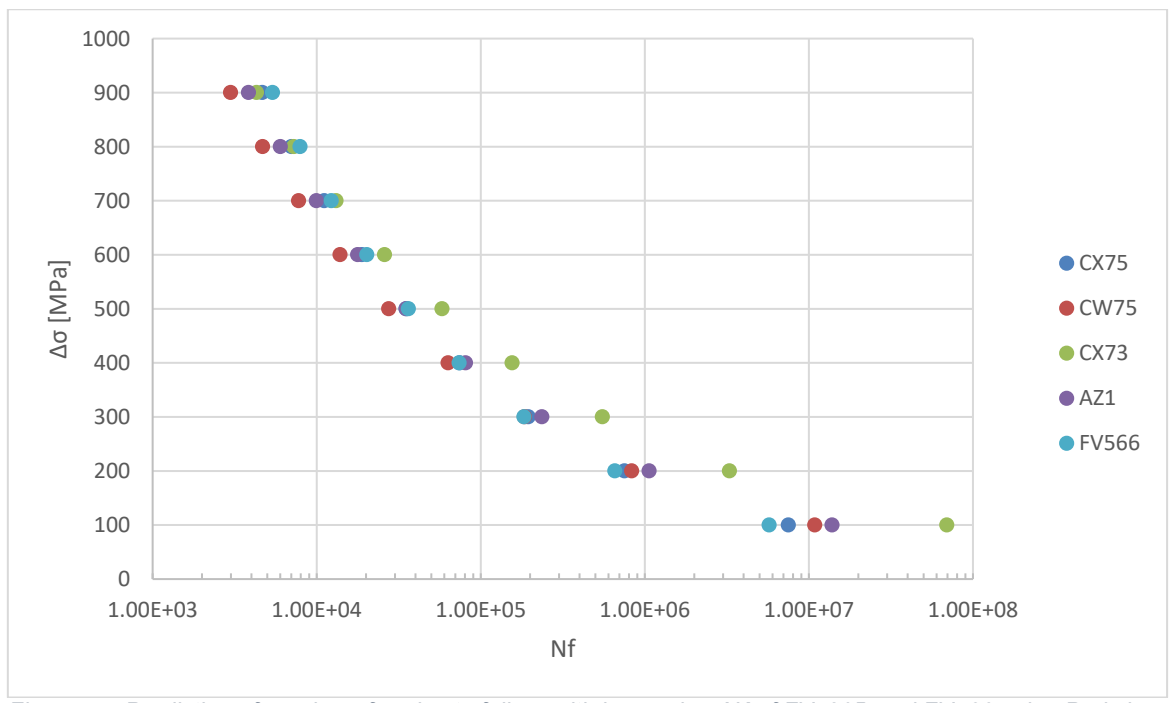


Figure 4-7 Prediction of number of cycles to failure with increasing  $\Delta K$  of FV520B and FV566 using Paris law material constants and assuming LEFM.

The differences in material properties (particularly yield strength) between blades were also considered by calculating the  $\Delta$ CTOD (Equation 4-2) and comparing da/dN on that basis, where  $\Delta$ CTOD can be calculated by:

$$\Delta CTOD = \frac{\Delta K^2}{\sigma_{YS}E} \quad \textit{Equation} 4-2$$

The resultant plot, Figure 4-8, shows little difference in Stage II crack growth behaviour between samples. When observing near threshold crack growth rates, the  $\Delta$ CTOD highlights a widening difference between samples, the standard deviation of  $\Delta$ CTOD is approximately 25%, while in the case of  $\Delta$ K<sub>th</sub> the deviation is 12%.

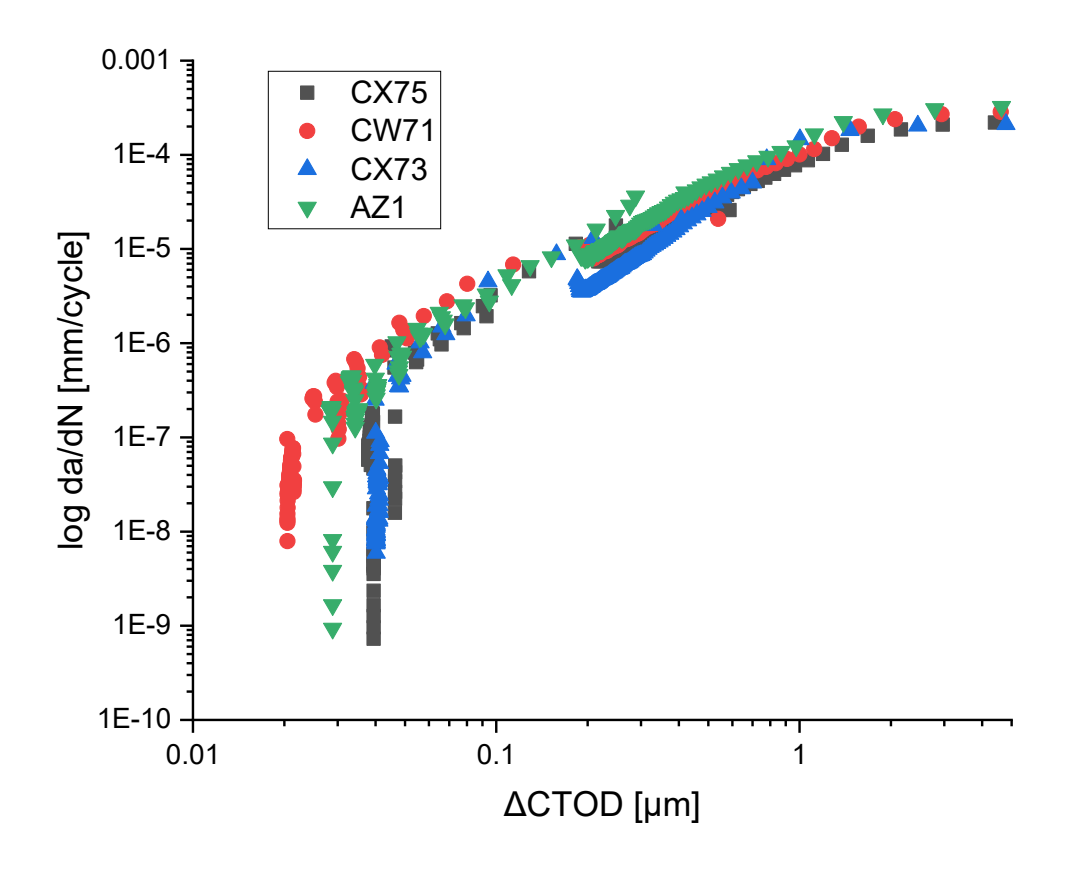


Figure 4-8 Crack tip opening displacement comparison between samples of different FV520B blades. Blades differ in yield strength and UTS as well as HV with blade 75 being the softest and 1 being the hardest. The crack tip opening displacement accounts for differences in strengths, Paris law regime behaviour is relatively unaffected while crack growth near threshold is more affected.

#### 4.3.2 Fatigue threshold relation to microstructural and mechanical properties

The fatique threshold and mechanical properties of 3 steel alloys (FV520B, FV566 and FV448) were plotted against hardness for comparison in Figure 4-9. Comparing the three alloys there was no noticeable and consistent correlation between hardness and fatigue threshold, the same is true when comparing fatigue threshold and mechanical properties. In FV520B an increased hardness showed a relative increase in mechanical properties. The threshold region of the crack growth showed somewhat noticeable differences between blades of different hardness. Overall the standard deviation (SD) between the population of  $\Delta K$  threshold (~0.43) and the coefficient of variation, relative to SD and mean in percentage was calculated as 12%. The variation between the threshold values is relatively low, typically ΔK<sub>th</sub> is higher when hardness is higher. FV566 does present the highest ΔK<sub>th</sub> and highest hardness which is consistent with literature expectations. The lack of clear correlation between the three alloys' ΔK<sub>th</sub> and mechanical properties may be attributed to the differences in microstructure and strengthening mechanism. The main strengthening mechanism in FV520B is the precipitation of copper based precipitates at the grain boundaries[98], [105], which may influence the available slip plane availability and consequent ΔK<sub>th</sub>. Also, a finer microstructure equates to higher number of grain boundaries which impede the crack growth resulting in a higher threshold value and higher hardness, which is consistent when considering ΔK<sub>th</sub> in relation to hardness between FV520B and FV566.

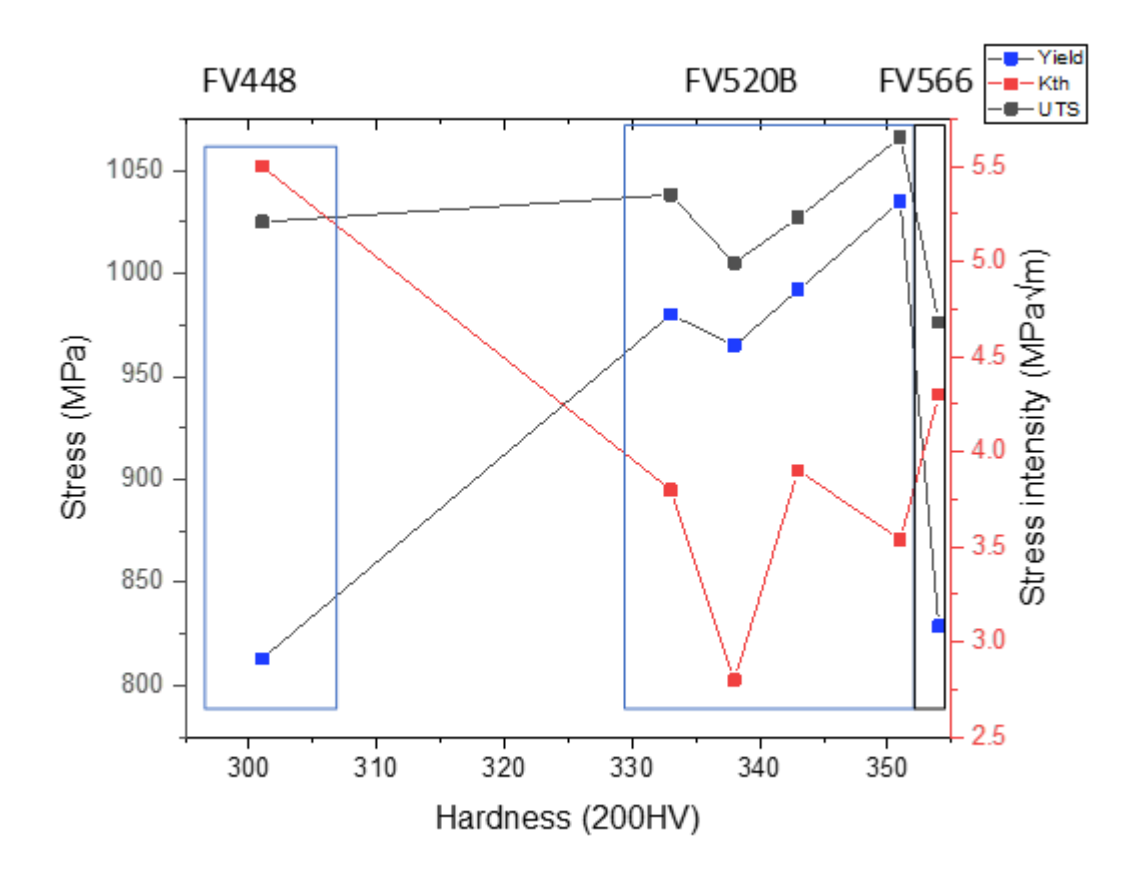


Figure 4-9 Comparison of strength and ΔKth with hardness for FV448, FV520B and FV566

#### 4.3.3 Effect of $\Delta K$ and microstructure on crack path behaviour

Long crack test sample fracture surfaces (FS) were imaged using an SEM, then nickelplated and sectioned to expose the cross section, polished and imaged after etching to reveal the microstructure around the crack path. The imaging, both at the FS and cross section, was performed at crack lengths corresponding to  $\Delta K_{th}$ ,  $\Delta K \sim 10$  MPa $\sqrt{m}$  and  $\sim 20$  MPa $\sqrt{m}$ . The fractography is represented in Figure 4-10, Figure 4-11, Figure 4-12, Figure 4-13 for blades 75, 71, 73 and 1 respectively. A hardness map indicates the hardness level in relation to the other blades for each case. Observation of the ΔK<sub>th</sub> crack growth features in Figure 10-13 (a-i-ii) showed an irregular intergranular crack propagation, where the crack follows fine microstructural features, martensite laths. At mid level ΔK of ~10 MPa√m, in Figure 10-13 (ci-ii) the crack path was observed as becoming more transgranular, the crack path was also relatively unaffected at this ΔK level by any alumina inclusions as observed in Figure 4-10(ci), At high, near failure ΔK levels the crack was observed to be fully transgranular. Figure 10-13 (d-i-ii) and evidence of secondary cracking was observed. At higher ΔK levels the alumina inclusions showed evidence of arresting cracks as observed in Figure 4-11 (d-iii). Overall, alumina inclusions observed showed little effect on crack growth behaviour except for at higher ΔK levels. The fractography comparison showed no significant difference in crack growth propagation between blades regardless of hardness variations. The inclusion population in FV520B may be considered beneficial at high ΔK acting as a potential crack arresting mechanism.

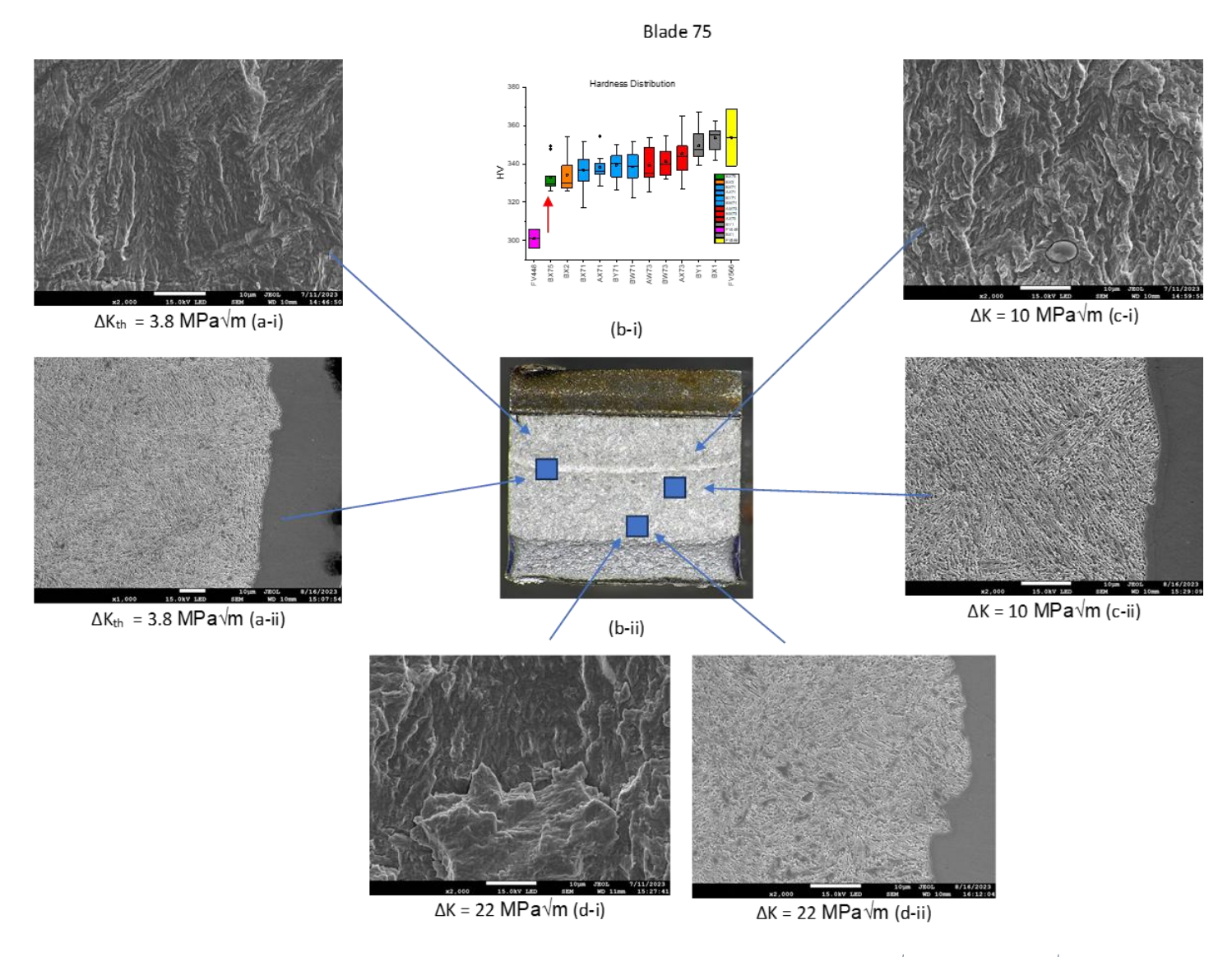


Figure 4-10 Long crack test fracture surface (a-i,d-i,c-i) and cross-section imaging (a-ii, d-ii, c-ii) at  $\Delta K_{th}$ ,  $\Delta K = 10$  MPa $\sqrt{m}$ ,  $\Delta K = 22$  MPa $\sqrt{m}$ . (a-i-ii) At  $\Delta K_{th}$  fracture surface suggests grain morphology, mainly the martensite laths, influence crack growth. This is also observed in the cross section of the fracture surface. (b-i-ii) As  $\Delta K$  increases and load remains constant (Paris law regime) the lath microstructure has less of an effect. The crack propagates more trans-granularly. Visible alumina inclusions show no effect on crack path. (d-i-ii) At high  $\Delta K$  the fine microstructure (laths) has a lesser effect on the crack growth rate. Secondary cracks are also observed.

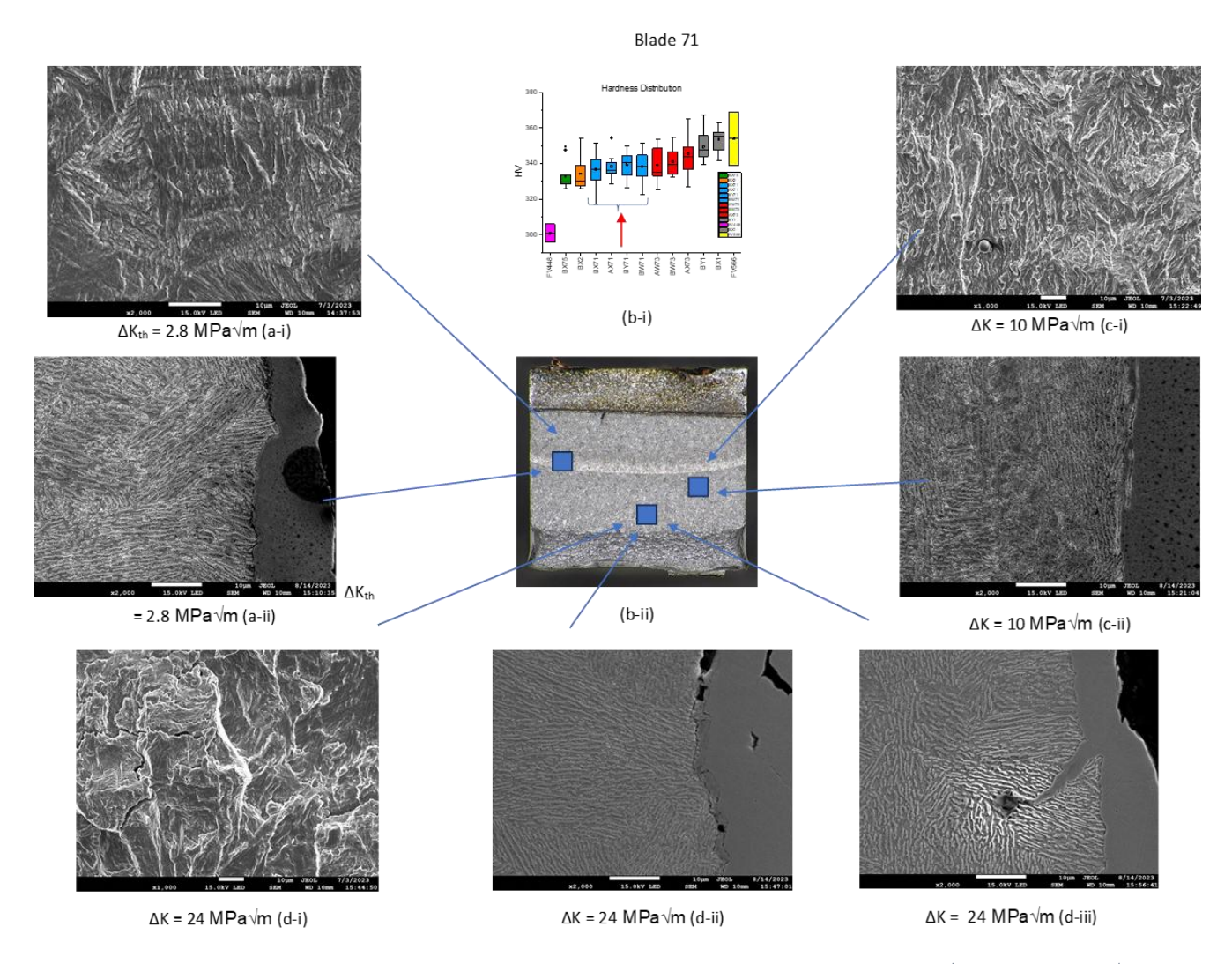


Figure 4-11 Long crack test fracture surface (a-i,d-i,c-i) and cross-section imaging (a-ii, d-ii-iii, c-ii) at  $\Delta K_{th}$ ,  $\Delta K = 10$  MPa $\sqrt{m}$ ,  $\Delta K = 22$  MPa $\sqrt{m}$ . (a-i-ii) At  $\Delta K_{th}$  fracture surface suggests grain morphology, mainly the martensite laths, influence crack growth. This is also observed in the cross section of the fracture surface. (b-i-ii) As  $\Delta K$  increases and load remains constant (Paris law regime) the lath microstructure has less of an effect. The crack propagates more trans-granularly. Visible alumina inclusions show no effect in crack path. (d-i-ii) At high  $\Delta K$  the fine microstructure (laths) has a lesser effect on the crack growth rate. (d-iii) Secondary cracks are also observed to be halted by alumina inclusion in their path.

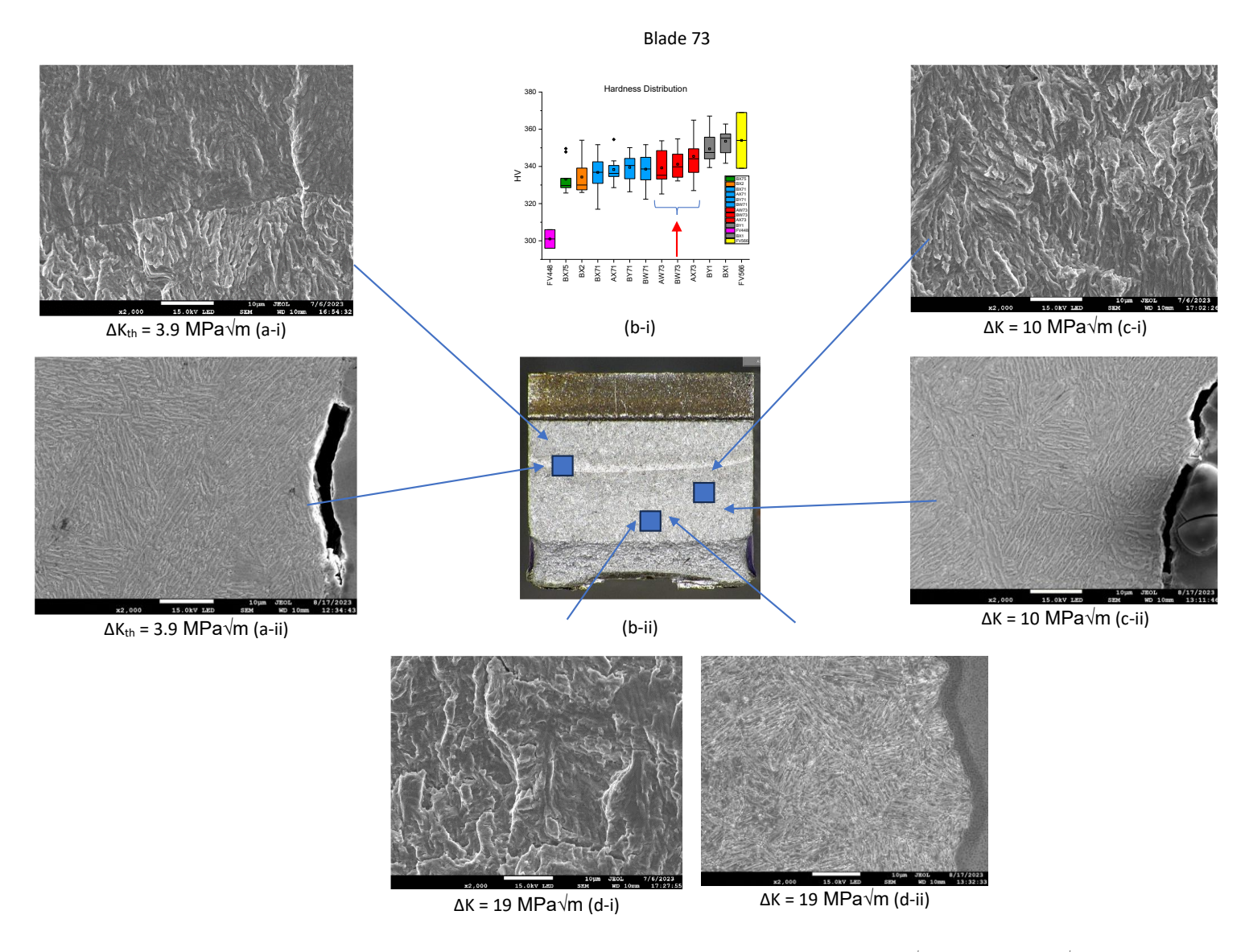


Figure 4-12 Long crack test fracture surface (a-i, d-i, c-i) and cross-section imaging (a-ii, d-ii, c-ii) at  $\Delta K_{th}$ ,  $\Delta K = 10$  MPa $\sqrt{m}$ ,  $\Delta K = 19$  MPa $\sqrt{m}$ . (a-i-ii) At  $\Delta K_{th}$  fracture surface suggests grain morphology, mainly the martensite laths, influence crack growth. This is also observed in the cross section of the fracture surface. (b-i-ii) As  $\Delta K$  increases and load remains constant (Paris law regime) the lath microstructure has less of an effect. The crack propagates more trans-granularly. Visible alumina inclusions show no effect in crack path. (d-i-ii) At high  $\Delta K$  the fine microstructure (laths) has a lesser effect on the crack growth rate. Secondary cracks are also observed.

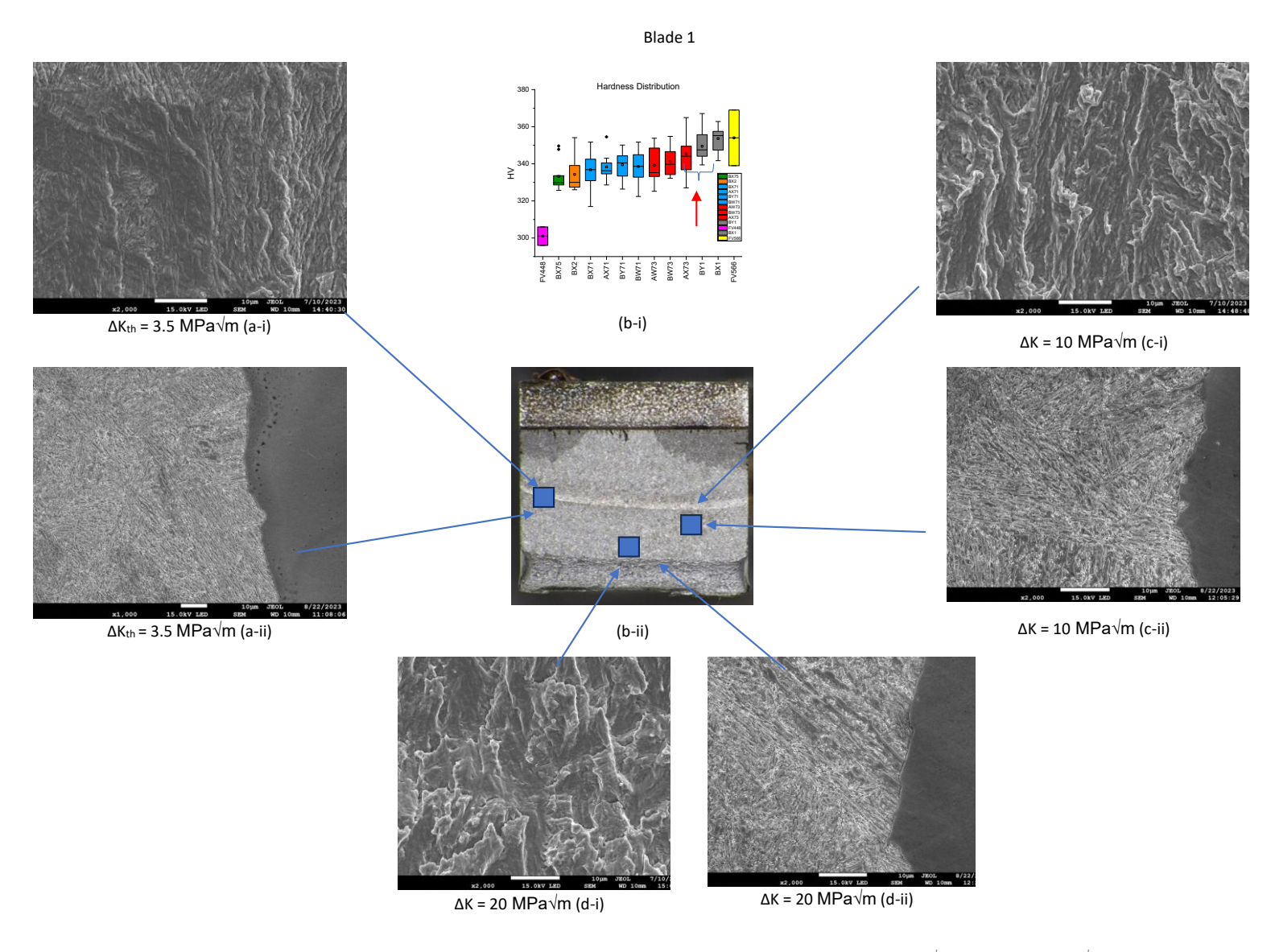


Figure 4-13 Long crack test fracture surface (a-i, d-i, c-i) and cross-section imaging (a-ii, d-ii, c-ii) at  $\Delta K$ th,  $\Delta K$  = 10 MPa $\sqrt{m}$ ,  $\Delta K$  = 20 MPa $\sqrt{m}$ . (a-i-ii) At  $\Delta K$ th fracture surface suggests grain morphology, mainly the martensite laths, influence crack growth. This is also observed in the cross section of the fracture surface. (b-i-ii) As  $\Delta K$  increases and load remains constant (Paris law regime) the lath microstructure has less of an effect. The crack propagates more trans-granularly. Visible alumina inclusions show no effect in crack path. (d-i-ii) At high  $\Delta K$  the fine microstructure (laths) has a lesser effect on the crack growth rate. Secondary cracks are also observed.

#### 4.4 Discussion

The evaluation of baseline fatigue properties of FV520B and the comparison with other blade materials was performed. Paris law behaviour between FV520B blades was found to be relatively consistent within the tested blade population which is consistent with literature where an alloy of same composition but dissimilar mechanical properties due to HT was studied[118], [119]. At ΔK<sub>th</sub> the variation between blades increases, this can be attributed to the variation in lath size as near  $\Delta K_{th}$  crack growth was observed to be intergranular and driven by fine microstructural features where larger grains typically result in higher threshold levels[117], [120], [121], [122]. It was noted that the change in  $\Delta K_{th}$  was not strongly correlated with hardness increase. A comparison was made between ΔK<sub>th</sub> and mechanical properties in relation to hardness between 3 similar alloys, FV520B, FV566 and FV448[8], [51], [102]. The comparison again didn't show a strong correlation between hardness and  $\Delta K_{th}$ , only when observing FV566 and FV520B there was a weak direct proportionality between hardness, mechanical properties and  $\Delta K_{th}$ . Given the typical relationship between larger grains and higher threshold, with decreasing hardness the threshold might be expected to increase due to enhanced crack deflection and associated intrinsic and extrinsic shielding effects. but this was not an observed trend for FV520B. The three alloys, although martensitic stainless steels, have different strengthening mechanisms and inclusion populations which may explain the inconsistencies observed[122], [123]. For instance FV520B differs from the rest, as it has a precipitation hardening HT phase which provides the main strengthening mechanism of the alloy[34], [98], [105]. The fatigue threshold is affected by slip band irreversibility, grain boundary interactions, grain size/shape and strengthening mechanisms in the alloy, which would explain the lack of a clear trend found in  $\Delta K_{th}$  between the alloys. Furthermore, FV520B fractography showed the crack path being intergranular and heavily dependent on fine microstructural features, due to the variation of lath size and prior austenite grain boundaries, observed in the previous chapter, this could explain the inconsistencies between FV520B samples. Typically, finer microstructures should provide a lower threshold level. Our results show a general trend for lower threshold for finer grain size, but this was not consistent for all samples. To account for yield strength variation effects we calculated the  $\Delta$ CTOD for each of the 4 samples analysed. The consistency in crack tip opening displacement controlling da/dN was maintained for stage II crack growth, with a minor widening of the crack growth rate. The near threshold ΔCTOD results showed scatter between samples but this did not compensate for the inconsistency between grain size and expected threshold level. In this study, the blade to blade variations seen in FV520B do not seem to be significant when considering long crack growth behaviour, and accounting for yield strength variations.

A simple prediction of fatigue lifetime was performed using material constants derived from Paris law empirical calculations. The predictions were calculated with respect to  $\Delta K$  and number of cycles to failure, assuming a simple starting crack geometry and shape factor but accounting for C and m differences as well as  $K_Q$  differences. The simple lifetime predictions showed an increase of standard deviation in FV520B lifetimes with lower  $\Delta \sigma$  levels. When compared to FV566 lifetime predictions calculated in the same way, the two alloys have relatively similar predicted lifetimes at relatively high  $\Delta \sigma$  the lifetimes do diverge with lower  $\Delta \sigma$  this may be explained by the effect of material properties in the different alloys, whilst we assumed a consistent starting defect of 20  $\mu$ m , [1], [14].

Fracture surface observations of FV520B tested samples showed consistency in crack path behaviour between blades, regardless of hardness variations. The near  $\Delta K_{th}$  crack path was observed to be intergranular and dependent on fine microstructural features, which is observed in Figure 4-10 (a-i,a-ii) Figure 4-11(a-i,a-ii) Figure 4-12(a-i,a-ii) Figure 4-13(a-i,a-ii). The variation in lath size did not seem to have a significant effect on  $\Delta K_{th}$  values. At increasing  $\Delta K$  the crack path was observed to be increasingly transgranular, hence less dependent on finer microstructure. At high  $\Delta K$  the crack path presented some secondary cracking, in one of the blades the secondary cracks were observed to be halted by the alumina inclusions present in the alloy, suggesting a potential beneficial effect of the inclusions in this regime of failure behaviour. The Alumina inclusions were also observed to have little to no effect on crack path at lower  $\Delta K$ .

# 4.5 Summary and conclusions

#### 4.5.1 Summary

The microstructural analysis, presented in chapter 3, showed a minor difference between FV520B in grain size, both from a martensite lath size and prior austenite grain size. Hardness distribution between blades was observed to have some scatter, this was also observed within the blades but to a smaller extent than between blades. Long crack testing and the resulting Paris law graphs show consistency in crack growth rates between blades for increasing ΔK between blades. The extrapolated material constants show little variation within FV520B with no strong correlation to measured hardness or grain size. The grain size differences identified in chapter 3 affected the crack growth rate most at near threshold ΔK regime where the crack path was observed as prevalently intergranular. When accounting for mechanical properties, hence calculating the range of Crack Tip Opening Displacement, an increased difference in crack opening displacement was observed near threshold. This also accentuates the crack growth rate at near stage I crack growth regimes. Fatigue lifetime estimations showed similar lifetimes between FV520B at higher stress ranges and an increased difference at lower stress ranges (longer lives). FV566 fatigue life estimates showed similar lives to the FV520B at high stress ranges but lower lifetimes at lower stress ranges (longer lifetimes). Hardness was shown to have a significant correlation with estimating UTS but not a strong correlation with estimating  $\Delta K_{th}$ . The comparison between FV520B and similar martensitic alloys, FV566 and FV448, showed no strong correlation between the three in regards to trends between hardness, mechanical properties and baseline fatique properties. The crack growth behaviour observed in FV520B, via observation of fracture surfaces and fracture surface cross section, were consistent between samples at all  $\Delta K$  observed. A prevalence in intergranular crack growth was observed at low ΔK while transgranular crack growth was observed as more prevalent at higher  $\Delta K$ . At lower  $\Delta K$  the effects of finer microstructure were more prevalent. Inclusions were not observed to influence the crack growth significantly, the only noticeable effects were at high  $\Delta K$  where the alumina inclusions were observed to act as crack arrestors for secondary cracks.

#### 4.5.2 Conclusions

• The slight differences between the three alloys might be attributed to the different strengthening mechanisms that characterise the alloy. In the case of FV520B, contrary to the other two alloys, the main strengthening mechanism has been previously identified as precipitation hardening via artificial aging process. The strengthening mechanism of the alloy is expected to affect the hardness, mechanical properties and the fatigue properties.

- Fatigue life estimates comparison between FV566 and FV520B showed consistency in lifetimes at high stress ranges with higher scatter in lifetime at low stress ranges between the FV520B variants.
- There was no noticeable crack growth behaviour difference between blades from fracture surface observations. The grain size effects were more prominent at near threshold ΔK.
- Inclusions in FV520B were not significant influencers in crack growth behaviour.
- In terms of the service application, it seems that there is little variability between blades in terms of the conventional fatigue properties investigated here.

# Chapter 5 Mitigation strategy effectiveness from shot peening

#### 5.1 Introduction

Legacy stainless steel alloy turbine blades are being extended well beyond their original expected fatigue lifetime as they experience more extreme load cycling. This is due to the requirement to cover energy supply needs that vary more as we move to more use of renewable energy sources in the grid. Understanding how much longer these turbine blades can be safely extended under these more extreme and more frequent load cycles is important as companies time the phasing-out of these legacy systems, avoiding unnecessary expensive blade replacements which will only be needed for a short period of lifetime extension. A maintenance process is proposed consisting of the grinding out of fatigue cracks detected in critical areas of the blade (the fir tree root notches) and peening of the surface to suppress further fatigue. The crack grind out and the consequent change of geometry effects were studied previously[7], [124] and are not a focus in the current work. The effectiveness of shot peening (SP) and the benefit when accounting for blade-to-blade variability for a given alloy, FV520B, is studied in the present work. Furthermore, a multi-phase lifetime prediction model is further studied, the model was developed by Cunningham[6], and accounted for the variation of crack growth rate at different stages of fatigue life in a component, Initiation, short crack growth, coalescence and long crack growth. The current work studies how the variability of blade-to-blade material properties and shot peening effectiveness affects the model predictions from Cunningham.

The peening process induces surface defects in the form of increased roughness and small cracks which act as initiation sites for short cracks[15], [102]. The effects of the underlying microstructural features has been shown in previous research to be less dominant after peening as the SP induced defects and residual compressive stresses dominate the initiation and short crack propagation processes [108]. The residual compressive stress profiles in FV520B and FV566, which have different yield strengths and average yield strengths are compared in terms of stress-depth profile and maximum stress levels. The microstructural and baseline fatigue performance differences between the two alloys are discussed in chapter 4. The effects of the same shot peening process on the fatigue performance on these two alloys are discussed further in this chapter. The predictive model from Cunningham has also been applied to the FV520B data for both polished and shot peened cases to assess how well it can predict behaviour in the FV520B blade material.

#### 5.2 Methods

### 5.2.1 Shot peening residual stress measurement via XRD

The use of X-ray diffraction (XRD), Figure 5-1 [108], is commonly used to determine the residual stresses found in shot peened samples. The method involves incrementally removing by electropolishing surface layers and performing successive surface XRD scans. The spatial and depth resolutions are better than mechanical method alternatives, like hole drilling.

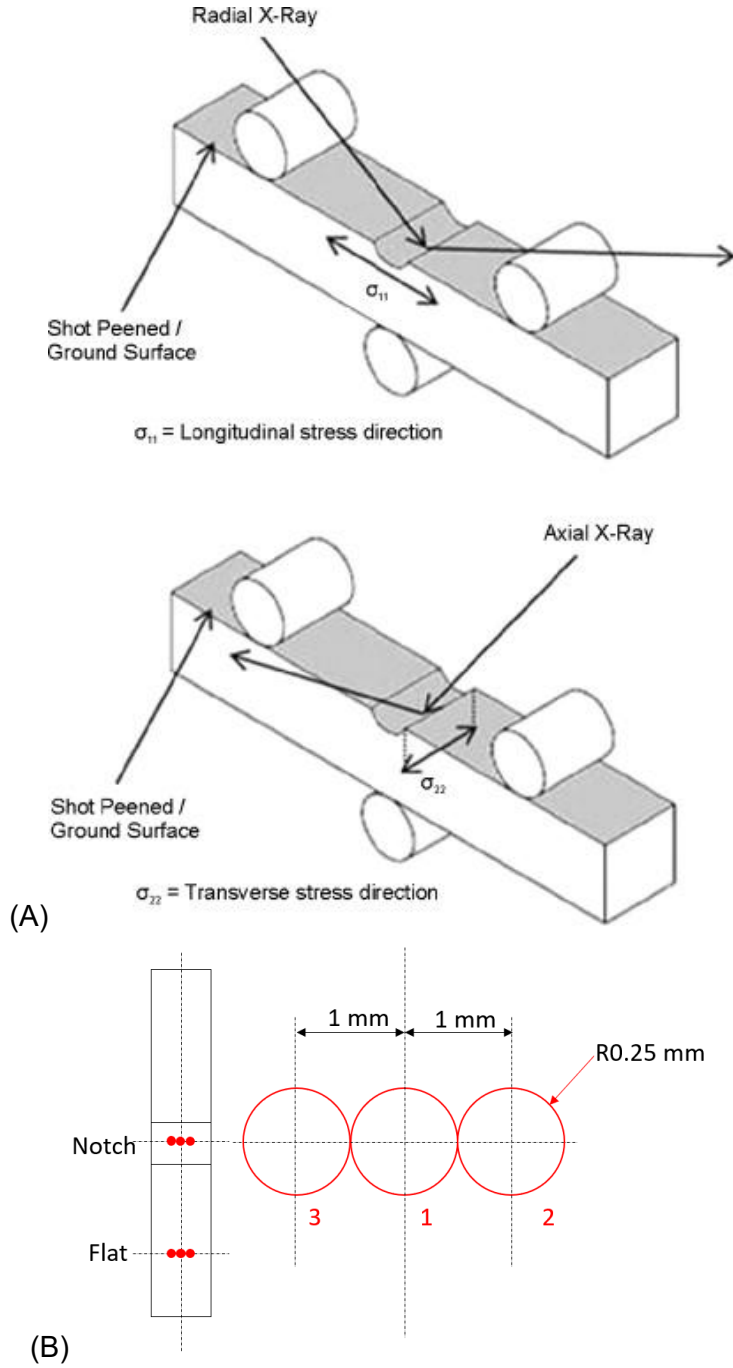
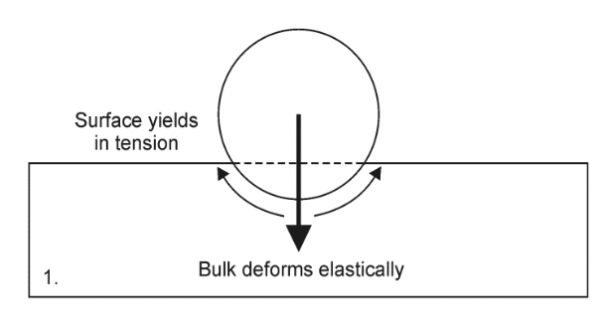


Figure 5-1 Schematic of XRD [108] set up for residual compressive stress analysis.(A) The stresses were measured in the longitudinal direction using radial x-rays and the transverse stresses using axial x-rays. The top grey area was peened,(B) measurements were taken both in the U-notch and on the peened flat surface.

The measurements were performed using the  $\sin^2\psi$  method using a Stresstech Xstress Robot and incremental layer removal was achieved by electropolishing. The measurements were performed at Coventry University, courtesy of Dr Mitchell Leering. The measurements were carried out in the longitudinal and transverse direction on the flat bend bar top surface and at three locations at the bottom of the U-notch to verify consistency in the residual stress profile in the notch as illustrated in Figure 5-1 (B). The equipment was calibrated and validated using stress free Fe powder. A collimator was used with an aperture diameter of 0.5 mm and exposure time of 20seconds over 12 tilts from -45° to 45°. The determination of measurement errors was done by taking a daily zero reading. The incremental material removal from the surface was performed via electro-polishing, using a Struers LectroPol, with A2 electrolyte and a mask of 0.5 mm² which is the equivalent area of measurement, 20 V flow rate of 14 for 12 seconds. The measurements were carried out with incremental removal until a 0 MPa reading was recorded for 100  $\mu$ m. The layer removal is necessary to accurately measure stress variation with depth.

# 5.2.2 Shot peening

The peening process applied to the material of interest FV520B and FV566 was conducted externally following the shot peening process outlined in prior research on FV566 and other similar alloys. The process, illustrated in Figure 5-2, works by firing shot of given dimension and hardness onto a surface with velocity, intensity and coverage that can be changed to generate a range of residual compressive stresses. The settings used in the current study are summarised in Table 5-1.



Surface tends to retain permanent deformation and is constrained by bulk material resulting in compressive residual stress

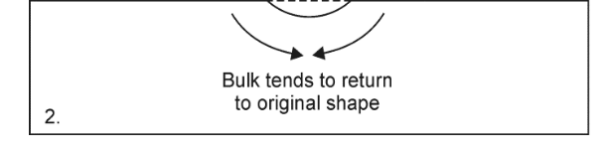


Figure 5-2 schematic representing the shot peening process effects when a shot hits the surface of the material treated [90].

Table 5-1 Shot peening settings used for samples in the current study on FV520B and on previous work on FV448 and FV566

Settings T0				
Intensity [A]	Shot Diam [mm]	Shot HRC	Shot velocity [m/s]	Coverage [%]
13	0.58	45-52	57	200

# 5.2.3 Roughness testing

Surface roughness Ra and Rz measurements were taken at the root of the notch before testing using a profilometer (Infratouch) following standard *BS EN 4288: 1998*. A 5mm long measurement length was used and an Lc value of 0.8, the profiles were taken in the transverse direction (perpendicular to the tensile axis) of the notch surface.

#### 5.2.4 Short crack fatigue testing

An Instron 8502 servo-hydraulic machine and all-electric dynamic test machine Instron E10000 with a 10kN load cell was used to perform fatigue tests on U-notched bars with a characteristic geometry of the fir tree root notch of a LD66 turbine blade taken from previous studies [125], as shown in Figure 5-3. A U-notch (Figure 5-3) was machined in the bend bars to create stress concentration factor of k = 1.6 which is similar to that of the fir tree root of the steam turbine blades analysed in this study.

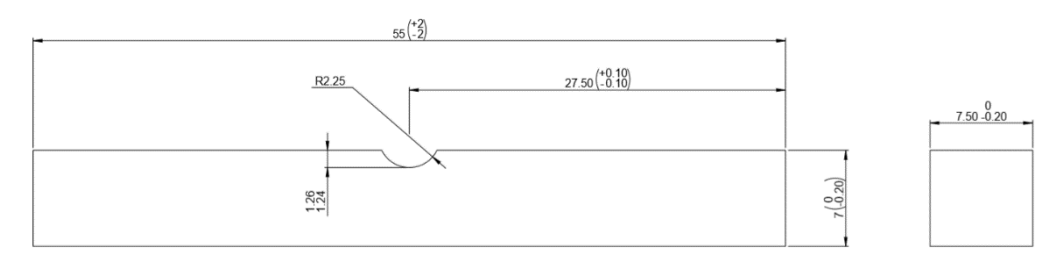


Figure 5-3 characteristic U-notch geometry with k=1.6

Three interrupted short fatigue crack tests were carried out at 3 nominal stress ranges at the notch root: 1152MPa, 1308MPa and 1397MPa. The equivalent strain range for each sample at the root was then calculated using FEA models used by Cunningham which allowed for blade to blade variability in yield stress [7]. The tests were carried out at a frequency of 20Hz with a sinusoidal waveform at a load ratio R of 0.1. The test was conducted using the workflow method in Figure 5-4 based on the total predicted fatigue lifetime of the sample. The fatique life was predicted using previously performed lifetime testing at the given strain ranges. The workflow involves initial fatiguing to 10% of lifetime, where cracks are not expected to be seen, then silicone replicas were taken at regular cyclcing intervals and inspected after curing for visible cracks. Subsequently, the test was run for 5% of the estimated lifetime and replicas continue to be taken until cracks are observed, where the test was run for 2% lifetime increments between each replica to capture crack evolution. On average 30 replicas were taken per test, although given lifetime variability the number of replicas varied between 15 to 34. The cracks were then measured and counted to obtain surface crack length (2c) as a function of number of cycles (N) data and subsequently to calculate da/dN v \( \Delta K. \) The replica record also allowed a visualisation of crack initiation and coalescence behaviour during the fatigue life. The surface crack length was measured as the projected length of the crack as shown in Figure 5-5.

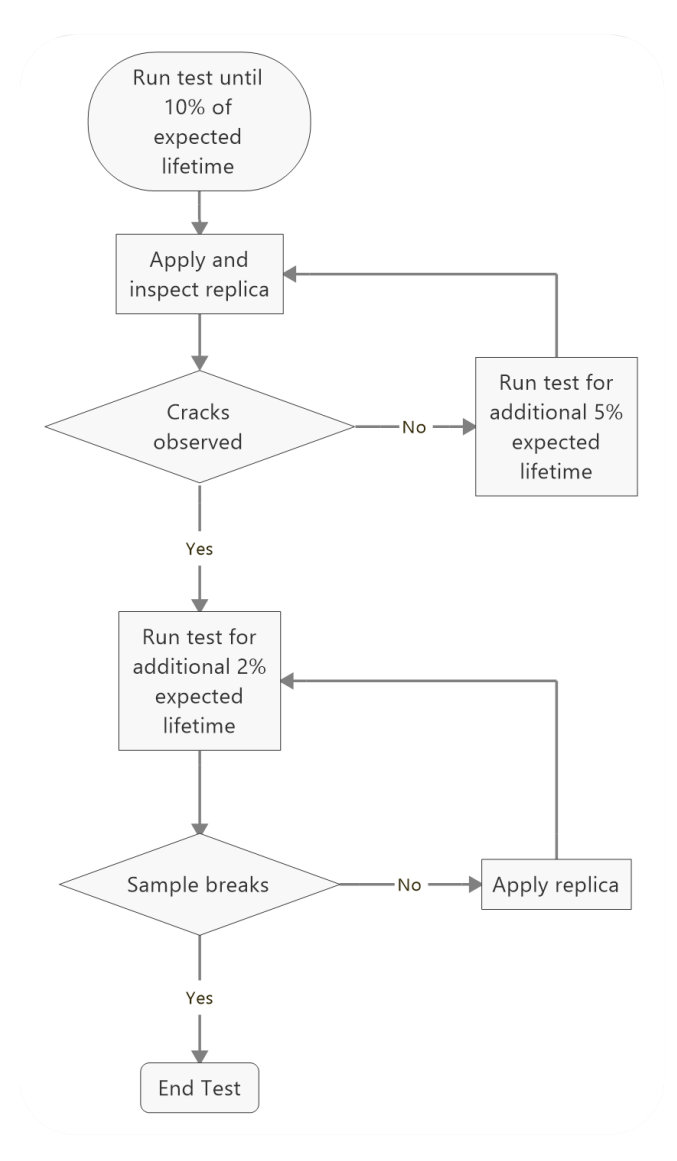


Figure 5-4 surface replication method workflow based on predicted fatigue lifetime of samples.

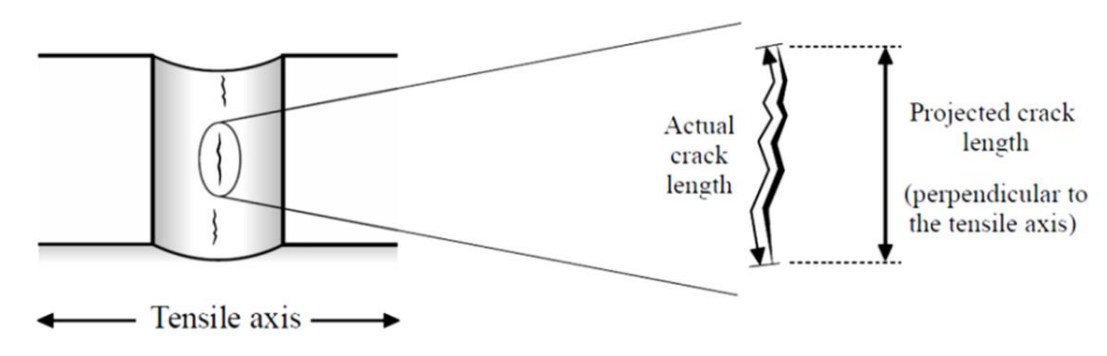


Figure 5-5 Projected length of crack in u-notched samples[35]

The projected surface crack lengths were defined as 2c and the depth of the crack was defined as a, as described in Figure 5-6. An a/c ratio of 0.8 was assumed based on previous literature based on fatigue crack evolution in similar material under similar testing conditions [126].

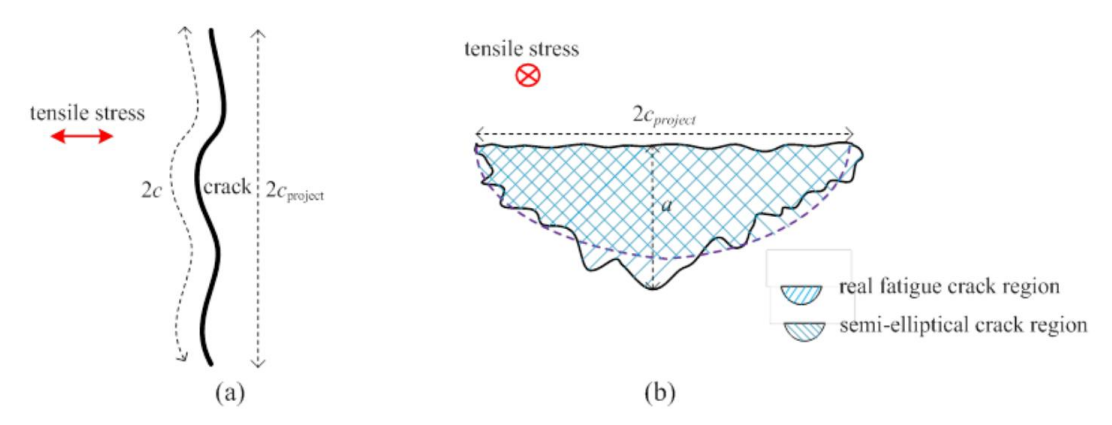


Figure 5-6 visual representation of the depth to length ratio of the measured cracks and of method used to determine the a/c ratio of cracks after heat tinting. The real fatigue crack region observed on a fracture surface is measured and then interpreted as a semi-ellipse with given length c, allowing to extrapolate a. [35]

The silicone replicas taken provide a reversed chronological record, Figure 5-7, where the main crack at approximately 100% fatigue life was measured as crack 1. Subsequent cracks in the previous replicas were designated as constituents of the final fracture crack as the replica record is analysed for earlier stages in the fatigue life.

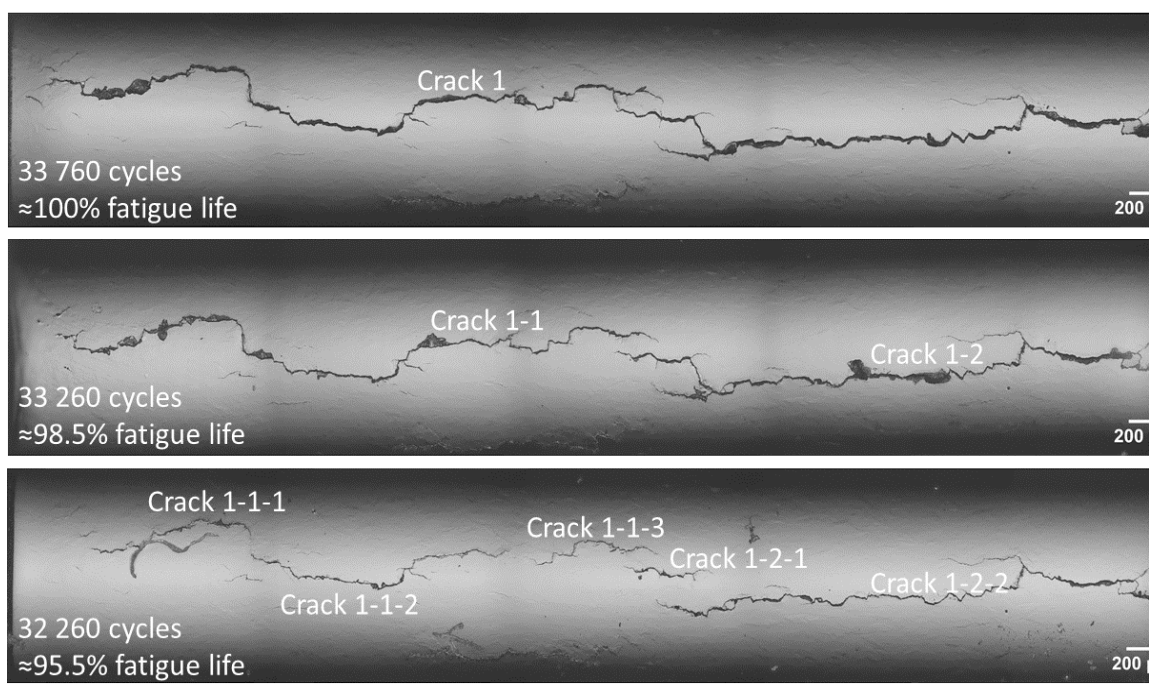


Figure 5-7 replica analysis example where the final fracture crack is measured in the last replica and the constituent cracks are then measured (and designated) in reverse chronological order

Fractography was also performed on the fracture surface using SEM, a JEOL JSM-6500, with accelerating voltage of 15 kV and working distance of 10 mm. to identify crack initiation sites. Lifetime tests were also performed on shot peened samples using the same conditions both for lifetime and replica testing.

#### 5.2.5 Depth to length ratio measurement

The projected half crack length *c* to crack depth *a* ratio, referred to as the a/c ratio, described in Figure 5-6, was determined by means of heat tinting and fractography

analysis. U-notched samples were fatigued to between 60-80% of predicted lifetime to achieve crack initiation and growth to obtain cracks of lengths between (50µm to 1000µm). The sample was then placed in a furnace for 1 hour at 600°C to oxidize the cracks. The sample was then allowed to cool to room temperature before a notch was cut on the back end of the sample to aid breaking open. The sample was then cryogenically cooled using liquid nitrogen, the frozen samples were then broken open using a mallet, this revealed the fracture surface with the oxidised cracks. These were then imaged using an SEM model JMS 7500. To measure the length to depth ratio of the cracks the real area of the crack was measured and interpreted as a semi elliptical area to normalise for the inhomogeneous shape of the cracks. The method was used both for single cracks as well as coalesced cracks as in Figure 5-8 (III).

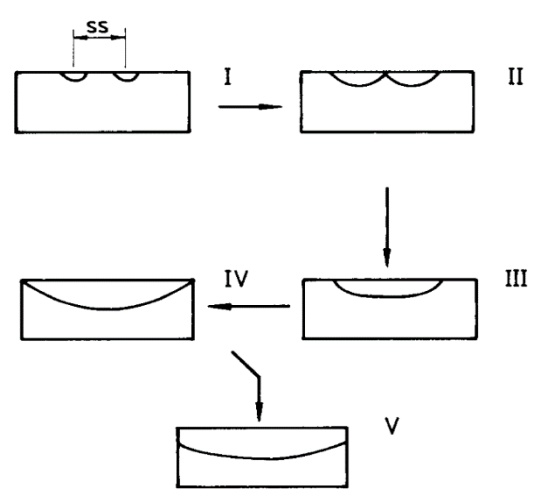


Figure 5-8 Representation of the process of coalescence between multiple crack in a short fatigue crack growth scenario. In (I) we observe two cracks initiating then growing in a semi-elliptical fashion (II) until fully coalesced (III) to then grow until the crack is extended through the width (IV) and (V)[35].

#### 5.3 Results

#### 5.3.1 Fatigue lifetime of blade steels

Baseline (un-peened) testing was performed on FV520B U-notched samples with a 1 mm polished surface condition in the notch to assess crack initiation from underlying microstructural features rather than surface roughness. The resultant ε-N results for FV520B were compared with results from literature on other legacy blade steel alloys in the polished and as-received condition. The as-received condition is interpreted as the condition of the part post-machining. The lifetimes of as-received tested samples, in Figure 5-9, were observed to have lower lifetimes for a given strain range at the notch when compared to the polished surface condition of the same material. FV520B was not tested in the as-received material, the polished condition was compared to the other observed alloys. FV520B exhibited a longer fatigue lifetime at relatively high strain ranges when compared to polished FV448. Lifetime data suggests FV520B exhibits a higher fatigue strength compared to FV566 and FV448, even when lifetimes are normalised by considering the strain range linked to the blade-to-blade variations in yield strength.

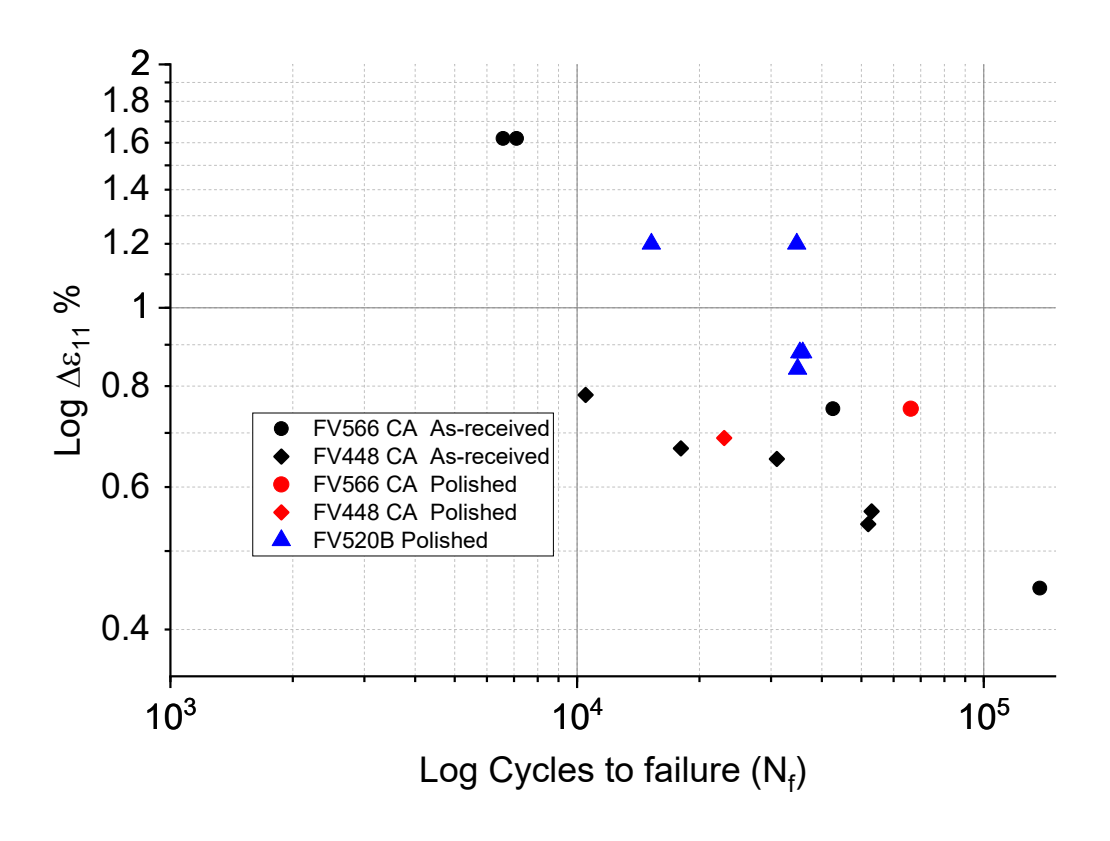


Figure 5-9 Fatigue lifetime comparison of 3 alloys (FV448, FV566 and FV520B) in the as received and polished surface conditions (All Un-peened) (with FV520B being only in the polished condition) of Unotched bend samples

### 5.3.2 Residual stress profile from shot peening

Residual compressive stress profiles of shot peened FV520B and FV566 were measured in the longitudinal and transverse direction using XRD at the U-notch root and the flat top surface of the sample. The results from the two locations were compared to verify the consistency of the effects of shot peening on the varying geometry of the sample and between the two alloys. The resultant residual stress profiles, Figure 5-10, showed consistency in the transverse and longitudinal direction in both the notch and flat area between FV520B and FV566. For both alloys the peak was found to be between 750-800MPa at a depth of 150  $\mu m$ . The residual compressive stress profile of FV520B was compared to that of FV448 from previous studies, Figure 5-11 and Figure 5-12, where the transverse and longitudinal direction stress profile respectively was measured in the as peened, 1 fatigue cycle and 50% of lifetime conditions. The residual compressive stresses in FV448 showed almost complete retention of residual stresses at 50% fatigue lifetime. The magnitude and depth profile of the residual compressive stresses between FV448 and FV520B was observed to be consistent between the two alloys for the given peening treatment.

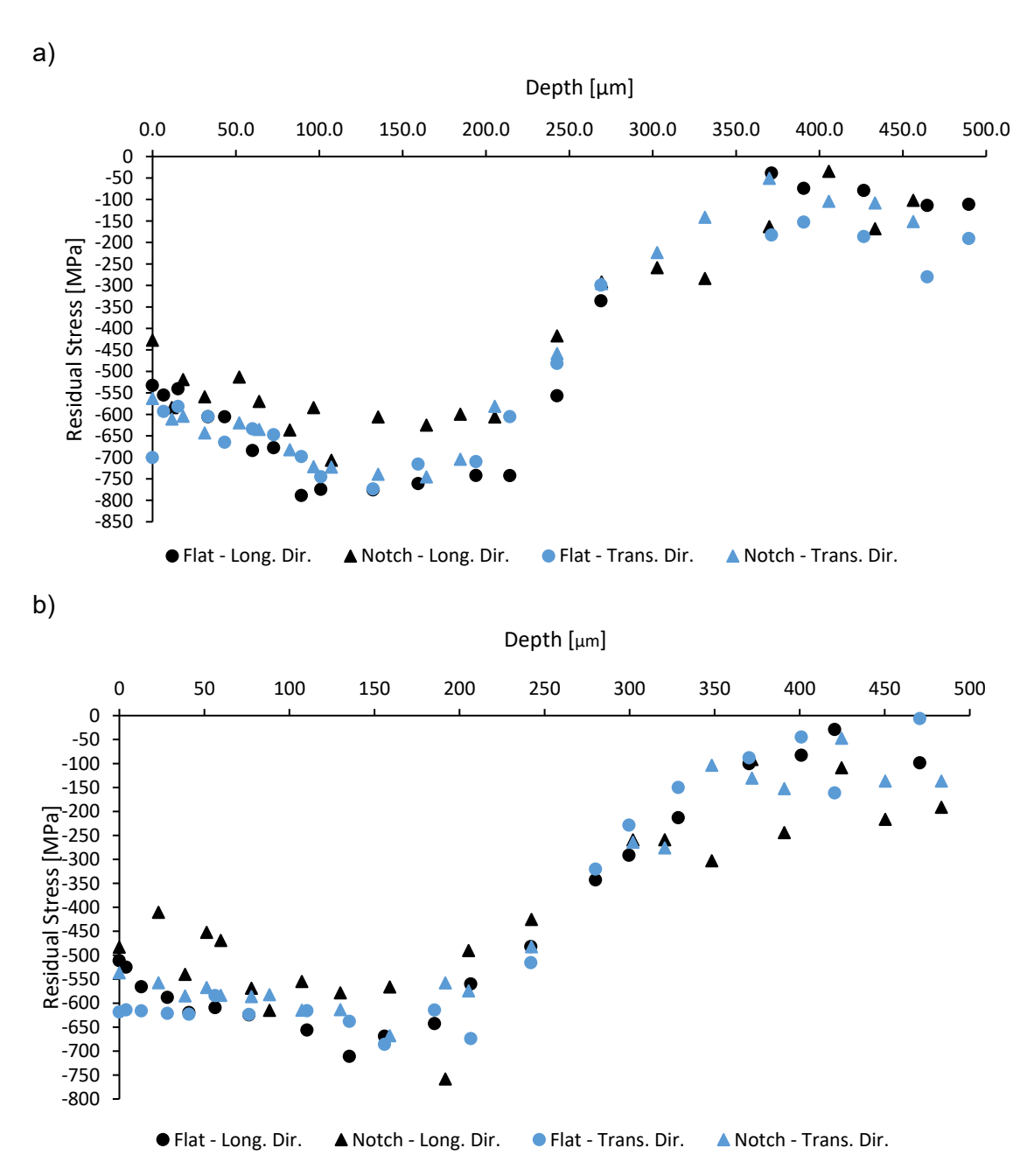


Figure 5-10 Compressive residual stress profile in the longitudinal and transverse direction measured via XRD of FV520B(a) and FV566 (b). The measurements were performed in the as-peened condition in the root of a U-notch bend sample and the flat region of the sample for comparison.

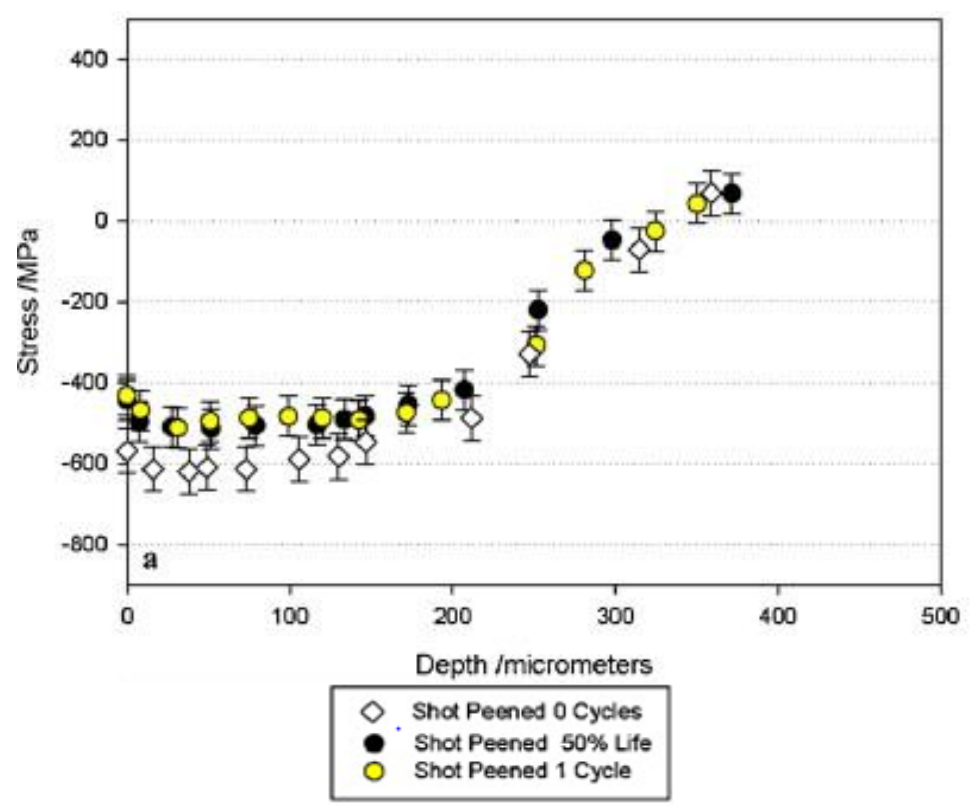


Figure 5-11 Compressive residual stress profile in the transverse direction measured via XRD of FV448. The measurements were performed in the as-peened, 50% fatigue lifetime and after 1 fatigue cycle in the root of a U-notch bend sample[8].

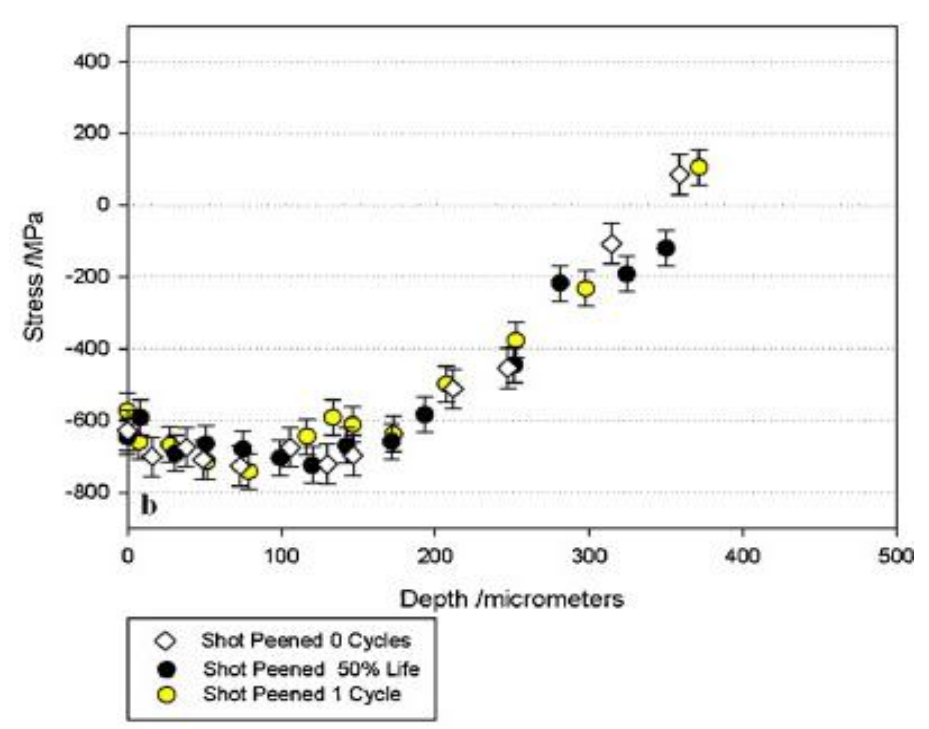


Figure 5-12 Compressive residual stress profile in the longitudinal direction measured via XRD of FV448. The measurements were performed in the as-peened, 50% fatigue lifetime and after 1 fatigue cycle in the root of a U-notch bend sample[8]

#### 5.3.3 Comparison of measured roughness after peening

The roughness of FV520B shot peened samples was measured and compared to that of FV448 from previous studies. The use of a contact profilometer was used for FV520B to maintain consistency with FV448 results. The Ra and Rz, which correspond to arithmetic mean of the measured roughness and the mean roughness depth respectively, were compared between FV520B and FV448. The roughness was found to not have periodicity. The hardness and yield strength of FV448 is lower than that of FV520B which resulted in a lower roughness in FV520B when compared to FV448 after the same peening process.

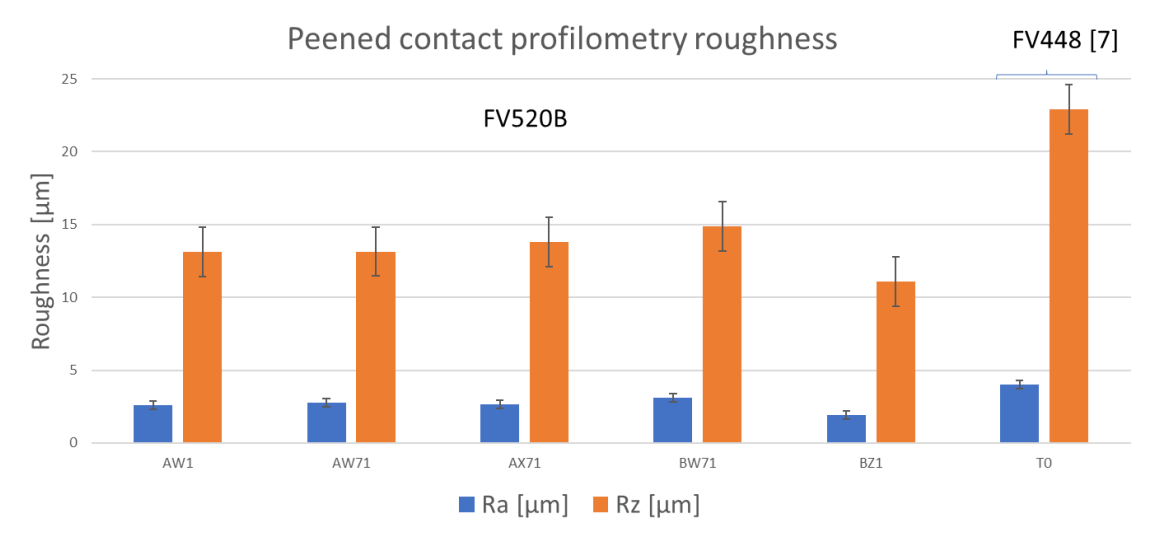


Figure 5-13 Roughness measurement comparison of peened samples between FV520B and FV448. Showing higher roughness levels in FV448 as it's the softest of the two alloys. FV520B samples show a consistent surface roughness condition.

#### 5.3.4 Fatigue lifetime comparison between peened and un-peened samples

Samples in the polished and peened surface conditions were fatigue tested to failure at different strain ranges to compare lifetimes. In *Figure 5-14* FV520B lifetime results are compared between polished and peened conditions, the strain ranges were adjusted for each sample to reflect the strain response based on the elasto-plastic behaviour of the blade of origin of the sample. Overall the lifetime of the peened samples showed a higher fatigue lifetime when compared to the polished samples. When compared to a similar stainless steel blade alloy, FV566, in Figure 5-15 we observe FV520B to have higher lifetimes at higher strain ranges comparatively. The peening induced residual compressive stresses were likely dissipated in FV566 at high strain ranges, while for FV520B the lifetime observations indicate a retention of the compressive residual stresses, likely resulting in higher lifetimes in higher strain range loading scenarios.

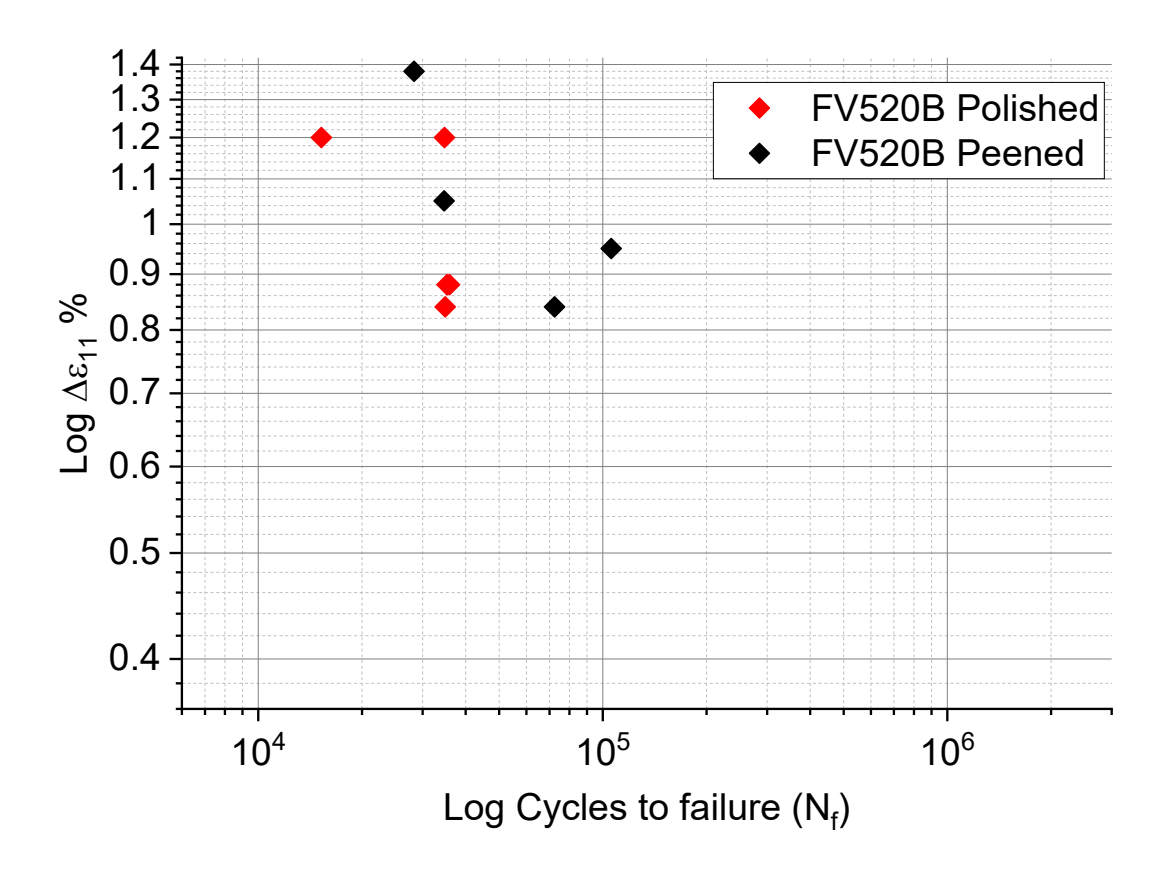


Figure 5-14 Lifetime comparison of FV520B U-notched polished (un-peened) and Peened samples at different strain ranges. The peened samples show an increase in lifetime in most cases at different strain ranges.

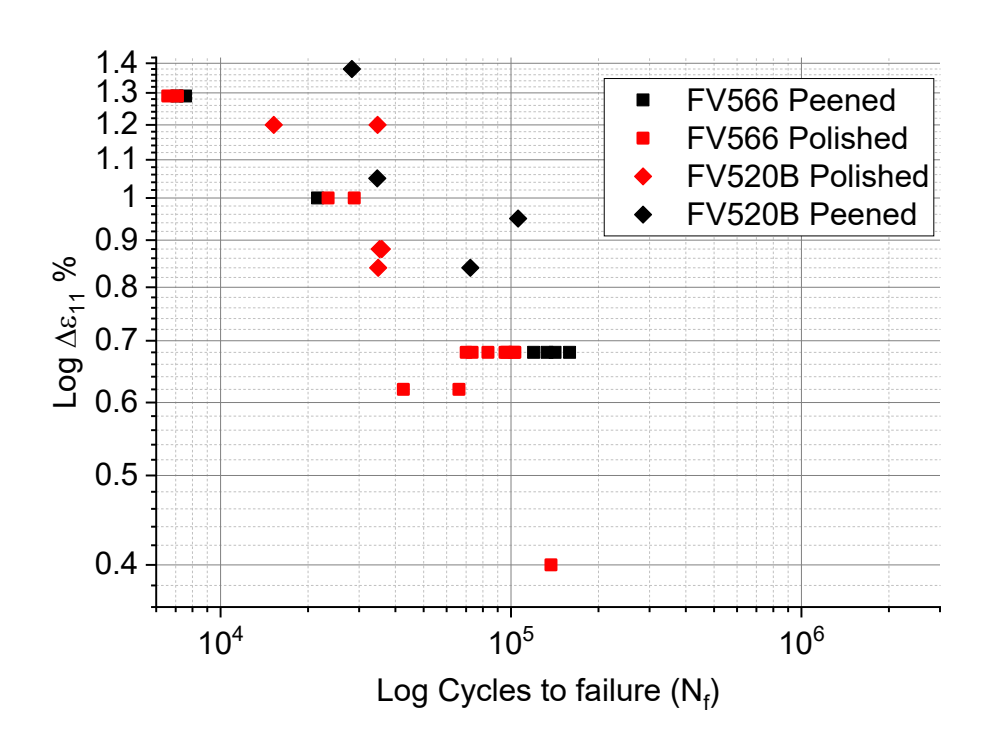


Figure 5-15 Lifetime in the polished (un-peened) and peened conditions of FV566 and FV520B, for equivalent strain ranges FV520B shows longer lifetime. At high strain ranges FV520B in its peened condition shows higher lifetimes compared to FV566, which indicated a higher retention of residual compressive stresses.

### 5.3.5 Fracture surface analysis of polished and peened steel

Fracture surface observations of polished and peened FV520B U-notched short fatigue crack samples were made to compare crack initiation behaviour between the two surface conditions. Crack initiations in polished samples, Figure 5-16 (a), were observed to be more microstructural feature linked rather than defect or inclusion induced initiations. The initiation sites for the polished samples were hypothesised to occur preferentially at the reverted austenite pockets at the grain boundaries or initiated when persistent slip bands formed. The peened sample initiation sites, Figure 5-16 (b), were observed to occur predominantly at defects caused from the shot peening process. The peening process created fold like features which acted as quasi-subsurface defects which acted as stress concentration features. The peening process was also observed to generate surface cracks which in some cases resulted in propagated fatigue cracks.

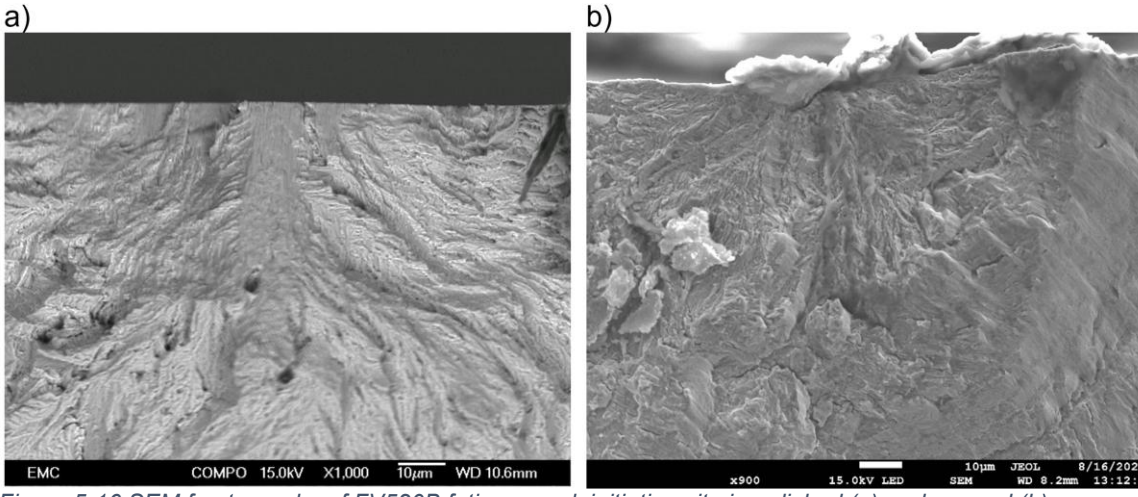


Figure 5-16 SEM fractography of FV520B fatigue crack initiation site in polished (a) and peened (b) samples. Polished sample crack initiation was observed to be microstructural dependent, while shot peened samples cracks were prevalently observed to originate by defects caused by the peening process.

The fracture surface analysis comparison between polished and peened samples showed no significant differences at similar strain ranges, Figure 5-17. The number of crack initiation sites between samples was compared between surface conditions, Table 5-2, the overall trend in both cases was a higher number of initiations for higher strain ranges for each case, with the trend being much more consistent oin the peened case, where as a lot more scatter was seen in the polished cases, Figure 5-18. Peened samples presented with a slightly higher number of crack initiations compared to polished samples for a given strain range.

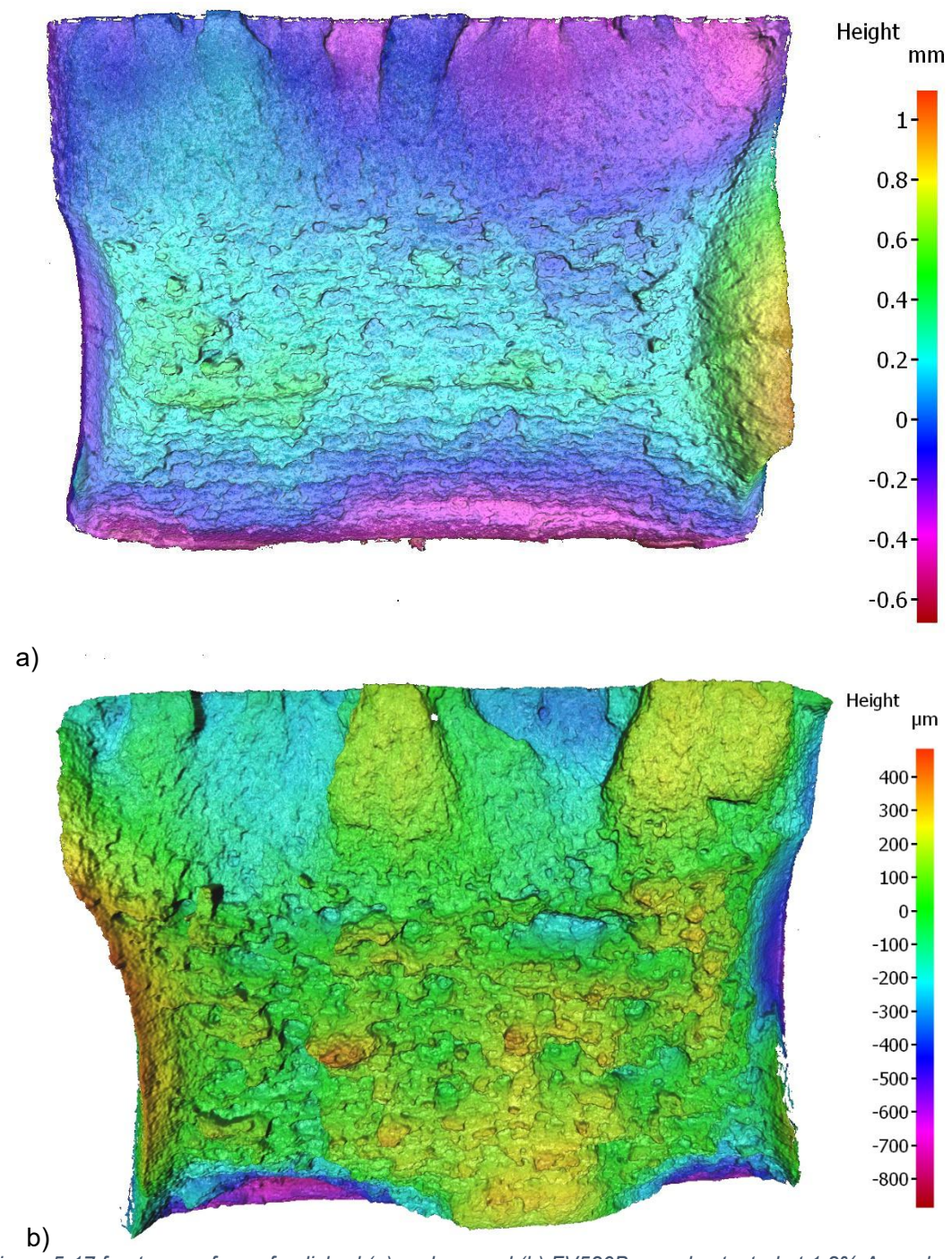


Figure 5-17 fracture surface of polished (a) and peened (b) FV520B samples tested at 1.2%  $\Delta \varepsilon$  and scanned using a focus-variation microscope. The fracture surfaces were not observed to have significant changes in number of crack initiations and crack growth behaviour after initiation.

Table 5-2 comparison of number of crack initiation sites between polished and peened samples at different tested strain ranges.

Sample	Conidtion	Strain Δε%	number of initations		Lifetime [cycles]
AW73	peened	1.38		23	28304
AX71	peened	1.05		17	34616
AX73	peened	0.95		16	105704
BW71	peened	0.84		13	72427
BW73	polished	1.2		22	34710
BY71	polished	1.2		30	15238
BX1	polished	0.88		20	35304
BY1	polished	0.88		15	35880
BX71	polished	0.84		22	34872

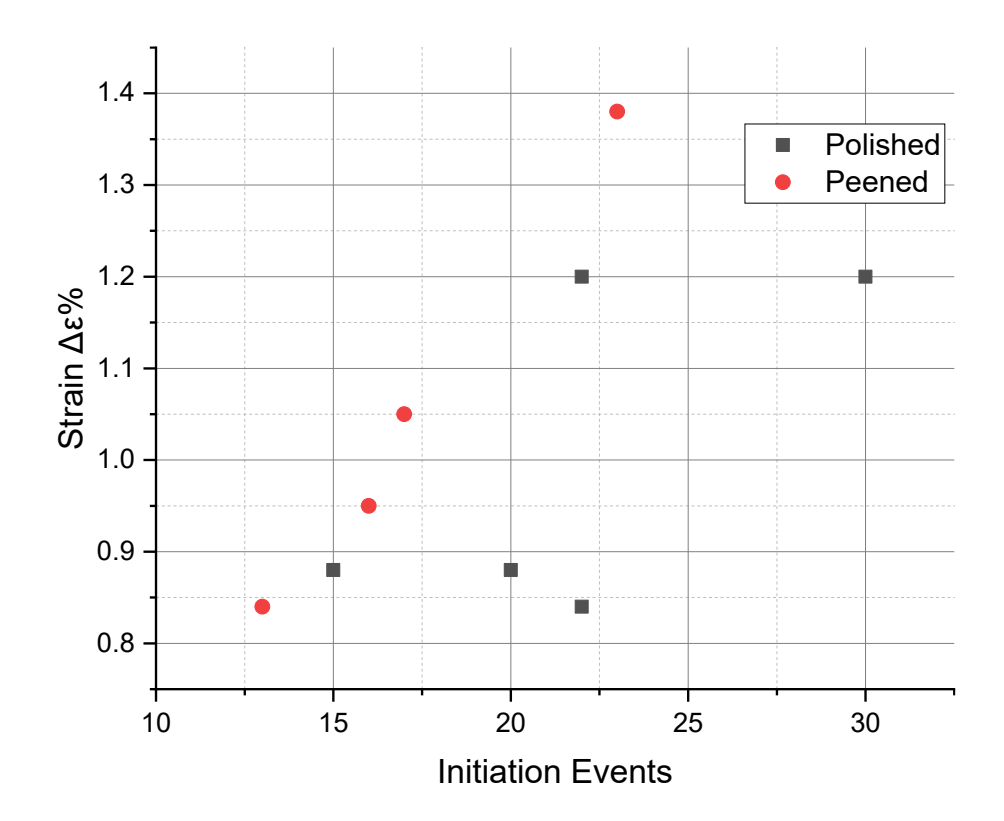


Figure 5-18 number of crack initiation events versus strain range applied to the U-notch for the peened and polished surface condition

# 5.3.6 Crack initiation and coalescence analysis in relation to strain range and shot peening

The initiation and coalescence behaviour of polished samples at different strain ranges was compared, Figure 5-19 and Figure 5-20. At higher strain ranges the initiation of cracks halted sooner when approaching end of fatigue life when compared to lower strain ranges. Also, lower strain ranges in polished samples presented with a higher number of coalescences at the end of fatigue life. In peened samples, Figure 5-21, the

initiation events mostly occur in very early stages of fatigue life, most were identified as pre-existing defects and cracks caused by the peening process, with few initiation events occurring at end of lifetime.

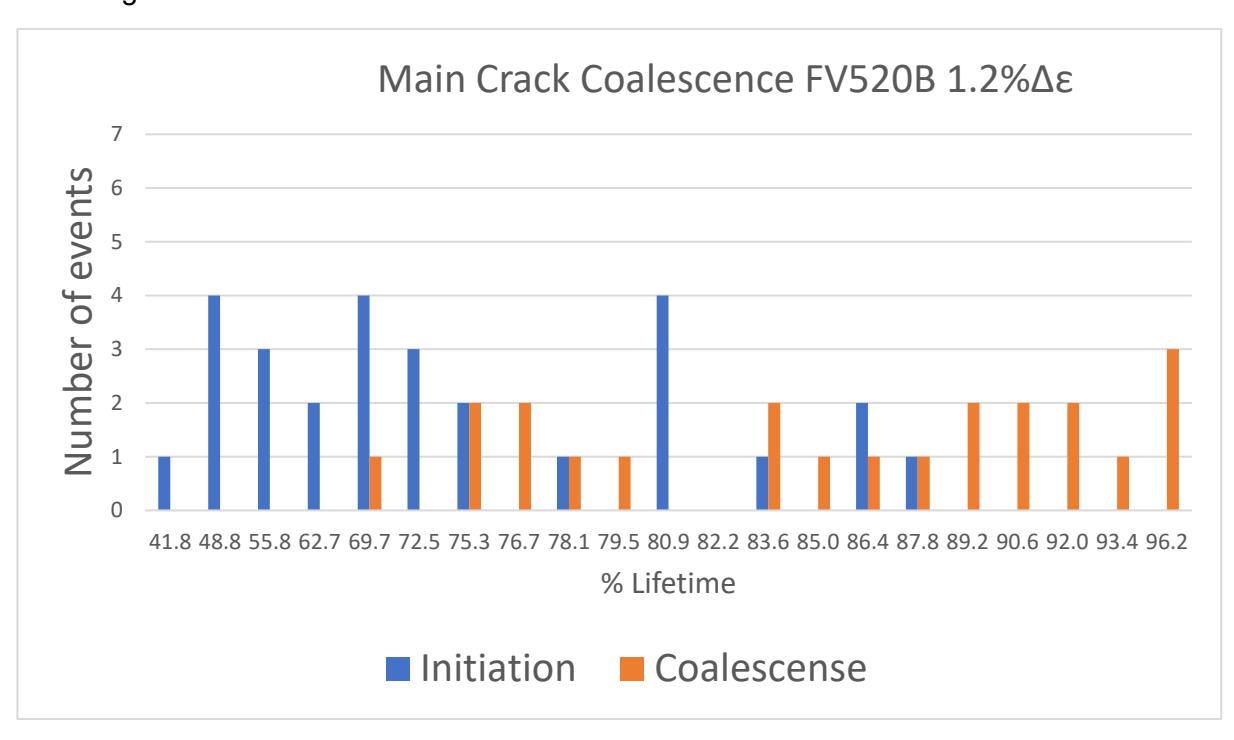


Figure 5-19 Short fatigue crack initiation and coalescence events of FV520B polished U-notched samples at a strain range of  $1.2\%\Delta\varepsilon$  where it was observed at the end of lifetime an increase of coalescence events and no initiations in the end 10% of lifetime.

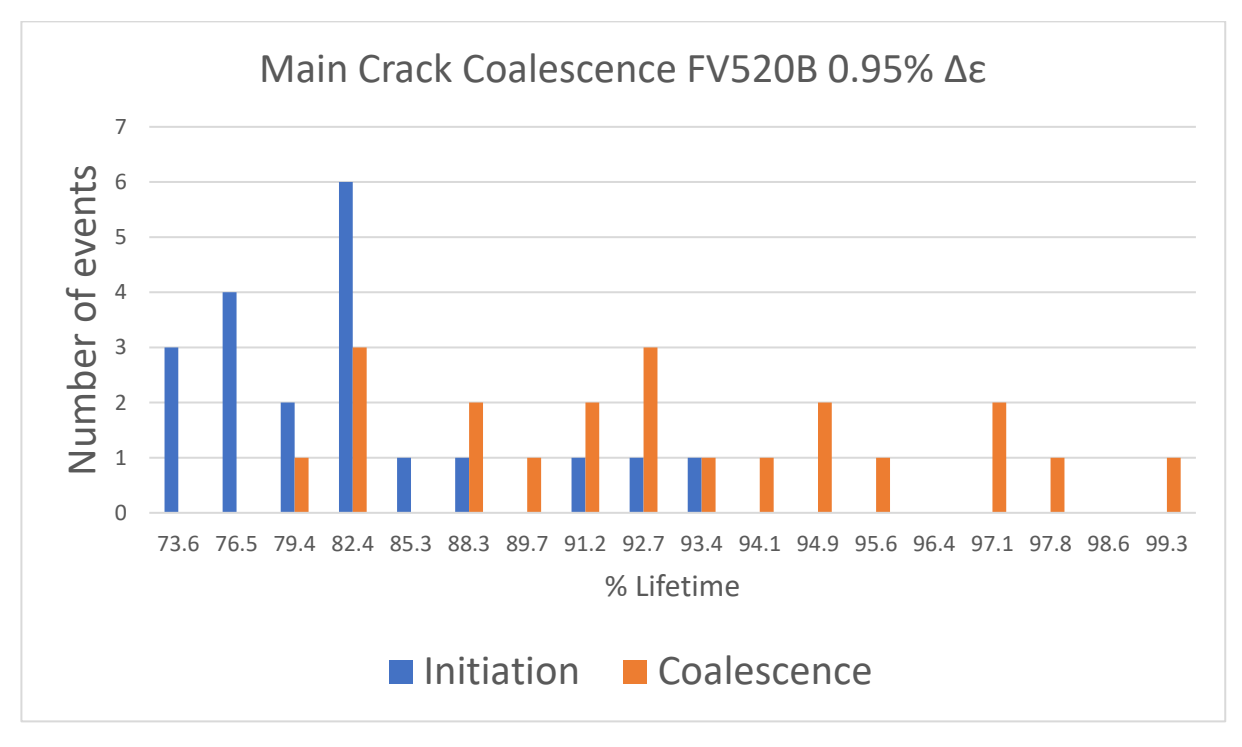


Figure 5-20 Short fatigue crack initiation and coalescence events of FV520B polished U-notched samples at a strain range of  $0.95\%\Delta\epsilon$  where it was observed a minor presence of initiations at the end stages of lifetime and lower number of coalescence events as opposed to higher strain range tests.

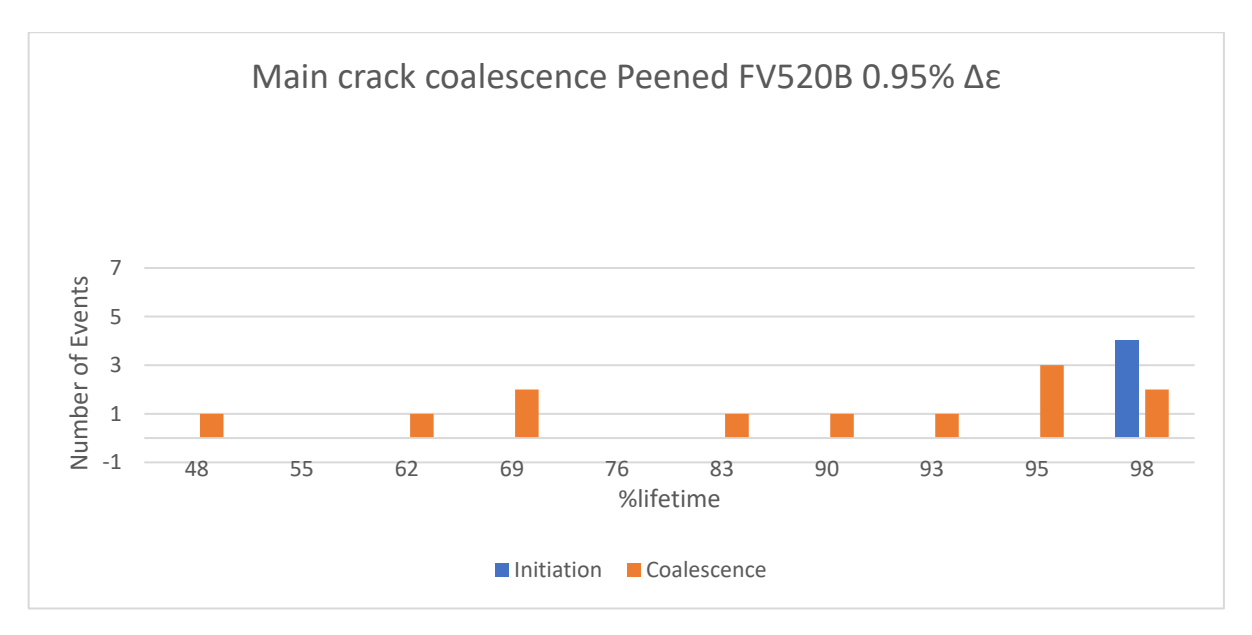


Figure 5-21 Short fatigue crack initiation and coalescence events of FV520B peened U-notched samples at a strain range of  $0.95\%\Delta\epsilon$  where it was observed a minimal number of main crack contributor crack initiation for the majority of the lifetime except for in the last 5%.

# 5.3.7 Crack aspect ratio

The peening process and the resultant sub-surface residual compressive stresses were deduced to retard crack growth into the depth when considered in terms of evolving crack aspect ratio as a function of crack growth. Crack aspect ratio grew consistently more shallowly into the depth as the crack grew in the peened samples compared to polished samples (which also showed more scatter in crack aspect ratio). The process of heat tinting and breaking open partially fatigued samples was used to measure crack depth vs surface length. The resultant graph in Figure 5-22 which represents the halflength of surface cracks c plotted against the ratio of half-length vs depth a/c suggests that as cracks grow longer in peened surfaces, they become more shallow. This can be due to either growth into an increasingly compressive residual stress field and/or, the greater number of initiation sites in peened samples, which as they coalesce will produce a shallower overall crack when compared to individual cracks in polished samples. When calculating the average between of the two sets of data we find the polished case to have an average a/c = 0.88 while peened samples have an a/c = 0.72. Further data points would increase confidence in the results, but due to limited time and sample availability no further datapoints were collected.

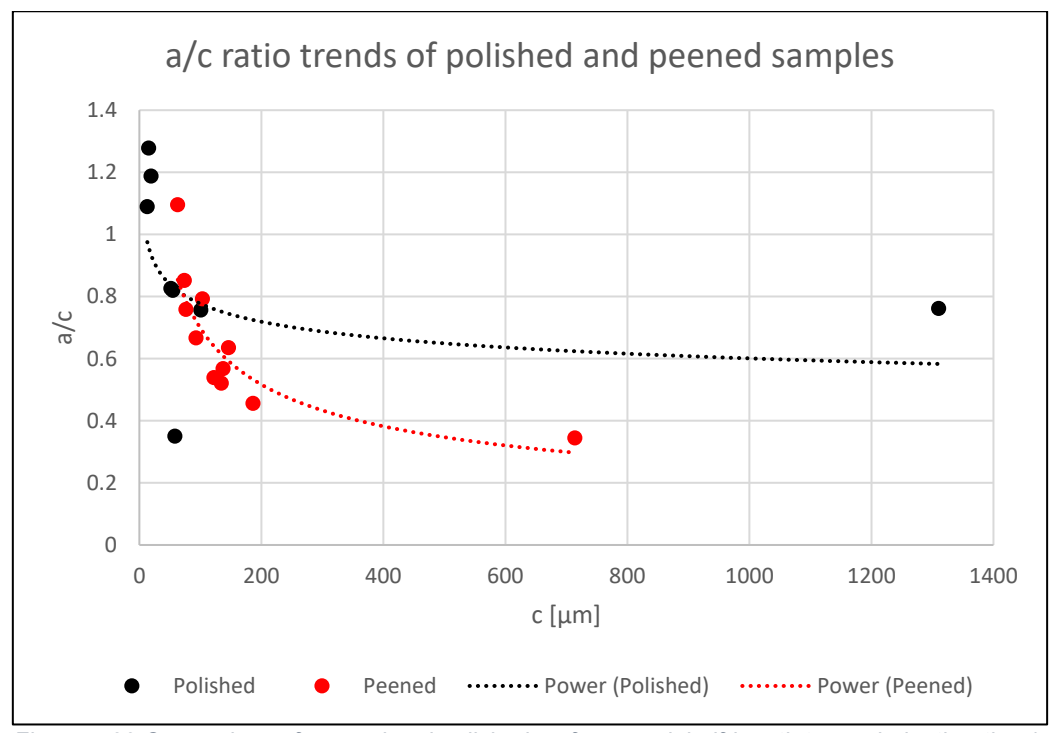


Figure 5-22 Comparison of peened and polished surface crack half-length to crack depth ratio a/c vs surface half length c. The crack depth was measured by using the semi-ellipse fit method. The resultant trend shows how cracks in peened samples are shallower for increasing surface crack length.

## 5.3.8 Crack growth behaviour

The crack growth rates of polished and peened U-notched samples were determined and compared. The ΔK calculations can be found in Appendix C. Polished samples were tested at two different strain ranges, from Figure 5-23 we observe how the crack growth rates (when compared on a ΔK basis) for the two strain ranges did not show significant differences. The peened sample crack growth rates, in Figure 5-24, compared to the polished sample results, show a reduced crack growth rate at both low and high  $\Delta K$ . The lower crack growth rates are linked to mean stress effects as the residual compressive stresses are expected to retard crack growth. We then compared long crack testing crack growth rates to the short crack growth rates, as observed in Figure 5-25, which was found to be comparable to the average of the polished sample results. Peened crack growth behaviour was observed to fall under the average crack growth rate when compared to long crack behaviour, Figure 5-26, with crack growth rates in the peened samples becoming comparable to that of long crack tests at higher ΔK levels. The alignment of crack growth rates between long and short crack tests at higher ΔK might be explained due to the cracks surpassing the residual compressive stress layer and growing similarly to a coalesced through thickness crack.

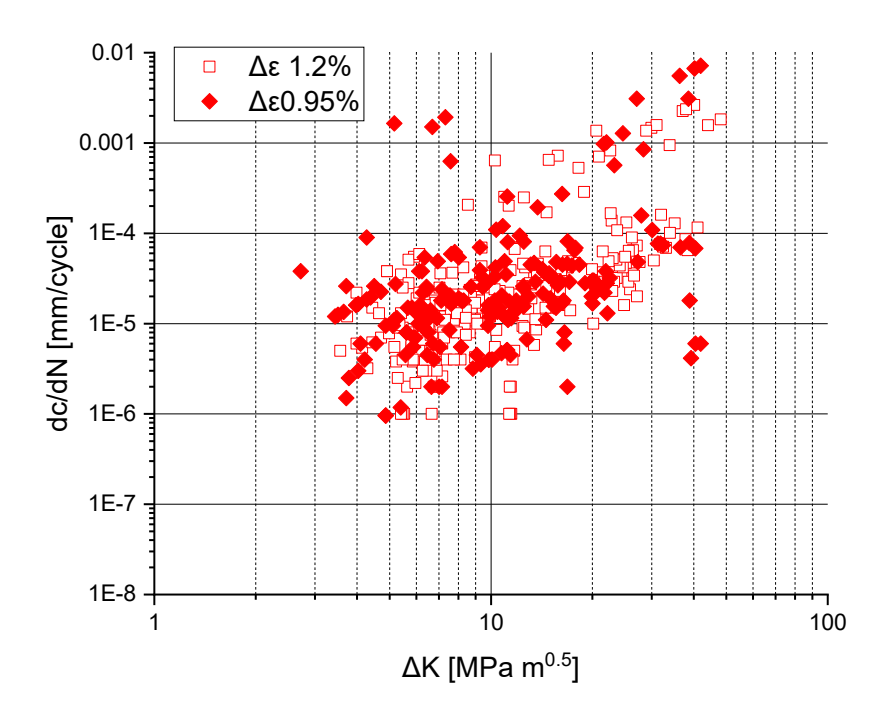


Figure 5-23 FV520B crack growth rate vs  $\Delta K$  of u-notched polished samples tested at two different strain ranges. The crack growth behaviour was observed to be consistent for the given surface condition regardless of strain range.

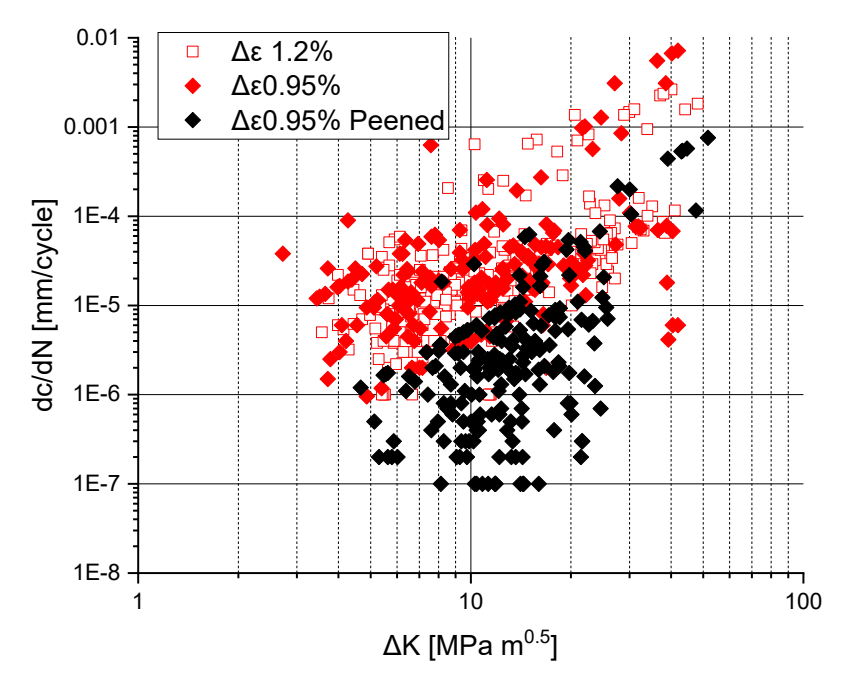


Figure 5-24 FV520B crack growth rate vs  $\Delta K$  of u-notched polished and peened samples tested at two different strain ranges. The crack growth behaviour was observed to have a lower growth rate in the peened condition for the same strain range, the lower growth rate was linked to residual stresses in the peened samples.

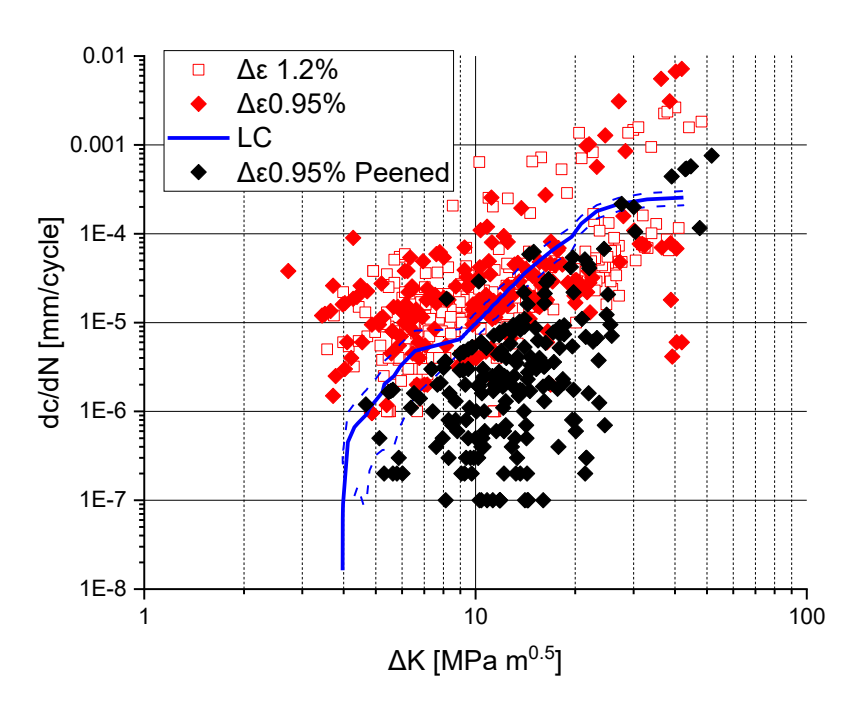


Figure 5-25 FV520B crack growth rate vs  $\Delta K$  of u-notched polished and peened samples tested at two different strain ranges compared to long crack testing of FV520B at constant load. The crack growth behaviour of long crack tests was observed to be consistent with short crack growth rate behaviour in the polished case. The Shot peened condition was observed to have an overall lower growth rate compared to long crack results.

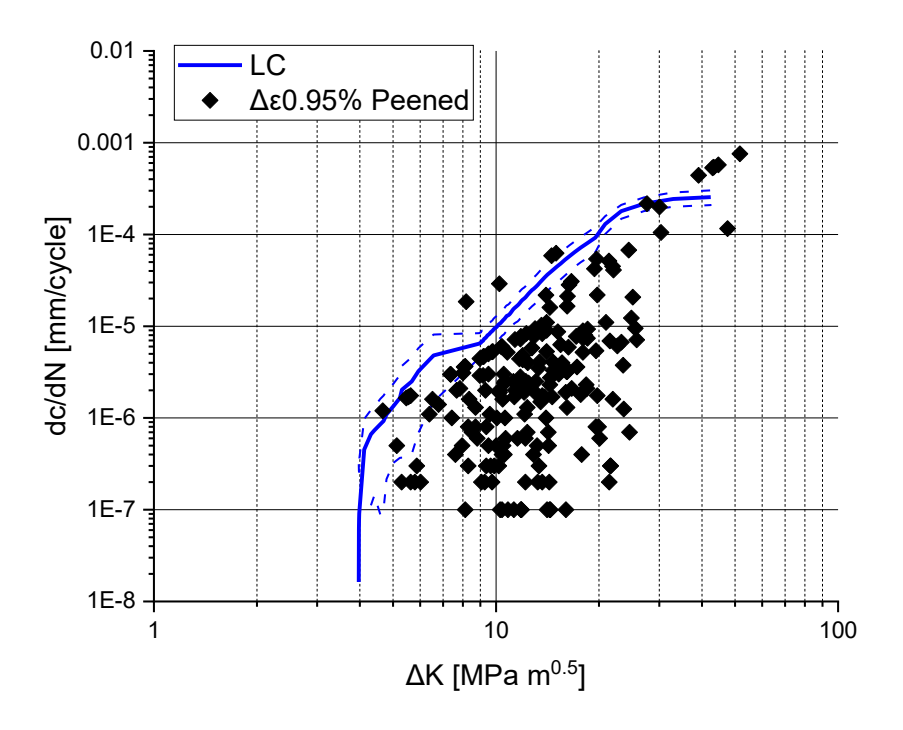


Figure 5-26 Comparison between long crack test results and shot peened U-notched crack growth rates in FV520B. The crack growth rate of peened samples were found to be lower than long crack results.

#### 5.3.9 Lifetime predictions

Fatigue lifetime predictions were calculated using the methodology described in Cunningham (2021). The method involved a multi-phase estimation of the number of cycles in different phases of the typical fatigue lifetime in a short crack growth scenario. These phases included the initiation phase, which was determined experimentally and accounted for approximately 40% of the fatigue lifetime for a polished sample. The Initiation phase for peened samples was set to zero as cracks were detected from N=0. For a polished sample the short crack growth phase was determined as starting when a crack was detected to be at 20  $\mu$ m in length. The lifetime prediction of the short crack growth phase involved using a Paris law estimation to calculate the number of cycles to a final length using the workflow in Figure 5-27. The initial cracks were assumed to be equally spaced and assumed to grow homogeneously.

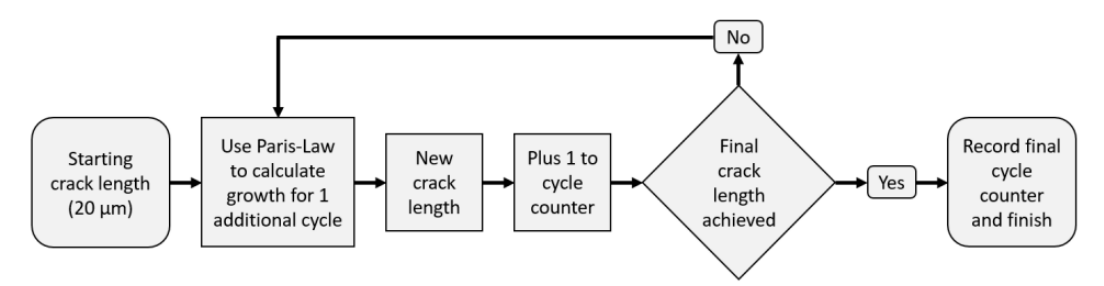


Figure 5-27 workflow to calculate the number of cycles for a short crack to reach a critical length in the multiphase predictive model[6].

The Paris law constants used for the crack growth rate can be seen in Table 5-3. For both the peened and polished crack growth behaviour the Paris law constants were determined by fitting a curve through the whole dataset assuming a homogeneous crack growth behaviour through the lifetime. For the purposes of verifying the method the assumed load P to calculate  $\Delta K$  was set as the same utilised in the test performed to measure the crack growth behaviour. The final crack length was determined by equation (1) where the width of the sample was divided by the number of crack initiations observed in the fracture surface of the sample, to estimate the point at which coalescence to a through thickness crack would occur.

Table 5-3 Paris law constants extrapolated from short crack growth behaviour and the number of crack initiation sites for each sample in the peened and polished surface conditions.

Sample	С	m	Crack initiations
Peened			
BW71	4.00E-09	2.45	13
Polished			
BY1	3.00E-07	1.72	15
BX71	1.00E-06	1.24	22

$$Final\ crack\ length = \frac{sample\ width}{number\ of\ crack\ initiations}\ \ (1)$$

The number of crack initiations used to calculate the final crack length was taken from the fracture surface specific to the sample from which the Paris law constants was

extracted. The overall trend of crack initiations for a given strain range applied at the root of the notch was determined via fracture surface observations. The trend, observed in Figure 5-28, shows an steady increase of number of initiations when strain range increases, the correlation was observed to be stronger in peened samples compared to polished samples although an overall increase was also observed for polished samples.

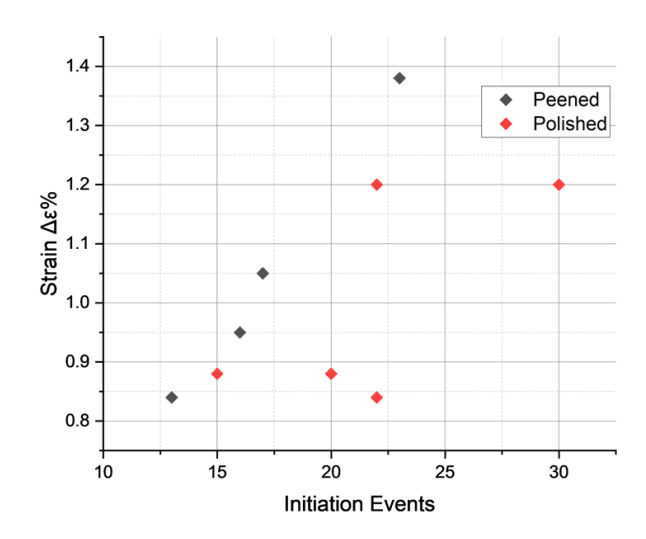


Figure 5-28 Crack initiation sites versus strain range comparison for FV520B U-notched samples in polished and peened conditions determined via fracture surface observations.

Once the final crack length for short crack growth was reached the final number of cycles was recorded and added to the number of cycles to initiation. The following phase, coalescence phase, is was omitted in the final lifetime prediction (assumed to be instantaneous,  $N_{\text{coalescence}} = 0$ ). Finally, the long crack phase was calculated using the Paris law equation and the respective Paris law constants determined from long crack testing. The total number of cycles to failure can be represented in equation (2).

$$N_{f \ predicted} = N_{inititation} + N_{Short \ crack} + N_{Coalescence} + N_{Long \ crack}$$
 (2)

The Resultant lifetime predictions are summarised in Figure 5-29 comparing estimated and experimentally determined (real) lifetimes for the peened and polished surface conditions. The number of cycles to failure for the peened sample were significantly over estimated, by a factor of 3, while for the polished samples the lifetime was suitably conservative and underestimated by 14-25%.

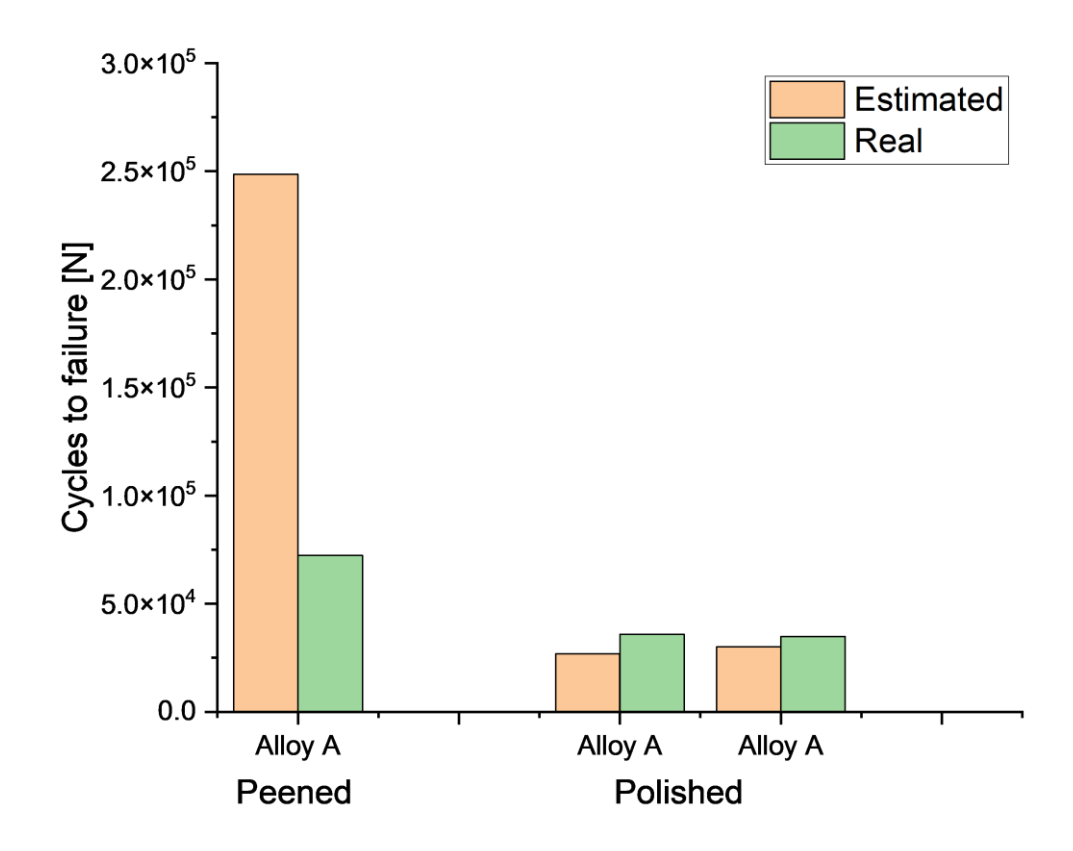


Figure 5-29 Comparison of predicted and real fatigue lifetimes of FV520B (Alloy A). Predicted lifetime for peened samples showed an overestimation of the lifetime by 3 times. Polished surface condition lifetime predictions underestimated the lifetime.

#### 5.4 Discussion

# 5.4.1 Fatigue lifetimes

Fatigue lifetimes of three martensitic stainless steel blade alloys were compared with different surface conditions in the form of  $\varepsilon$ -N curves. The use of  $\varepsilon$ -N curves as opposed to S-N curves was to normalise the fatigue lifetime by allowing for the variations in elastio-plastic material properties between the three materials, and also blade-to-blade variations in elastolastic material properties between blades of FV520B. All three alloys were tested in bend with a U-notched bend bar sample to reproduce a representative strain field of in-service turbine blades. As expected from the literature the surface conditions had an effect on the fatigue lifetime, with the as-received surface condition in FV448 and FV566 generally having a lower fatigue lifetime compared to a smoother polished sample[84], [127]. The higher surface roughness of as-received samples increases the number of surface defects which favour crack initiation as opposed to polished conditions where microstructural features predominantly initiate cracks. Additionally, FV520B was observed to have generally higher fatigue lifetimes at higher strain ranges than the other alloys. The possible scatter in FV520B performance might be explained by the differences in microstructural features between samples of different blades even when normalising for slight yield strength differences [128], [129].

# 5.4.2 Peening effects in residual compressive stresses and surface roughness

The residual compressive stresses in FV566 and FV520B were measured in the U-notch and the flat top surface of the samples in the transversal and longitudinal direction via XRD. The resultant residual stress profiles show consistent magnitude and depth profile between the U-notch and the flat top surface region, this indicates a consistent effectiveness of the procedure even in non-homogeneous geometries[7], [8], [130]. The two alloys compared also show consistency in the depth profile which peaks at 150µm for a compressive stress of 750-800MPa. The differences in material properties in this case showed little effect on the resultant compressive stress profile after shot peening.

From literature on similar alloys and test geometries we found the compressive stresses were expected to be retained after cyclic loading, this effect was observed in FV448 a martensitic stainless steel[108]. The residual compressive stress retention in a constrained notch geometry under bend was also observed in literature and was found to be dependent in part on the intensity of the peening process, the bending loading conditions and the fatigue loading regime[16], [86], [131]. The residual stresses were found to be comparable to the as peened conditions at 50% of estimated fatigue lifetime for FV448, this highlighted how the selected process had the potential to be effective in the turbine blade case study.

The surface roughness measured after the peening process of FV520B was compared to FV448 from literature. The roughness for a variety of FV520B samples was found to be overall lower than in FV448 both for Ra and Rz. The lower roughness levels in FV520B were attributed to the higher yield strength and hardness of the alloy compared to FV448 explaining the reduced roughness compared to the same intensity of shot peening [82].

#### 5.4.3 Peening effects on fatigue lifetimes

The fatigue lifetime of FV520B in the polished and peened surface conditions was compared to the performance of FV566 for the same surface conditions. The effects of peening were observed to generally have a beneficial effect on the lifetime of both alloys. The effects of peening when testing at relatively high strain ranges was observed to have almost no effect on FV566, showing little improvement in the fatigue lifetime[51]. The beneficial compressive stresses were likely to be relaxed at higher applied strain ranges, in agreement with literature[132]. Comparatively, FV520B has a longer fatigue life at higher strain ranges than FV566, although similar lifetimes were seen at lower strain ranges. In FV520B the compressive stresses were possibly retained at higher strain ranges as indicated by slightly greater lifetime after peening compared to FV566 at similar high strain ranges. The retention of residual compressive stress after cyclic loading, which was discussed in chapter 5.4.2, may be dependent on the material properties of the alloy. Typically a higher strength alloy benefits more from the peening process, but harder materials are harder to peen, the higher strength relative to FV566 would explain the enhanced fatigue resistance at higher strain ranges. This suggests that beyond the lack of differences in the depth and magnitude of the residual compressive stress the retention of the stresses was a more significant difference.

# 5.4.4 Fracture surface, crack initiation and coalescence behaviour of peened and polished steels

The use of silicone replica records and fracture surface microscopy allowed the differences between crack initiation and coalescence to be compared between polished and peened fatigue samples. From replica records of polished samples, the crack initiation events were noted to reduce towards the end of fatigue life although the total number of cracks were higher for higher strain ranges. At lower strain ranges the

initiation of cracks occurred even at later fatigue life stages compared to high strain levels. Coalescence in polished samples was dominant in lower strain ranges more prevalently at end of fatigue life. Generally, strain range has little effect on crack growth rate when normalised for  $\Delta K$ , as is seen in chapter 5.3.8, but it was observed to affect the number of crack initiations, with higher strain ranges causing more cracks through the fatique lifetime. Peened sample initiation and coalescence behaviour through the fatigue lifetime shows a coalescent dominant behaviour. The peened surface presents with numerous pre-existing cracks and other crack inducing defects. Pre-existing cracks were observed on the surface prior to fatiguing and were observed in fracture surface analysis both in failed samples and heat tinted samples used for a/c ratio measurements. Also, features resembling folds were observed on fracture surfaces of peened samples, which acted as crack concentration points quasi-subsurface, which initiated cracks. The fold-like features rendered, in some cases, the tracing of early crack initiations difficult. due to the crack-like appearance on silicone replicas. The cracks originating from the folds were able to be tracked once they reached a length larger than the defect hence growing sufficiently to be observed. The fold features were observed in literature where the peening process used in this study was applied to similar steel alloys[9], [35]. Cracks in polished samples were not found to have initiated by surface defects or inclusions, this suggests a microstructural dependent crack initiation process. Persistent slip bands likely formed on the surface which then acted as initiation sites, we hypothesise that reverted austenite packs were the preferential origin sites, but this has not been conclusively proven. The microstructural dependent initiation process for polished samples would explain the higher number of initiations found as a higher strain range would increase the likelihood and number of persistent slip band formations on the surface. On the other hand, due to the non-microstructural dependency of crack initiation in peened samples, the increased number of initiation sites observed can be attributed to an increase in number of relatively small surface defects surpassing fatigue threshold levels and initiating as cracks.

#### 5.4.5 Crack aspect ratio comparison between peened and polished steels

The effectiveness of shot peening in slowing crack growth in FV520B was further investigated by comparing the crack aspect ratio between cracks in polished and peened samples as a function of crack length. The observations were carried out from two samples of each surface condition, the crack lengths observed were between 26-2600 µm in length at the surface. In both polished and peened samples cracks were observed that were either single cracks or coalesced. The resultant curves suggest peened samples resulted in shallower cracks as the surface length increased while in polished samples the cracks were relatively deeper, which was found to be consistent with findings in literature[133]. It should be noted that no cracks of half-length c between 200-600 µm were recorded, but longer cracks indicate consistency with the observed trend. It should be noted how relatively small cracks, in both polished and peened samples, had a a/c ratio close to 1, hence being close to semicircular and only as the cracks grew, they presented as more shallow. Residual compressive stresses may induce crack closure which would explain the shallower growth of cracks into the depth in peened samples, as a crack grew into the depth it would experience residual compressive stresses down to a depth of ~ 300mm. This was also observed in literature on crack growth in peened steels and other materials[87], [89], [134]. The a/c ratio measurements at various depths were used to calculate the stress intensity factor ΔK at the crack tip. The measured a/c ratio, due to relatively low amount of data collected was compared to that found in the literature for similar materials, for example FV566, and was found to be consistent with previous research[90], [115], [135]. The lower average peened a/c ratio was also supported by previous research. These ratio datasets have been utilised in the literature to calculate ΔK progressively as the a/c changes with changing crack length. In our case

an a/c ratio of 0.8 was maintained for both cases, as it allowed easier comparison with prior research on legacy steel turbine materials.

Further observation of the peened fracture surfaces during crack depth measurements confirmed that the initiation sites, as described above in section 5.4.4, were prevalently induced by surface defects such as pre-existing cracks or the above mentioned "folds". These observations were again consistent with prior literature on short crack fatigue initiation in similar materials following the peening process applied in this work[102].

#### 5.4.6 Crack growth rate comparison of peened and polished steels

Crack growth rate vs  $\Delta K$  of short fatigue cracks was measured using surface replication methods on polished and peened samples. Polished samples were tested at two different strain ranges to analyse the effects of strain range on crack growth, the results suggest no effects from strain range. The lack of effect from strain range was expected as the stress intensity factor  $\Delta K$  normalised the variations between stress (and hence strain) ranges. Furthermore, the short crack growth behaviour was found to be consistent with the crack growth rate of FV520B measured using long crack testing, this was mostly observed at increasing  $\Delta K$  levels. Although short crack growth rate presents with a much larger scatter than long crack growth rate the trends were observed to be comparable. The scatter in short crack growth rates was due to complex crack interactions, crack shielding and crack initiation location variation, which was also observed in the literature and was found to be an expected phenomena of short cracks in steels[50], [51], [102], [108].

Short crack testing on shot peened samples for crack growth rate analysis was performed on only one sample at one strain range, which corresponded to the strain range of one of the polished samples. The crack growth rate of the peened sample was observed to be lower for a given  $\Delta K$  than that of polished samples. The reduced crack growth rate was attributed to the compressive residual stresses induced by shot peening slowing crack growth. As the  $\Delta K$  increased for the peened sample the crack growth rate was observed to eventually increase to levels similar to the long crack results. The change in crack growth behaviour is considered due to the crack depth exceeding the residual compressive stress layer induced by shot peening.

#### 5.4.7 Mechanistic based fatigue lifetime prediction model

A mechanistic based fatigue lifetime prediction model, originally developed by Cunningham for FV566, was also used on FV520B to verify the effectiveness of the model on other martensitic steels[6]. The method in Cunningham was not directly compared to the lifetimes obtained in testing FV520B as it was used to study the effects of overloads and other influencing factors on fatigue lifetimes[51]. The model used experimentally obtained fatigue behaviour information to generate a multi-phase model which includes initiation, short crack growth, coalescence and long crack phases. The initiation phase constitutes the lifetime of the sample before a small crack, of 20µm, was detected. This was valid for polished samples with no preexisting cracks or defects. The initiation phase for the peened case was assumed to be null, as the peened surface presented with cracks at or above 20µm. The first phase in Cunningham was averaged between a series of short crack tests conducted at different strain ranges. In the current study the model was applied and compared to the results of the short crack tests directly. The reason for direct comparison was to evaluate the conservatism of the model to empirical results. The model was modified in part, by excluding the coalescence phase,

which constitutes the smallest percentage of the fatigue lifetime. The short crack phase growth phase of the model used an iterative method where Paris law constants were used applied to the ΔK for a small crack until the crack reached a given length. The initial crack length of 20µm was used as it was determined cracks of 20µm or longer were past stage I of crack growth and transitioned to stage II. The final crack length was determined dividing the width of the sample by the number of crack initiation sites observed on the fracture surface of the comparative sample. The method used to determine the final crack length for short crack growth phase assumes that the initial cracks were equally spaced through the width and grew at the same rate with little influence from other surrounding cracks. The Paris law constants that were used to calculate the crack growth rate were extracted from the crack growth rate data by using a power fit that included the entire dataset, this assumes an averaging of the crack growth for a given  $\Delta K$ , this assumption was also made for the peened case crack growth rate. Also, in the peened crack growth behaviour we observed how the rate could have varied depending on the depth of the crack due to the variation of the residual compressive stresses through the thickness of the sample. Furthermore, the crack length to depth ratio through the short crack growth phase was assumed to be constant at 0.8. The last phase of the model assumes a fully coalesced crack grew at the rate corresponding to that measured using long crack testing until the final crack length measured from the fracture surface of the sample.

The fatigue lifetime predictions for polished and peened samples varied in outcome. A conservative underestimation of the fatigue lifetime was achieved in the polished cases but with a significant overestimation in the peened case. Calculated lifetimes for the polished case were found to underestimate by 14-25% the observed fatigue lifetime. For the polished case the most likely explanation for this is the model not accounting for arrested cracks, these halt their growth due to effects from nearby crack shielding but do also influence the growth rate of surrounding cracks but this is not captured in the Paris law constants used. Also, final crack length is an estimation with the assumption that all constituent cracks grow uniformly and equally spaced, this was found to not be the case from experimental observations, in fact cracks originate in unpredictable locations, grow non-homogeneously and were affected by crack coalescence. The Paris law constant fits are also not accounting for the observed scatter in the short crack growth data.

For the peened case the predicted lifetime was overestimated 3 fold, the crack growth for shot peened cases should account for crack growth in the residual compressive layer and at a different rate beyond the compressive residual stress layer before full coalescence. Hence a better model would account for 2 short crack growth phases with two different sets of Paris law constants and a long crack phase. Similarly to the polished case, similar additional assumptions were made for the peened case, such as even spacing of cracks and homogenous crack growth between them, not considering coalescence events due to clustering of initiation sites, nor the effect of arrested cracks and the effects of crack shielding and anti-shielding between cracks. This is likely to have been an even more significant issue in the peened case, which tended to have more crack initiations, so we expect coalescence and anti-shielding effects to be more significant.

The model was found to have promise in cases where no shot peening residual stresses affect crack growth and was able to be used, albeit yielding a conservative estimation, in its simplified form excluding the coalescence phase. When applied to the peened case, the simplifications and assumptions caused an overestimation of the lifetime, which was clearly not desirable. A modification of equation 2 was found to be necessary to reduce overestimation, hence a revisited equation 3 was generated. Where SC RCSL stands for Short crack in Residual Compressive Stress Layer. In equation 3 the short crack phase

was devised to be split in 2 parts, the first within the residual compressive stress layer and the second beyond the compressive stress layer. The constant a/c ratio assumption was required to change, requiring an adjusted method to include a/c variation. Further analysis and testing of samples will be needed to verify and refine the method to be applied to peened samples, and in particular to consider how to model the effect of multiple and irregularly spaced crack initiations on coalescence and anti-shielding of crack growth. Equation 3 was used by Cunningham for FV566 and cyclic loading with overloads, but further work will be necessary to further improve on the predictive model for a more general application for steel alloys with shot peened surfaces.

$$N_{f \ predicted} = N_{inititation} + (N_{SC \ RCSL} + N_{SC \ post \ RCSL}) + N_{Coalescence} + N_{Long \ crack}$$
 (3)

The literature on fatigue lifetime prediction of peened components supports the need for larger data sets as well as the difficulty in prediction by assuming an average crack growth rate, cycles to crack initiation and effects of geometry[13], [34], [136], [137], [138], [139].

### 5.5 Summary and conclusions

The work presented studied the effects of shot peening on martensitic stainless steel on fatigue life compared to a control polished surface and proposed a mechanistically based fatigue lifetime prediction method. The conclusions can be summarised as follows:

- Shot peening was found to have beneficial effects in lifetime extension on the analysed martensitic stainless steels observed in a constrained notch geometry tested under bend loading.
- Shot peening on FV520B generated a residual compressive stress profile with comparable compressive stress magnitude and depth to other similar turbine blade alloys.
- The lifetime extension benefits of peening on FV520B was found to be retained at higher strain ranges compared to FV566. Suggesting a better residual compressive stress retention.
- In peened samples the surface roughness appears to be the main fatigue crack initiator.
- Fracture surface observations found crack initiation to be defect dominated in peened samples and microstructurally dominated in polished samples.
- The crack aspect ratio evolution through the fatigue life showed the peening process induces shallower cracks compared to polished samples.
- Strain range was found to have little effect on crack growth rate.
- Crack growth rate was found to be generally lower in shot peened samples when compared to polished samples.
- Fatigue life appears heavily controlled by initiation events, short crack growth and coalescence events in LCF regime, and the relative balance between these contributions.
- The mechanistic based lifetime prediction model generates conservative lifetime estimation in polished samples.
- The model however overestimates the fatigue lifetime of peened samples due to simplifying assumptions related to crack initiation spacing, propagation and residual compressive stress effects.

110

A reformulated model equation was proposed which requires further verification to reduce overestimation of peened sample lifetimes.

# **Chapter 6 Summary and Conclusions**

### 6.1 Summary

The aim of this project was to look at potential effects of blade-to-blade variability on the fatigue behaviour of shot peened ex-service stainless steel blades and the impact of any variability on fatigue behaviour and associated lifetime predictions.

#### 6.2 Materials characterisation

Material characterisation of the provided ex-service blade material, FV520B, verified the alloy was consistent with the expected alloy characteristics. An especial focus was the need to assess the heat treatment condition of the material given the literature review highlighted the variability of mechanical properties based on any differences in the applied HT. The materials specification and heat treatment condition of such legacy turbine blade materials needed to be clarified by direct observation of a number of exservice blades to assess blade to blade and intra-blade variations.

Metallographic analysis was conducted using optical and scanning electron microscopy on polished and etched samples. The observed microstructure was found to be a typical martensitic microstructure, characterised by prior austenite grain boundaries and martensite lath packs. Reverted austenite packs were observed at the prior austenite grain boundaries and globular alumina inclusions were also observed. The most likely HT of FV520B for use in blade material was deduced to be peak hardened from available literature, hence investigation to verify the actual HT condition after many years of service (albeit at low service temperatures, ~250°C) was conducted. Hardness testing was performed on a range of samples from five different ex-service blades of FV520B, the resulting distribution of hardness was plotted and the scatter of hardness was assessed. It was observed that the average hardness between blades and within an individual blade did vary somewhat, overall the hardness of FV520B samples had a difference range of 80 HV approximately over the whole dataset. Furthermore, the measured hardness was lower than that expected in a peak hardened FV520B (420 HV). The ageing phase of the applied heat treatment was found (from literature) to be the likeliest potential source of hardness variation. The temperature and hold time of the precipitation hardening phase of the HT is expected to greatly affect the hardness, the expected ageing temperature (450°C) and hold time (4 hours) may have varied somewhat from blade to blade and this may have caused a decrease in the hardness of the material due to overageing. The hardness of FV520B was also compared to that of similar tempered martensitic stainless steel alloys (FV566 and FV448) and was found to be intermediate to the other alloys, with FV566 being the hardest on average.

EBSD and XRD scans were conducted on samples from 4 different blades to measure the lath size, prior austenite grain size and to determine/quantify the phases (reverted austenite) in FV520B. The average lath size of each blade was measured using a line intercept method on representative EBSD maps. The measurements showed a range of lath sizes between 4-14 µm, this is larger than the expected average lath thickness of 1 µm, this may reflect other variations in the HT (for example cooling rate differences in the blade cross-section and between blades) but this cannot be further investigated. The purpose of this investigaton was to quantify microstructural features and assess the effects on subsequent performance and fatigue response. The lath size of the blades was plotted against the average hardness and showed a direct correlation between a small lath size and increased hardness, this is in line with the expected Hall-Petch relationship, where finer laths and more lath boundaries are expected to resist dislocation movement more, leading to higher strengths (and hardnesses). The prior austenite grain boundary sizes were not fully quantified, but qualitatively showed a similar trend to lath size and hardness relationship, with a finer apparent prior austenite

grain size also leading to higher hardness/strength. XRD scans to compare the resultant microstructure with results from the literature indicated similar peaks to that of a peak hardened FV520B from literature, but the magnitude of the peaks was different. Further investigation of the XRD results, combined with higher resolution characterisation (e.g. TEM analysis) is necessary to understand the discrepancy in detail, but it may indicate differing proportions of minor phases (which may also affect strengthening). This was beyond the scope of the current PhD work.

Monotonic tensile testing was performed on four blades, the results showed some scatter in the results but an overall consistent yield strength which was similar to what a peak hardened condition would exhibit. However the UTS values obtained showed increased scatter and were lower than would be expected from literature. The UTS was found to correlate well with 3 times the measured hardness of the blade material, this relation can be used to estimate the mechanical properties via hardness NDT on a blade in service. The results from FV520B were compared to FV566 and FV448 and it was found that FV520B, although being of intermediate hardness, was the alloy with the highest overall yield strength. This indicated FV520B had a somewhat different work hardening response when compared to the other two alloys.

### 6.3 Baseline fatigue properties

The baseline da/dN versus ΔK fatigue response of FV520B samples from different blades were assessed and compared to FV566 via long crack testing (SENB samples with a through-thickness crack). The ΔCTOD of FV520B was calculated to observe material property effects (particularly variation in yield strength) on crack tip opening, to see if this would explain any scatter seen in long crack growth curves. Fractography of the long crack tests performed on FV520B was done to observe if any changes in crack growth behaviour were due to microstructural features affecting the micromechanical response. The long crack testing performed consisted in applying a load shedding process to find  $\Delta K_{threshold}$  and a grow out (under constant load range and increasing  $\Delta K$ ) phase to measure Stage II crack growth. The resultant da/dN vs ΔK trends showed consistency in stage II crack growth rate in all tested samples of FV520B and a similar growth rate with FV566. In the near threshold regime the 4 samples exhibited different threshold  $\Delta K$ -values, at low or near threshold stress intensity factors the crack growth is heavily dependent on the microstructure. The different lath sizes in different blades seemed to affect the threshold region crack growth rate, the fracture surface observations confirmed a more tortuous crack path in near threshold regions, linked to the propagation between laths. Crack tip opening displacement calculations revealed a slightly increased scatter in da/dN versus  $\Delta$ CTOD in stage II crack growth and hence showed some differences in crack opening displacement between blades, linked to variations in yield strength, this might have affected crack closure effects and indicates factors contributing to differences in  $\Delta K_{threshold}$  linked to varying crack path tortuosity with varying lath size. When plotting ΔK<sub>threshold</sub> with hardness only a weak correlation was observed, hence hardness may not be a reliable indicator of  $\Delta K_{threshold}$ .

A simple estimation of lifetimes was calculated by integration of the Paris-law relationship based solely on the variation in Paris-law constants derived by the long crack testing. The lifetimes for a given stress range were found to be relatively consistent for all FV520B blades and with FV566.

Fractography of long crack testing of the four blades revealed a very consistent crack growth behaviour in all of the samples at varying  $\Delta K$ . At  $\Delta K_{threshold}$  the crack was very tortuous and microstructurally dependent (linked to lath size), at increasing  $\Delta K$  the crack transitioned to smoother transgranular growth, with Stage II growth at high  $\Delta K$ . Some evidence of secondary cracking was observed at very high  $\Delta K$ , for one blade secondary

cracking was observed to be arrested by globular alumina inclusions. The inclusions were not observed to have a significant effect in any other observations. Overall, the baseline fatigue behaviour was found to vary very little between blades in long crack stage II growth.

# 6.4 Short crack fatigue behaviour in U-notches with residual compressive stresses

Short crack testing under constant load range testing on U-notched bend bar samples was used in testing as a representation of crack initiation and growth in a fir tree root notch geometry stress field. Shot peening was applied to the U-notched samples and its effect on the residual stress field, fatigue lifetime and short fatigue crack growth was evaluated.

The effects of shot peening on residual compressive stresses was assessed via XRD and the measurements were taken both in the notch root and flat part of the bend bars. The analysis was performed both on FV520B and FV566, the resultant residual stress depth profiles and magnitudes for the two alloys in the notch and flat regions were consistent. The effects of residual compressive stresses on the lifetime of FV520B was assessed via lifetime testing and compared to results obtained by previous researchers in FV566. Samples with peened surfaces were compared to polished samples and lifetime compared at a variety of calculated notch root strain ranges.  $\Delta \epsilon$ -N curves were considered to allow for the effect of varying yield strength between blades. It was found that peening generally increased lifetimes in both FV520B and FV566, with FV520B exhibiting lifetime extensions at higher strain ranges when compared to FV566 where the effects dissipated.

Short crack growth behaviour was observed via surface replication methods to determine dc/dN vs ΔK growth rates in polished and peened FV520B samples. The resulting crack growth behaviour of polished FV520B was found to be in line with results from long crack testing, except at lower  $\Delta K$ , which was found in agreement with the literature to be an effect of LEFM assumptions, where higher da/dN is typically seen in the short crack case. The crack growth data also showed a lot more scatter (again as expected in the short crack case). Two different strain ranges were considered in the baseline polished sample testing but when short crack growth data was compared in da/dN versus ΔK terms this had little effect on growth rate. In shot peened samples, the crack growth rate was significantly lower than the unpeened short crack and the long crack growth data at low  $\Delta K$  (shorter crack lengths), while at high  $\Delta K$  (as the cracks grew beyond the short peen affected zone) the rate merged more with long crack tests and short crack polished results. The change in rate is explained by the varying residual compressive stress field as the crack grows deeper beyond the shot peen induced compressive stress field. Fracture surface analysis revealed a microstructurally dominant initiation (deduced to be from RA packets) in polished sample while a surface and sub-surface dominant initiation was seen in peened samples, linked to surface roughness and surface folding from the shot peening process). Surface crack length to depth ratio was measured in peened and polished samples. As expected, due to the residual compressive stress field, peened samples generally presented shallower cracks compared to polished samples, this was especially true as the crack grows longer on the surface (which is also linked to the greater likelihood of crack coalescence occurring).

### 6.5 Mechanistic based fatigue lifetime prediction model

A mechanistic based lifetime prediction approach for short crack growth in notches, developed by Cunningham, was applied in a simplified way to FV520B. The prediction model was based on the calculation and summing of cycles in different phases of the short crack growth development. The phases include initiation, estimated experimentally,

short crack growth, calculated using Paris-law constants derived from short crack testing, a simplified coalescence criterion (based on observed numbers of initiation sites on the final fracture surface) and long crack growth (also estimated using the long crack Parislaw constants). The model makes assumptions in (i) estimating the short crack growth phase, (ii) the number of cracks are taken based on fracture surface observations and not total cracks in the notch, (iii) the cracks are assumed to nucleate in an evenly spaced way and grow laterally homogeneously (iv) the Paris-law constants for short crack growth in peened samples was taken assuming homogenous growth through the depth and thickness, while neglecting possible rate changes due to compressive stress distributions. In our case the coalescence phase cycles were ignored.

The predictive model was applied both to polished and peened samples, the resulting estimations for polished samples were conservative while the lifetime for the peened case was significantly overestimated. The differences between experimental and predicted lifetimes is likely to be mostly due to the assumptions on crack initiation and their homogeneous spacing through the width of the sample. In addition, arrested cracks and complex crack behaviour and interaction in the short cracks was ignored in both polished and peened cases. For the peened case overestimation, the most likely explanation is the coalescence phase being predicted as occurring much later (due to the even spacing assumptions) and also the change in growth rate as the crack depth increases not being taken into account. Hence a reformulated equation was proposed for peened samples.

### 6.6 Conclusions

- The ex-service blade material was unambiguously identified as FV520B martensitic stainless steel, which presented with blade-to-blade (and some intra blade) variability in hardness, lath and prior austenite grain size and a link between larger lath size and lower strength was noted.
- Baseline long crack fatigue behaviour was found to be consistent between the blades in terms of stage II crack growth with some differences noted in the near threshold stress intensity factor value, linked to the greater tortuosity in crack paths near threshold, reflective of lath size differences.
- Fracture surface observations also indicate consistent growth behaviours at different ΔK levels for FV520B.
- Shot peening was observed to produce similar residual compressive stress fields
  distributions in terms of maximum depth and magnitude for similar alloys FV520B
  and FV566 (where testing was conducted by another researcher).
- Fatigue life in peened notched samples was found to increase compared to unpeened polished samples for a various notch root strain ranges. FV520B was observed to retain benefits from shot peening at higher strain ranges compared to FV566.
- Short crack fatigue growth rates versus ΔK levels in polished FV520B samples were unaffected by strain range and were found to be relatively consistent with long crack growth behaviour, in particular at higher ΔK.
- Shot peening greatly reduced crack growth rates of short cracks, the reduced rates are particularly evident at low ΔK but the rate increases to merge with long crack data as the crack grow into stage II growth regime and beyond the shot peen affected region.
- Crack surface length to depth ratio was lower in peened samples at increasing surface crack lengths when compared to polished samples due to residual compressive stresses hampering crack growth into the depth (and the increased initiation sites from the shot peening process also meant coalescence was more prevalent, leading to shallower coalesced cracks).

- The proposed mechanistic lifetime prediction model (Cunningham 2022) was found to underestimate lifetimes in polished notched samples but to significantly overestimate lifetimes for peened samples.
- The assumptions on crack initiation spacing (and hence coalescence), propagation and residual compressive stress effects on the crack growth rate variation were the likely cause of these discrepancies.

### **Chapter 7 Future work**

The literature review highlighted some areas of interest that were relevant to the current work and are worth exploring. The blade-to-blade variability and its effects on fatigue crack behavior and lifetime prediction were the main areas identified as requiring additional work. Furthermore, the work in the above chapters highlighted the need for additional experimental data to be collected as well as further analysis on collected data to be conducted. The increased availability of experimental data would aid in refining the lifetime prediction model proposed and reduce conservatism or overestimation of lifetimes.

Further investigation is needed on the blade-to-blade mechanical properties variations and relation to the microstructural features such as prior austenite grain boundaries and reverted austenite for a higher number of blades. The additional data would allow creation of a database to predict the mechanical properties and some fatigue properties, such as  $\Delta K$  threshold of the blade. This would require further detailed EBSD data analysis, partially to properly quantify prior austenite grain size and further investigate lath size distribution and the correlation with hardness for FV520B and other alloys such as FV566.

Further analysis on residual compressive stresses for blade materials at the blade-to-blade extreme ranges to evaluate possible variations in the compressive residual stress field should be conducted. The findings on the study suggest that for a given alloy and shot peening process, the variations of residual compressive stresses should be minimal, but experimental data to back the hypothesis is required. The retention of residual compressive stresses is dependent on yield strength and loading conditions, hence the effects on a wider range of blades is recommended. XRD for residual stress analysis for different yield strength blades at different stages of fatigue life in FV520B should be carried out to further establish a comprehensive database.

The above should be matched with further short crack fatigue testing which could be used to create a correlation database to suggest Stage II Paris law constants for an array of shot peened FV520B samples depending on mechanical properties estimated by NDT.

The complex nature of short fatigue crack growth rate and its influencing factors, such as crack shielding, crack coalescence and defect induced crack initiation require further investigation. The data collection process for short crack growth behavior is a long and tedious process both from an experimental and data analysis prospective. Nonetheless, an increased data set on the fatigue life phases such as the initiation phase, which was determined experimentally, would allow to better establish the likely lifetime percentage to initiation for peened sample, rather than the current model assuming cracks being initiated from N = 0 due to large pre-existing defects. Additionally, the effects of strain range on number of crack initiations and the influence on the crack growth behaviour need to be further studied to establish potential corrective factors in the predictive model. The effects of strain range on residual compressive stress relaxation and related effects on fatigue crack growth also need further investigation. The stochastic nature of initiation site number and distribution and how this affects coalescence behaviour could be simulated to assess how much this affects lifetime scatter at the notch root strain ranges and likely lifetime investigated.

Furthermore, short fatigue crack growth rates through the residual compressive layer and changes in growth rate post residual compressive stress layer via comprehensive crack aspect ratio studies is necessary for FV520B. This would allow to improve on the iterative fatigue crack growth prediction model proposed by Cunningham and its application to FV520B.

The lifetime prediction model was applied to a limited number of test samples in the current work. Additional applications of the model to the tested samples directly to establish the effectiveness of the model is required. Also, Cunningham explored the effects of overloads on FV566 and the effects on lifetime prediction, these results should also be validated for FV520B.

The reliability of the presented model should be evaluated for reliability when applied to more complex geometries used in service. Fir tree root geometries involve notch geometry variations and loading variations at different locations in the blade root. Large scale testing of a turbine blade for fatigue life is not a viable option, hence further research on the effects of geometric variations in a single component and the potential effects on fatigue crack growth should be carried out.

# Chapter 8 Appendix A: Long crack testing procedure 8.1 Appendix A: SEN bend test setup

The following is based on Appendix A from Cunningham (2022)[6].

All long crack testing was carried out to British Standards *BS ISO 12108:2012*. The SENB3 (single edge notch 3-point bend) sample was placed in an INSTRON 8502 hydraulic cyclic test machine in 3-point bending test configuration with a top roller span of 40 mm. Conductive wires were spot welded onto the surfaces of the sample and connected to a DCM-2 DCPD (Direct Current Potential Difference) crack growth monitoring machine using the configuration shown in Figure 8-1. The surfaces of the sample were polished using progressively finer grinding and polishing stages to 1 µm suspension to increase the spot- welding contact strength. Ten Amps were applied through the sample. The time and the potential difference reading across the crack were recorded. The potential difference across a section of the sample with no crack was measured as a reference reading to account for variables such as temperature and humidity that may affect the baseline reading.

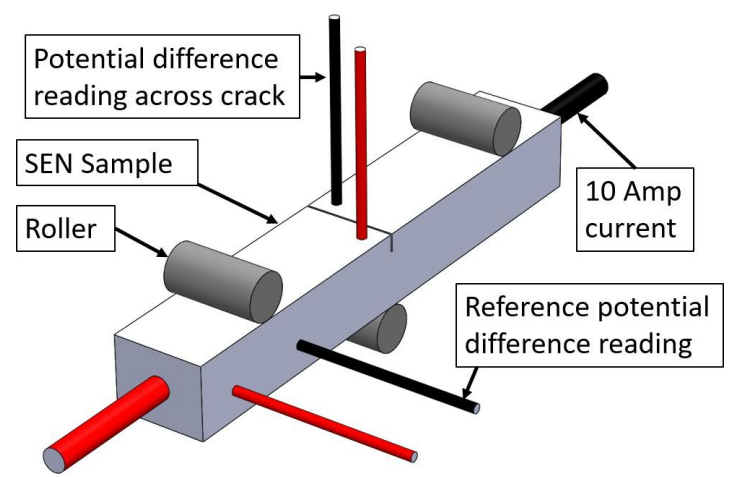


Figure 8-1 Schematic model of the SEN bend sample showing the configuration of the wires spot welded to the sample and the roller locations for 3-point bending.

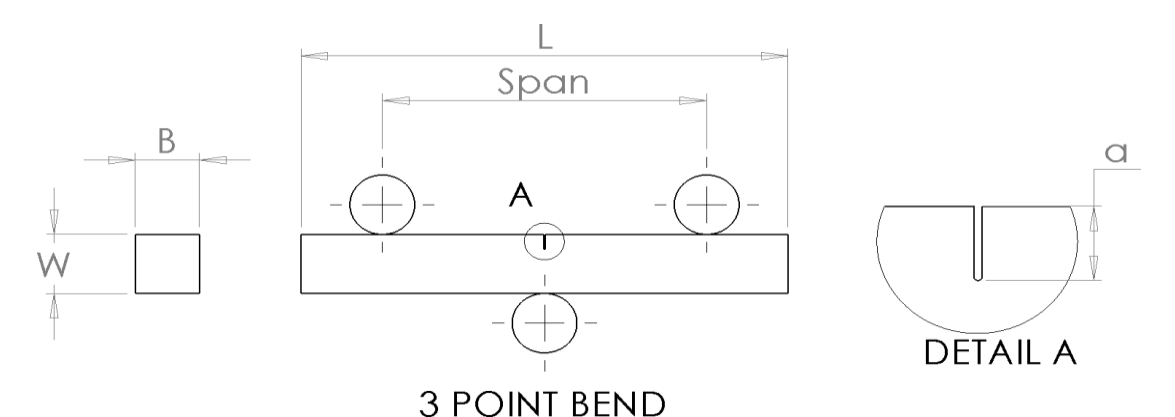


Figure 8-2 SENB3 sample drawing showing the dimensions of a (crack length), *W* (sample width) and *B* sample breadth.

As the crack grows, the potential difference across the crack increases. A calibrated empirical relationship found from a previous calibration test (private communication, University of Southampton, April 2018) was used to relate the potential difference across the crack in mV with crack length. The relationship was expressed as a 3<sup>rd</sup> degree polynomial that can be scaled appropriately for individual test samples.

### 8.1.1 Calculation of load range for target ΔK value

The following procedure was carried out to calculate the load input data required to achieve a target  $\Delta K$  value that is typically found from literature for pre-cracking purposes. Equation A-1 is used to find the  $X_0$  value that is the expected potential difference reading in mV from calibration testing and was found using an iterative solver tool in Microsoft Excel.

$$\left(\frac{a}{W}\right)_i = AX_0^3 + BX_0^2 + CX_0 + D$$
 Equation A-1

Where  $\left(\frac{a}{W}\right)_i$  was calculated by measuring the width of the sample W and the initial crack length a prior to testing (Figure A-2). The cubic constants A, B, C and D were found from calibration testing empirically.

The potential difference across the crack (X) to reference potential difference ratio (R) is recorded by the DCM2 machine. This is multiplied by the reference potential difference (R) to initial potential difference across crack from calibration tests (X<sub>0</sub>). Since the reference potential difference did not change throughout the test, the resulting calculation is a  $\frac{X}{X_0}$  ratio.

Testing in variable environmental conditions such as high temperature testing, the reference potential difference will change throughout the test. Hence a  $\frac{V}{V_0}$  ratio was used to account for this possibility (Equation A-2).

$$\frac{V}{V_0} = \frac{X}{R} \times \frac{R}{X_0}$$
 Equation A-2

The  $\frac{V}{V_0}$  ratio will increase during the test as the crack grows and therefore as  $\frac{a}{W}$  ratio increases. The relationship between crack length and potential difference from calibration tests (scaled for this particular test) can be used to calculate the  $\frac{a}{W}$  ratio at

any given  $\frac{V}{V_0}$  reading (Equation A-3) and therefore at any given  $\frac{X}{R}$  reading (typically displayed on DCM2 machines).

$$\frac{a}{W} = A \left(\frac{V}{V_0}\right)^3 + B \left(\frac{V}{V_0}\right)^2 + C \left(\frac{V}{V_0}\right) + D$$
 Equation A-3

The geometry correction factor (Y) from Equation A-4 extracted from British Standards BS ISO 12108:2012 [157] was used to account for the change in sample compliance as the crack grows, necessary when calculating the load range  $\Delta P$ .

$$Y = \frac{6\left(\frac{a}{W}\right)^{\frac{1}{2}}}{\left[\left(1+2\frac{a}{W}\right)\left(1-\frac{a}{W}\right)^{\frac{3}{2}}\right]} \left[1.99 - \frac{a}{W}\left(1-\frac{a}{W}\right)\left(2.15 - 3.93\frac{a}{W} + 2.7\left(\frac{a}{W}\right)^{2}\right)\right]$$
 Equation A-4

Equation A-5 can be used to find the cyclic load range ( $\Delta P$ ) and therefore the mean load ( $P_{mean}$ ) and amplitude ( $P_{amp}$ ) values to achieve a specific  $\Delta K$  value as the crack grows.

$$\Delta P = \frac{\Delta K \times B\sqrt{W}}{Y \times 10^{1.5}}$$
 Equation A-5

Where B is the breadth of the sample (Figure A-2). As the crack grows, the  $\frac{X}{R}$  ratio increases and thus the  $\Delta K$  value increases if ( $\Delta P$ ) remains constant. A target  $\frac{X}{R}$  ratio is found by calculating the change in the  $\frac{X}{R}$  ratio that results in an increase of the  $\Delta K$  value by approximately 1 %. The load values are decreased accordingly when the target  $\frac{X}{R}$  ratios have been achieved during testing to maintain a constant  $\Delta K$  value  $\pm$  1 %.

### 8.1.2 Calculating adjusted $\Delta K$ value during post-test analysis

The a W ratio at the beginning of the grow-out stage and at final failure was estimated during testing based upon the relationship found during calibration. The actual a W ratio at final failure was found by measuring the final crack length of the fracture surface after testing to British Standards BS ISO 12108:2012 [157] using image processing software. It is likely, that the a W ratio estimation from calibration testing does not match the measured a W ratio, and therefore a linear adjustment process is required to fine tune the estimation using Equation A64:

$$\left(\frac{a}{W}\right)_{adj} = \left(\frac{a}{W}\right)_g + \frac{\frac{a}{W} - \left(\frac{a}{W}\right)_g}{\left(\frac{a}{W}\right)_f - \left(\frac{a}{W}\right)_g} \times \frac{\left(a_f - a_g\right)}{W}$$
 Equation A-6

Where  $\left(\frac{a}{W}\right)_{adj}$  is the adjusted  $\frac{a}{W}$  ratio,  $\left(\frac{a}{W}\right)_g$  is the  $\frac{a}{W}$  ratio at the beginning of the grow-out stage,  $\left(\frac{a}{W}\right)_f$  is the  $\frac{a}{W}$  ratio at final failure,  $a_f$  is the measured crack length at failure and  $a_g$  is the measured crack length at the beginning of the grow-out stage. The adjusted  $\frac{a}{W}$  ratios were used to calculate the adjusted geometry factor  $Y_{adj}$  in Equation A-7.

$$Y_{adj} = \frac{6\left(\frac{a}{W}\right)_{adj}^{\frac{1}{2}}}{\left[\left(1+2\left(\frac{a}{W}\right)_{adj}\right)\left(1-\left(\frac{a}{W}\right)_{adj}\right)^{\frac{3}{2}}\right]} \times \left[1.99 - \left(\frac{a}{W}\right)_{adj}\left(1-\left(\frac{a}{W}\right)_{adj}\right)\left(2.15 - 3.93\left(\frac{a}{W}\right)_{adj} + 2.7\left(\frac{a}{W}\right)_{adj}^{2}\right)\right]}$$
Equation A-7

Equation A-3 was rearranged to find the final  $\Delta K$  values in Equation A-8.

$$\Delta K_{adj} = \frac{\Delta P \times Y_{adj} \times 10^{1.5}}{B\sqrt{W}}$$
 Equation A-8

The number of cycles was found from time stamp recording and the frequency of the test.

#### 8.1.3 Noise reduction

The potential difference reading across the crack fluctuated during the test which produced noise. The raw data was smoothed using the LOESS function with a 4th degree polynomial and sampling size of 0.1 [4].

# Chapter 9 Appendix B: Crack growth rate calculations

DCPD measures the voltage across a SEN sample crack and the reference voltage across the bulk of the material every three seconds, the set up is illustrated in figure A-1. The voltage across the crack is lower than through the bulk at the start of the test and as the crack grows the cross section of the sample decreases, increasing the resistance across the across crack wires, increasing the voltage recorded across the crack. The DCPD records Voltage and time stamps during the test. Therefor there is a relationship between increasing crack length and voltage. We can convert the voltage reading V to the crack length (a) by using the known initial crack length after pre-cracking  $a_i$  and final crack length  $a_f$  from the fracture surface analysis.

Using data from long crack testing of sample AZ1 we provide a step by step guide on the derivation of crack growth rate.

The typical output of a test will look similar to Figure 9-1. The data is smoothed using the method described in Appendix A 8.1.3. The smoothing was performed using a LOESS function with a 4<sup>th</sup> degree polynomial and sampling size of 0.1. The resulting dataset contains 100 data points. Given the data acquisition method and the assumption that the smoothing assumes the data follows a polynomial relationship and stage III cracking deviates from that relationship the stage III crack growth is not accurately captured by the smoothing.

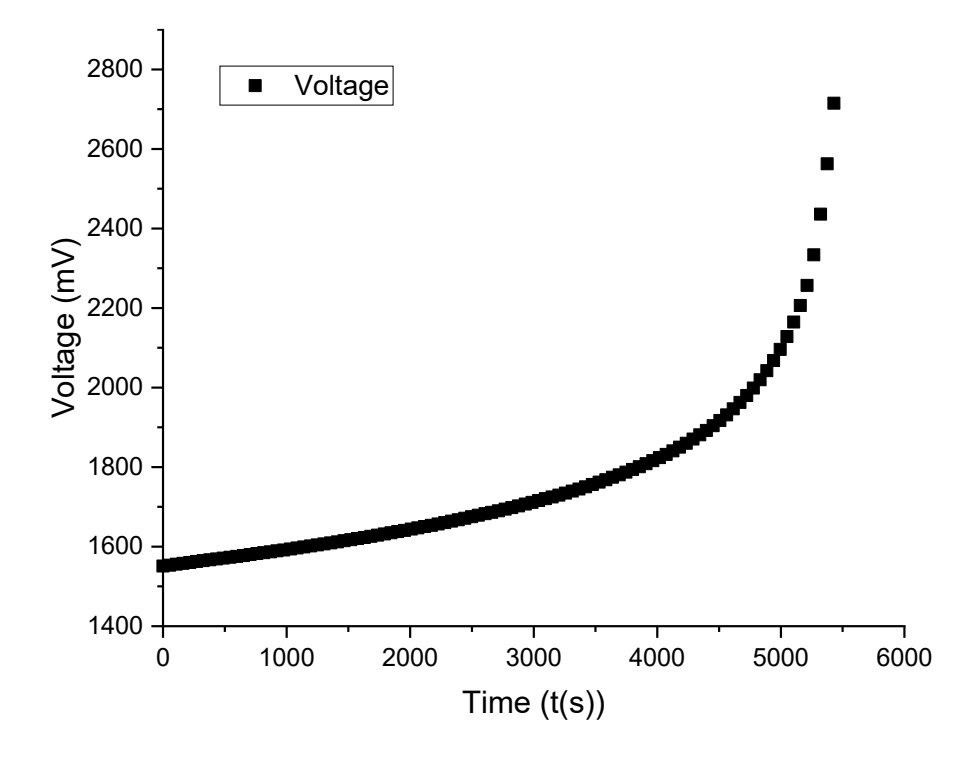


Figure 9-1 Smoothed DCPD data output for a SEN fatigue test. Where the variable voltage output is plotted against time.

The number of cycles were determined by knowing the frequency of the test in Hz and multiplying that by the time.

We use our known initial notch length a from the SEN sample machining and our

measured W to determine the initial  $\frac{a}{w}$ . We then use Equations A-1 and solve for  $X_0$  to

empirically fit the data. This allows us to determine out initial  $\frac{X}{X_0}$  where X is our recorded initial voltage via DCPD.

We then calculate the expected (not calibrated)  $\frac{a}{w}$  for increasing X values using Equation A-1. This expected  $\frac{a}{w}$  is used to calculate our expected a for increasing X values. At this stage we use our measured crack length after pre-cracking  $a_i$  and our final measured final crack length  $a_f$  with our known sample thickness w to generate our calibrated  $\frac{a}{w_{calibrated}}$  using Equation A-6. We now use our calibrated  $\frac{a}{w_{calibrated}}$  to calculate our  $a_{calibrated}$ . We can now plot our crack length versus our number of cycles in Figure 9-2.

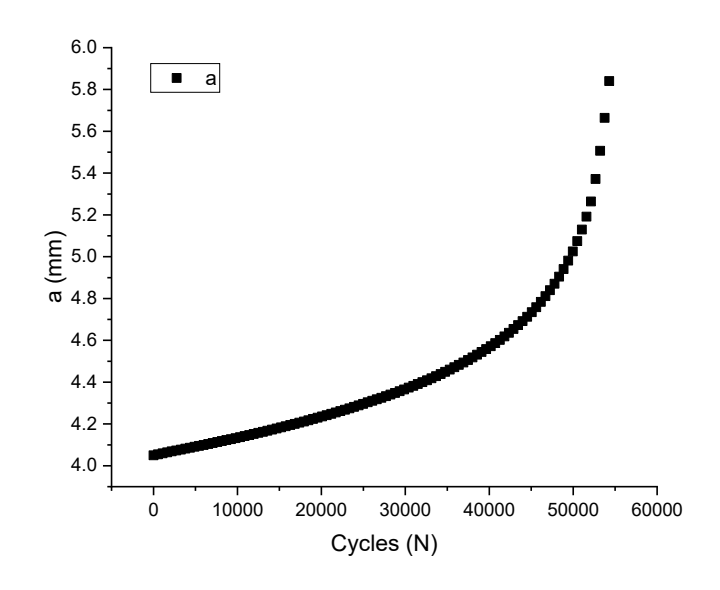


Figure 9-2 Calibrated crack length (a) plotted against number of cycles.

We then use the derived a vs N data to derive da/dN using the secant method every 3 datapoints, as illustrated in Figure 9-3.

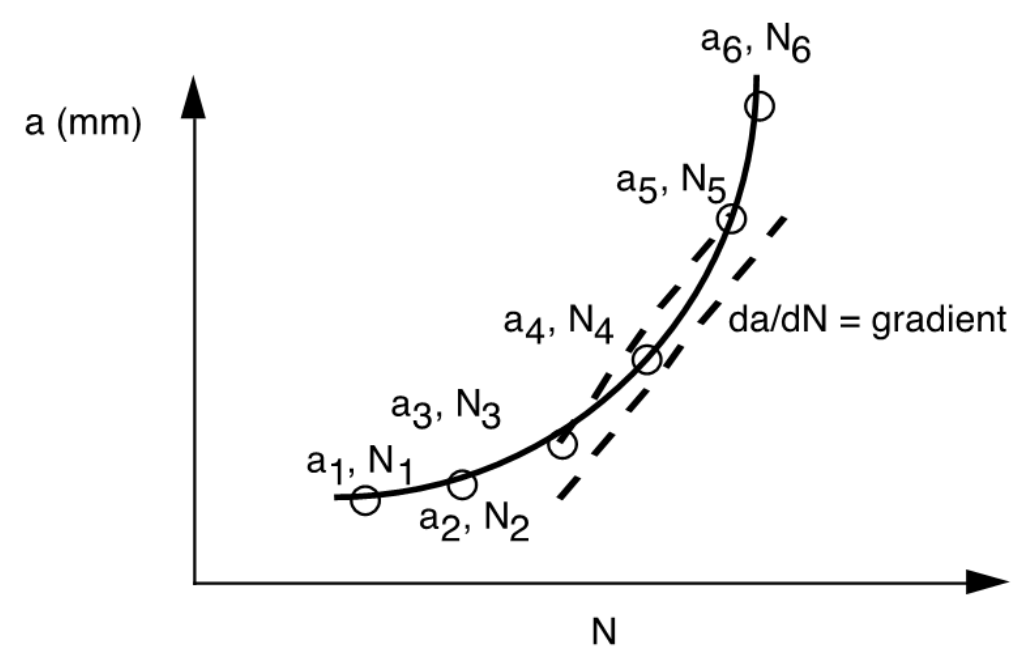


Figure 9-3 Secant method to determine the gradient of a vs N to determine da/dN

The secant method follows Equation B-1

$$\frac{da_4}{dN_4} = \frac{a_5 - a_3}{N_5 - N_3}$$
 Equation B-1

The resultant da/dN crack growth rate for a typical growout test is illustrated in Figure 9-4.

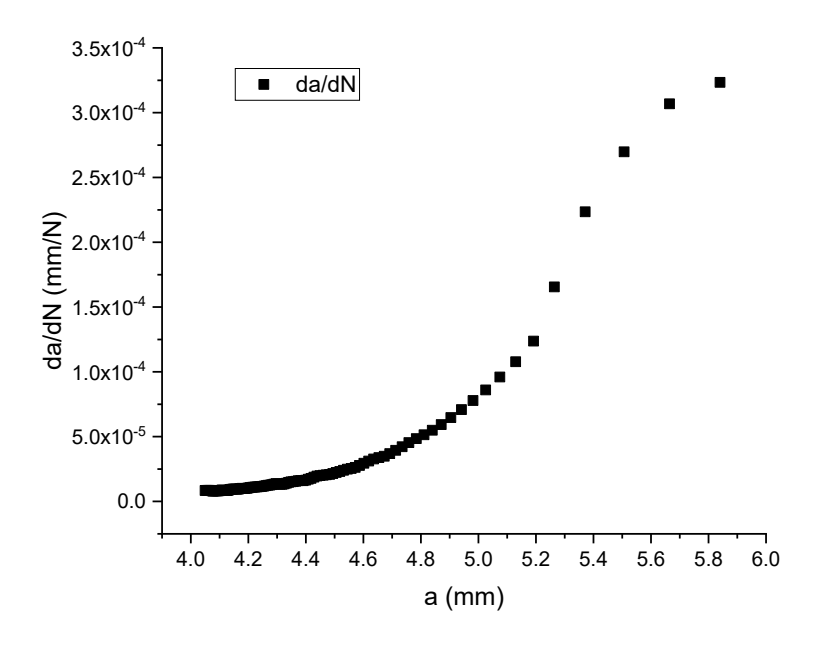


Figure 9-4 Crack growth rate plotted against calibrated crack length for a SEN fatigue test using DCPD crack monitoring.

We then use the formulas in appendix A do derive  $\Delta K$  to plot da/dN vs  $\Delta K$ .

# Chapter 10 Appendix C: Determination of short crack ΔKsurface

The following was based on the Appendix C from Cunningham (2022)[6].

The calculation of  $\Delta K_{Surface}$  of short crack surfaces is based upon the work of Scott and Thorpe [52] and Holdbrook and Dover [53].

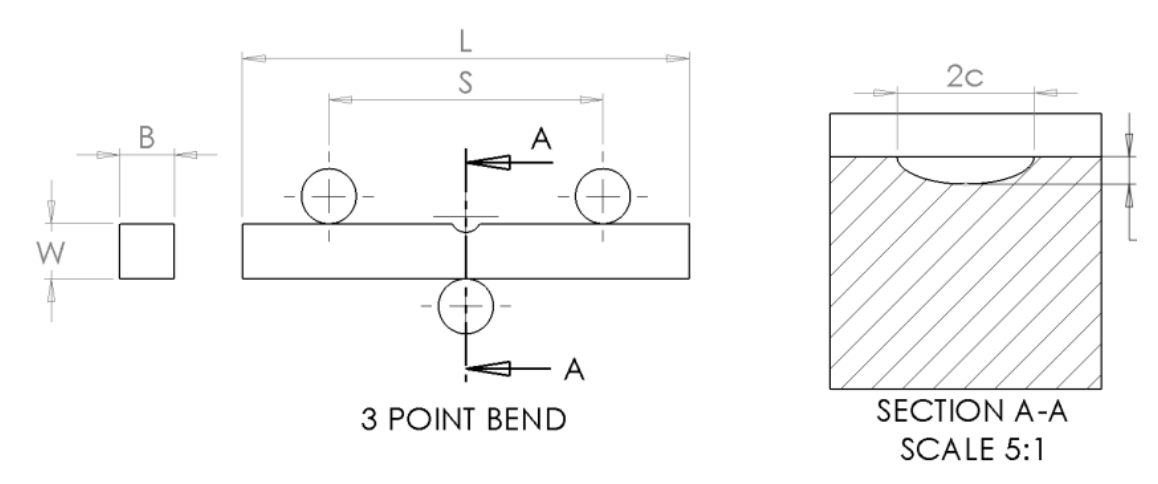


Figure 10-1 Drawing of U-notch sample with dimensions labelled. Cross section of U-notched sample through notch centre containing semi-elliptical crack with dimensions labelled.

The theoretical  $\frac{a}{c}$  ratio of a semi-elliptical short crack depends upon its projected surface crack length (2c) and can be calculated using Equation C-1 [50]. Therefore, the theoretical a c ratio is calculated for each surface crack measurement and the calculation of  $\Delta K_{\text{Surface}}$  assumes a perfect semi-ellipse shape.

$$\frac{a}{c} = 0.8238 - 8.4487 \times 10^{-5} (2c) + 5.1931 \times 10^{-9} (2c)^2$$
 Equation C-1

Where c is half the projected surface crack length and a is the semi-elliptical crack depth (Figure C-1).

A 'crack tip stress intensity factor' ( $\Delta K_1$ ) for semi-elliptical cracks in a semi-finite plate and under pure bending conditions is proposed by Scott and Thorpe [52] in Equation C-2:

$$\Delta K_1 = \left[ \left[ M_{f(0)} \left( 1 - 0.3 \left( \frac{a}{W} \right) \right) \left( 1 - \left( \frac{a}{W} \right)^{12} \right) \right] + \left[ 0.394 \, E(k) \left( \frac{a}{W} \right)^{12} \sqrt{\frac{c}{a}} \right] \right] \frac{\sigma_b}{E(k)} \sqrt{\pi a}$$
 Equation C-2

where W is the depth of the sample (Figure C-1) and  $\sigma_b$  is the pure bending stress at the notch surface calculated using Equation C-3 or via FE modelling.

$$\sigma_b = \frac{3k_t F(S_t - S_b)}{2BW^2}$$
 Equation C-3

Where F is the total maximum force,  $S_t$  is the top roller span,  $S_b$  is the bottom roller span (for 3-point bending this value is 0), B is the sample breadth (Figure C-1) and  $k_t$  is the notch stress concentration factor (Equation C-4).

$$k_t = \frac{\textit{maximum tensile stress on U-notch surface}}{\textit{maximum tensile stress calculated from}}$$
 
$$\textit{beam theory with equaivalent CSA}$$

Equation C-4

A 'front face correction factor'  $M_{f(0)}$  (Equation C-5) and an 'elliptic integral of the second kind' E(k) (Equation C-6) were found via 'empirical observation of crack shape during fatigue' to account for finite plate thickness and surface dimension effects [52].

$$M_{f(0)} = \left[1.21 - 0.1\left(\frac{a}{c}\right) + 0.1\left(\frac{a}{c}\right)^4\right]\sqrt{\frac{a}{c}}$$

Equation C-5

$$E(k) = \sqrt{1 + 1.47 \left(\frac{a}{c}\right)^{1.64}}$$

Equation C-6

A 'finite width correction factor' (Equation C-7 to Equation C-10) found by empirical fitting and interpolation of experimental data by Holdbrook and Dover [53] can be used to calculate the final  $\Delta K_{Surface}$  for semi-elliptical short cracks.

$$B_w = 1 + \frac{F\left(\frac{a}{c}\right)G\left(\frac{c}{B}\right)H\left(\frac{a}{W}\right)}{(0.2745)^2}$$

Equation C-7

Where:

$$F\left(\frac{a}{c}\right) = 0.381 - 0.141\left(\frac{a}{c}\right) - 0.366\left(\frac{a}{c}\right)^2 + 0.569\left(\frac{a}{c}\right)^3 - 0.248\left(\frac{a}{c}\right)^4$$

Equation C-8

$$G\left(\frac{c}{R}\right) = -0.0239 + 1.434\left(\frac{c}{R}\right) - 2.984\left(\frac{c}{R}\right)^2 + 7.822\left(\frac{c}{R}\right)^3$$

**Equation C-9** 

$$H\left(\frac{a}{W}\right) = -0.0113 + 0.323\left(\frac{a}{W}\right) + 0.749\left(\frac{a}{W}\right)^2 - 0.535\left(\frac{a}{W}\right)^3$$

Equation C-10

The final  $\Delta K_{Surface}$  for each crack is found by multiplying the finite width correction factor by the crack tip stress intensity factor  $\Delta K1$  (Equation C-11).

$$\Delta K_{Surface} = B_w \times \Delta K_1$$

Equation C-11

# **Chapter 11 Appendix D: Summary of tested samples**

The following is a summary of the performed tests on the samples listed in the thesis in Table 11-1.

Table 11-1 Summary of tested samples.

Sample	TENSILE	Hardness	Long crack	Short crack	comment
ID	TEST	testing	testing	testing	S
BX75	NO	YES	NO	NO	
CX75	NO	NO	YES	NO	
AY75	YES	NO	NO	NO	
BX2	NO	YES	NO	NO	
					un-
BX71	NO	YES	NO	YES	peened
AX71	NO	YES	NO	YES	peened
					un-
BY71	NO	YES	NO	YES	peened
BW71	NO	YES	NO	YES	peened
CW71	NO	NO	YES	NO	
AY71	YES	NO	NO	NO	
					un-
BX71	NO	NO	NO	YES	peened
AW73	NO	YES	NO	YES	peened
					un-
BW73	NO	YES	NO	YES	peened
AX73	NO	YES	NO	YES	peened
CX73	NO	NO	YES	NO	
CW73	YES	NO	NO	NO	
BY1	NO	YES	NO	NO	
					un-
BX1	NO	YES	NO	YES	peened
AZ1	NO	NO	YES	NO	
CW1	YES	NO	NO	NO	
					un-
BY1	NO	NO	NO	YES	peened

# **Chapter 12 References**

- [1] M. A. Delucchi and M. Z. Jacobson, "Providing all global energy with wind, water, and solar power, Part II: Reliability, system and transmission costs, and policies," *Energy Policy*, vol. 39, no. 3, pp. 1170–1190, 2011, doi: 10.1016/j.enpol.2010.11.045.
- [2] N. Kumar, S. Paterson, K. Coleman, C. Lee, D. Agan, and S. Lefton, "Power plant cycling measure Evaluating historical cycling to model future grid operations," in *2013 IEEE Power & Energy Society General Meeting*, IEEE, 2013, pp. 1–5. doi: 10.1109/PESMG.2013.6672754.
- [3] Morris A., "Last stage steam turbine blades," 2018, *Internal Communication*.
- [4] K. A. Soady, "Reducing conservatism in life assessment approaches: Industrial steam turbine blade to disc interfaces and the shot peening process," Thesis, University of Southampton, 2013.
- [5] M. James, M. Newby, D. Hattingh, A. S.-P. Engineering, and undefined 2010, "Shot-peening of steam turbine blades: Residual stresses and their modification by fatigue cycling," ElsevierMN James, M Newby, DG Hattingh, A SteuwerProcedia Engineering, 2010 • Elsevier, Accessed: Mar. 05, 2025. [Online]. Available: https://www.sciencedirect.com/science/article/pii/S1877705810000494
- [6] B. M. D. Cunningham, "EXTENDING FATIGUE LIFE OF INDUSTRIAL LOW-PRESSURE FV566 TURBINE BLADES: EFFICACY OF A LIFETIME EXTENSION STRATEGY TO EXTEND SERVICE LIFE," 2022, doi: 10.5258/SOTON/T0044.
- [7] B. M. D. Cunningham *et al.*, "Fatigue crack initiation and growth behavior within varying notch geometries in the low-cycle fatigue regime for FV566 turbine blade material," *Fatigue Fract Eng Mater Struct*, no. April, pp. 2845–2863, 2023, doi: 10.1111/ffe.14036.
- [8] K. A. Soady, B. G. Mellor, J. Shackleton, A. Morris, and P. A. S. Reed, "The effect of shot peening on notched low cycle fatigue," *Materials Science and Engineering A*, vol. 528, no. 29–30, pp. 8579–8588, 2011, doi: 10.1016/j.msea.2011.08.003.
- [9] B. Y. He, K. A. Soady, B. G. Mellor, A. Morris, and P. A. S. Reed, "Effects of shot peening on short crack growth rate and resulting low cycle fatigue behaviour in low pressure turbine blade material," *Materials Science and Technology (United Kingdom)*, vol. 29, no. 7, pp. 788–796, 2013, doi: 10.1179/1743284713Y.0000000230.
- [10] K. Dalaei, B. Karlsson, L. S.-P. Engineering, and undefined 2010, "Stability of residual stresses created by shot peening of pearlitic steel and their influence on fatigue behaviour," Elsevierk Dalaei, B Karlsson, LE SvenssonProcedia Engineering, 2010 Elsevier, Accessed: Mar. 05, 2025. [Online]. Available: https://www.sciencedirect.com/science/article/pii/S1877705810000676
- [11] Y. Gao, X. W.-A. Materialia, and undefined 2011, "Experimental investigation and fatigue life prediction for 7475-T7351 aluminum alloy with and without shot peening-induced residual stresses," *ElsevierYK Gao, XR WuActa Materialia, 2011•Elsevier*, Accessed: Mar. 05, 2025. [Online]. Available: https://www.sciencedirect.com/science/article/pii/S1359645411001601

- [12] Y. Xiang and Y. Liu, "Mechanism modelling of shot peening effect on fatigue life prediction," *Fatigue Fract Eng Mater Struct*, vol. 33, no. 2, pp. 116–125, Feb. 2010, doi: 10.1111/j.1460-2695.2009.01422.x.
- [13] A. Bag, M. Lévesque, and M. Brochu, "Effect of shot peening on short crack propagation in 300M steel," *Int J Fatigue*, vol. 131, Feb. 2020, doi: 10.1016/j.ijfatigue.2019.105346.
- [14] K. Dalaei, B. Karlsson, and L. Svensson, "Stability of shot peening induced residual stresses and their influence on fatigue lifetime," *Materials Science & Engineering A*, vol. 528, no. 3, pp. 1008–1015, 2011, doi: 10.1016/j.msea.2010.09.050.
- [15] J. Walker, D. J. Thomas, and Y. Gao, "Effects of shot peening and pre-strain on the fatigue life of dual phase Martensitic and Bainitic steels," *J Manuf Process*, vol. 26, pp. 419–424, 2017, doi: 10.1016/j.jmapro.2017.03.010.
- [16] E. Maleki, O. Unal, and K. R. Kashyzadeh, "Effects of conventional, severe, over, and reshot peening processes on the fatigue behavior of mild carbon steel," *Surf Coat Technol*, vol. 344, no. September 2017, pp. 62–74, 2018, doi: 10.1016/j.surfcoat.2018.02.081.
- [17] F. Masuyama, "History of Power Plants and Progress in Heat Resistant Steels," vol. 41, no. 6, pp. 612–625, 2001.
- [18] B. M. D. Cunningham, "Increasing service life of industrial LP turbine blades: fatigue behaviour of martensitic stainless steel materials in notches with overloads," 2019.
- [19] N. K. Mukhopadhyay, S. G. Chowdhury, G. Das, S. K. Chattoraj, S. K. Das, and D. K. Bhattacharya, "AN INVESTIGATION OF THE FAILURE OF LOW Pressure steam turbine blades," *Eng Fail Anal*, vol. 5, no. 3, pp. 181–193, 1998.
- [20] G. Das, S. G. Chowdhury, A. K. Ray, S. K. Das, and D. K. Bhattacharya, "Turbine blade failure in a thermal power plant," vol. 10, pp. 85–91, 2003.
- [21] W. D. Callister and D. G. Rethwisch, *Materials Science and Engineering*, 9th ed. Wiley, 2011.
- [22] J. Fan, X. Guo, C. Wu, V. Crupi, and E. Guglielmino, "Influence of Heat Treatments on Mechanical Behavior of FV520B Steel," pp. 55–64, 2013, doi: 10.1111/ext.12019.
- [23] A. Clark, "Fatigue mechanisms in FV520B, a turbine blade steel.," 1999.
- [24] P. Liu, A. Hultin Stigenberg, and J. O. Nilsson, "Isothermally Formed Quasicrystalline Precipitates used for Strengthening in a New Maraging Stainless Steel.," *Scripta Metallurgica*, vol. 31, no. 3, pp. 249–254, 1994.
- [25] S. Floreen, "The Physical Metallurgy of Maraging Steels," *Metallurgical Reviews*, no. 126, pp. 115–128, 1968.
- [26] Q. Wu, X. Chen, Z. Fan, D. Nie, and R. Wei, "Corrosion fatigue behavior of FV520B steel in water and salt-spray environments," *Eng Fail Anal*, vol. 79, no. May, pp. 422–430, 2017, doi: 10.1016/j.engfailanal.2017.05.012.
- [27] L. Xiang, J. Pan, S. Chen, and Y. Zhong, "Experimental investigation on the stress corrosion cracking of FV520B welded joint in natural gas environment with ECP and SSRT," *Eng Fract Mech*, vol. 200, no. December 2017, pp. 166–174, 2018, doi: 10.1016/j.engfracmech.2018.07.026.

- [28] H. Nakagawa and T. Miyazaki, "Effect of retained austenite on the microstructure and mechanical properties of martensitic precipitation hardening stainless steel," vol. 4, pp. 3901–3908, 1999.
- [29] "Firth Vickers Data Handbook," 1988, Sheffield Forgemasters Limited Publ., Sheffield.
- [30] A. Clark, "Fatigue mechanisms in fv520b, a turbine blade steel," no. April, 1999.
- [31] H. Schneider, "Investment casting of high-hot strength 12% chrome steel," *Foundry Trade J*, vol. 108, pp. 562–563, 1960.
- [32] S. Suresh, "Cyclic deformation in polycrystalline ductile solids" *Fatigue of materials*. Cambridge university press, 1998.
- [33] S. Suresh, "Fatigue crack initiation in ductile solids" *Fatigue of materials*. Cambridge university press, 1998.
- [34] Y. Zhang, J. Wang, Q. Sun, H. Zhang, and P. Jiang, "Fatigue life prediction of FV520B with internal inclusions," *Mater Des*, vol. 69, pp. 241–246, Mar. 2015, doi: 10.1016/j.matdes.2014.12.022.
- [35] B. He, "Fatigue crack growth behaviour in shot peened low pressure steam turbine blade material," University of Southampton, 2015.
- [36] J. Man, K. Obrtlík, and J. Polák, "Extrusions and intrusions in fatigued metals. Part 1. State of the art and history," *Philosophical Magazine*, vol. 89, no. 16, pp. 1295–1336, Jun. 2009, doi: 10.1080/14786430902917616.
- [37] J. Man, P. Klapetek, O. Man, A. Weidner, K. Obrtlík, and J. Polák, "Extrusions and intrusions in fatigued metals. Part 2. AFM and EBSD study of the early growth of extrusions and intrusions in 316L steel fatigued at room temperature," *Philosophical Magazine*, vol. 89, no. 16, pp. 1337–1372, Jun. 2009, doi: 10.1080/14786430902917624.
- [38] J. Man, K. Obrtlík, C. Blochwitz, and J. Polák, "Atomic force microscopy of surface relief in individual grains of fatigued 316L austenitic stainless steel," 2002. [Online]. Available: www.actamat-journals.com
- [39] J. Polák, J. Man, T. Vystavěl, and M. Petrenec, "The shape of extrusions and intrusions and initiation of stage I fatigue cracks," *Materials Science and Engineering: A*, vol. 517, no. 1–2, pp. 204–211, Aug. 2009, doi: 10.1016/j.msea.2009.03.070.
- [40] J. Polak, "On the Role of Point Defects in Fatigue Crack Initiation," 1987.
- [41] A. A. Griffith, "VI. The phenomena of rupture and flow in solids," *Philosophical Transactions of the Royal Society of London. Series A, Containing Papers of a Mathematical or Physical Character*, vol. 221, no. 582–593, pp. 163–198, Jan. 1921, doi: 10.1098/rsta.1921.0006.
- [42] D. S. Dugdale, "YIELDING OF STEEL SHEETS CONTAINING SLITS," Pergsmon Press Ltd, 1900.
- [43] J. H. Bulloch, "Fatigue threshold in steels Mean stress and microstructure influences," 1994.
- [44] C. Vallellano, A. Navarro, F. J. García-Lomas, and J. Domínguez, "On the estimation of microstructural effects in the near-threshold fatigue of small cracks," *Journal of Strain Analysis for Engineering Design*, vol. 43, no. 5, pp. 337–347, 2008, doi: 10.1243/03093247JSA351.

- [45] P. Paris and F. Erdogan, "A Critical Analysis of Crack Propagation Laws," 1963. [Online]. Available: http://asmedigitalcollection.asme.org/fluidsengineering/article-pdf/85/4/528/5763569/528\_1.pdf
- [46] R. O. Ritchie, "Mechanisms of fatigue-crack propagation in ductile and brittle solids," 1999.
- [47] K. J. Miller, "THE BEHAVIOUR OF SHORT FATIGUE CRACKS AND THEIR INITIATION PART II-A GENERAL SUMMARY," *Fatigue Fract Eng Mater Struct*, vol. 10, no. 2, pp. 93–113, Feb. 1987, doi: 10.1111/j.1460-2695.1987.tb01153.x.
- [48] K. J. MILLER, "THE SHORT CRACK PROBLEM," *Fatigue Fract Eng Mater Struct*, vol. 5, no. 3, pp. 223–232, Jul. 1982, doi: 10.1111/j.1460-2695.1982.tb01250.x.
- [49] M. H. El Haddad, K. N. Smith, and T. H. Topper, "Fatigue Crack Propagation of Short Cracks," *J Eng Mater Technol*, vol. 101, no. 1, pp. 42–46, Jan. 1979, doi: 10.1115/1.3443647.
- [50] B. Y. He, K. A. Soady, B. G. Mellor, G. Harrison, and P. A. S. Reed, "Fatigue crack growth behaviour in the LCF regime in a shot peened steam turbine blade material," *Int J Fatigue*, vol. 82, pp. 280–291, 2016, doi: 10.1016/j.ijfatigue.2015.03.017.
- [51] B. M. D. Cunningham *et al.*, "Fatigue crack initiation and growth behavior in a notch with periodic overloads in the low-cycle fatigue regime of FV566 ex-service steam turbine blade material," *Fatigue Fract Eng Mater Struct*, vol. 45, no. 2, pp. 546–564, 2022, doi: 10.1111/ffe.13617.
- [52] P. M. Scott and T. W. Thorpe, "A critical review of crack tip stress intensity factors for semielliptic cracks\*," vol. 4, no. 4, pp. 291–309, 1981.
- [53] S. J. Holdbrook and W. D. Dover, "THE STRESS INTENSITY FACTOR FOR A DEEP SURFACE CRACK IN A FINITE PLATE," vol. 12, no. 2, 1979.
- [54] M. Kamaya, "Influence of the Interaction on Stress Intensity Factor of Semielliptical Surface Cracks," *J Press Vessel Technol*, vol. 130, no. 1, Feb. 2008, doi: 10.1115/1.2826424.
- [55] J. T. Tan and B. K. Chen, "A new method for modelling the coalescence and growth of two coplanar short cracks of varying lengths in AA7050-T7451 aluminium alloy," *Int J Fatigue*, vol. 49, pp. 73–80, Apr. 2013, doi: 10.1016/j.ijfatigue.2012.12.011.
- [56] T. Hoshide, M. Miyahara, and T. Inoue, "LIFE PREDICTION BASED ON ANALYSIS OF CRACK COALESCENCE IN LOW CYCLE FATIGUE," 1987.
- [57] P. R. Frise and R. Bell, "Modelling fatigue crack growth and coalescence in notches," *International Journal of Pressure Vessels and Piping*, vol. 51, no. 1, pp. 107–126, 1992, doi: 10.1016/0308-0161(92)90008-4.
- [58] Z. Han, C. Qian, and H. Li, "Investigation of the enhancement interactions between double parallel cracks on fatigue growth behaviors," *Materials*, vol. 13, no. 13, pp. 1–19, Jul. 2020, doi: 10.3390/ma13132952.
- [59] F. Lefebvre and I. Sinclair, "Micromechanical aspects of fatigue in a MIG welded aluminium airframe alloy. Part 2 Short fatigue crack behaviour," *Materials Science and Engineering: A*, vol. 407, no. 1–2, pp. 265–272, Oct. 2005, doi: 10.1016/j.msea.2005.07.014.

- [60] Y. -Z. Wang, J. D. Atkinson, R. Akid, and R. N. Parkins, "CRACK INTERACTION, COALESCENCE AND MIXED MODE FRACTURE MECHANICS," *Fatigue Fract Eng Mater Struct*, vol. 19, no. 4, pp. 427–439, Apr. 1996, doi: 10.1111/j.1460-2695.1996.tb00979.x.
- [61] F. Le Poulain, M. Touzet, M. Puiggali, and I. Aubert, "Mechanical behaviour of a solid with many stress corrosion growing cracks."
- [62] M. Kamaya and T. Haruna, "Influence of local stress on initiation behavior of stress corrosion cracking for sensitized 304 stainless steel," *Corros Sci*, vol. 49, no. 8, pp. 3303–3324, Aug. 2007, doi: 10.1016/j.corsci.2007.01.011.
- [63] A. Ali, M. W. Brown, and C. A. Rodopoulos, "Modelling of crack coalescence in 2024-T351 Al alloy friction stir welded joints," *Int J Fatigue*, vol. 30, no. 10–11, pp. 2030–2043, Oct. 2008, doi: 10.1016/j.ijfatigue.2008.02.014.
- [64] M. Kamaya and M. Itakura, "Simulation for intergranular stress corrosion cracking based on a three-dimensional polycrystalline model," *Eng Fract Mech*, vol. 76, no. 3, pp. 386– 401, Feb. 2009, doi: 10.1016/j.engfracmech.2008.11.004.
- [65] C. R. Soderberg, "Factor of safety and working stress," *Trans Am Soc Mech Eng*, vol. 52, pp. 13–28, 1939.
- [66] J. Goodman, Mechanics applied to engineering. Longmans, Green, 1919.
- [67] H. Gerber, Bestimmung der zulässigen spannungen in eisen-constructionen. Wolf, 1874.
- [68] M. A. Miner, "Cumulative damage in fatigue journal of applied mechanics 12 (1945) no. 3, pp," *A159-A164*, 1945.
- [69] T. Yokoi, K. Kawasaki, M. Takahashi, K. Koyama, and M. Mizui, "Fatigue properties of high strenght steels containing retained austenite," vol. 17, pp. 210–212, 1996.
- [70] V. F. Silva, L. F. Canale, D. Spinelli, and O. R. Crnkovic, "Influence of Retained Austenite on Short Fatigue Crack Growth and Wear Resistance of Case Carburized Steel," vol. 8, no. October, pp. 543–548, 1999.
- [71] G. Gao, R. Liu, K. Wang, X. Gui, R. D. K. Misra, and B. Bai, "Scripta Materialia Role of retained austenite with different morphologies on sub-surface fatigue crack initiation in advanced bainitic steels," vol. 184, pp. 12–18, 2020, doi: 10.1016/j.scriptamat.2020.03.036.
- [72] T. Hilditch, H. Beladi, P. Hodgson, and N. Stanford, "Role of microstructure in the low cycle fatigue of multi-phase steels," *Materials Science & Engineering A*, vol. 534, pp. 288–296, 2012, doi: 10.1016/j.msea.2011.11.071.
- [73] Z. Z. Hu, Y. Q. Liu, and J. H. Liu, "The effect of austenite on low cycle fatigue in three-phase steel," vol. 19, pp. 641–646, 1997.
- [74] G. Chai, "The formation of subsurface non-defect fatigue crack origins," *Int J Fatigue*, vol. 28, pp. 1533–1539, 2006, doi: 10.1016/j.ijfatigue.2005.06.060.
- [75] H. Neuber, "Theory of Stress Concentration for Shear-Strained Prismatical Bodies With Arbitrary Nonlinear Stress-Strain Law," *J Appl Mech*, vol. 28, no. 4, pp. 544–550, Dec. 1961, doi: 10.1115/1.3641780.
- [76] T. H. Topper, R. M. Wetzel, and J. Morrow, "Neuber's rule applied to fatigue of notched specimens," *Defense Technical Information Center*, p. 21, 1967.

- [77] M. Kobayashi, T. Matsui, and Y. Murakami, "Mechanism of creation of compressive residual stress by shot peening," vol. 20, no. 5, pp. 351–357, 1998.
- [78] K. Dalaei, B. Karlsson, and L. Svensson, "Stability of shot peening induced residual stresses and their influence on fatigue lifetime," *Materials Science & Engineering A*, vol. 528, no. 3, pp. 1008–1015, 2011, doi: 10.1016/j.msea.2010.09.050.
- [79] K. A. Soady, B. G. Mellor, J. Shackleton, A. Morris, and P. A. S. Reed, "The effect of shot peening on notched low cycle fatigue," *Materials Science & Engineering A*, vol. 528, no. 29–30, pp. 8579–8588, 2011, doi: 10.1016/j.msea.2011.08.003.
- [80] K. A. Soady, B. G. Mellor, G. D. West, G. Harrison, A. Morris, and P. A. S. Reed, "Evaluating surface deformation and near surface strain hardening resulting from shot peening a tempered martensitic steel and application to low cycle fatigue," *Int J Fatigue*, vol. 54, pp. 106–117, 2013, doi: 10.1016/j.ijfatigue.2013.03.019.
- [81] E. Björklund and E. Björklund, "The Influence of Hardness and Retained Austenite on the Fatigue Limit after Shot Peening," no. 14001, p. 59, 2014, [Online]. Available: https://www.diva-portal.org/smash/get/diva2:709736/FULLTEXT01.pdf
- [82] V. Llaneza and F. J. Belzunce, "Study of the effects produced by shot peening on the surface of quenched and tempered steels: Roughness, residual stresses and work hardening," *Appl Surf Sci*, vol. 356, pp. 475–485, Nov. 2015, doi: 10.1016/j.apsusc.2015.08.110.
- [83] E. Maleki, G. H. Farrahi, K. Reza Kashyzadeh, O. Unal, M. Gugaliano, and S. Bagherifard, "Effects of Conventional and Severe Shot Peening on Residual Stress and Fatigue Strength of Steel AlSI 1060 and Residual Stress Relaxation Due to Fatigue Loading: Experimental and Numerical Simulation," *Metals and Materials International*, vol. 27, no. 8, pp. 2575–2591, Aug. 2021, doi: 10.1007/s12540-020-00890-8.
- [84] D. Wu, C. Yao, and D. Zhang, "Surface characterization and fatigue evaluation in GH4169 superalloy: Comparing results after finish turning; shot peening and surface polishing treatments," *Int J Fatigue*, vol. 113, pp. 222–235, Aug. 2018, doi: 10.1016/j.ijfatigue.2018.04.009.
- [85] C. You, M. Achintha, K. A. Soady, and P. A. S. Reed, "Low cycle fatigue life prediction in shot-peened components of different geometries Part II: Life prediction," vol. 44, no. 0, pp. 1–26.
- [86] M. A. S. Torres and H. J. C. Voorwald, "An evaluation of shot peening, residual stress and stress relaxation on the fatigue life of AISI 4340 steel," 2002. [Online]. Available: www.elsevier.com/locate/ijfatigue
- [87] S. Keller, M. Horstmann, N. Kashaev, and B. Klusemann, "Crack closure mechanisms in residual stress fields generated by laser shock peening: A combined experimental-numerical approach," *Eng Fract Mech*, vol. 221, Nov. 2019, doi: 10.1016/j.engfracmech.2019.106630.
- [88] R. A. Cláudio, J. M. Silva, J. Byrne, J. M. Silva, C. M. Branco, and J. Byrne, "Fatigue life prediction of shot peened components," researchgate.netRA Cláudio, JM Silva, CM Branco, J ByrneCiência & Tecnologia dos Materiais, 2008 researchgate.net, vol. 20, no. 2, 2008, doi: 10.1108/17579861211281191.

- [89] M. E. Fitzpatrick and L. Edwards, "Fatigue Crack/Residual Stress Field Interactions and Their Implications for Damage-Tolerant Design."
- [90] K. A. Soady, "Life assessment methodologies incoroporating shot peening process effects: mechanistic consideration of residual stresses and strain hardening Part 1 effect of shot peening on fatigue resistance Life assessment methodologies incoroporating shot peening," vol. 0836, 2013, doi: 10.1179/1743284713Y.0000000222.
- [91] G. Webster, A. E.-I. journal of fatigue, and undefined 2001, "Residual stress distributions and their influence on fatigue lifetimes," *Elsevier*, Accessed: Mar. 05, 2025. [Online]. Available: https://www.sciencedirect.com/science/article/pii/S0142112301001335
- [92] Y. Xiang, & Y. L.-F. & F. of E. M., and undefined 2010, "Mechanism modelling of shot peening effect on fatigue life prediction," *Wiley Online LibraryY Xiang, Y LiuFatigue & Fracture of Engineering Materials & Structures, 2010 Wiley Online Library*, vol. 33, no. 2, pp. 116–125, Feb. 2010, doi: 10.1111/j.1460-2695.2009.01422.x.
- [93] E. D. L. Rios, ... M. T.-F. & fracture of, and undefined 2000, "Modelling fatigue crack growth in shot-peened components of Al 2024-T351," Wiley Online LibraryER De Los Rios, M Trull, A LeversFatigue & fracture of engineering materials & structures, 2000•Wiley Online Library, vol. 23, no. 8, pp. 709–716, 2000, doi: 10.1046/j.1460-2695.2000.00287.x.
- [94] R. Fathallah, A. Laamouri, ... H. S.-I. J. of, and undefined 2004, "High cycle fatigue behavior prediction of shot-peened parts," *Elsevier*, Accessed: Mar. 05, 2025. [Online]. Available: https://www.sciencedirect.com/science/article/pii/S0142112304000581
- [95] S. Cao, H. Zhang, J. Hu, C. Li, and B. Li, "Fatigue life prediction model for shot-peened laser powder bed fused 304L steel considering residual stress relaxation and defect distribution," *Eng Fail Anal*, vol. 162, p. 108423, Aug. 2024, doi: 10.1016/J.ENGFAILANAL.2024.108423.
- [96] Z. Gao, J. Gan, H. Liu, X. Liu, and W. Wu, "Fatigue crack growth prediction for shot-peened steel considering residual stress relaxation," *Mater Des*, vol. 234, p. 112301, Oct. 2023, doi: 10.1016/J.MATDES.2023.112301.
- [97] Firth Vickers Data Handbook. Sheffiled: Sheffield Forgemasters Limited Publ, 1988.
- [98] A. Clark, "Fatigue mechanisms in fv520b, a turbine blade steel," no. April, 1999.
- [99] N. K. Mukhopadhyay, S. G. Chowdhury, G. Das, S. K. Chattoraj, S. K. Das, and D. K. Bhattacharya, "AN INVESTIGATION OF THE FAILURE OF LOW Pressure steam turbine blades," *Eng Fail Anal*, vol. 5, no. 3, pp. 181–193, 1998.
- [100] Firth Vickers Data Handbook. Sheffiled: Sheffield Forgemasters Limited Publ, 1988.
- [101] K. A. Soady, B. G. Mellor, and P. A. S. Reed, "Life assessment methodologies incoroporating shot peening process effects: Mechanistic consideration of residual stresses and strain hardening: Part 2 Approaches to fatigue lifting after shot peening," *Materials Science and Technology (United Kingdom)*, vol. 29, no. 6, pp. 652–664, 2013, doi: 10.1179/1743284713Y.0000000223.
- [102] B. Y. He *et al.*, "Effects of shot peening on short crack growth rate and resulting low cycle fatigue behaviour in low pressure turbine blade material Effects of shot peening on short crack growth rate and resulting low cycle fatigue behaviour in low pressure turbine blade ," vol. 0836, 2013, doi: 10.1179/1743284713Y.0000000230.

- [103] "Standard Test Method for Microindentation Hardness of Materials," ASTM International, West Conshohocken, PA. doi: 10.1520/E0384.
- [104] Z. Ming, W. Weiqiang, W. Pengfei, L. I. U. Yan, and L. I. Jianfeng, "Fatigue behavior and mechanism of FV520B-I in ultrahigh cycle regime," *Procedia Materials Science*, vol. 3, pp. 2035–2041, 2014, doi: 10.1016/j.mspro.2014.06.328.
- [105] J. Fan, X. Guo, C. Wu, V. Crupi, and E. Guglielmino, "Influence of Heat Treatments on Mechanical Behavior of FV520B Steel," pp. 55–64, 2013, doi: 10.1111/ext.12019.
- [106] A. Clark, "Fatigue mechanisms in FV520B, a turbine blade steel.," 1999.
- [107] W. Yang, Q. Guo, J. Fan, X. Guo, and Y. Zhao, "Effect of aging temperature on energy dissipation and high-cycle fatigue properties of FV520B stainless steel," *Eng Fract Mech*, vol. 242, no. December 2020, p. 107464, 2021, doi: 10.1016/j.engfracmech.2020.107464.
- [108] K. A. Soady, B. G. Mellor, J. Shackleton, A. Morris, and P. A. S. Reed, "The effect of shot peening on notched low cycle fatigue," *Materials Science & Engineering A*, vol. 528, no. 29–30, pp. 8579–8588, 2011, doi: 10.1016/j.msea.2011.08.003.
- [109] K. A. Soady, "Life assessment methodologies incoroporating shot peening process effects: mechanistic consideration of residual stresses and strain hardening Part 1 effect of shot peening on fatigue resistance Life assessment methodologies incoroporating shot peening," vol. 0836, 2013, doi: 10.1179/1743284713Y.0000000222.
- [110] P. P. Suikkanen, C. Cayron, A. J. DeArdo, and L. Pentti Karjalainen, "Crystallographic Analysis of Martensite in 0.2C-2.0Mn-1.5Si-0.6Cr Steel using EBSD," 2011.
- [111] G. Miyamoto, N. Takayama, and T. Furuhara, "Accurate measurement of the orientation relationship of lath martensite and bainite by electron backscatter diffraction analysis," *Scr Mater*, vol. 60, no. 12, pp. 1113–1116, Jun. 2009, doi: 10.1016/j.scriptamat.2009.02.053.
- [112] D. Huang and W. Feng, "Hot Deformation Characteristics and Processing Map of FV520B Martensitic Precipitation-Hardened Stainless Steel," *J Mater Eng Perform*, vol. 28, no. 4, pp. 2281–2291, Apr. 2019, doi: 10.1007/s11665-019-03974-8.
- [113] W. Yang, Q. Guo, J. Fan, X. Guo, and Y. Zhao, "Effect of aging temperature on energy dissipation and high-cycle fatigue properties of FV520B stainless steel," *Eng Fract Mech*, vol. 242, Feb. 2021, doi: 10.1016/j.engfracmech.2020.107464.
- [114] K. Kwak, Y. Mine, S. Morito, T. Ohmura, and K. Takashima, "Correlation between strength and hardness for substructures of lath martensite in low- and medium-carbon steels," *Materials Science and Engineering: A*, vol. 856, Oct. 2022, doi: 10.1016/j.msea.2022.144007.
- [115] B. M. D. Cunningham, "Increasing service life of industrial LP turbine blades: fatigue behaviour of martensitic stainless steel materials in notches with overloads," 2019.
- [116] G. R. Irwin, "Plastic zone near a crack and fracture toughness," in *Proceedings of the 7th Sagamore Ordnance Materials Conference*, New York, 1960, pp. 63–78.
- [117] Y. Deng, Y. Liang, F. Zhao, F. Xu, M. Yang, and S. Long, "Influence of Microstructure on Tensile Properties and Fatigue Crack Propagation Behavior for Lath Martensitic Steel," *Crystals (Basel)*, vol. 13, no. 9, Sep. 2023, doi: 10.3390/cryst13091392.

- [118] M. L. Zhu, F. Z. Xuan, and G. Z. Wang, "Effect of microstructure on fatigue crack propagation behavior in a steam turbine rotor steel," *Materials Science and Engineering: A*, vol. 515, no. 1–2, pp. 85–92, Jul. 2009, doi: 10.1016/j.msea.2009.02.050.
- [119] M. Yang, Y. Zhong, and Y. L. Liang, "Competition mechanisms of fatigue crack growth behavior in lath martensitic steel," *Fatigue Fract Eng Mater Struct*, vol. 41, no. 12, pp. 2502–2513, Dec. 2018, doi: 10.1111/ffe.12851.
- [120] J. P. Lucas and W. W. Gerberich, "Temperature and Grain Size Effects on Threshold and Fatigue Crack Propagation in a High Strength Low Alloy Steel," 1981.
- [121] Y. Nakai and K. Tanaka, "THE EFFECTS OF STRESS RATIO AND GRAIN SIZE ON NEAR-THRESHOLD FATIGUE CRACK PROPAGATION IN LOW-CARBON STEEL," 1981.
- [122] T. Xu, Y. Feng, S. Song, and D. Wang, "Fatigue crack propagation behaviour of steels with different microstructures," *Materials Science and Engineering: A*, vol. 551, pp. 110–115, Aug. 2012, doi: 10.1016/j.msea.2012.04.103.
- [123] L. Dimithe Aboumou, G. Henaff, M. Arzaghi, and S. Pommier, "Influence of temperature and long term ageing on the Fatigue Crack Growth in a precipitation hardened martensitic stainless steel," in *Procedia Engineering*, Elsevier Ltd, 2013, pp. 226–232. doi: 10.1016/j.proeng.2013.12.077.
- [124] B. M. D. Cunningham *et al.*, "Fatigue crack initiation and growth behavior in a notch with periodic overloads in the low-cycle fatigue regime of FV566 ex-service steam turbine blade material," *Fatigue Fract Eng Mater Struct*, vol. 45, no. 2, pp. 546–564, 2022, doi: 10.1111/ffe.13617.
- [125] K. A. Soady, "Reducing conservatism in life assessment approaches: Industrial steam turbine blade to disc interfaces and the shot peening process," University of Southampton, 2013.
- [126] B. He, "Fatigue crack gowth behaviour in a shot peened low pressure steam turbine blade material," University of Southampton, 2015.
- [127] J. Hebert and M. M. Khonsari, "Effect of surface roughness and polishing orientation on fatigue life and fracture fatigue entropy," *Fatigue Fract Eng Mater Struct*, vol. 47, no. 5, pp. 1514–1530, May 2024, doi: 10.1111/ffe.14260.
- [128] A. Casagrande, G. P. Cammarota, and L. Micele, "Relationship between fatigue limit and Vickers hardness in steels," *Materials Science and Engineering: A*, vol. 528, no. 9, pp. 3468–3473, 2011, doi: 10.1016/j.msea.2011.01.040.
- [129] J. C. Pang, S. X. Li, Z. G. Wang, and Z. F. Zhang, "Relations between fatigue strength and other mechanical properties of metallic materials," *Fatigue Fract Eng Mater Struct*, vol. 37, no. 9, pp. 958–976, 2014, doi: 10.1111/ffe.12158.
- [130] M. Benedetti, V. Fontanari, B. Winiarski, M. Allahkarami, and J. C. Hanan, "Residual stresses reconstruction in shot peened specimens containing sharp and blunt notches by experimental measurements and finite element analysis," *Int J Fatigue*, vol. 87, pp. 102–111, Jun. 2016, doi: 10.1016/j.ijfatigue.2016.01.020.
- [131] J. C. Kim, S. K. Cheong, and H. Noguchi, "Residual stress relaxation and low- and high-cycle fatigue behavior of shot-peened medium-carbon steel," *Int J Fatigue*, vol. 56, pp. 114–122, 2013, doi: 10.1016/j.ijfatigue.2013.07.001.

- [132] C. You, M. Achintha, K. A. Soady, N. Smyth, M. E. Fitzpatrick, and P. A. S. Reed, "Low cycle fatigue life prediction in shot-peened components of different geometries—part I: residual stress relaxation," *Fatigue Fract Eng Mater Struct*, vol. 40, no. 5, pp. 761–775, May 2017, doi: 10.1111/ffe.12543.
- [133] B. Y. He, K. A. Soady, B. G. Mellor, G. Harrison, and P. A. S. Reed, "Fatigue crack growth behaviour in the LCF regime in a shot peened steam turbine blade material," pp. 1–28.
- [134] M. Pavan, D. Furfari, B. Ahmad, M. A. Gharghouri, and M. E. Fitzpatrick, "Fatigue crack growth in a laser shock peened residual stress field," *Int J Fatigue*, vol. 123, pp. 157–167, Jun. 2019, doi: 10.1016/j.ijfatigue.2019.01.020.
- [135] K. A. Soady, "Life assessment methodologies incoroporating shot peening process effects: Mechanistic consideration of residual stresses and strain hardening: Part 1 - Effect of shot peening on fatigue resistance," *Materials Science and Technology (United Kingdom)*, vol. 29, no. 6, pp. 637–651, 2013, doi: 10.1179/1743284713Y.0000000222.
- [136] E. Natkowski, P. Sonnweber-Ribic, and S. Münstermann, "Determination of fatigue lifetimes with a micromechanical short crack model for the high-strength steel SAE 4150," *Int J Fatigue*, vol. 156, Mar. 2022, doi: 10.1016/j.ijfatigue.2021.106621.
- [137] W. Jiang *et al.*, "Fatigue life prediction of 316L stainless steel weld joint including the role of residual stress and its evolution: Experimental and modelling," *Int J Fatigue*, vol. 143, Feb. 2021, doi: 10.1016/j.ijfatigue.2020.105997.
- [138] D. W. MacLachlan, V. Karamitros, and F. P. E. Dunne, "Mechanistic modelling of fatigue nucleation and short crack growth in polycrystalline alloys," *J Mech Phys Solids*, vol. 177, Aug. 2023, doi: 10.1016/j.jmps.2023.105314.
- [139] H. Li, J. Zhang, L. Hu, and K. Su, "Notch fatigue life prediction of micro-shot peened 25CrMo4 alloy steel: A comparison between fracture mechanics and machine learning methods," *Eng Fract Mech*, vol. 277, Jan. 2023, doi: 10.1016/j.engfracmech.2022.108992.